Universitat de València – Estudi General

Departament de Física de la Terra i Termodinàmica

New algorithms for atmospheric correction and retrieval of biophysical parameters in Earth Observation. Application to ENVISAT/MERIS data

---

TESIS DOCTORAL
Luis Guanter
2006

José F. Moreno Méndez, Profesor Titular de Física de la Tierra, Departamento de Física de la Tierra y Termodinámica, Facultad de Física, Universidad de Valencia,

INFORMA:

Que la Tesis Doctoral titulada “New algorithms for atmospheric correction and retrieval of biophysical parameters in Earth Observation. Application to ENVISAT/MERIS data.” ha sido realizada bajo su dirección en el Departamento de Física de la Tierra y Termodinámica de la Universidad de Valencia por Don Luis Guanter Palomar.

Y para que conste a los efectos oportunos, presenta la memoria del mencionado trabajo y firma este informe.

Burjassot, 20 de Diciembre de 2006.

Agradecimientos

No es ésta una de esas tesis que parecen más un tornado que una investigación por la calma que dejan cuando se acaban. En mi caso no siento que me he quitado un gran peso de encima. Más bien al revés, he disfrutado haciendo el trabajo que hay debajo, y casi también poniéndolo en papel, que supongo que es de lo que se trata cuando alguien se dedica a algo tan ingrato en lo material como la investigación. Sí que es verdad que ha habido que hacer un asfixiante sprint final para llegar a cumplir los plazos administrativos. Espero que no se note demasiado en los resultados (alguna errata sí se ha escapado, seguro). Sin embargo, es éste el momento en que no me gustaría ir rápido, pues tengo mucha gente alrededor que se merece más que unas palabras apresuradas.

En primer lugar está Jose Moreno como director de la tesis. Es obvio decir que sin su contribución este trabajo no habría visto la luz. Estando cerca de alguien con un conocimiento tan grande de todos los aspectos que rodean a este negocio parece que la tesis se dirija sola, sin que haya una persona encima diciendo qué hacer a cada paso. Aún así estoy muy agradecido por el tiempo que me ha dedicado, que, hasta donde yo sé, es su bien más escaso. Es fácil trabajar con alguien que siempre tiene la respuesta cuando tú no sabes qué camino tomar. Espero haber estado a la altura.

Dentro del mismo grupo LEO he de nombrar en primer lugar a Luis, por las incontables horas compartidas y conversaciones tenidas, algunas veces sobre temas científicos y muchas otras sobre todo lo contrario. Nunca dejará de asombrarme la capacidad de ayudar que tiene cuando alguien se lo pide, aun a costa de dejar lo que está haciendo. Compañero, he aprendido mucho de ti, pero te necesito doctor pronto, así que empieza a decir que no, a mí y al resto. También en el día a día han estado el acento murciano de Gloria (véase la portada de la tesis para una muestra de su arte) y últimamente Jordi, a los que agradezco muchos ratos y una bonita convivencia. Miembro del grupo en pleno derecho, aunque la veamos poco, es Sole Gandía, la Directora de Departamento más encantadora que ha habido en la Universidad de Valencia. Es difícil de explicar cómo contagia su alegría con sólo entrar al laboratorio para saludar. Siguiendo con la gente del grupo a la que vemos menos de lo que quisiéramos queda la exiliada Mari Carmen, que también lleva lo suyo con MERIS en lejanos lugares.

También quiero acordarme de mucha gente del Departamento, que los 4 años que llevo en él dan para mucho. Agradecimientos particulares a Carlos, por una plantilla de LaTeX tan buena como ésta y por una amistad que ya viene de largo, a Víctor, por muchos datos y discusiones sobre aerosoles, y a Juan Carlos Jiménez porque le debo una portada para su próxima tesis (nota: sí, la portada la he hecho yo, pero ha tenido influencias muy beneficiosas). No puedo citar a todo el resto de becarios/precarios aquí porque son muchos (y buenos). Una muestra "random": Álex, Bea, Almu, Mónica, Guillem, Raquel, Jose Luis, Vladimir... También un agradecimiento general para la gente "mayor" del Departamento, y en especial a Quique O Rei de Secretarios y a Pilar Utrillas por lo mucho que me están facilitando los ∞ trámites administrativos que hay que cubrir para presentar una tesis en esta nuestra Universidad.

Luis Gómez Chova, Javier Calpe y el resto del grupo GPDS (Julia, Joan, Gustavo...) no son ni del grupo LEO ni del Departamento, pero puede que sea la gente con la que más y mejor colaboración científica he tenido. Y con los que más veces he comido también. Particularizando, Luis parece que puede hacerlo todo, y todo bien. Sólo le falta aplicarlo a la tesis, como su tocayo Alonso. Ya llevamos bastantes batallas juntos en las cosas de MERIS y CHRIS, y por mi parte que no se acaben nunca. Javier es algo así como el "jefe que todos querríamos tener", por capacidad de trabajo, simpatía y respeto. Un espejo en el que mirarse para los años que vienen. El resto, pues igualmente competentes, tanto en el trabajo diario como en el análisis de calidad de las diferentes cafeterías del campus.

Siguiendo con personas especiales, hay alguien a quien no sé dónde colocar, porque no puedo decidir si me ha influido más en lo personal o en lo universitario. Es Jesús (Yosu de nombre artístico). Lleva muchos años siendo una especie de inspiración que guía los pasos que doy en la investigación. Podría hasta convencerme de que me dedicara al crecimiento cristalino como su fiel escudero. Sólo yo sé lo que le echo de menos desde que se fue de Valencia, y espero que algún día la vida nos vuelva a poner los despachos cerca.

Sin duda importantísimas para el desarrollo final de la tesis han sido las estancias en el DLR y el University College London. En inglés, I want to thank Dr. Rudolf Richter and the people from the DLR Imaging Spectroscopy Group for the nice and fruitful days we shared during my stay in Munich. Dear Rolf, your contribution to this thesis has been extremely significant, for all the discussions about atmospheric correction issues and for the accurate review of the manuscript. I've just taken up German lessons, but I'm already able to say "Danke schön mein Freund". I also want to acknowledge Dr. Philip Lewis and the other people from the Department of Geography of UCL (Mat, Tristan, Martin...) for their warm hosting during otherwise cold days in London. I got a good background in BRDF models from their wide expertise there, which unfortunately couldn't be included in this dissertation because of time constraints. Please, Lewis, don't be disappointed, I know that the work deserved to be here. I wish we could keep on collaborating in the future.

A un nivel de importancia parecido tengo que poner a los que, sin tener nada que ver con la Universidad, me permiten mantener un cierto equilibrio vital cuando la corrección atmosférica se pone demasiado densa. A Cristóbal, Josep, Máximo y demás jugones por tantos, tantos, tantos buenos ratos, y por unos pocos menos partidos ganados. No podría dedicarme a esto como lo hago si al apagar el ordenador y llegar al entrenamiento no hubiera alguien preguntándome "base, cuántas atmósferas has corregido hoy?" Amunt Moncada! También tengo que acordarme de Nacho y de su futura mujer Cristina (que mayores nos hacemos, amigo) por ser de ese tipo de gente que sabes que siempre estará ahí, pase lo que pase, y que te hace sentir afortunado por su amistad.

En un entorno más "institucional", quiero agradecer al Ministerio de Educación y Ciencia por la beca predoctoral que me ha permitido dedicarme a esto durante los últimos 4 años; a Ramón Peña, Jose Antonio y Antonio, del CEDEX, por las muchas veladas en Frascati, los datos de sus medidas en los pantanos y la financiación para implementar el algoritmo de forma que pueda ser distribuido a la comunidad de MERIS; a la red AERONET-NASA y sus investigadores por los datos proporcionados para la validación de las estimaciones de aerosoles y vapor de agua, y a la Agencia Espacial Europea por los datos y las campañas sobre los que se construye este trabajo.

Y por último, aunque por entrega, preocupación, cariño y mil cosas más deberían de ser los primeros, mi familia, en especial mis padres, mi hermana y mi tía. A veces me asusta pensar lo mucho que me dais para lo poco que recibís a cambio. Os quiero mucho.

Luis Guanter

Valencia,
18 de Diciembre de 2006.

Contents

Abstract

An algorithm for the derivation of atmospheric and surface biophysical products from the MEdium Resolution Imaging Specrometer Instrument (MERIS) on board ENVIronmental SATellite (ENVISAT/MERIS) Level 1b data over land has been developed. Georectified aerosol optical thickness (AOT), columnar water vapor (CWV), spectral surface reflectance and chlorophyll fluorescence (CF) maps are generated. Emphasis has been put on implementing a robust software able to provide those products on an operational manner, making no use of ancillary parameters apart from those attached to MERIS images. For this reason, it has been named *Self-Contained Atmospheric Parameters Estimation from MERIS data* (SCAPE-M). The fundamentals of the algorithm and the validation of the derived products are presented in this thesis. Errors of ±0.03, ±4% and ±8% have been estimated for AOT, CWV and surface reflectance retrievals, respectively, by means of a sensitivity analysis. More than 200 MERIS images have been processed in order to assess the method performance under a range of atmospheric and geographical conditions. A good comparison is found between SCAPE-M AOT retrievals and ground-based measurements taken during the SPectra bARrax Campaigns (SPARC) 2003 and 2004, except for a date when an episode of Saharan dust intrusion was detected. Comparison of SCAPE-M retrievals with data from AErosol RObotic NETwork (AERONET) stations showed a square Pearson's correlation coefficient R^2 of about 0.7–0.8. Those values grow up to more than 0.9 in the case of CWV after comparison with the same stations. A good correlation is also found with the ESA Level 2 official CWV product, although slight different performances with varying surface elevation are detected. Retrieved surface reflectance maps have been intercompared with reflectance data derived from MERIS images by the Bremen AErosol Retrieval (BAER) method in the first place. A good correlation in the red and near-infrared bands was found, although a considerably higher proportion of processed pixels was provided by SCAPE-M. The comparison with reflectance maps derived from the Compact High Resolution Imaging Spectrometer (CHRIS) on board the PRoject for On–Board Autonomy (PROBA), in turn validated with ground-based reflectance measurements, was also achieved. The estimation of CF from MERIS data has been presented in the last place. Comparison with other vegetation products and finer spatial resolution Compact Airborne Spectrographic Imager (CASI) -derived CF maps suggest CF to be a promising tool in the monitoring of the vegetation status from space.

Introduction

Earth Observation covers those procedures focused on monitoring our planet by means of electromagnetic radiation sensors located on spaceborne or airborne platforms. The information they provide represents spatial and temporal scales completely different to those obtained from ground measurements. Particularly, the optical passive remote sensing lies on the study of the surface by means of the solar radiation reflected by the observed target and transmitted through the atmosphere to the sensor.

Many advances in instrumental design and processing algorithms have been achieved in the last decade. Those advances have enabled the launch of the ENVISAT mission by the European Space Agency (ESA). Different Earth Observation instruments were placed on board ENVISAT. MERIS is one of them. The following paragraph is written at the European Space Agency web site section devoted to the ENVISAT/MERIS mission:

> Medium Resolution Imaging Spectrometer (MERIS) has been launched by the European Space Agency (ESA) onboard its polar orbiting Envisat Earth Observation Satellite. MERIS, primarily dedicated to Ocean Colour Observations has in the past broadened its scope of objectives to atmospheric and land surface related studies. This is permitted by the large flexibility that sensor and ground segment provide[1].

The work presented in this thesis is intended to support that renewed interest in MERIS data for atmospheric and land studies: to provide new operational tools for the retrieval of atmosphere and surface biophysical parameters from MERIS data taken over land. With this purpose, new algorithms for the derivation of aerosol optical thickness, precipitable water vapor, surface reflectance and chlorophyll fluorescence maps have been developed.

Deriving atmosphere and surface parameters from remote sensing data implies accounting for the coupling between atmosphere and surface radiative effects. If there were no atmosphere around the Earth, the solar radiation would only be perturbed when it reached the surface. Thus, solar radiation would provide a useful representation of the surface nature and the associated dynamics when it is registered by a satellite sensor. Nevertheless,

---

[1] `http://envisat.esa.int/object/index.cfm?fobjectid=1665&contentid=3744`

Figure 1: A mosaic of global land cover from ENVISAT's MERIS instrument. Credit: ESA.

the atmospheric influence on the visible and infrared radiation is strong enough to modify the reflected electromagnetic signal, causing the loss or the corruption of part of the carried information. The interaction of the solar radiation with the atmospheric components consists of absorption and scattering processes. The absorption decreases the intensity of the radiation arriving at the sensor, what causes a loss of the brightness of the target, while the scattering acts modifying the propagation direction, resulting in, e.g., the backwards atmospheric reflection of part of the incoming radiation without reaching the surface, the contamination of the data by photons coming from the target environment scattered in the observation direction or the attenuation of the signal by the removal of photons in their travel to the sensor. As a result, any set of remote sensing data needs for a previous removal of the atmospheric effects in the initial processing steps, to ensure a maximal accuracy and reliability in the results inferred by the latter exploitation of the data. This is the fundamental base of the atmospheric correction in optical remote sensing: the elimination of the atmospheric effects from the useful signal reflected by the target in the observer's line of sight. A traditional statement of the problem can be found, for instance, in Kaufman [1989].

For an accurate atmospheric correction, the ideal situation would be the availability of an atmospheric product containing the main atmospheric information simultaneous to the image acquisition and with the same spatial resolution. This can be accomplished if atmospheric retrievals are done from the data themselves, by means of the inversion of the measured radiances in some properly selected wavelengths. In addition, having a global scale monitoring of the atmospheric components is becoming more and more important in climatologic aspects: aerosols are considered to contribute significantly to the global radiation budget, with its role in the direct radiative forcing and cloud formation (e.g., Charlson et al. [1992]; Kaufman et al. [2002]; Ramanathan et al. [2001]), and gases, especially water vapor, are responsible for the atmospheric greenhouse effect (e.g., Peixoto and Oort [1992]; Raval and Ramanathan [1989]; Rind [1998]). As a result, the satellite remote sensing of atmospheric properties is not only a single step in the atmospheric correction process, but also a requirement for an adequate modelling of the Earth's climate.

Moreover, more than 30 years of research at the laboratory level support the vegetation chlorophyll fluorescence emission to be one the most direct indicators of the vegetation photosynthetic activity. Attempts of retrieving that signal also at the satellite level are just being started. The measurement of such weak signal usually involves measuring inside absorption bands, where the emitted radiation is enhanced respecting to the reflected contribution. The accurate characterization of the O_2-A absorption at MERIS band 11 enables the estimation of chlorophyll fluorescence from MERIS data. The fact that fluorescence retrieval is based on the evaluation of an atmospheric absorption band, affected by factors such as surface elevation or aerosol loading, suggests it must be framed in a proper atmospheric correction scheme.

In this framework, a full atmospheric correction processor for MERIS data over land has been implemented. Two major points motivated the selection of MERIS data and atmospheric correction to be put together in this thesis. On the one hand, MERIS offers a unique spectral configuration for the retrieval of both atmosphere and surface parameters: two fine bands measuring at the O_2-A and water vapor absorptions are combined with other thirteen channels providing high-accuracy measurements at the blue to the near-infrared spectral regions (see Appendix B for further technical information). On the other hand, the lack of operative methods for the aerosol retrieval and atmospheric correction of MERIS data over land, as well as identified problems in the corresponding ESA Official Level 2 reflectance and aerosol optical thickness products, were known. Indeed, no software for the atmospheric correction of MERIS Level 1b data is yet available for the scientific community, but only Level 2 data can be converted to surface reflectance with the tools freely supplied by ESA. For this reason, the algorithm presented in this thesis has been implemented in an operational form, under the name *Self-Contained Atmospheric Parameters Estimation from MERIS data* (SCAPE-M). Detailed descriptions of the method features and performance are given along this document.

The work is organized in 4 parts:

- The first one is dedicated to a global introduction of some topics related to atmospheric correction, and is divided into two chapters. One is devoted to a review of general aspects of atmospheric radiative transfer, with a description of the atmospheric constituents and their optical properties, an overview of the common mathematical formulations of the problem and the ways it may be handled, and some comments on the computer codes implemented for an operational evaluation of the radiative transfer across the atmosphere. The second chapter is a short compilation of the current state-of-the-art atmospheric correction methods, with a brief description of the most representative algorithms.

- The second part addresses the developed methodology for the obtainment of the biophysical products. A general description of the SCAPE-M algorithm is made in the third chapter. Firstly, it presents the rationale for obtaining final aerosol optical thickness, water vapor and surface reflectance maps. Secondly, the design of the look-up table generated for the atmospheric radiative transfer computation is presented. Estimations of the errors associated to aerosol, water vapor and reflectance retrievals are carried out by a sensitivity analysis discussed in the last section of the chapter.

  The fourth chapter deals with the validation of the atmospheric and reflectance products. A wide data-base of MERIS images has been processed and compared with both local measurements taken during dedicated field campaigns and with atmospheric measurements from the AERONET stations spread all over the world. Surface reflectance retrievals are compared with another MERIS-based reflectance product and with reflectance maps derived from CHRIS-PROBA.

  The estimation of vegetation fluorescence from MERIS data is detailed in the fifth chapter. It is included in the radiative transfer scheme as an extra source function at the surface so that a proper evaluation of all the atmospheric and geometrical/spectral factors affecting the O_2-A absorption depth is achieved. Estimations of chlorophyll fluorescence from remote sensors in radiance units are presented. MERIS-derived fluorescence maps are compared with other vegetation products and with fluorescence estimations from a hyperspectral airborne sensor.

- After, a chapter summarizing the main points discussed along the thesis and highlighting the main conclusions is included.

- The work is closed by a series of appendices about different aspects related to the topics discussed along the thesis.

Part I

Background

Chapter 1

Principles of Atmospheric Radiative Transfer

This chapter provides a theoretical introduction to the interaction between atmosphere, surface and radiation, which supports the basis of the atmospheric correction of remote sensing data. The absorption and scattering processes affecting the solar electromagnetic radiation in its path across the atmosphere are described. In particular, a brief description of the atmospheric components, gases and aerosols, and its particular influence on the radiation is done firstly; next, some mathematical formulations of the macroscopic radiative transfer are detailed. Finally, the way those formulations are implemented in computer codes is described, focusing on those codes actually used in this work. Some references which cover widely these topis are Hapke [1993]; Lenoble [1993]; Liou [2002].

1.1. Absorption and Scattering of Solar Radiation in the Atmosphere

1.1.1. Earth Atmosphere and Solar Radiation

The inner atmospheric layer surrounding the Earth surface, formed by the lower and middle atmosphere, is an homogeneous gaseous blend with a thickness of about 80 or 90 km. It is permanently composed of 78% of nitrogen, 21% of oxygen and 1% of argon, and presents variable concentrations of other minor components. In the bulk of this gaseous mixture are also the aerosols, solid and liquid particles with different sources and sizes, ranging from the small molecular clusters to raindrops or snowflakes. Both molecules and aerosols are optically active, causing the absorption and the scattering of the electromagnetic radiation.

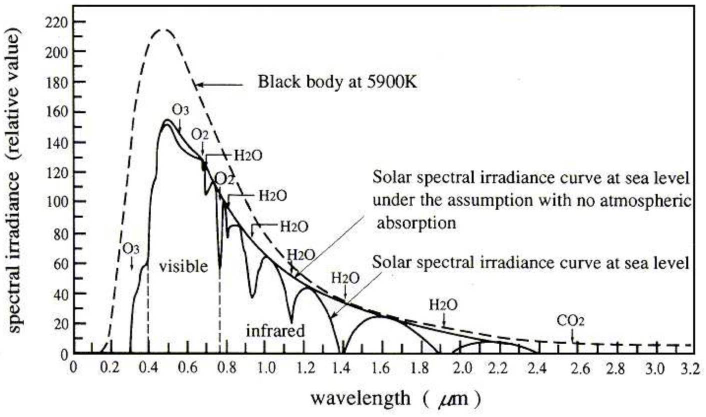

Figure 1.1: Solar irradiance at the top of the atmosphere and at the sea level, and blackbody emission spectrum at 5900 K.

The solar radiation that we use for the observation of the surface travels throughout this complex media before being reflected by the surface and arriving at the sensor. The Sun is the most powerful energy source in the spectral region from 0.3 to 3.0 μm, which is known as solar spectrum. The solar radiation spectrum follows the shape of the Planck's emission for a blackbody of about 5900 K. Figure 1.1 shows the spectral features of the solar radiation, outside the atmosphere (external line) and at the sea level (internal line). The maximum is located in 0.47 μm, being about 20% of the solar energy in wavelengths lower than that, and a 44% in the visible band, between 0.40 and 0.76 μm.

The difference between the two lines means the depletion of the solar flux in a clear atmosphere. The depletion of solar irradiance[1] in the ultra-violet (UV) region (< 0.4 μm) is chiefly due to the absorption of molecular oxygen and ozone. In the visible (VIS, 0.4-0.7 μm), the depletion of solar flux is caused by the absorption produced by oxygen red bands, the ozone visible bands, and some water vapor weak bands. In the near-infrared (NIR, 0.7-1.0 μm), the prime absorber is water vapor with contributions from carbon dioxide in the 2.0 and 2.7 μm wavelengths. Other minor absorbers, such as N_2O, CO and CH_4 also contribute to the depletion of the solar flux, but are less significant. It is evident that water vapor is the most important absorber in the solar NIR spectrum, which contains about 50% of the solar energy.

1.1.2. Gaseous Absorption in the Visible and Near-infrared

The main absorptive gaseous species in the solar spectrum are then molecular oxygen, ozone, water vapor and carbon dioxide. The absorption features these gases cause in

---

[1] The term irradiance is referred to the radiant flux (radiant energy per unit time) density received on a differential surface element from an isotropic source. It is usually given in $Wm^{-2}\mu m^{-1}$.

the top-of-atmosphere (TOA) radiances are those we have to deal with when facing the atmospheric correction of remote sensing data. A typical transmittance spectrum in the visible and near-infrared regions (VNIR) covered by MERIS is plotted in Fig. 1.2. The main absorption bands due to molecular oxygen, water vapor and ozone are pointed out.

Molecular Oxygen

Molecular oxygen has absorption bands in the VNIR region. The most important bands in the red are the A band, centered at 0.762 μm, the B band, at 0.688 μm, and the γ band, at 0.628 μm. The absorption of the solar radiation due to O_2 in the visible is important in the middle and upper atmospheres, and affects the solar flux available in the surface. The accurate characterization of the oxygen-A absorption in MERIS provides an unprecedent source of information in medium-resolution spaceborne sensors which can be used for a number of applications. For example, the oxygen-A band has been proposed for the remote sensing of the cloud top pressure [Fischer et al., 2000; Preusker et al., 2002], and also of the surface pressure [Ramon and Santer, 2003; Santer et al., 1999], due to the correlation between the depth of this band and the pressure at the observed surface level. It is also the basis of the algorithm designed for the estimation of solar-induced vegetation fluorescence which will be described in Chapter 5.

Ozone

Ozone shows weak absorption bands in the VNIR regions from about 0.44 to 1.8 μm. These bands are referred to as *Chappuis bands*. The absorption coefficients in these bands are only slightly dependent on the temperature, although the ozone absorption does not present strong temporal or spatial variations. The strongest O_3 absorption around 600 nm is skipped by the MERIS band configuration so that only a residual continuum absorption affects MERIS measurements.

Water Vapor

Water vapor is an asymmetric molecule with a permanent dipole moment, showing then a pure rotation spectrum located in the infrared, extending approximately between 16 and 150 μm, with a total intensity around 1850 $\mathrm{cm}^{-2}\mathrm{atm}^{-1}$ at 296 K. However, overtones and combination bands are present in the NIR region, resulting in an important absorption of solar radiation. They are centered at 0.90, 0.94, 0.97, 1.1, 1.38 and 1.87 μm, and are commonly identified in groups by the Greeks letters $\rho\sigma\tau$ (for the association of the three first bands to form a wider one centered in 0.94 μm), ϕ, Ψ, and ω, respectively. There are two other weak bands in the red-NIR regions, centered at 0.72 and 0.82 μm, with a significant contribution to the solar heating of the atmosphere. The absorption of weaker bands in the visible region can be neglected. The left wing of the $\rho\sigma\tau$ band centered at 940 nm is used for the retrieval of columnar water vapor from MERIS data, as it will be discussed in Chapter 3.

Carbon Dioxide

Apart from two strong bands in the middle ($\sim 4.3\mu$m) and thermal IR ($\sim 15.0\ \mu$m) used for the nighttime detection of atmospheric temperatures, carbon dioxide exhibits a number of rather weak overtones and combination bands in the solar region: 2.0, 1.6 and 1.4 μm. The stronger 2.7 μmband of CO_2 overlaps with the 2.7 μm band of H_2O and contributes to the absorption of solar flux in the lower stratosphere. None of them is located in the spectral range covered by MERIS.

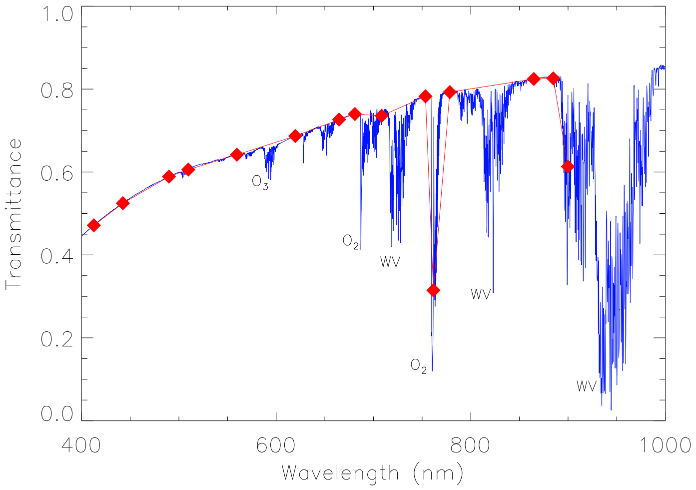

Figure 1.2: Direct atmospheric transmittance spectrum due to the main gaseous absorbers in the VNIR spectral regions. Diamonds show the same spectrum after resampling to the MERIS band configuration.

1.1.3. Atmospheric Scattering

After the collision with an atmospheric particle, molecule or aerosol, a part of the energy carried by the radiation is scattered, creating the diffuse radiation field. The evaluation of this phenomenon becomes easier if the assumption of spherical particles is made, as the Maxwell equations to be solved can be written in scalar spherical coordinates, instead of complex tensorial formulations, and a spherical symmetry can be considered.

The solution is particularly simple if the particle is much smaller than the radiation wavelength, as well as being spherical. This solution was proposed by Lord Rayleigh in 1871 [Rayleigh, 1871a,b], and is used to explain the scattering by molecules and the related blue color of the sky.

When the particle size is similar to the incident radiation wavelength the Rayleigh theory is no longer valid. A more general theory was introduced separately by Lorenz [1890] and Mie [1908], so it referred to as *Lorenz-Mie scattering.* They derived the solution for the interaction of a plane wave with an isotropic homogeneous sphere. Nevertheless, the scattering by particles of any size and shape can, in principle, be solved with Lorenz-Mie theory, which relies on classical electromagnetic equations with continuity conditions at the boundary between the particle and its surroundings. However, in practice, only simple geometrical shapes, such as cylinders, ellipsoids, and spheres can be handled. The Rayleigh theory is a particular case of the Lorenz-Mie theory.

The effect of particle size on scattering is inferred by a physical term called *size parameter.* For a spherical particle it is defined as the ratio of the particle circumference to the incident wavelength λ; i.e., $x = 2\pi a/\lambda$, where a is the particle radius. If λ is given in meters, it is considered that:

- When $x << 1$, scattering is well explained by the Rayleigh theory; in clear sky conditions it is applied to molecules, with a size about 1 Å.
- When $x >> 1$, scattering is analyzed by means of the Geometric Optics.
- Intermediate case, scattering is interpreted by the Lorenz-Mie theory; aerosols, larger than 10 Å, are the predominant scatterers.

Some of these comments are summarized in Fig. 1.3. It also connects typical values of a and λ with the aerosol types and the use of the radiation in these conditions.

In those media with a high concentration of scatterers, the photons scattered by a particle are likely to collide with other ones, taking place the process called *multiple scattering* (radiation scattered more than once) which is the source of diffuse radiation. Some of the incident light that has been first scattered away from a single direction may reappear in this direction by means of multiple scattering. This is an important process for the transfer of radiant energy in the atmosphere, especially when aerosols and clouds are involved.

In atmospheric scattering, it is generally assumed that the light scattered by molecules and particles has the same wavelength as the incident light. It is noted, however, that high-energy laser light can produce phenomena such as *Raman scattering* by shifting frequencies, which can be used for the remote sensing of water vapor. Atmospheric molecules and particles are separated by distances much greater than their sizes, and to some extent

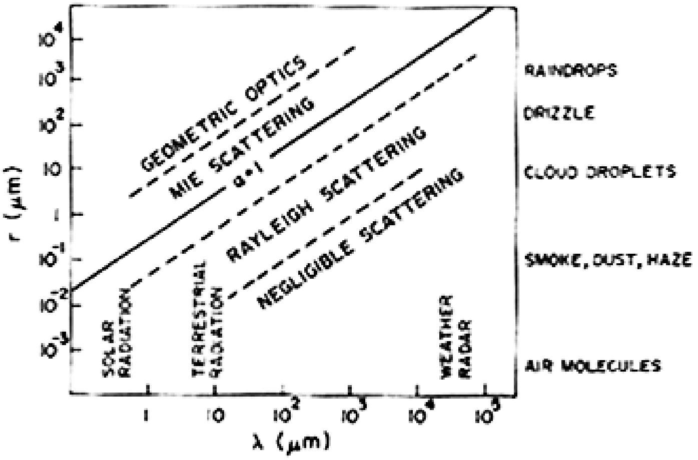

Figure 1.3: Scattering as a function of the incident radiation wavelength and of the radius of the scatterer.

describe random trajectories, so there is not a systematic relation between the phases of the scattered waves. Then, the intensities of different colliding rays may be simply added, as if each particle scattered light in exactly the same way as if all other particles did not exist. This is referred to as *independent scattering*, and greatly simplifies the problem of light scattering by a collection of particles, because it allows the use of energy quantity instead of electric field in the analysis of the propagation of electromagnetic waves in planetary atmospheres.

Two magnitudes must be introduced to quantify the intensity of the scattered light, the *phase function*, $P(\Theta)$, and the *scattering cross section*, σ_s. The phase function describes the spatial distribution of the scattered radiation. It is normalized in the way

$$\int_{4\pi} P(\Theta)\, d\Theta = 4\pi, \tag{1.1.1}$$

where Θ is the scattering angle (angle between the incident and scattered waves). The scattering cross section represents the amount of incident energy that is removed from the original direction because of a single scattering event such that the energy is redistributed isotropically on the area of a sphere whose center is the scatterer and whose radius is r. The scattered intensity is proportional to those variables, and can be expressed, for molecules and aerosols, by

$$I(\Theta) = I_0 \frac{\sigma_s}{4\pi r^2} P(\Theta) \tag{1.1.2}$$

where I_0 is the intensity of the incident radiation and r the distance to the scatterer center.

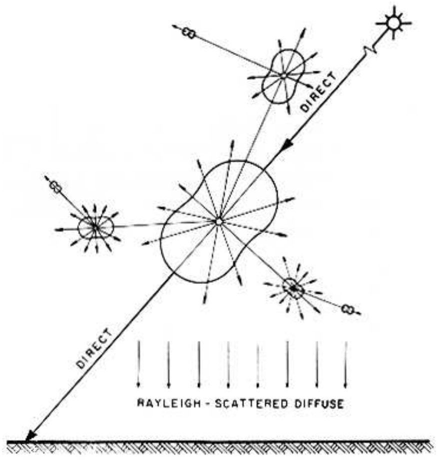

Figure 1.4: Scheme of the molecular scattering of solar radiation.

Molecular scattering

By assuming that the solar radiation is unpolarized, the Rayleigh theory calculates the expressions of the phase function

$$P(\Theta) = \frac{3}{4}(1 + cos^2\Theta) \tag{1.1.3}$$

and the scattering cross section

$$\sigma_s = \frac{\alpha^2 128\pi^5}{3\lambda^4} \tag{1.1.4}$$

being α the *polarizability* of a small particle, that relates the incident electric field with the induced dipole moment. In general, α is a tensor, but in most cases those two vectors are aligned, being α a scalar. It is related to the atmospheric refractive m index by the *Lorentz-Lorenz formula*

$$\alpha = \frac{3}{4\pi N_s}\left(\frac{m^2-1}{m^2+2}\right), \tag{1.1.5}$$

where N_s is the number of molecules per unit volume. The refractive indices of atmospheric particles and molecules are complex numbers, with the real part corresponding to the scattering properties and the imaginary to the absorption. The imaginary part is so small in the case of air molecules in the solar visible spectrum that the absorption in this case can be neglected in the scattering discussion.

The term $1+\cos^2\Theta$ in Eq. 1.1.3 gives the angular distribution of the scattered photons. This an even function, what leads to a symmetry of the scattering in the forward and backward directions, as shown in Fig. 1.4.

Substituting in Eq. 1.1.2 the expressions in Eq. 1.1.3 and 1.1.4, we have the original formula derived by Rayleigh for the scattering of small nuclei,

$$I(\Theta) = \frac{I_0}{r^2}\alpha^2 \left(\frac{2\pi}{\lambda}\right)^4 \frac{1 + cos^2\Theta}{2}. \tag{1.1.6}$$

By this formula, the intensity of unpolarized sunlight scattered by a molecule depends on the wavelength of the incident light and the refractive index of air molecules contained in the polarizability. Although the refractive index is also slightly dependent on the wavelength, it can be stated that the intensity scattered by air molecules follows a law

$$I_\lambda \backsim \lambda^{-4} \tag{1.1.7}$$

This is a direct consequence of the Rayleigh theory, and the foundation for the explanation of the blue color of the sky. According with Eq. 1.1.7, blue light ($\lambda \approx 0.425$ μm) scatters about 5.5 times more intensity than red light ($\lambda \approx 0.650$ μm). Besides, as shown in Fig. 1.1, most of the solar light between the blue and the red regions of the visible spectrum, so it is apparent that the λ^{-4} law causes more blue light to be scattered than red, green and yellow, and so the sky, when viewed away from the Sun's disk, appears blue.

Of course, this effect is present in the top of atmosphere (TOA) spectral data acquired by a spaceborne sensor: even in clear sky conditions, with a low aerosol content, the radiances in the smaller wavelengths (around blue) show higher values than a ground-measured spectrum in the same location. Thus, in terms of atmospheric correction, a good parametrization of the gases characteristics (concentrations, surface pressure, vertical profiles ...) is important to remove the atmospheric effects, even outside the main absorption bands.

Particle scattering

Even though the nature and the shape of the atmospheric aerosols is highly variable, the Lorenz-Mie theory for spherical particles is usually employed for the study of their optical properties because of the advantages in the modelling that it provides.

The *Mie efficiency factor* Q_s is a dimensionless magnitude related to the strength of the scattering process. It is defined as the ratio between the scattering and the geometrical cross sections

$$Q_s \equiv \frac{\sigma_s}{\pi a^2}, \tag{1.1.8}$$

where a is the radius of the scatterer. For non-absorbing particles, the Mie efficiency factor can be derived from the Lorenz-Mie theory, expressed as a function of the Mie size parameter and the real refractive index by the following expansion:

$$Q_s = c_1 x^4 (1 + c_2 x^2 + c_3 x^4 + \ldots), \tag{1.1.9}$$

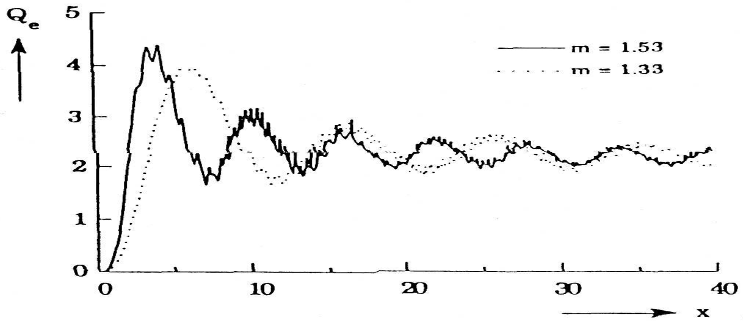

Figure 1.5: Mie efficiency factor Q_s versus Mie size parameter for two refractive indices (from Lenoble [1993]).

being the c_i coefficients given by

$$c_1 = \frac{8}{3}\left(\frac{m^2-1}{m^2+2}\right)^2 \tag{1.1.10a}$$

$$c_2 = \frac{6}{5}\left(\frac{m^2-1}{m^2+2}\right) \tag{1.1.10b}$$

$$c_3 = \frac{3}{175}\frac{m^6+41m^4-28m^2+284}{(m^2+2)^2} + \frac{1}{900}\left(\frac{m^2+2}{2m^2+2}\right)^2 [15+(2m^2+3)^2] \tag{1.1.10c}$$

A plot of Q_s versus the size parameter for two refractive indices is displayed in Fig. 1.5. The leading term is the dipole mode contribution associated with Rayleigh scattering. For molecules, $a \sim 10^{-4}\mu$m, so $x \sim 10^{-3}$ in the visible. Thus, the higher order terms can be neglected and the scattered intensity is proportional to λ^{-4}. For aerosols and cloud particles, $a \gtrsim 0.1\mu$m, and $x \gtrsim 1$ in the visible. In this case, the scattered intensity is less wavelength dependent and more size dependent. As a result, clouds and non-absorbing aerosols in the atmosphere generally appear white. In a cloudy atmosphere, the sky appears blue diluted with white scattered light, resulting in a less pure blue sky than would have been expected from pure Rayleigh scattering.

For very large particles, Fig. 1.5 shows that the extinction coefficient tends to $2\pi a^2$ with oscillations around this value. This limit can be explained in the following way: a fraction πa^2 of the radiant energy is intercepted by the particle and follows the laws of geometrical optics (reflection and refraction), whereas another fraction πa^2 corresponds to the perturbation introduced to the incident way by the obstacle of the particle and is diffracted. Some oscillations in Q_s are also observable: this is an interference phenomenon between the portion of the wave front that passes near the sphere and the portion transmitted through it. The part of the wave propagating outside the sphere undergoes a change in phase equal to $2\pi a/\lambda$ in a distance equal to a. The phase of the wave travelling through the sphere changes by $m2\pi a/\lambda$ in this distance, with m the real refractive index. Thus, destructive

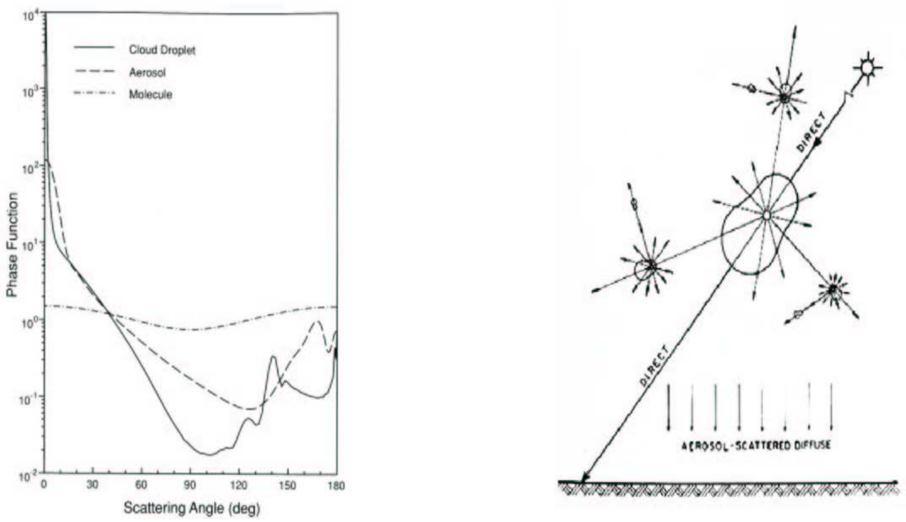

Figure 1.6: Spatial distribution of particle scattering. Left (a), phase functions for cloud droplets (∽ 10 μm), aerosols (∽ 1 μm) and molecules (∽ 10^{-4} μm) illuminated by 0.5 μmlight, computed from the Lorenz-Mie theory (from Liou [2002]). Right (b), analog scheme to the one in Fig. 1.4 for aerosol scattering.

interference will occur if the difference in phases, $(m-1)x$, is an odd multiple of π, and constructive interference if it is an even multiple of π. Those oscillations are not present if the absorption in the particle is significative.

Concerning the phase function, the other dependency in the scattered intensity showed in Eq. 1.1.2, it can be calculated from the Lorenz-Mie theory for spheres. The resultant phase functions for aerosols present a strong peak in the forward direction, bigger as the size parameter increases. It can also be explained for the wave diffraction after reaching the particle. Fig. 1.6a shows typical examples of the phase function for polydispersed cloud droplets (∽ 10 μm), aerosols (∽ 1 μm) and molecules (∽ 10^{-4} μm) illuminated by visible light. The mean size parameters in these cases are about 100, 10, and 10^{-3}, respectively. The forward diffraction peaks are observable for cloud droplets and aerosols. Fig. 1.6b presents the same scheme than in Fig. 1.4 for the case of aerosols. The dominant scattering in the forward direction is shown.

The sign of the atmospheric influence on the radiation arriving at an elevated sensor (increase or decrease respecting the measured signal at the ground level) depends strongly on the aerosols nature, as well as on the surface reflectance and on the viewing and illumination directions. In most cases, the net atmospheric effect is positive in the visible wavelengths, and negative in the longer ones. This is due to the dominant role played by the atmospheric scattering in the shorter wavelengths, as discussed in this section, and to the absorption by gases and aerosols in the NIR. The final brightness enhancement or reduction is the result of a tradeoff between scattering and absorption in each wavelength.

All these aspects must to be quantified in the atmospheric correction of the remote sensing data for a proper compensation of the atmospheric effects, as we shall describe in following chapters.

1.2. Aerosols

1.2.1. Importance of aerosol characterization

The influence that the atmospheric components have on the solar radiation has been described in the previous section. As a consequence of this influence, there is a need for an adequate characterization of gases and aerosols in order to eliminate the atmospheric effects from the measured TOA radiances. In this way, the nature of aerosols and gases is completely different. Scattering by molecules is well understood, thanks to several aspects: they are well mixed, the vertical air mass is almost uniform over large areas, and the scattering properties are simple. Then, the contribution of the permanent gases to the at-satellite signal is usually properly calculated. On the contrary, aerosols are a heterogeneous group, with particles covering wide ranges of sizes, origins and properties, as well as with strong temporal and spatial variability. As already said, the scattering function is not known exactly, whereas it is for gases, and another factor is the strong forward component of the aerosol scattering, which makes accurate radiative transfer modelling difficult. Thus, a correct parametrization of aerosols is a challenging task in atmospheric modelling, and, therefore, in atmospheric correction.

Moreover, apart from being needed for the atmospheric correction, the aerosol information is important in its own right, due to the aerosol impact on the global climate dynamics. Anthropogenic aerosols are intricately linked to the climate system and to the hydrologic cycle [Charlson et al., 1992; Kaufman et al., 2002; Ramanathan et al., 2001]. Aerosols cool the climate system by reflecting sunlight. However, depending on their composition, aerosols can also absorb sunlight in the atmosphere, what results in the cooling of the surface and in the warming of the atmosphere in the process. These effects of aerosols on the temperature profile, along with the role of aerosols as cloud condensation nuclei, impact the hydrologic cycle, through changes in cloud cover, cloud properties and precipitation.

1.2.2. Origin, characteristics, distribution

According to the definition given by the World Climate Research Program (1980), an aerosol is a liquid or solid particle suspended in the air, with the exception of the clouds droplets. Aerosols are a complex component of the atmosphere; indeed, a full characterization of them requires the knowledge of their chemical composition, their shape, their size distribution and, of course, the amount of particles. Their sizes range from clusters of a few molecules (10^{-3} μm) to particles of several micrometers. From the radiative point of view, the most important aerosols are about the size range $0.1 - 1.0$ μm: the smaller aerosols, although numerous, have a small individual influence, whereas the larger ones, that have a strong individual impact, are very rare. For the same reasons, most of the aerosol mass is contained in the same size range ($0.1 - 1.0$ μm).

Aerosol characteristics depend on their origin. The liquid particles are spherical, but the solid particles have various, irregular and complex shapes. In most cases, it is probably not unrealistic to assume that on the average nonspherical randomly distributed particles behave as if they were spherical in the evaluation of the scattering process, as described with the Lorenz-Mie thery in Section 1.1.3. Moreover, there is no available theory for such irregular particles (opposite to what happens for cloud ice crystals), and measurements are not accurate enough to prove a difference between the real aerosol characteristics and those computed from the Lorenz-Mie theory.

Since most of the aerosol sources are at ground level, it can be derived that most of them are concentrated in the lower tropospheric layers, where their residence time is of the order of days. These tropospheric aerosols are very variable with time and location, and are related to the conditions of production and transport. For example, desert dust is raised by strong winds in dust storms. The largest particles settle rapidly to the ground, whereas the smaller ones produce a dry haze extending over hundreds of kilometers during several days. Some particles can also reach higher levels (4-6 km) and be transported over large distances, as it is the case the Saharan African particles crossing the Atlantic ocean and reaching the American coast. Another example of long-distance transport is the arrival of carbonaceous particles to the arctic zone from industrial areas.

In the stratosphere, the aerosol concentration is at a maximum around 18-20 km in the so-called Junge aerosol layer. The stratospheric aerosols are mostly formed by gas-to-particle conversion. They present a rather uniform distribution over the globe and have a residence time of months to years. Their concentrations can be highly increased by strong volcanic eruptions, taking years to return to the normal situation. The extinction profile is approximately constant in the first 10 km above the tropopause, and decreases exponentially above.

d'Almeida et al. [1991] classified atmospheric aerosols according to different origins and compositions:

Extraterrestrial sources

Extraterrestrial sources or interplanetary dust yield solid particles, which have a diameter ranging from some tenths of a micrometer to some millimeters. The origin of these extraterrestrial particles is associated with comet debris and meteor showers that desegregate on collision. These particles reach the troposphere trough scavenging processes, and have a residence time in the atmosphere ranging from some months to years. The total quantity of these aerosols is evaluated to 16-18 tons/year.

Sea-salt particles

In maritime environment, bubbles building and jet drop generate sea-salt particles. This aerosol type is composed of the following characteristic elements: Na, Cl, K, Ca and Mg. From these ones, other particles are formed by recrystallization in evaporating sea-spray drops and by fractionation after drying: NaCl, KCl, $CaSO_4$, $(NH_4)_2SO_4$,…It has been indicated that sea-salt particles have radius ranging from 0.1 mm to 100 mm.

Crustal aerosols

Crustal-derived particles essentially result from weathering and wind-blown sand abrasion of bedrock in arid regions of the world. The following substances Al, Fe, Ti, Si and Ca compose crustal aerosols. The size spectrum of crustal particles varies from 0.2 mm to some 100 mm. However, during sandstorm particles larger than 100 mm are extracted from the soil and remain suspended in the atmosphere. The observed size distribution of crustal aerosols is represented by a tri-modal log-normal function, corresponding to small, transition and ultra-giant particle modes.

Sulfates particles

Sulfate is an important atmospheric aerosol because it is the stable form of sulfur-bearing gases in the presence of oxygen. Sulfur-bearing gases are generated both naturally (marine flora, terrestrial biota, volcanic eruption …) and anthropogenically (combustion processes such as coal and oil burning, smelting and petroleum refining, and traffic).

Nitrate particles

Nitrate is also a major constituent of atmospheric aerosol because it is an end product of various reactions in the atmosphere. Precursor gases, which are either produced naturally or/and anthropogenically, are nitrogen oxides, nitrogen-bearing acids and gaseous nitrates.

Organic particles

The mechanism of organic aerosol production is not well identified. Organic particles have both natural and anthropogenic production, but the latter seems to be negligible. Forests are significant natural sources of volatile material (isoprene and terpene). It also exists a seasonal production of natural organic particles (pollen, sporen, fungi, algae, etc.), but these sources are generally neglected because of their relatively low density.

Carbonaceous substances

Carbonaceous aerosols are produced by the solid, liquid or vapor combustion. They are generated either directly through aggregation of molecules formed in combustion processes leading to soot particles (primary carbon), or indirectly, by means of condensation from supersaturated gas produced by chemical reactions and resulting in secondary organic (secondary carbon). Primary carbon is both composed by graphitic carbon and by primary organic. Carbonaceous materials size is mostly confined to the submicrometer range. Number and mass concentration of single subcomponents such as graphite, coal and soot, are highly variable functions of space and time.

Volcanic aerosols

Volcanic eruptions produce large quantity of sulfur dioxide (SO_2) and eject large particles of dust and ash, which can reach directly the stratosphere. These weighted particles fall down rapidly on the ground. The SO_2 contributes to the formation of stratospheric aerosols by gas-to-particle conversion. Aerosols resulting from volcanic eruptions are generally considered to be confined to the stratosphere. A great part of these ones are however transported and scavenged in tropospheric layers. Volcanic eruptions generally produce non-soluble dust or ash, such as SiO_2, Al_2O_3 and Fe_2O_3, and significant quantities of reactive gases (H_2S, SO_2, HCl, ...). Size distribution of volcanic aerosol shows generally two modes: particles ranging between 0.001 mm and 1 mm which are largely H_2SO_4 droplets, and particles larger than 1 mm which are likely to be ash.

1.2.3. Size distribution

Collecting particles and measuring their size distribution is not a trivial matter, and all the various techniques measure particles only in a limited size range. Moreover, most methods perturb the real aerosol population. The size distribution depends on the source and transport time of the aerosol and is highly variable, even for the same kind of aerosol. The size distribution characterization is very relevant in order to analyze the effects of aerosols on the radiation, as the absorption and dispersion caused by them is strongly dependent on the ratio between the size of the scatterer and the incident wavelength, as it was shown in Section 1.1.3.

From a mathematical point of view, the *size distribution function* $n(r)$ is the number of particles with a given radius r per unit volume. It is related with the particle concentration N by

$$N = \int_0^\infty n(r)\ dr. \tag{1.2.1}$$

It is convenient to represent the size distribution by a mathematical expression with a few adjustable parameters. The three most popular forms are:

1. The Junge power law

   $$n(r) = \begin{cases} Cr^{-\nu-1}, & r_1 \leq r \leq r_2 \\ 0, & r < r_1 \text{ and } r > r_2, \end{cases} \tag{1.2.2}$$

   being the adjustable parameters ν and r_1. The constant C is fixed by the total number of particles N. A modification is the truncated power law, with different exponents ν_i in successive size ranges $(r_i - r_{i+1})$.

2. The modified gamma distribution (MGD)

   $$n(r) = Cr^{-\alpha} exp(-\beta\ r^{\gamma}), \tag{1.2.3}$$

   with three adjustable parameters. If γ is chosen equal to 1, Eq. 1.2.3 reduces to the standard gamma distribution. The constant C is related to N.

3. The log-normal distribution (LND)

   $$n(r) = \frac{N}{\sqrt{2}\ \pi\ r\ ln\ \sigma}\ exp\left[-\frac{ln^2\ r - ln^2\ r_m}{2\ ln^2\ \sigma}\right], \tag{1.2.4}$$

   with the modal radius on a logarithmic scale r_m and σ as adjustable parameters. The log-normal size distribution was introduced because the Junge power law did not accurately account for large particles. Since then, it has been the most used, because it appears as universal, and it is entirely determined with only two parameters. Intrinsic mathematical properties of this law are even interesting because they emphasize individual components in a mixture of particles of different sources. Each component keeps its specific modal radius, its standard deviation, and its refractive index. It appears that log-normal function is the best-suited distribution law to characterize the aerosol components, the aerosol types, and their spatial and temporal variability.

Two or several LND or MGD can be associated to build bimodal or multimodal size distributions. As the extinction or the scattering cross section of the particle (when it is not too small) varies approximately as the geometrical cross section πr^2 (see Section 1.5), an important parameter is the *effective radius*, defined by

$$r_{eff} = \frac{\displaystyle\int_0^\infty r^3\, n(r)\, dr}{\displaystyle\int_0^\infty r^2\, n(r)\, dr}. \tag{1.2.5}$$

The associated effective variance is

$$\upsilon_{eff} = \frac{\displaystyle\int_0^\infty (r - r_{eff})^2\, r^2\, n(r)\, dr}{\displaystyle r_{eff}^2 \int_0^\infty r^2\, n(r)\, dr}, \tag{1.2.6}$$

where r_{eff} and ν_{eff} can be expressed in terms of the size distribution parameters, using Eqs. 1.2.2, 1.2.4 and 1.2.3. Two different distributions, for instance a LND and a MGD, that give the same r_{eff} and ν_{eff} lead to similar characteristics of the aerosols, which confirms the usefulness of these parameters in practice.

1.2.4. Optical properties

Refractive index

The scattering and absorption of radiation by a single aerosol particle is expressed by its complex refractive index ($n = n_r + in_i$), where the real part represents scattering and the imaginary part represents absorption. The refractive index is strongly dependent on the chemical composition of the particle. The real and imaginary parts of the complex refractive index for urban, rural and maritime aerosols, as a function of wavelength, are shown in Fig. 1.7. An important variability in scattering and absorption is observed for different aerosol compositions. Thus, different radiative responses are expected for different aerosol models.

The real part of the refractive index is generally known with sufficient precision, because the results are not too sensitive to its value, and the uncertainty introduced in the scattering characteristics by the refractive index is generally smaller than the one due to the relatively poor information on the size distribution. So, default values of the real part of the refractive index are generally used in calculations. Common values are $n_r = 1.33$ for maritime aerosols, $n_r = 1.44$ for continental aerosols, and $n_r = 1.55$ for urban and Saharan aerosols types. The major difficulty concerns the imaginary part of the refractive index, as there is a real variability as well as a large uncertainty in the measurements, what leads to a huge dispersion in the results.

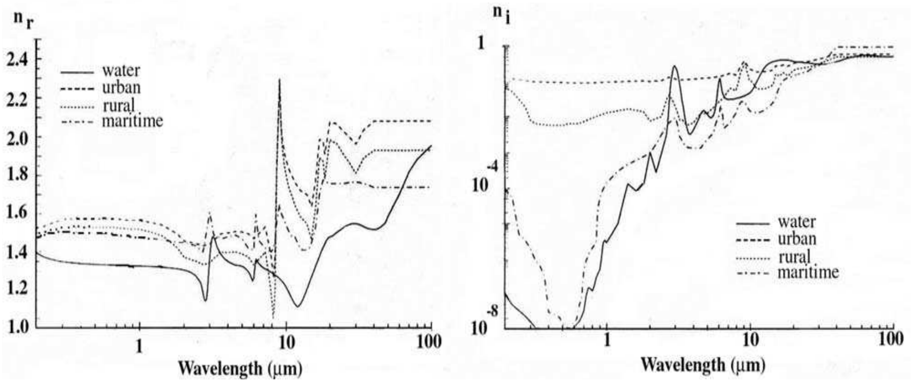

Figure 1.7: Spectral real and imaginary parts of the refractive index for different aerosol models (from Shettle and Fenn [1979]).

Radiative quantities

The phase function (Eq. 1.1.1, Fig. 1.6), the scattering cross section and the Mie efficiency (Eq.1.1.9, Fig. 1.5) were introduced in Section 1.1.3 in order to describe the scattering of radiation. However, other variables must be added when absorption is coupled to scattering. In particular, scattering efficiency factors are generalized to consider absorption as well, by defining analogous absorption and extinction efficiency factors, following Eq. 1.1.8:

$$Q_a \equiv \frac{\sigma_a}{\pi a^2} \tag{1.2.7a}$$

$$Q_e \equiv Q_s + Q_a \tag{1.2.7b}$$

where σ_a is the corresponding absorption cross section, and the extinction cross section can be defined as $\sigma_e \equiv \sigma_s + \sigma_a$. The Mie extinction efficiency is plotted for various aerosol models in Fig. 1.8. It can be stated that the aerosol influence on the radiation has a strong dependence on the aerosol type, by means of the different scattering and absorption effects for different size and chemical composition.

In macroscopic terms, the extinction process happens in multi-particulate media, so that the extinction by a single particle cannot be isolated. A magnitude taking into account this fact is the *volume extinction coefficient*, β_e, which gives the amount of lost incident flux per unit volume. For a medium with a particle concentration N, it is given by

$$\beta_e = N\sigma_e. \tag{1.2.8}$$

If the scattering and absorption cases are treated separately, again we have

$$\beta_e = \beta_s + \beta_a. \tag{1.2.9}$$

The well-known *Bouguer-Lambert-Beer law* uses this coefficient to quantify the radiation reduction after crossing an absorbing and scatterer medium, by considering it to be

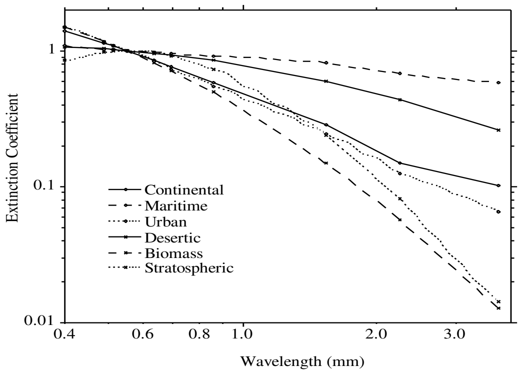

Figure 1.8: Spectral Mie extinction efficiency for various aerosol models (from Vermote et al. [1997b]).

proportional to the radiation intensity and the crossed thickness. An associated parameter is the *aerosol optical thickness* (AOT, τ), which takes into account the total loss of energy in a discrete path $x_2 - x_1$ due to the extinction by aerosols:

$$\tau = \int_{x_1}^{x_2} \beta_e dx \tag{1.2.10}$$

This is maybe the most used magnitude in the aerosol characterization, as it appears in the evaluation of the radiative transfer within any atmospheric path, by means of the Bouguer-Lambert-Beer or other related laws.

An empirical formulation for the spectral dependence of the optical thickness is the *Ångström's turbidity law*,

$$\tau = \beta \lambda^{-\alpha}. \tag{1.2.11}$$

The β coefficient is related to the total aerosol loading, and is also called *turbidity coefficient*. It is equal to the aerosol optical depth at a wavelength of 1 μm if the wavelength is given in micrometers (definition from the *American Meteorological Society*). The α coefficient is related to the particle size distribution. Generally, the smaller the α parameter is, the larger the aerosols are. Thus, the Angström's law is very useful in describing both the aerosol total loading and the type, which is usually the final goal of any satellite aerosol retrieval technique.

In remote sensing applications, the parameters mostly used in the characterization of the total aerosol content are the *optical thickness at 550 nm* (τ_{550}), the *visibility* (V) and the *meteorological range* (V_r), which are closely related to the extinction coefficient at 550 nm β_{550} (considering now the Rayleigh contribution as well as the aerosol one). The calculation of τ_{550} from β_{550} is straightforward using Eq. 1.2.10. The meteorological range, also called standard visibility or standard visual range, is the distance, under daylight conditions, at which the apparent contrast between a specified type of target and its background becomes just equal to a fixed threshold contrast (in turn, the minimum contrast at which an observer can just distinguish a target object from its surroundings, both definitions by the *American Meteorological Society*). Numerically, it is defined by the so-called *visual range equation* or *Koschmieder formula*:

$$V_r = \frac{1}{\beta_{550}} ln \frac{|C|}{\epsilon} \tag{1.2.12}$$

where the threshold contrast ϵ is set equal to 0.02 and the contrast C to 1, to avoid the dependence on the observer which exists implicitly in the contrast determination. Thus, the only dependency is on the extinction coefficient at 550 nm. Visibility can be considered the “subjective” version of the meteorological range, as it includes the contrast dependence on the observer stated in Eq. 1.2.12. This equation establishes the relationship

$$V = V_r \frac{ln\frac{|C|}{\epsilon}}{ln\frac{1}{0.02}} \tag{1.2.13}$$

Other important magnitude in the characterization of aerosol absorption is the *single scattering albedo* ω, which accounts for the relative importance of scattering and absorption. It is defined as

$$\omega = \frac{Q_s}{Q_e} = \frac{\beta_s}{\beta_e} \tag{1.2.14}$$

and gives the fraction of scattered radiation in terms of the total extinguished radiation. The limiting case $\omega = 1$ is referred to as conservative case, as there is no loss of radiative energy, while the case $\omega = 0$ corresponds to a perfectly absorbing aerosol. The plot of the single scattering albedo for the aerosol types in Fig. 1.8 is displayed in Fig. 1.9. It can be noted that scattering is dominant versus the absorption in most of the species, except for the urban model, in which the soot component makes absorption almost as strong as scattering.

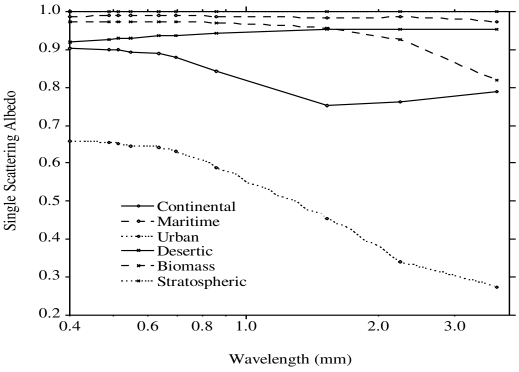

Figure 1.9: Spectral single scattering albedo for various aerosol models (from Vermote et al. [1997b]).

One parameter closely related to the phase function is the *asymmetry factor* g, which represents the average of the cosine of the scattering angle, and is defined as follow

$$g = \frac{1}{2}\int_{-1}^{+1} \mu P(\mu) d\mu. \tag{1.2.15}$$

Theoretically, g can vary from -1 to +1. The more the particles scatter in a given direction, the higher is the absolute value of the asymmetry factor. The case $g = 1$ corresponds to a total forward scattering medium, when $g = -1$ corresponds to a total backward scattering medium. Isotropic scattering properties correspond to the case $g = 0$. The asymmetry factor corresponds to the first moment of the Legendre polynomial decomposition of the phase function. Accordingly, it does not represent the totality of the information contained in the phase function, but it is generally sufficient to describe the scattering properties of an optically thick medium.

Moreover, the asymmetry factor shows irregular shapes reflecting the particles size and composition. Values close to 1, predominant forward scattering, are mostly observed in the shorter wavelengths. The asymmetry factor is larger for those types with high concentrations of large particles, while those types with smaller particles also present small asymmetry factors. However, it is positive for all aerosol types found in nature.

1.2.5. Aerosol Models

Aerosol models are generally built using basic components. These components represent well the diversity of aerosols and have been selected after the compilation of the available climatologies. Then, different components can be mixed in order to represent as well as possible the local aerosol characteristics. In most of the applications this is done by the concept of external mixing, where the basic components are considered to coexist in an air parcel, but not to be internally mixed inside one particle. In that case the radiative properties of the mixing is obtained by the weighted average of individual radiative properties. The weights are the mixing ratio expressed in number of particles. The basic component characteristics are the size distribution (generally represented by a log-normal distribution) and the refractive index. They can be obtained from different databases in the literature that provide the properties for both the basic types and the corresponding suggested models made up from the types. Some standard aerosol models are:

Continental aerosols

This term is referred to a heterogenous group, composed of types with different density and mixing ratio, including the following:

- Rural: contains dust-like and water soluble particles, with a major contribution of the latter ones. This type is predominant in continental regions far from pollution sources in urban nuclei, as well as in the Savannah and in rural environments.
- Forest: typical in African and South American forests, with an important load of sulphur compounds from biogenic sources.
- Average continental: representative in zones with a weak human influence, such as industry or traffic. Dust-like, soot and water soluble particles can be found in these regions, typically in Europe.
- Urban: found in zones with a high human influence. The main contamination sources are industrial nuclei (so-called *residential sources*) and traffic (*mobile source*). As well as these anthropogenic aerosols, particles from forestal fires or agricultural activities can also be present, consisting of nitrates, sulphur, carbon, mineral dust and ash.

Maritime aerosols

The maritime model is considered a mixture of water soluble substances and saline particles. Three subgroups are considered:

- Clean or pure maritime: formed in big air masses over the ocean, far away from the coast. It is compounded by biogenic sulfates and salt particles. The concentration variation is strong on a daily basis, with an average value between 500 and 700 cm^{-3}.
- Mineral maritime: its origin is the mixing of the clean maritime aerosols with desert ones, that can travel long distances inside the atmosphere. The result is an aerosol type typical in the Mediterranean regions, by the collision of oceanic air masses with other coming from the arid regions in Northern Africa. A typical mode between 0.1 and 5 μm often appears. This aerosol model usually presents two layers, a maritime background in the lower one and a variable mineral component over it.
- Intermediate: in an analogous way, the continental air masses with anthropogenic particles from urban nuclei can reach some pure maritime layer, so that a mixture of both types arises, with the corresponding modification in the size distribution. This type of aerosol is very important in the cloud formation, and so in the atmospheric radiative budget.

Desert aerosols

This model may present the highest variability in the physical and optical properties, and are important turbidity sources. Desert aerosols come from the arid and semiarid regions around the world, and have a huge lifetime in the atmosphere before its deposition, what makes these aerosols can travel long distances. For instance, Saharan aerosol streams can be detected in Florida.

In order to illustrate the effect of the aerosol model on the signal measured by a sensor at the TOA, this has been simulated combining different aerosol loadings and models. The results are displayed in Fig. 1.10. The aerosol loading is represented by the horizontal visibility from medium (23 km) to atmospheric turbidity (5 km). It can be stated that, for the same aerosol loading (left plot), the atmospheric influence on the signal varies considerably with the aerosol model. Moreover, this influence on the model can also be noticed in a wavelength basis when varying the visibility (right plot): the maritime model shows a strong sensibility on the total aerosol loading in the visible wavelengths, while the signal distortion is hardly noticeable in the NIR wavelengths. On the other hand, for the continental model the atmospheric behavior is relatively constant in all the wavelengths.

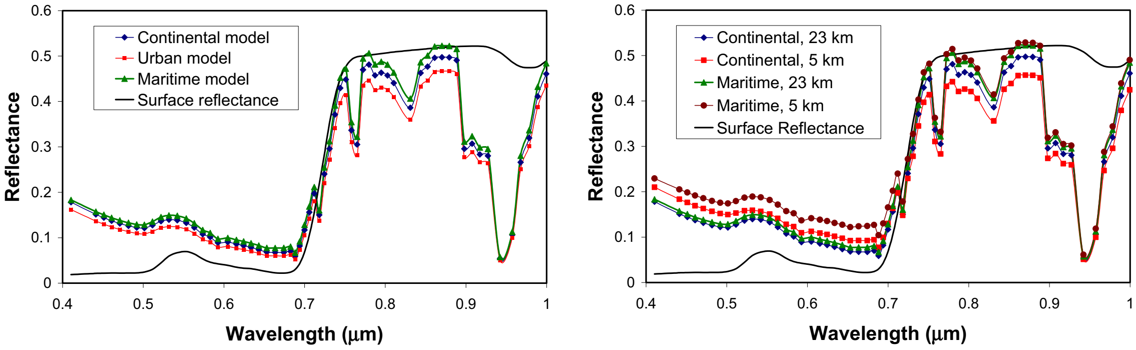

Figure 1.10: TOA reflectances simulated for several aerosol settings. The bare line corresponds to the surface reflectance spectrum used in the simulations.

1.3. Water Vapor

Water vapor is an important variable constituent of the atmosphere. Most of it is contained in the troposphere. It plays a major role in redistribution of water and energy within the global atmosphere–land–ocean system. The interaction of the troposphere with solar radiation at wavelengths larger than 700 nm is dominated by water vapor absorption. At the same time, terrestrial radiation in the thermal infrared spectral region is also to a large amount subject to absorption by water vapor, except for the atmospheric window from 8 to 13 μm. Given that absorption of radiation leads to atmospheric heating, understanding the amount and wavelength dependence of absorption by water vapor and other atmospheric species is essential for climate studies. Besides accounting for most of Earth's natural greenhouse effect, which warms the planet, gaseous water also condenses to form clouds, which may act to warm or cool, depending on the circumstances. In this context, knowledge about the spatial distribution of water vapor is also of importance since in the atmosphere–ocean–earth interaction energy is transported in the form of latent heat. An indirect effect is the occurrence and development of clouds, also partly dependent on the available amount of atmospheric water vapor, which by reflecting and scattering of incoming solar radiation also affects the atmosphere's energy budget. With satellite-based instruments, information about atmospheric water vapor content can be determined on a global scale.

As the temperature of the atmosphere rises, more water is evaporated from ground storage (rivers, oceans, reservoirs, soil). Because the air is warmer, the relative humidity can be higher, leading to more water vapor in the atmosphere. The higher concentration of water vapor is then able to absorb more thermal IR energy radiated from the Earth, thus further warming the atmosphere. Then, the warmer atmosphere can hold more water vapor. This is referred to as a "positive feedback loop". However, huge scientific uncertainty exists in defining the extent and importance of this feedback loop. As water vapor increases in the atmosphere, more of it will eventually also condense into clouds, which are more able to reflect incoming solar radiation (thus allowing less energy to reach the Earth's surface and heat it up). The future monitoring of atmospheric processes involving water vapor will be critical to fully understand the feedbacks in the climate system leading to global climate change. Also, while we have good atmospheric measurements of other key greenhouse gases such as carbon dioxide and methane, we have poor measurements of global water vapor, so it is not certain by how much atmospheric concentrations have risen in recent decades or centuries, though satellite measurements, combined with balloon data and some in-situ ground measurements indicate generally positive trends in global water vapor.

The annual average of columnar water vapor (CWV) varies between 0.25 $\text{g}\cdot\text{cm}^{-2}$ in polar regions to over 5 $\text{g}\cdot\text{cm}^{-2}$ in the tropics [Peixoto and Oort, 1992]. The annual mean global concentration of water vapor would yield about 2.5 $\text{g}\cdot\text{cm}^{-2}$ of liquid water over the entire surface of the Earth if it were to instantly condense. However, the mean annual precipitation for the planet is about 1 meter, which indicates a rapid turnover of water in the air. The average residence time of water molecules in the troposphere is about 10 days. Water depleted by precipitation is replenished by evaporation from the seas, lakes, rivers and the transpiration of plants, and other biological and geological processes.

The 0.5-5 $\text{g}\cdot\text{cm}^{-2}$ water vapor range will be confirmed within the MERIS-derived water vapor maps generated for this thesis. The ability to reproduce the temporal and spatial distribution of water vapor from MERIS data will also be demonstrated in Section 4.3.

1.4. Mathematical Formulation

1.4.1. Generalities

The simulation of the interaction between the atmosphere and the radiation is a need in the study of the atmospheric effect on the signal arriving at an elevated sensor. Forward runs of suitable radiative transfer models provide meaningful information about the features of the problem and the sensitivity of the measured radiance[2] to external parameters, such as the scene geometrical configuration or the concentrations of atmospheric components. In the inverse mode, radiative transfer simulations are a necessary tool in the inversion of the TOA radiances to estimate the corresponding atmospheric or biophysical parameters. The availability of a solid mathematical base to formulate the radiative transfer problem is very important to implement radiative transfer codes (RTCs) as reliable as possible for the simulation task.

In the general case, the electromagnetic radiation travelling within a medium is modified by physical phenomena acting on its intensity, its polarization or its phase. Two formalisms are used when evaluating that process: the wave approach and the intensity approach.

The wave approach lies on the Maxwell equations. It may be exactly formulated and works very well in the analysis of phase-related phenomena, such as diffraction. Nevertheless, to be applied on a operational basis it must consider simplifying hypothesis, as the associated equations can become very complex.

The intensity approach focuses on the processes affecting the energy carried by the wave, although polarization effects can also be taken into account by means of the Stokes parameters. Even though the common formulation considers the radiation well described by the first Stokes parameter, neglecting the polarization information, a matrix formalism describing intensity and polarization is more general. Besides, since the Stokes parameters are additive in the case of incoherent light, there is no coupling between them, so the scalar case can be recovered simply by the omission of the second, third and forth parameters.

Although only a rigorous treatment of the transferred energy can provide sought results, the information that can be extracted from the analysis of the effects associated to the intensity is usually enough in physical phenomena related to the radiation and atmosphere interaction. In terms of atmospheric correction, the polarization is not taken into account by most of the sensors, so the matrix formalism of the wave approach is not needed in this work, even though the study of the light polarization in order to retrieve the aerosol

---

[2] The term radiance is defined as the radiant flux (radiant energy per unit time) in a differential solid angle crossing a differential surface element perpendicular to the axis of the radiation beam. It is usually given in $\mathrm{Wm^{-2}sr^{-1}\mu m^{-1}}$.

information may be a future challenge in remote sensing (some preliminary tests have already been done [Herman et al., 1997]).

The main objective of this section is to establish the Radiative Transfer Equation (RTE) from a general scalar formulation, focusing on our practical problem of the radiation coming from the sun to the Earth being affected by the atmosphere and the surface.

1.4.2. The Radiative Transfer Equation

The energy transfer in a complex medium, such as the atmosphere, is generally affected by absorption, scattering and emission.

In the case of the Earth both surface and atmosphere have a temperature range covering from 150 to 300 K, so the corresponding blackbody emission is centered in the thermal infrared wavelengths. Thus, the emission process can be neglected if we are dealing with radiation in the solar spectrum, although we will consider the increase of energy in a given direction **s** due to thermal emission until some simplifying assumptions are needed to solve the equation.

As described in Section 1.1, the absorption acts decreasing the radiation in **s**, while the scattering may increase or decrease the intensity in the same direction, by means of the deviation of the radiation propagating towards other directions $\mathbf{s}'$ into **s** or, on the contrary, modifying the direction of the radiation moving in **s**. Thus, we have four ways of changing the radiation moving in a given direction, two causing the extinction in this direction and two increasing it. The RTE quantifies the global influence of gain and loss processes, by means of the balance between them in a volume element located in the complex medium, by asserting the energy conservation.

Radiation extinction

The extinction term groups the absorption and the scattering associated to the loss of energy in **s**. As we mentioned in Section 1.2.4, absorption and scattering can be treated altogether by means of the volume extinction coefficient β_e, which is the sum of the volume absorption and scattering coefficients (Eq. 1.2.9). The extinction action on the radiation can be formulated by means of the Bouguer-Lambert-Beer law, a simple differential equation considering that the radiance loss is proportional to the total energy amount and to the crossed distance. If we consider a layer of thickness dx in an absorbing and scatterer medium perpendicular to a radiation beam of radiance L , the radiance has been changed to $L + dL$, so the variation is given by

$$dL = -\beta_e L dx \tag{1.4.1}$$

If we integrate between the two positions, x_1 and x_2

$$L(x_2) = L(x_1)exp\left[-\int_{x_1}^{x_2} \beta_e(x)dx\right] = L(x_1)exp(-\tau) \tag{1.4.2}$$

where we have used the concept of extinction optical thickness introduced in Eq. 1.2.10. Eq. 1.4.2 is known as *Beer's exponential extinction law*. It provides the expression of the *transmittance* $T(x_1, x_2)$ of the layer between x_1 and x_2 along the direction of propagation by

$$T(x_1, x_2) = \frac{L(x_2)}{L(x_1)} = e^{-\tau} \tag{1.4.3}$$

Radiation sources

The increase of radiation in a propagation direction can be parameterized by a function quantifying the supplied radiance in each wavelength for a given spatial point M and direction $\mathbf{s}$. We define the *source function coefficient* $j(M, \mathbf{s})$ such that the increase in radiance due to scattering and emission in a direction $\mathbf{s}$ after traversing a thickness dx is given by

$$dL(M, \mathbf{s}) = j(M, \mathbf{s})dx. \tag{1.4.4}$$

It has two contributions, one accounting for scattering $j^{sc}(M, \mathbf{s})$ and another for emission $j^{em}(M, \mathbf{s})$

$$j(M, \mathbf{s}) = j^{sc}(M, \mathbf{s}) + j^{em}(M, \mathbf{s}). \tag{1.4.5}$$

Scattering source function

To establish the radiation scattered in the $\mathbf{s}$ direction, the angular distribution of the photons which have interacted with a scatterer nuclei must be known. This distribution is given by the *scattering function* $f(M, \mathbf{s}, \mathbf{s}')$, that describes the number of those photons arriving at a scatterer located in the position M from the direction $\mathbf{s}$ which are scattered towards the $\mathbf{s}'$ direction. The scattering function is closely related to the element $(1, 1)$ of the Stokes matrix and to the phase function in Eq. 1.1.1.

It is easy to relate the scattering function and the volume scattering coefficient. Let us consider a differential volume dV of a given scatterer medium, with section $d\Sigma$ and length dx. If an irradiance E arrives at dV from a direction $\mathbf{s}'$, the radiant flux scattered by dV into a direction $\mathbf{s}$ within a solid angle $d\Omega$ can be written

$$d^2\Phi = f(M, \mathbf{s}, \mathbf{s}')EdVd\Omega \tag{1.4.6}$$

The total flux loss because of scattering is obtained by integrating Eq. 1.4.6 over $d\Omega$ for all directions. The incident flux Φ on dV is therefore changed to $\Phi + d\Phi$, where

$$d\Phi = -dV \int_{4\pi} f(M, \mathbf{s}, \mathbf{s}')Ed\Omega. \tag{1.4.7}$$

We can compare with the Bouguer-Lambert-Beer law for a scatterer medium with volume scattering coefficient β_s and length dx

$$d\Phi = -\beta_s \Phi dx = -\beta_s E dV, \tag{1.4.8}$$

where the relation $\Phi = E d\Sigma$ between the irradiance and the flux has been used, to find the sought equation relating the scattering function and the volume scattering coefficient:

$$\beta_s(M, \mathbf{s}') = \int_{4\pi} f(M, \mathbf{s}, \mathbf{s}') d\Omega. \tag{1.4.9}$$

At this point, it is convenient to define the normalized phase function already introduced in Eq. 1.1.1, now by means of a physical discussion, as

$$P(M, \mathbf{s}, \mathbf{s}') = \frac{4\pi}{\beta_s(M, \mathbf{s}')} f(M, \mathbf{s}, \mathbf{s}'). \tag{1.4.10}$$

From Eq. 1.4.9, one can notice that β_s is assumed to be dependent on the position and the incidence direction (i.e., there is a dependence in the way the particles interact with the radiation on the direction it comes), which is the most general situation. However, provided that the particles do not introduce any asymmetry around the direction of incidence, which is most often the case, this direction dependence disappears. Thus, we shall consider isotropic each point in the medium hereinafter, although the spatial dependence for nonhomogeneous media will be still taken into account: $\beta_s(M, \mathbf{s}) \simeq \beta_s(M)$. Moreover, with this assumption both the scattering and the phase functions do no longer depend explicitly on the incidence and scattering directions, but they only depend on the scattering angle Θ between them.

In an analogous way, we can characterize the radiant flux gained in a given direction $\mathbf{s}$ because of the scattering by a scatterer volume $dV = d\Sigma dx$ of a light beam propagating with $\mathbf{s}'$ direction. Using Eq. 1.4.10 and

$$E = L(M, \mathbf{s}') d\Omega', \tag{1.4.11}$$

we can rewrite Eq. 1.4.6 as

$$d^2\Phi = \frac{\beta_s(M)}{4\pi} P(M, \mathbf{s}, \mathbf{s}') L(M, \mathbf{s}') d\Omega' d\Sigma dx d\Omega \tag{1.4.12}$$

The expression for the gained flux in $\mathbf{s}$ is obtained after integrate over all incidence directions:

$$d\Phi = \frac{\beta_s(M)}{4\pi} d\Sigma dx d\Omega \int_{4\pi} P(M, \mathbf{s}, \mathbf{s}') L(M, \mathbf{s}') d\Omega' \tag{1.4.13}$$

On the other hand, from the definition of scattering source function coefficient (Eq. 1.4.4), the radiant flux gained in dV in a direction $\mathbf{s}$ by the scattering process can be written

$$d\Phi = j^{sc}(M, \mathbf{s}) dx d\Sigma d\Omega. \tag{1.4.14}$$

For practical aspects, we define the *scattering source function* J^{sc} (radiance units) from the scattering source function coefficient, as

$$J^{sc}(M,\mathbf{s}) = \frac{j^{sc}(M,\mathbf{s})}{\beta_e(M)}. \tag{1.4.15}$$

So, Eq. 1.4.14 may be rewritten

$$d\Phi = \beta_e(M) J^{sc}(M,\mathbf{s}) d\Sigma dx d\Omega. \tag{1.4.16}$$

Finally, by using the definition of the single scattering albedo in Eq. 1.2.14 and comparing Eqs. 1.4.13 and 1.4.16, the scattering source function is given by

$$J^{sc}(M,\mathbf{s}) = \frac{\omega(M)}{4\pi} \int_{4\pi} P(M,\mathbf{s},\mathbf{s}') L(M,\mathbf{s}') d\Omega'. \tag{1.4.17}$$

From the definition in Eq. 1.4.15, it can be checked that $\beta_e J^{sc}(M,\mathbf{s})dx$ is the radiance gained in a $\mathbf{s}$ direction due to the scattered radiation after crossing a differential medium located at M and with thickness dx. It can also be noticed that Eq. 1.4.16 is equivalent to the Bouguer-Lambert-Beer law (Eq. 1.4.1) thanks to the definition in Eq. 1.4.15, but with the positive sign corresponding to a source effect.

Emission source function

Emission terms refer to those processes adding energy to the medium in a given wavelength, by means of the conversion from other types of radiant energy, such as heat, molecular decaying or any other energy external source. In remote sensing, the most important emission process is the thermal emission, although other phenomena, such as vegetation fluorescence, may be considered, especially in the VNIR spectral region (this phenomenon will be described in Chapter 5). The maximum value of the thermal emission at terrestrial temperatures is around 12 μm, so the role it plays in the optical spectrum is very small, and it can be neglected in practical applications. However, we shall consider it to arrive at a general version of the RTE as sought in this section.

Under the assumption of local thermodynamic equilibrium, quite accurate in the troposphere and in the lower stratosphere, emission is given by Planck's law, which relates the emitted monochromatic radiance by a blackbody L^B to the wavelength and the temperature T of the emitting substance. In the wavelength domain, it is written

$$L^B(T) = \frac{2hc^2}{\lambda^5[exp^{hc/\lambda KT} - 1]} \tag{1.4.18}$$

with h the Planck constant, K the Boltzmann constant and c the velocity of light. The deviation from Planck's law for natural bodies is given by the *emissivity* (defined as the ratio of the emitting intensity to the Planck function). In the general case, the emission process presents directional effects, so emissivity is dependent on the direction. This is the case of most of the terrestrial surfaces, but we can neglect the directionality when considering the atmosphere emission, due to the atmospheric particles can be considered randomly oriented. Nevertheless, the spatial dependence due to gradients of the temperature field will be taken into account.

We can build up a source function for the emission process in a similar way than the followed in the case of scattering. *Kirchhoff's law* states that the emissivity of a medium in a given wavelength is equal to its absorptivity under thermodynamic equilibrium. Thus, the radiant flux gained by emission in a path dx inside a medium with volume absorption coefficient β_a is

$$d\Phi = \beta_a(M)L^B(T(M))d\Sigma dx d\Omega. \tag{1.4.19}$$

Using Eqs. 1.4.4, 1.2.14 and 1.4.15 for the emission case, we find the expression for the emission source function

$$J^{em}(M) = (1-\omega(M))L^B(T(M)). \tag{1.4.20}$$

Derivation of the Radiative Transfer Equation

Once those processes which modify the radiant energy in a complex absorbing and scattering medium have been properly parameterized, we can establish explicitly the equation that governs the energy transfer by means of the energy conservation constraint.

We consider a monochromatic radiation beam $L(M, \mathbf{s})$ at a point M propagating in the direction $\mathbf{s}$, inside a material characterized by an extinction coefficient $\beta_e(M)$, a single scattering albedo $\omega(M)$ and a phase function $P(M, \mathbf{s}, \mathbf{s}')$. The variation in the radiant flux Φ_1 after traversing a differential volume with section $d\Sigma$ and length ds (Fig. 1.11) is the difference between the incident flux and the exiting flux,

$$\Phi_1 = \frac{dL(M, \mathbf{s})}{ds} ds d\Sigma d\Omega. \tag{1.4.21}$$

This variation is due to the unbalance between the extinction and source processes inside the volume. The flux lost by absorption and scattering along ds is, according to the

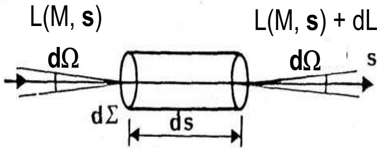

Figure 1.11: Energy balance in a differential volume.

Bouguer-Lambert-Beer describe in Eq. 1.4.1,

$$\Phi_2 = -\beta_e L(M, \mathbf{s}) ds d\Sigma d\Omega. \tag{1.4.22}$$

On the contrary, the flux gained along ds by the scattering into the $\mathbf{s}$ direction and the thermal emission is, using Eqs. 1.4.4 and 1.4.15 for the extinction case,

$$\Phi_3 = \beta_e J(M, \mathbf{s}) ds d\Sigma d\Omega, \tag{1.4.23}$$

where

$$J(M, \mathbf{s}) = J^{sc}(M, \mathbf{s}) + J^{em}(M, \mathbf{s}) \tag{1.4.24}$$

as previously defined.

Energy conservation leads to

$$\Phi_1 = \Phi_2 + \Phi_3, \tag{1.4.25}$$

or, using Eqs. 1.4.21, 1.4.22 and 1.4.23, to

$$\frac{dL(M, \mathbf{s})}{ds} = -\beta_e [L(M, \mathbf{s}) - J(M, \mathbf{s})]. \tag{1.4.26}$$

Writing explicitly the source terms in Eqs. 1.4.17 and 1.4.20 arrive at

$$\begin{aligned} \frac{dL(M, \mathbf{s})}{ds} &= -\beta_e(M) \Big[L(M, \mathbf{s}) - \tfrac{\omega(M)}{4\pi} \textstyle\int_{4\pi} P(M, \mathbf{s}, \mathbf{s}') L(M, \mathbf{s}') d\Omega' \\ &\qquad -(1 - \omega(M)) L^B(T(M)) \Big] . \end{aligned} \tag{1.4.27}$$

This is the general 1-D radiative transfer equation without any coordinate system imposed, which is fundamental to the discussion of any radiative transfer process. This equation, with the boundary conditions, defines completely the radiance field in the medium.

The RTE for plane-parallel atmospheres

In practical radiative transfer applications, a useful approach is to consider a plane-parallel geometry for the atmosphere layers: each layer consists of a infinite plane, parallel one to each other, where the optical properties are constant. This approach is quite reliable, unless the illumination or observation zenith angles are extremely large. Wang [2003] have estimated the error associated with this approximation to be very little for view zenith angles less than 80°. Other situations where the plane-parallel approximation does not work well are twilight problems, limb observations or analysis of atmospheric water vapor. In this latter case, atmospheric layers are horizontally non-homogeneous, because the evaporation takes place in a turbulent regime, so a fluctuation in the contents might appear within layers at the same altitude.

The plane-parallel approach considers the vertical gradients much stronger than the horizontal ones. Then, in Cartesian coordinates, the variation in a beam moving in a direction given by the angle $\theta = \cos^{-1}\mu$ with the Z axis and by the azimuth ϕ counted from the X axis can be written

$$\frac{dL}{ds} = (1-\mu^2)\cos\phi\frac{\partial L}{\partial x} + (1-\mu^2)\sin\phi\frac{\partial L}{\partial y} + \mu\frac{\partial L}{\partial z} \simeq \mu\frac{\partial L}{\partial z}. \tag{1.4.28}$$

Then, the only position variable is the altitude z, instead of $M(x, y, z)$, and the direction is given by (μ, ϕ). In this terms, Eq. 1.4.27 is given by

$$\begin{aligned}\mu\frac{dL(z,\mu,\phi)}{dz} &= -\beta_e(z)\left[L(z,\mu,\phi) - \tfrac{\omega(z)}{4\pi}\textstyle\int_{4\pi} P(z,\mu,\phi,\mu',\phi')L(z,\mu',\phi')d\Omega'\right.\\ &\qquad\left.-(1-\omega(z))L^B(T(z))\right].\end{aligned} \tag{1.4.29}$$

An equivalent formulation of the RTE is generally associated to the plane-parallel approach. In this formulation, the distances along the Z-axis are written in terms of the atmospheric optical thickness (Eq. 1.2.10) between a given height z and the TOA:

$$\tau = \int_z^\infty \beta_e(z')dz'. \tag{1.4.30}$$

With this substitution, Eq. 1.4.29 can be rewritten as

$$\begin{aligned}\mu\frac{dL(\tau,\mu,\phi)}{d\tau} &= L(\tau,\mu,\phi) - \tfrac{\omega(\tau)}{4\pi}\textstyle\int_{4\pi} P(\tau,\mu,\phi,\mu',\phi')L(\tau,\mu',\phi')d\Omega'\\ &\qquad-(1-\omega(\tau))L^B(T(\tau)).\end{aligned} \tag{1.4.31}$$

An analog approximation is used in those cases where the zenith angles are large, considering the Earth atmosphere compound of spherical concentric layers. In the case of azimuthal symmetry, the equivalent for Eq. 1.4.28 is

$$\frac{dL}{ds} = \mu\frac{\partial L}{\partial r} + \frac{1-\mu^2}{r}\frac{\partial L}{\partial \mu}. \tag{1.4.32}$$

A typical situation of spherical geometry is the study of finite clouds, where the plane-parallel approach is no longer valid. Eq. 1.4.32 represents then a proper formulation of the problem.

1.4.3. Boundary Conditions

Theoretically speaking, the RTE is a linear first-order integro-differential equation, so only one boundary condition is needed in order to completely define the radiance field in the medium. In the case of the radiative transfer in the terrestrial surface/atmosphere system, this condition must be the extraterrestrial irradiance reaching the utter atmospheric layers, as it represents the energy source entering the system. However, the particular configuration of the problem in the optical region suggests the establishment of two separate boundary conditions: on the one hand, the Earth surface acts as a discontinuity layer because it does not transmit radiation (only reflection and absorbtion can be assumed) as it does the atmospheric layers; on the other hand, the subsequent applications of the RTE in optical remote sensing are the study of the surface reflectance. So, an independent treatment of the surface radiative properties, from both the spectral and the angular perspectives, is highly suitable.

Then, this section will be separated in two subsections, one devoted to the boundary condition in the upper atmospheric layer and the other one to the boundary condition in the surface. The first one deals with the solar extraterrestrial radiation reaching the Earth, and the second one focuses on the analysis of the reflection of solar radiation in the surface, which is quite complex in the general case of non-homogeneous surfaces.

Boundary condition in the upper atmospheric layer

The radiative transfer problem must be constrained by a boundary condition in the TOA layer, specifying the radiation field entering the atmosphere. There are different radiation sources arriving at the Earth: the major fraction of energy comes directly from the Sun, although residual radiation sources are also the reflection of solar radiation in the moon surface and the extraterrestrial microwave background. Since the first one is orders of magnitude bigger than the others in the solar spectrum, we will consider only the direct solar radiation.

Focusing on direct radiation, it is usual to consider a highly collimated beam coming from a given direction, so the Sun is modelled as a point source. It can be written by means of a Dirac δ function:

$$L(M_{TOA}, \mathbf{s}) = J_{TOA}\delta(\mathbf{s} - \mathbf{s}_0). \tag{1.4.33}$$

M_{TOA} stands for any point in the outer atmospheric layer, defined as the layer where the density of the atmospheric components tends to zero. The direction $\mathbf{s}_0$ is the Sun direction from the Earth surface. Last, J_{TOA} is the radiance arriving from the Sun at the TOA height, or, equivalently, the solar irradiance on a plane perpendicular to the solar beam located in the top of the atmosphere. It can be quantified in terms of the *solar constant*, solar irradiance in a distance equals to the mean Sun-Earth distance (see Fig. 1.1), by

$$J_{TOA} = \frac{\mu_0}{\pi} I_{sc} \left[\frac{\bar{R}}{R}\right]^2 \tag{1.4.34}$$

where R is the Sun-Earth instantaneous distance and $\bar{R}$ is the mean one, and μ_0 is the cosine of the solar zenith angle.

This modelling presents important advantages in the simplification of the RTE solution. Nevertheless, there are other ways to parameterize the solar TOA irradiance that may be more realistic, even though they not provide any improvement in the RTE resolution. One of them comes from the consideration of a finite apparent radius for the Sun, instead of being treated as a punctual source. Then, the Dirac δ function could be substituted by a Gaussian function centered in the direction of the Sun center and with a full width half maximum equals to the Sun apparent diameter as seen from the Earth.

Concerning the incidence direction $\mathbf{s}_0$, this is the direction of the radiation beam arriving at the TOA layers. However, this is not the direction of the beam when reaching the ground, as the refractive index changes with the height in the atmosphere, so the beam propagation direction is curved. Some radiative transfer codes do take into account these radiation slants paths in the atmosphere, e.g. the MODTRAN4 code which will be described in the next section.

Boundary condition in the surface

Concerning the lower boundary condition, we have two main contributions in the radiance travelling from the surface to the atmosphere, the solar radiation reflected by the surface and the thermal radiation emitted by the surface, each one predominating depending on the spectral region. Since we are dealing with the radiative transfer problem in the solar spectrum, we will omit the study of the thermal radiation emitted by the surface to focus on the interaction between the downward solar radiation and the surface.

Natural terrestrial surfaces are generally illuminated from the whole hemisphere. So, they receive both direct and diffuse solar radiation because of multiple scattering processes. The surface modifies the radiative field causing a great part of the downward radiation to be reflected to the atmosphere, raising an upward radiation field. The spectral quantity and angular distribution is closely related to the surface nature, so this one can be characterized according to its spectral response to radiation. This is the main principle of optical remote sensing to retrieve information about the surface from multispectral/multiangular measurements.

For each wavelength, the magnitude describing the angular reflectance pattern of a surface is the *Bidirectional Reflectance Distribution Function* (BRDF) [Schaepman-Strub et al., 2006], f_r, defined by

$$f_r(M_{sur}, \mathbf{s}', \mathbf{s}) = \frac{dL_r(M_{sur}, \mathbf{s}', \mathbf{s})}{dE_i(M_{sur}, \mathbf{s}')} \tag{1.4.35}$$

where $E_i(M_{sur}, \mathbf{s}')$ is the irradiance arriving at a surface point M_{sur} from the direction $\mathbf{s}'$, and $L_r(M_{sur}, \mathbf{s}', \mathbf{s})$ is the radiance reflected in the $\mathbf{s}$ direction from that coming from

$\mathbf{s}'$. Both the incoming and the reflected beams are considered inside a differential solid angle, which is the reason for using the term *directional*. Helmholtz principle of reciprocity [Minnaert, 1941], accounting for the inversion invariance of the optical path for a light beam, is matched by f_r:

$$f_r(M_{sur}, \mathbf{s}', \mathbf{s}) = f_r(M_{sur}, \mathbf{s}, \mathbf{s}'). \tag{1.4.36}$$

According to the definition in Eq. 1.4.35, the boundary condition specifying the upwards radiance field in the surface in a given direction $\mathbf{s}$ is obtained after the integration over all the incidence directions:

$$L_r(M_{sur}, \mathbf{s}) = \int_{\Omega'=4\pi} f_r(M_{sur}, \mathbf{s}', \mathbf{s}) L_i(M_{sur}, \mathbf{s}') \mu' d\Omega'. \tag{1.4.37}$$

However, some aspects must be pointed out on the use of the BRDF in the description of real surfaces. The surface BRDF is defined only for infinitesimal viewing and illumination solid angles and an infinitesimal wavelength interval. Consequently, it cannot be directly measured. In remote sensing applications, illumination is typically over a hemisphere with both direct and diffuse sources (solar illumination and sky radiance, respectively). Viewing is typically over some finite sensor instantaneous field-of-view (IFOV), defined by the sensor optics and geometry, with a spectral response over some finite wavelength interval rather than at some discrete value of the wavelength. To overcome the problem that the BRDF is a non-measurable property, it is defined a bidirectional reflectance factor (BRF), which is the ratio of radiance leaving the surface in a finite solid angle in the viewing direction to the radiance from a perfect Lambertian reflector under the same illumination conditions as the target, into the same finite solid angle. This is the magnitude used in the specification of the angular properties when real measurements of reflected radiation are available, being the BRDF being mostly use in numerical simulations. Anyway, we shall continue using the BRDF concept in this theoretical description to avoid confusing notations.

The mathematical parametrization of f_r depends on the complexity of the surface nature. We will consider two different cases in terms of the directional distribution of the reflected radiation: Lambertian and non-Lambertian

Lambertian surfaces

This is the simplest case, including those surfaces in which the reflected radiance is isotropous or perfectly diffuse, i.e., L_r is a constant. Thus, the reflected field is the same for all of the points in the surface (uniform), and independent of the view angle θ (Lambertian): $L_r(\theta) = L_r(0)$. This is equivalent to the *Lambert's cosine law* for the reflected flux density $I_r(\theta)$,

$$I_r(\theta) = I_r(0) \cos\theta \tag{1.4.38}$$

With these conditions, independence on the point and the direction, the mathematical expression for f_r is a constant, $f_{r,d}$, characterizing the reflectance in every point of the surface. So, the reflected radiance is given by

$$L_{r,d}(M_{sur}) = f_{r,d} \int_{4\pi} L_i(M_{sur}, \mathbf{s}')d\Omega' = f_{r,d}E_i(M_{sur}) \tag{1.4.39}$$

Even though there is no real surface showing a strict Lambertian behavior, many of them can be represented with this approximation to a reasonable extent. The consideration of an uniform Lambertian surface strongly simplifies the decoupling between surface and atmosphere radiative transfer effects. As it will be shown in subsequent sections, atmosphere and surface are a coupled system, that must be solved by means of numerical approximations. However, the Lambertian assumption leads to analytically invertible equations to express the surface reflectance as a function of the TOA radiance and the atmospheric parameters (see Eq. 1.4.47), what provides a straightforward calculation of the sought surface reflectance in the atmospheric correction procedure.

Non-Lambertian surfaces

In the most general case, natural surfaces present directional properties in their reflectance patterns, more or less complex depending on different structural and biophysical parameters. For instance, real surfaces may have strong backward (3D vegetation canopies) or forward reflectance peaks (snow and water surfaces) in their reflectance patterns, as it is shown in Fig. 1.12.

In fact, the analysis of multiangular datasets is becoming an important information source in the characterization of the terrestrial surfaces. The directional dependence of surface reflectance on structural properties implies that observations of the directional signal will contain information related to these properties. If it is possible to relate radiant energy from a vegetation canopy to observed reflectance using a model of some kind, then it may also be possible to use such a model to relate variations in observed reflectance to surface properties causing these variations.

The determination of the most suitable BRDF model for a given application is a complex task, apart from some surfaces with a well-known angular behavior. There are several approaches to build up a BRDF model. Roughly, they can be classified in four groups [Disney, 2001]:

- *Empirical models* are arbitrary functions not related to the physical properties of the system under observation designed to fit multiangular data [Minnaert, 1941; Walthall et al., 1985]. The advantages of this approach are firstly that no assumptions are made regarding the type of canopy under observation, i.e. whether it is largely

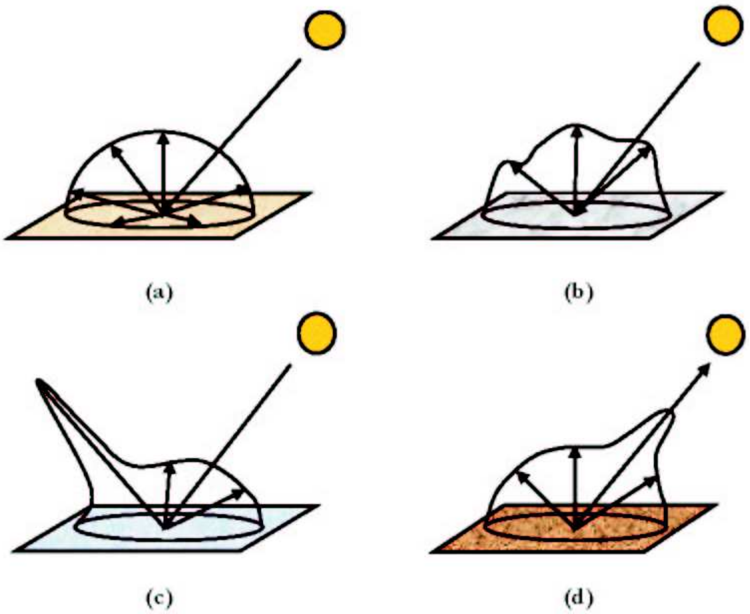

Figure 1.12: Four cases of surface reflectance in terms of directionality: (a) Lambertian reflectance (b) non-Lambertian (directional) reflectance (c) specular (mirror-like) reflectance (d) retro-reflection peak (hotspot) (from Disney [2001]).

homogeneous (e.g. grassland) or more spatially discrete (e.g. tree crowns in a forest canopy). Secondly, the chosen function can be arbitrarily complex in order to describe the surface reflectance behavior. Then, they are usually quite simple, and generally fit the measured data well. However, they require many directional samples to constrain the fit, and are not valid for extrapolation, as their domain of applicability is bounded by the limits of the measurements from which they were derived.

- *Physical models* are based on radiative transfer physical analysis [Goel, 1988; Hapke, 1981], so their parameters have a full physical meaning. Thus, it is also possible to make reasonable a priori estimations of the model parameters, and to constrain them to physically realistic values to invert the measured data. The main shortcoming is that they are generally complex and require numerical inversion.

- *Computer simulation models* can represent surface scattering at in almost arbitrary detail, including 3D structures, but are often computationally intensive, and are not invertible directly due to the very large number of parameters. Thus, they are commonly used to validate other less accurate but faster models.

- *Semiempirical or kernel-driven models* attempt to bridge the gap between physical and empirical modelling approaches. The aim is to maintain some physical basis, but allowing quick analytical inversion. The assumption is made that scattering from heterogeneous surfaces will be composed of separable scattering components (kernels). Each kernel represents a particular component of the surface scattering behavior, and contributes to the overall reflectance "shape". Kernel-driven models bridge the gap between simple empirical and complex physical descriptions of BRDF. Kernels describing various scattering properties can be linearly combined to describe BRDFs [Rahman et al., 1993; Ross and Marshak, 1989; Roujean et al., 1992; Wanner et al., 1995]. Kernel-driven models can be used to interpolate or extrapolate from limited samples of BRDF, and can be effectively inverted against measured reflectance at arbitrary scales.

1.4.4. TOA Signal Formulation

Up to this point, the different terms that must be considered in the computation of the general atmospheric radiative transfer have been discussed. The general RTE quantifying scattering and absorption processes in any atmospheric path has also been stated. However, we have not presented a practical parametric formulation of the signal measured by a spaceborne sensor yet. This formulation would provide the TOA radiance as sum of radiative terms from different processes, such as the radiation scattered by the atmosphere into the sensor line of sight or the direct radiation multiply scattered between the atmosphere and the surface. These contributions are calculated by solving the RTE for the given conditions.

One useful and accurate formulation is the one proposed by Tanré et al. [1981], which is implemented in the *Second Simulation of the Satellite Signal in the Solar Spectrum* (6S) code [Vermote et al., 1997c], and is part of the operative MODIS atmospheric correction algorithm [Vermote et al., 1997a]. In this formulation, the gaseous absorption is calculated separately to the scattering, and is added as a multiplicative factor. This approach is not realistic in those wavelengths with strong gaseous absorptions, but the simplifications in the equations and the subsequent saving in computation time make it is a useful expression in simulations tasks.

The contribution of the target to the upward TOA radiances is decomposed as the sum of five terms, which are shown in Fig. 1.13: (1) the photons reflected by the atmosphere before reaching the surface, (2a) the photons directly transmitted from the Sun to the target and directly reflected back to the sensor, (2b) the photons scattered by the atmosphere then reflected by the target and directly transmitted to the sensor, (3a) the photons directly transmitted to the target but scattered by the atmosphere on their way to the sensor, and, finally, (3b) the photons having at least two interactions with the atmosphere and one with the target.

Following [Vermote et al., 1997c] notation, the apparent reflectance at the TOA, given

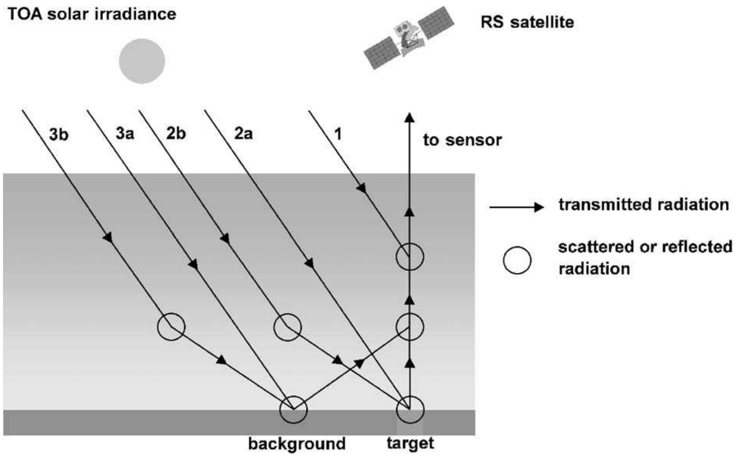

Figure 1.13: Contributions to TOA signal from surface and atmosphere (from Verhoef and Bach [2003]).

in terms of the TOA radiance L_{TOA}, the solar constant I_{sc} and the cosine of the solar zenith μ_s angle by

$$\rho_{\text{TOA}} = \frac{\pi L_{\text{TOA}}}{\mu_s I_{sc}} \tag{1.4.40}$$

is simulated following

$$\begin{aligned}
\rho_{\text{TOA}}(\mu_s, \mu_v, \phi) \quad = \quad & t_g(\mu_s, \mu_v) \Bigg[\rho_0(\mu_s, \mu_v, \phi) + e^{\frac{-\tau}{\mu_s}} e^{\frac{-\tau}{\mu_v}} \rho_s(\mu_s, \mu_v, \phi) \\
& + e^{\frac{-\tau}{\mu_v}} t_d(\mu_s)\bar{\rho} + e^{\frac{-\tau}{\mu_s}} t_d(\mu_v)\bar{\rho}' \\
& + t_d(\mu_s) t_d(\mu_v)\bar{\bar{\rho}} \\
& + \frac{\left[e^{\frac{-\tau}{\mu_s}} + t_d(\mu_s) \right] \left[e^{\frac{-\tau}{\mu_v}} + t_d(\mu_v) \right] S(\bar{\bar{\rho}})^2}{1 - S\bar{\bar{\rho}}} \Bigg]
\end{aligned} \tag{1.4.41}$$

where t_g is the transmittance due to gases; ρ_0 is the intrinsic atmospheric reflectance, also called atmospheric path reflectance; ρ_s is the surface reflectance; S is the spherical albedo, reflectance of the atmosphere for isotropic light entering it from the surface; μ_v is the cosine of the view zenith angle; ϕ is the relative azimuth between the Sun and viewing directions; $e^{-\tau/\mu_s}$ and $t_d(\mu_s)$ are the downward direct and diffuse transmittances of the atmosphere along the path of the incoming solar beam; $e^{-\tau/\mu_v}$ and $t_d(\mu_v)$ are the upward direct and diffuse transmittances of the atmosphere in the viewing direction; $\bar{\rho}$, $\bar{\rho}'$ and $\bar{\bar{\rho}}$ are the surface hemispherical-directional, directional-hemispherical and hemispherical-hemispherical reflectances, respectively. These latter terms are also called *coupling terms*, as they are responsible for the coupling between atmospheric radiative transfer with the surface reflectance properties. They are written as

$$\bar{\rho} = \frac{\int_0^{2\pi}\int_0^1 \mu L_{\downarrow}(\mu_s, \mu, \phi') \; \rho_s(\mu_s, \mu_v, \phi' - \phi) d\mu d\phi'}{\int_0^{2\pi}\int_0^1 \mu L_{\downarrow}(\mu_s, \mu, \phi') d\mu d\phi'} \tag{1.4.42}$$

$$\bar{\rho}'(\mu_s, \mu_v, \phi) = \bar{\rho}(\mu_v, \mu_s, \phi) \tag{1.4.43}$$

$$\bar{\bar{\rho}} = \overline{\bar{\rho}'(\mu_s, \mu_v, \phi)} \tag{1.4.44}$$

where $L_{\downarrow}(\mu_s, \mu, \phi')$ is the downward diffuse irradiance with the Sun at μ_s. In the 6S code (1.4.42) and (1.4.43) are computed exactly using the downward radiation field given by the successive orders of scattering method for several directions. Eq. 1.4.44 involving at least two interactions between the atmosphere and the surface is approximated by taking $\bar{\bar{\rho}}$ equal to the hemispherical albedo of the target, expressed

$$\bar{\bar{\rho}} \simeq \frac{\int_0^1\int_0^{2\pi}\int_0^1 \rho_s(\mu, \mu', \phi)\mu\mu' d\mu' d\mu d\phi}{\int_0^1\int_0^{2\pi}\int_0^1 \mu\mu' d\mu' d\mu d\phi} \tag{1.4.45}$$

This approximation is justified by the limited impact on the total signal of this last contribution, as well as the fact that multiple scattering tends to be azimuthally independent, leading to change a double integration by a single one.

When the Lambertian assumption is made for the target reflectance,

$$\bar{\rho} = \bar{\rho}' = \bar{\bar{\rho}} = \rho_s, \tag{1.4.46}$$

so Eq. 1.4.41 becomes

$$\rho_{TOA}(\mu_s, \mu_v, \phi) = t_g(\mu_s, \mu_v)\left[\rho_0(\mu_s, \mu_v, \phi) + \frac{\left[e^{\frac{-\tau}{\mu_s}} + t_d(\mu_s)\right]\left[e^{\frac{-\tau}{\mu_v}} + t_d(\mu_v)\right]\rho_s}{1 - S\rho_s}\right] \tag{1.4.47}$$

which is an analytically invertible equation in ρ_s, widely used in operational atmospheric correction procedures as it will be discussed later.

When scattering and absorption processes are computed concurrently along the same atmospheric path, the path radiance and the transmittance associated to atmospheric scattering do include the contribution by gaseous absorptions. In terms of radiance, the TOA signal registered by a sensor looking at a homogeneous Lambertian target would be given by

$$L_{\mathrm{TOA}} = L_0 + \frac{1}{\pi}\frac{\rho_s E_{\mathrm{g}} T_{\uparrow}}{1 - S\rho_s} \tag{1.4.48}$$

where L_0 is the atmospheric path radiance, $T_{\uparrow} = e^{\frac{-\tau}{\mu_v}} + t_d(\mu_v)$, E_{g} is the global irradiance (direct plus diffuse) arriving at the surface. This is the equation followed by MODTRAN4 for the simulation of TOA radiances from a Lambertian surface, and the one that will be employed in the radiative transfer simulations performed along this work.

1.4.5. On the BRDF/Atmosphere Coupling Correction

In the general case, a Lambertian surface must be assumed for atmospheric correction. Except for instruments providing simultaneous multiangular information of the imaged target, such as the Multi-angle Imaging SpectroRadiometer (MISR) [Diner et al, 1998], the POLarization and Directionality of the Earth's Reflectances (POLDER) instrument [Deschamps et al., 1994] or the Compact High Resolution Imaging Spectrometer (CHRIS) on board the PRoject for On–Board Autonomy (PROBA) [Barnsley et al., 2004], considering directional effects in atmospheric correction is a difficult task. The Lambertian assumption becomes mandatory for the atmospheric correction of single-view sensors, as multiangular information can only be obtained from multitemporal image series, which are not generally available for the processing of separate images. The MERIS data this algorithm is intended for are taken from a nadir view, with view zenith angle variations in the across-track direction up to about ±35°. This reduced angular sampling would make difficult the retrieval of directional properties even from multitemporal composites. The Lambertian assumption will be adopted for the processing of MERIS data instead. Some remarks about the evaluation of BRDF effects on atmospheric correction will be made in this section.

When considering directional effects in the target, instead of a Lambertian behavior, Eq. 1.4.41 is a useful approach. However, it can be noted that this equation is not analytically invertible to retrieve ρ_s, because ρ_s is embedded in the integrals accounting for the coupling terms in Eqs. 1.4.42, 1.4.43 and 1.4.45. Then, for the evaluation of the coupling terms ρ_s is, in turn, needed. Eq. 1.4.41 results in an integral equation, which may be solved by an iterative process.

Thus, there is a need for techniques that can provide information about the surface to be used in the calculations of the coupling terms. In practical considerations, there are several ways to get these initial estimates of the surface reflectance. Most of them depend on the availability of other surface products, but some authors [Hu et al., 1999; Vermote et al., 1997a] have suggested surface BRDF information can be retrieved from an initial correction assuming a Lambertian surface, where coupling terms are not needed. The angular pattern retrieved by means of the Lambertian assumption is fitted to a BRDF model, which is used to perform the integrals in the coupling terms. Once the coupling terms are known, a newer set of ρ_S angular values is obtained. This is again used to update the coupling terms and the subsequent ρ_S values. The procedure continues in this fashion until convergence in two consecutive iterations is found.

This iterative procedure has been tested using CHRIS-PROBA data. The PROBA platform provides pointing in both across–track and along–track directions. In this way, the CHRIS-PROBA system has multiangular capabilities, acquiring up to 5 consecutive images from 5 different view angles in the same satellite overpass. The BRDF model used

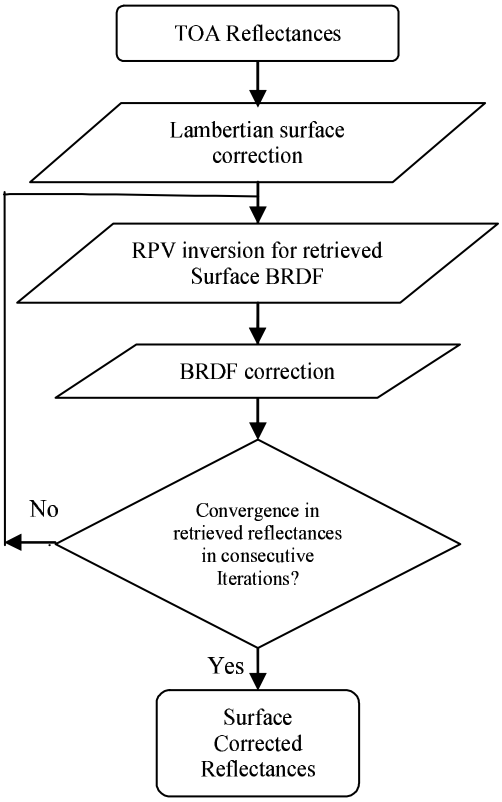

Figure 1.14: Flux diagram of the BRDF/Atmosphere coupling correction process.

to fit the angular pattern ρ_S in each iteration is the Rahman-Pinty-Verstraete (RPV) model [Rahman et al., 1993] (see Section 1.4.3), which offers a good balance between number of free parameters, three, and flexibility in the representation of distinct BRDF shapes. The retrieved angular pattern is fitted to the RPV model by means of the Powell's Minimization Method [Press et al., 1986], and the angular integrals for the coupling terms are numerically calculated with the Gaussian quadratures method. The flux diagram of this procedure is shown in Fig. 1.14. The final output of this BRDF coupling correction is a second order correction of the surface reflectance obtained from the Lambertian assumption, more substantial at the largest observation angles. Moreover, the calculation of the spectral surface albedo is straightforward from Eq. 1.4.45, which is also a product of this process.

From an operational point of view, the application of this procedure to a set of images, as it should be in the case of the 5 angles provided by PROBA, is quite complex:

- Fitting the RPV model is computationally very expensive on a pixel by pixel basis. Thus, the time needed in each iteration would be prohibitive for practical applications.
- The geometric correction of CHRIS images has an associated error of around three pixels, what corresponds to around 100 m in the surface. This leads to important problems in the evaluation of the borders of different surfaces in the images, as differ-

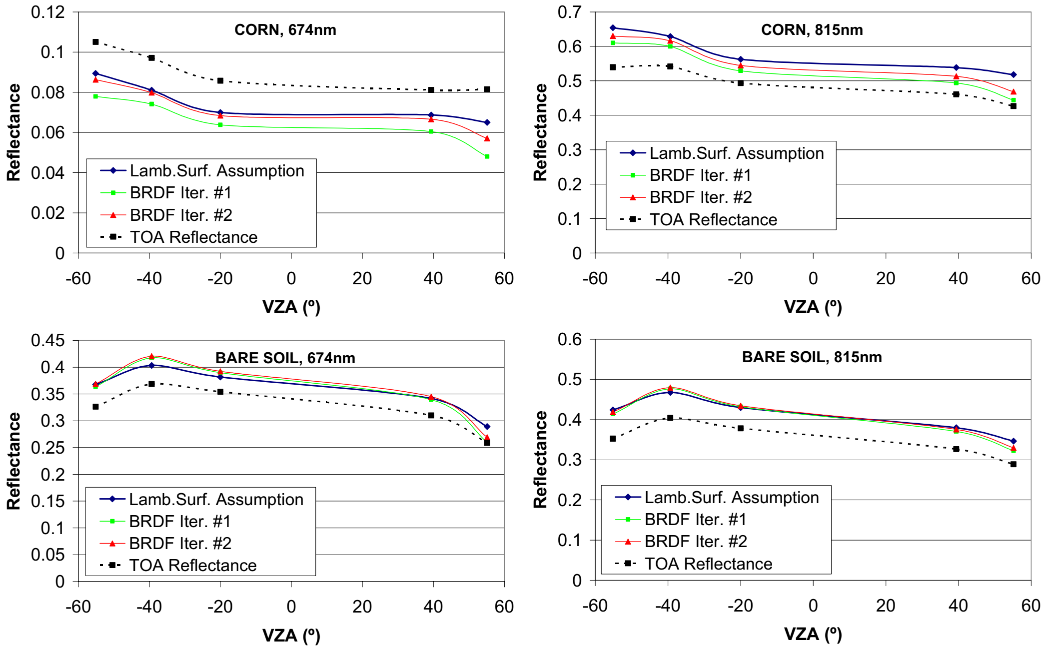

Figure 1.15: Successive BRDF retrievals with the scheme presented in this section.

ent surfaces might be viewed in both sides of boundaries from different observation angles. Geometric correction errors will also make difficult the inversion of the model in heterogeneous targets.

- Usually, there is only a partial overlapping in the observed region for the 5 images. A test of the number of angles needed to perform an adequate BRDF correction should be done for those areas not viewed from all of the angles.

In any case, the iteration accounting for the BRDF/atmosphere coupling has been made for some pixels in the PROBA/CHRIS images, taken visually from the center of uniform surfaces in the overlapped region to avoid the problems with the geometric correction. The resultant angular patterns for some iterations are collected in Fig. 1.15, for two different wavelengths (red and NIR) and surfaces. Convergence is considered in the second BRDF iteration. The pixels have been extracted from the same point in the 5 TOA radiance images for the 5 angles. It can be noted that directional effects do not cause important modifications of the results obtained with the Lambertian assumption, as expected for a geometric configuration out of the principal plane, what reinforces the use of the Lambertian approach. Only in ±55° angles the effect can be noted, more strongly in the corn surface than in the bare soil one. This result partially justifies the Lambertian assumption, at least when no "especial" Sun-Target-Sensor combinations are present. This is usually the case of MERIS, in which the poor angular sampling hardly provide principal plane configurations.

1.5. Radiative Transfer Codes

1.5.1. MODTRAN4 code

MODTRAN (MODerate resolution atmospheric TRANsmittance and radiance code) is a 2 cm-1 resolution band-model code, developed jointly by *Spectral Sciences, Inc.* and the *Air Force Research Laboratory/Space Vehicles Directorate (AFRL/VS).* In its initial steps it was an improved version of the LOW resolution TRANsmittance 7 (LOWTRAN7) model [Kneizys et al., 1996], covering from the UV-visible spectral regions to the longer wavelengths (0.2 to ∞ μm). MODTRAN4 [Berk et al., 2003, 1998] is the latest publicly released version of MODTRAN, adding several improvements to previous versions.

One of the most noticeable capabilities of the MODTRAN family is the use of a spherically symmetric atmosphere, consisting of homogeneous layers, each of which is characterized by the layer boundary specification of temperature, pressure and atmospheric species concentrations; Snell's law is used to calculate the curvature of beams because of refraction.

Another important point in MODTRAN4 is the rigorous treatment of absorption and scattering coupling and multiple scattering. The atmospheric extinction due to molecules and aerosols is considered altogether for every light path, accounting for absorption between two consecutive scattering events, in contrast with other formulations such as the one in the 6S code. This leads to an adequate evaluation of the radiative transfer, even in those bands with strong gaseous absorptions, although the computation time is increased.

Concerning multiple scattering, the DIScrete Ordinate Radiative Transfer (DISORT) algorithm [Stamnes et al., 1988] has been integrated in the MODTRAN4 code for high accuracy multiple scattering calculations. DISORT solves the RTE for multiple scattering and emitting layered media by means of a proper implementation of the discrete ordinate method. The physical processes included are thermal emission, scattering, absorption, and bidirectional reflection and emission at the lower boundary. The medium may be forced at the top boundary by parallel or diffuse radiation and by internal and boundary thermal sources as well. DISORT, in contrast to MODTRAN, uses a plane-parallel layered atmosphere without refraction. DISORT is mainly intended to be used as a subroutine which receives scattering and extinction optical depths, and phase functions for each layer as input from a driver program. This enables MODTRAN to accommodate refraction in DISORT.

For the absorption band model, HIgh resolution TRANsmittance 96 (HITRAN96) [Rothman et al, 1998] database is used, with two options for the bandwidth: as well as the traditional MODTRAN4 1 cm^{-1} band model, an optimized 15 cm^{-1} model is available with comparable accuracy when higher spectral resolution results are unnecessary. In the case of aerosols, the atmosphere is divided into four vertical regions: 0-2 km (boundary layer aerosols), 2-10 km (tropospheric aerosols), 10-30 km (stratospheric aerosols) and 30-100 km. Several models are defined for the boundary layer region, e.g. rural, maritime, urban, tropospheric or desert [Shettle and Fenn, 1979], while seasonal profiles are chosen in the upper regions. In any case, the code presents a high flexibility in the aerosol specification, so multiple user inputs, such as particular profiles or extinction coefficients, may be entered.

Regarding the ground surface, MODTRAN4 includes the effects of BRDF. The BRDF is entered using standard parameterizations. Some BRDF models coincident with those in the 6S code are implemented, such as Hapke, Walthall, Verstraete, RPV or Roujean. MODTRAN4 also provides the user with an option to assign distinct surface properties for the imaged-pixel and the area-averaged ground. The imaged-pixel is coupled to MODTRAN4 directly transmitted surface radiance terms, which include surface emission, reflected solar irradiance, and reflected thermal and solar flux contributions. The area-averaged ground surface serves as the lower boundary condition for the multiple scattering calculations, and, as such, influences all radiation scattered into the sensor direction.

With all of those features, MODTRAN4 code is maybe considered the most accurate one among the radiative transfer codes designed for remote sensing simulations. Thus, it has been utilized for the generation of the atmospheric Look-Up Table (LUT) which provides the atmospheric parameteres that simulate the TOA radiance in Eq. 1.4.48. The design of this LUT will be discussed in Section 3.2, and the modifications performed over the original MODTRAN4 to make it suitable for atmospheric correction of remote sensing data is detailed in Appendix C

1.5.2. 6S code

The name 6S stands for *Second Simulation of the Satellite Signal in the Solar Spectrum* [Vermote et al., 1997b,c]. It was developed mainly at *Laboratoire d'Optique Atmosphérique, Université des Sciences et Technologies de Lille*. It is an improved version of the 5S code [Tanré et al., 1990], which is able to simulate the signal observed by a satellite sensor for a Lambertian target at sea level altitude, in the solar spectrum wavelengths (0.25-4.0 μm). The 6S code enlarges the application field of 5S, adding new possibilities such as non-Lambertian surface conditions, target elevation, near-nadir plane observations and new absorbing species.

In the 6S code, the Rayleigh contribution to the atmospheric parameters in Eq. 1.4.41 is computed from analytical expressions [Vermote and Tanré, 1992]. For the aerosol+Rayleigh coupled system, the successive orders of scattering (SOS) method is used. The accuracy achieved is better than 10^{-4} (reflectance units). The downward radiation field is computed with 12 Gauss angles and 13 layers, even though these numbers are parameters of the code, so they can be changed to 24 angles and 26 layers when a very high accuracy is needed (with an increase of the computation time of about 4 times).

Concerning the coupling between absorption and scattering, gaseous absorption is decoupled from the scattering process, as it has been mentioned previously. The transmittance resulting from gaseous absorption is exactly calculated by means of statistical models, while the scattering is calculated with the SOS method. The separation of the two processes is not appropriate for water vapor, because the coupling between its absorption and scattering by aerosols can be important. This is due to the fact that aerosols and water vapor may be located at the same atmospheric level (first 2-3 km). So, the absorption should be computed along every path after each scattering event, which is not possible with the signal construction in Eq.1.4.41.

The solution given in the 6S code to this problem is computing three extreme cases, the water vapor above the aerosol layer, the water vapor under the aerosol layer, and an average case where it is considered that half of the water vapor present in the atmosphere absorbs the aerosol path radiance. The first and the second cases maximizes and minimizes the effect, and the third one is statistically meaningful. For each case, the TOA reflectance is computed, so the uncertainty due to the variable vertical distribution of aerosols versus water vapor is considered. The coupling between water vapor and molecular scattering is neglected, as water vapor bands are located mostly at wavelengths where the molecular scattering is weak.

For the surface contribution, both Lambertian and non-Lambertian surfaces are considered. In the first case, the TOA apparent reflectance is given by Eq. 1.4.47, and the value of the surface reflectance must be either provided by the user or by a default spectrum chosen from the code database. Four typical spectra are defined: *vegetation*, *clear water*, *sand* and *lake water*. In the second case, The TOA reflectance is built according to Eq. 1.4.41. The angular distribution of the surface reflectance may be also given by the user from multiangular in-situ measurements, although the usual option is choosing a parametric model from those implemented in the code, e.g. Hapke [1981]; Rahman et al. [1993]; Roujean et al. [1992]; Walthall et al. [1985]

Regarding the atmospheric database, the spectral resolution is set to 2.5 nm. The radiative properties of the basic aerosol types defined by the International Radiation Commission of IAMAP [World Meteorological Organization, 1986], dust-like, water soluble, oceanic and soot, are included, as well as their mixing ratios to build continental, maritime and urban models. Other models implemented are stratospheric, desertic and biomass. The band absorption parameters has been computed using the HITRAN database at 10 cm^{-1} resolution, and the gases taken into account are H_2O, O_2, O_3, CH_4, CO, NO_2, the most important ones in the 0.25-4.0 μm spectral interval.

The following inputs are necessary:

- Geometrical conditions: μ_s, μ_v and ϕ.
- Atmospheric model for the gaseous vertical profiles, and the water vapor and ozone column contents if the model default values have to be overwritten.
- Aerosol loading (optical depth in 550 nm or visibility) and the aerosol model or proportions of basic types.
- Spectral range: monochromatic wavelength or spectral interval with a filter function (implemented in the database for several satellite sensors).
- Ground reflectance, depending on the kind of reflectance surface (uniform/non-uniform, Lambertian/non-Lambertian).

Several outputs are returned by the code. Some of the most important are:

- TOA apparent reflectance.
- Integrated values of the irradiance at the ground level (direct, diffuse and environment).
- Gaseous transmittances for downward and upward radiation.
- Scattering transmittances due to molecules and aerosols, for downward and upward radiation.
- Spherical albedo, optical thickness, path reflectance, phase function and single scattering albedo, for both molecules and aerosols.
- Directional coupling terms (Eqs. 1.4.42, 1.4.43 and 1.4.44).

The main limitations of the 6S code are the inability to deal with spherical atmospheres and the inaccuracy in strong gaseous absorption bands. On the one hand, the 6S mathematical formulation is based on the plane-parallel assumption, so it has problems with calculations for large zenithal angles, being very inadequate for limb observations. On the other hand, the decoupling between scattering and absorption makes it not recommended for simulations in wavelengths where the gaseous absorption is strong, as the decoupling is no longer realistic. However, despite this shortcomings, thanks to its particular mathematical formulation 6S is an accurate yet rapid radiative transfer code. Thus, it is a suitable code to be used in those applications where a great number of runs is needed.

Chapter 2

Review of Reference Atmospheric Correction Algorithms

A small compilation of reference atmospheric correction algorithms is presented in this chapter. These algorithms represent the state-of-the-art atmospheric correction techniques. We will focus on the algorithms applied to the atmospheric correction of the last generation of satellite-borne sensors, such as MERIS [Santer et al., 1999; von Hoyningen-Huene et al., 2003], MODIS [Kaufman et al., 1997; Vermote et al., 1997a], MISR [Diner et al., 2005; Martonchik et al., 2002, 1998] and AATSR [Grey et al., 2006; North et al., 1999]. Besides, a section will also be devoted to Landsat TM [Liang et al., 2001], due to its particular role in the development of Earth Observation disciplines.

2.1. MERIS Atmospheric Correction

2.1.1. ESA Level 2 Product – Santer et al. (1999)

It corresponds to the atmospheric correction method implemented in the MERIS ground segment for the derivation of the Level 2 reflectance product. The main objective is to derive surface reflectance from MERIS images, except for bands 11 and 15, that are affected by important gaseous absorptions. The description given in this point is a summary of that presented in Santer et al. [1999]. Thus, deviations of the current algorithm status from what is detailed here are possible.

The conversion from radiance to reflectance involves three steps. In the first stage, gaseous absorption is removed from the signal. The well known ozone correction is based on European Centre for Meteorology and Weather Forecasting (ECMWF) data. For water vapor absorption, a differential method between 900 and 890 nm bands is proposed to derive the water vapor content. However, the retrieval by directly associating the ratio of the radiances at 900 and 890 nm to the water vapor transmittance in other bands is more accurate in terms of atmospheric correction. In doing so, systematic errors affecting the water vapor absorption are cancelled, such as the coupling between aerosol scattering and gaseous absorption. The same technique is applied for the O_2 transmittance by associating the O_2 transmittance at 760 nm to the ratio 760/753.75 nm. Simulations which include coupling between absorption and scattering indicate that this direct association is more accurate than a computation which involves O_2 or H_2O concentration as inputs.

The second step corrects for Rayleigh scattering. Computations with a SOS code indicated that a schematic vertical structure of the atmosphere with a pure molecular layer above the aerosols could be used with good accuracy. A 5S-like formulation of the signal (Eq. 1.4.47) is applied to convert the TOA radiance into a top of aerosol radiance. Simple and reduced LUTs to correct Rayleigh primary scattering from multiple scattering and a simple formulation for Rayleigh transmittance are also proposed. Rayleigh contribution depends on the barometric pressure. This pressure is determined using two MERIS bands at 760 and 753.75 nm in a differential method using the O_2 transmittance which only depends on the product of air mass times pressure squared. A simple correction for the coupling between scattering and absorption versus surface reflectance is proposed. This surface pressure retrieval is shown to have a better accuracy as compared to ECMWF data associated with a digital map to correct for surface elevation.

Finally, the third step removes the remaining aerosol effects from the resultant ground-aerosol system. The aerosol remote sensing is performed over Dark Dense Vegetation (DDV) [Kaufman and Sendra, 1988]. Once the DDV surfaces are identified, aerosol properties are retrieved, assuming a standard value for the DDV reflectance at 412, 442 and 665 nm where the spectral reflectance is the lowest. For the aerosols spectral behavior, 12 aerosol models are defined, by 3 values for the real part of the refractive index m (1.33, 1.44 and 1.55) and 4 values of the Angström coefficient α (0.0, 0.5, 1.0 and 1.5), considering the size distribution described by a power law (see Section 1.2.3):

$$n(r) \simeq r^{-(\alpha-3)}, \tag{2.1.1}$$

where $n(r)$ is the number of particles with a radius included in r to $r + dr$.

The aerosol retrieval algorithm starts with the selection of a refractive index for the aerosols from the climatology. Four aerosol models are therefore selected, corresponding to 4 values of α . For each one of them, top of aerosol reflectance is computed according to a 6S-like formulation of the signal

$$\rho_{aG}(\mu_s, \mu_v, \phi) = \rho_a + \frac{T_a(\mu_s)T_a(\mu_v)\rho_{DDV}}{1 - S_a\rho_{DDV}} \tag{2.1.2}$$

where ρ_{aG} is the reflectance of the ground-aerosol system; ρ_a, T_a and S_a are, respectively, the intrinsic reflectance, the transmittance and the spherical albedo relative to the aerosols, and ρ_{DDV} is the surface reflectance of DDV.

The DDV reflectance ρ_{DDV} at 412, 442 and 665 nm will be known from a LUT. The atmospheric functions ρ_a, T_a and S_a, for a given aerosol model, depend on the aerosol optical thickness τ_a only. A loop on τ_a is made in order to retrieve the MERIS reflectances after absorption and Rayleigh correction. This retrieval is performed for the 4 aerosol models in the 3 MERIS bands. The retrieved aerosol model is the model for which the Angström coefficient is the closest to the one obtained from the τ_a retrieval, while the retrieved aerosol optical thicknesses are those computed for the retrieved aerosol model.

Once the functions ρ_a, T_a and S_a are known, the surface reflectance ρ_s is given by the inversion of Eq. 2.1.2,

$$\rho_s = \frac{\rho_a^c}{1 + \rho_a^c S_a}, \tag{2.1.3}$$

with

$$\rho_a^c = \frac{\rho_{aG} - \rho_a}{T_a(\mu_s) T_a(\mu_v)} \tag{2.1.4}$$

However, problems in the practical implementation of the algorithm have caused it is not operational by the time this work is being written, resulting in MERIS Level 2 product lacks of images completely atmospherically corrected (an initial correction of molecular scattering and gaseous absorption is applied instead). The result is that only “Top-of-Aerosols” reflectance is provided as official ESA Level 2 product.

2.1.2. BAER – von Hoyningen et al. (2003)

The Bremen AErosol Retrieval algorithm (BAER) [von Hoyningen-Huene et al., 2003] is another code used for the MERIS atmospheric correction. It has been implemented in the Basic ERS & Envisat (A)ATSR and MERIS (BEAM) Toolbox [Fomferra and Brockmann, 2005] in order to convert from Level 2 Top-of-Aerosols reflectance to surface reflectance in its present form. It is not available for the atmospheric correction of MERIS Level 1b data.

The RTE to be solved does not consider gaseous absorption and Rayleigh scattering, which are supposed to be removed in the Level 2 product. Following von Hoyningen-Huene et al. [2003] notation,

$$\rho_{\mathrm{AER}} = \rho_{\mathrm{TOA'}} - \frac{T_{1\_\mathrm{AER}} T_{2\_\mathrm{AER}} \rho_{\mathrm{SURF}}}{1 - \rho_{\mathrm{HEM\_AER}} \rho_{\mathrm{SURF}}} \tag{2.1.5}$$

where $\rho_{\mathrm{TOA'}}$ is the Top-of-Aerosol reflectance in MERIS Level 2, ρ_{AER} is the reflectance due to aerosols, T_{1_AER}, T_{2_AER} are the total transmission functions accounting for the radiation extinction due to aerosol scattering, ρ_{SURF} is the surface reflectance to be derived, and $\rho_{\mathrm{HEM\_AER}}$ is the hemispheric reflectance of the system surface-atmosphere.

AOT at MERIS bands 1–7 (412-665 nm) is derived by solving Eq. 2.1.5 by means of an iterative procedure. The atmospheric parameters and the surface reflectance are the unknowns. The first ones are calculated in each iteration by interpolation from LUTs using the updated aerosol loading. The variable surface albedo over land is considered by a mixing model of surface reflectance, yielding it as fractions of "green vegetation" and "bare soil". Both vegetation and soil surface spectral reflectance in the short-wave region ($< 0.5\ \mu$m) decrease with wavelength. It is assumed that the apparent spectral surface reflectance over land in the satellite scene is composed from surface parts covered with vegetation and bare soil. Thus the apparent surface reflectance is given by a weighted mix of "green vegetation" and "bare soil" spectra (ρ_{VEG} and ρ_{SOIL}, respectively). The Normalized Difference Vegetation Index (NDVI) [Tucker, 1979] provides the necessary information about the vegetation amount in the pixel to calculate the weights:

$$\rho_{\mathrm{SURF}} = F(NDVI\rho_{\mathrm{VEG}} + (1 - NDVI)\rho_{\mathrm{SOIL}}) \tag{2.1.6}$$

the factor F being a scaling factor acting over the overall simulated reflectance. It is related to the atmospheric status, as it is calculated from ratios between TOA and aerosol reflectances.

The resulting AOT spectrum is smoothed following the Ångström's law. Iterations finish when the retrieved AOT matches the smoothed AOT, according to convergence criteria. For insufficient smoothness of the spectral AOT, the surface reflectance has to be modified iteratively. The described procedure estimates the spectral AOT for the MERIS bands 1–7 on a per-pixel basis. Its application for atmospheric correction of 13 MERIS bands (all but 11 and 15) requires the extrapolation of AOT to NIR bands.

2.2. MODIS Atmospheric Correction

The MODIS (*Moderate Resolution Imaging Spectroradiometer*) [Justice et al., 1998] scan mirror assembly uses a continuously rotating double-sided scan mirror to scan +/-55°. The optical system consists of a two-mirrors telescope which directs energy to four refractive objective assemblies; one for each of the VIS, NIR, Short-Wave Infrared, and Long-Wave Infrared spectral regions, up to 36 spectral channels. Two passive radiative coolers provide cooling to 83 K for the two HgCdTe focal plane assemblies for the 20 infrared bands. For the visible and NIR bands silicon photodiodes are used. MODIS includes four on-board calibrators as well as a view to space: a solar diffuser, a spectroradiometric calibration assembly including an integrating sphere, a mono-chromator unit and a solar diffuser stability monitor. MODIS data have global coverage within 2 days.

The atmospheric correction algorithm used in the processing of Level 2 MODIS products provides surface reflectance from the MODIS calibrated radiance data in bands 1 through

7 (centered at 648, 858, 470, 555, 1240, 1640 and 2130 nm, respectively). A complete description of the algorithm is presented in Vermote et al. [1997a]. They use MODIS atmospheric products (MOD04: aerosols, MOD05: water vapor, MOD07: ozone, MOD35: cloud mask) and ancillary data sets (Digital Elevation Model, Atmospheric Pressure) as an input to the atmospheric correction.

For the aerosol retrieval, the operational algorithm [Kaufman et al., 1997] is based on the dark pixel approximation. It is limited to densely vegetated areas in the humid geographical regions. The algorithm principle can be separated in the following steps:

1. **Selection of dark pixels**: the retrieval of aerosol properties is performed over dark pixels only with a default reflectance $\rho < 0.06$ in the MODIS bands at 470 nm and 660 nm. These low values can be found over DDV pixels. In order to identify the DDV pixels, two mid-IR channels at 2.1 μm and 3.8 μm are being used. In these channels the reflectance over DDV pixels is also small, what is due to the light absorption by liquid water, which is usually present in green vegetation. For most of the non-desert dust aerosol types, the aerosol effect on the measured radiance in the mid-infrared can be neglected. Pixels with reflectance $0.01 \leq \rho(2.1\mu m) \leq 0.05$ are used with first priority. If less than 5% of the pixels in a 10 × 10 km grid box are reaching this criteria, other thresholds for the reflectance in the two mid-infrared channels are applied. Pixels with $\rho(2.1\mu m) \geq 0.15$ are not being used.

2. **Relating the visible channels to the mid-IR channels**: for the selected dark pixels the surface reflection in the two visible channels is estimated from the measured reflectance in the 2.1 μm channel,

$$\rho_s(0.47\mu m) = \rho(2.1\mu m)/4 \tag{2.2.1}$$

$$\rho_s(0.66\mu m) = \rho(2.1\mu m)/2 \tag{2.2.2}$$

   For pixels with $\rho(2.1\mu m) \geq 0.05$ and $\rho(3.8\mu m) \leq 0.025$, the reflectance is set to $\rho_s(0.47\mu m) = 0.01$, $\rho_s(0.66\mu m) = 0.02$.

3. **Determination of appropriate aerosol model**: In order to find the final aerosol optical thickness τ_a, a preliminary aerosol optical thickness τ_p is retrieved from the measured radiance in the two channels with the help of the LUTs. The estimated surface reflectance and a constant continental aerosol type are being used. Surface reflectance and radiance are averaged over the 10-40% of the darkest pixels of a 10 × 10 km grid box. With the retrieved $\tau_p(0.47\ \mu m)$, $\tau_p(0.66\ \mu m)$, and the continental aerosol model phase function $P_c(\lambda)$ and single scattering albedo $\omega_{0c}(\lambda)$, the preliminary single scattering aerosol path radiance $L_{ps}(\lambda)$ is calculated :

$$L_{ps}(\lambda) = \tau_p(\lambda)P_c(\lambda)\omega_{0c}(\lambda) \tag{2.2.3}$$

For $\tau_p(0.66\ \mu m) < 0.15$, no aerosol type is estimated and the continental model is retained in further calculations. The aerosol type for higher optical depths is derived from $L_{ps}(0.47\mu m)/L_{ps}(0.66\mu m)$. According to two thresholds of this ratio, a dust aerosol model or a non-dust model are applied. Between these thresholds a mixture of the two models is used. The thresholds depend on the single scattering angle. The aerosol model for the non-dust contribution to the aerosol is chosen according to the geographical location and season.

4. **Determination of aerosol optical thickness**: the phase function $P(\lambda)$ and the single scattering albedo $\omega_0(\lambda)$ of the derived aerosol type are being used to determine the aerosol optical depth $\tau_a(\lambda)$ from the preliminary aerosol optical depth τ_p:

$$\tau_a(\lambda) = \tau_p(\lambda)\frac{P_c(\lambda)\omega_{0c}(\lambda)}{P(\lambda)\omega_0(\lambda)}. \tag{2.2.4}$$

The derived aerosol optical depths $\tau_a(\lambda)$ are given for the 10 × 10 km grid box.

Once atmospheric parameters are known from the mentioned MODIS products, adjacency effects and BRDF/atmosphere coupling are taking into account, after an initial correction under the Lambertian assumption. For the adjacency treatment, an scheme based on the formulations explained in Section 3.1 is used. Concerning the correction of directional effects, 6S formulation in Eq. 1.4.41 is employed.

2.3. MISR Atmospheric Correction

The optical system of the Multi-angle Imaging SpectroRadiometer (MISR) [Diner et al, 1998] consists of 9 pushbroom cameras fixed on an optical bench. One nadir looking camera, four fore-looking cameras and four aft-looking cameras are observing the same ground points under different viewing angles (angles: 0°, 26.1°, 45.6°, 60° and 70.5°, forward and afterward). Each camera uses a four Charge-Coupled Device (CCD) line array in a single focal plane. A medium band filter is used for each line to provide one of the 4 spectral bands (443, 555, 670 and 865 nm). The footprint size of the globally produced MISR data is nominally 1.1 km. Calibration is performed by a pair of deployable diffuse panels, which are used to diffusely reflect sunlight over the North Pole and South Pole in the field-of-view of the cameras. The calibration of the panels is monitored in-flight by different photodiode systems. Global coverage is found within 9 days.

The aerosol retrieval [Diner et al., 2005; Martonchik et al., 2002, 1998] is performed over a 16×16 array of subregions, i.e., a 17.6×17.6 km area. The general retrieval strategy is based on some assumptions:

- Atmospheric aerosols are laterally homogeneous within a 17.6×17.6 km region at the surface, growing to about 74×17.6 km (the area contained within the view of the two 70.5° camera) at an altitude of 10 km. With this assumption, different optical paths for the radiation vary in a predictable way.

- Retrievals are performed by comparing observed radiances with modelled ones, calculated for a suite of aerosol compositions and size distributions. These comparisons are performed in both the spectral and angular domains, leading to a set of 4 bands $\times$ 9 angles = 36 combinations of TOA radiances.

- The χ^2 formalism is used in the comparisons measurement/model, and reports aerosol model inside the acceptance criteria.

- The largest uncertainty in the retrieval algorithm is the reflectance of the underlying surface. Initially, 3 different algorithms were designed to be applied to different surfaces, two for land surfaces (over DDV and over heterogeneous land) and one for ocean. Later, the algorithm for heterogeneous land showed good skills when applied to dark land pixels, as well as having a wider application range, so the algorithm for aerosol retrieval over DDV was eliminated as an operational algorithm.

- As the atmosphere is considered horizontally homogeneous, no aerosol retrievals are performed over land when the surface topography is complex.

- In regions where the aerosol retrieval is unsuccessful, a default optical depth equal to the average optical depth of all successful retrievals in a domain nearby the domain containing the unsuccessful region is assigned.

The required set of predetermined aerosol models is contained in the Aerosol Climatology Product, composed of three parts: an aerosol physical and optical properties file, a tropospheric aerosol mixture file and an aerosol climatology file. Their associated radiative atmospheric parameters are calculated in advance for selected aerosol types with monomodal particle size distributions and are stored as a function of angular geometry and aerosol amount in various LUTs as part of the Simulated MISR Ancillary Radiative Transfer (SMART) dataset. Mixtures of two or three aerosol types produce a wide variety of aerosol models, described by bimodal or trimodal size distributions, and these mixture models are the ones used by the MISR aerosol retrieval algorithms.

Radiative transfer calculations include a correction for Rayleigh polarization effects, two Rayleigh scattering amounts (in order to account for surface pressure and elevation effects), and a fixed, standard atmosphere water vapor amount that affects very slightly only the radiances in band 4. No ozone is included since the MISR measurement are corrected for its effects prior to the use of the SMART dataset. This contains aerosol dependent path radiance, diffuse transmittances, irradiances and bihemispherical albedos. Using them, the TOA radiances required by the aerosol retrieval algorithms are then computed for all aerosol mixture models. The TOA radiance at the wavelength λ is expressed taking into account the coupling between atmosphere and surface BRDF thanks to the multiangular capabilities of the MISR instrument. Using their notation,

$$\begin{aligned} L^{TOA}(-\mu, \mu_0, \phi - \phi_0; \tau_\lambda) \ = \ & \\ & L_\lambda^{atm}(-\mu, \mu_0, \phi - \phi_0; \tau_\lambda) \\ & + e^{-\tau_\lambda/\mu} \cdot L^{surf}(-\mu, \mu_0, \phi - \phi_0; \tau_\lambda) \\ & + \int_0^{2\pi} T_\lambda(-\mu, -\mu', \phi - \phi'; \tau_\lambda) \\ & \cdot L^{surf}(-\mu, -\mu', \phi - \phi'; \tau_\lambda) d\mu' d\phi', \end{aligned} \tag{2.3.1}$$

where μ and μ_0 are the cosines of the view and sun angles (minus sign refers to upwelling radiation), $\phi - \phi_0$ is the view azimuthal angle with respect to the sun position, L^{TOA} is the simulated TOA radiance, L_λ^{atm} is the atmospheric path radiance, L^{surf} is the surface-leaving radiance, T_λ is the diffuse upward transmittance, and τ_λ is the optical depth of the atmosphere (Rayleigh + aerosols).

The specific algorithm for “heterogeneous land” does not rely on the presence of a particular, well described surface type, but instead uses the presence of spatial contrasts within the 17.6 km retrieval region to derive an empirical orthogonal function (EOF) representation of the region-averaged surface contribution to the TOA radiances. It does not require surface bidirectional reflectance or albedo assumptions, but surface must have spatial contrasts.

Once the required atmospheric optical parameters in Eq. 2.3.1 are known for the 17.6×17.6 km regions, the surface retrieval step starts, solving Eq. 2.3.1 using the atmospheric values stored in the SMART dataset, by means of different specific algorithms depending on the reflectance function to be derived. It must be remarked here that, even if an aerosol retrieval was successful, some 1.1 km subregions within a given region may not be suitable for a surface retrieval, due to cloudiness, cloud shadows or instrument-related reasons.

2.4. AATSR Atmospheric Correction

The Advanced Along-Track Scanning Radiometer (AATSR) on board the ENVISAT platform acquires two observations of the same area of the Earth's surface at a viewing angle of 55° (forward view at the surface) and then approximately 120 s later at an angle close to vertical (nadir view). The swaths are approximately 500 km wide, and the nominal size of each pixel at nadir is 1×1 km. There are seven spectral bands, but only four in the visible and NIR (555, 660, 870, and 1610 nm) spectral regions. These spectral bands are about 20 nm width, and avoid atmospheric water vapor absorption bands. The instrument is identical to its predecessor, the ATSR-2 sensor launched in 1995, and provides continuity to the ATSR-1 and ATSR-2 data sets.

As in the case of MISR, the multiangular data provided by AATSR can be used to improve aerosol estimations. The observations made in forward view are more influenced by atmospheric scattering and absorption than in the nadir view because the path length is approximately twice that of the nadir view. However, a proper modelling of the surface directional reflectance must be designed for taking profit of multiangular capabilities. Such model is the basis of an aerosol retrieval scheme specifically intended for AATSR/ATSR-2 data [Grey et al., 2006; North et al., 1999]. This model is based on the spectrally invariance of the surface directional reflectance at different viewing positions, which causes the angular variation of surface reflectance is dominated by wavelength independent geometric effects. Following North et al. [1999] notation, the surface BRF is modelled as

$$R_{\text{mod}}(\lambda,\Omega) = (1-D(\lambda))P(\Omega)\omega(\lambda) + \frac{\gamma\omega(\lambda)}{1-g}[D(\lambda)+g(1-D(\lambda))] \tag{2.4.1}$$

where $g = (1-\gamma)\omega(\lambda)$, λ is the wavelength, Ω is the viewing geometry, R_{mod} is the modelled BRF, γ is the fraction contributing to higher order scattering, D is the fraction of diffuse irradiance, P is a structural parameter and ω is a spectral parameter. The first and second terms of Eq. 2.4.1 refer to direct and diffuse scattering, respectively. $P(\Omega)$ and $\omega(\lambda)$ are free parameters that are retrieved.

This reflectance model and the 6S RTC are employed to invert the TOA reflectance measured by AATSR at the 4 VNIR bands and forward and nadir view angles. As a result, surface reflectance at those 4 bands and 2 angles and an estimation of the atmospheric AOT are obtained. The inversion is performed in two steps. In the first one, spectral surface reflectance for the two view angles and diffuse irradiance are estimated by assuming default aerosol loading and type. The second steps returns AOT after using the outputs from the first step as inputs for a 1-D inversion. This procedure is repeated for different aerosol models, and the one leading to the best fit between measured and modelled TOA reflectance is assumed as most representative of the atmospheric conditions.

A Pearson Correlation coefficient about 0.7 are obtained from comparison of AATSR retrievals with AOT values from the AErosol RObotic NETwork (AERONET) sunphotometer measurements all around the world [Grey et al., 2006]. This value increased up to 0.84 when AATSR retrievals were compared with MISR results, but it was lower when the comparison was against MODIS data.

2.5. Landsat TM/ETM Atmospheric Correction

The Landsat Thematic Mapper (TM) is an advanced, multi-spectral scanning, Earth resources sensor designed to achieve higher spatial resolution, sharper spectral separation, improved geometric fidelity, and greater radiometric accuracy and resolution than the previous Multispectral Scanner (MSS) sensor. The imager operates with a FOV of $\pm 7.2°$ (swath width of 185 km). It is a nadir viewing instrument. TM data are scanned simultaneously in 7 spectral bands. Band 6 scans thermal (heat) infrared radiation, the other ones scan in the visible and infrared. A Landsat 4 and 5 TM scene has an IFOV of 30 m^2 in bands 1 through 5 and band 7 ; band 6 has an IFOV of 120 m^2 on the ground. The image size (or scene) is 185×172 km, or 5760 lines × 6928 pixels. The Enhanced Thematic Mapper-Plus (ETM+) on Landsat7 [Goward and Williams, 1997] that was launched on April 15, 1999 is providing observations at a higher spatial resolution and with greater measurement precision than the previous TM.

There is a relatively long history of the quantitative atmospheric correction of TM imagery. All methods reported in the literature can be roughly classified into the following groups [Liang et al., 2001]:

- **Invariant-object**: the Invariant-Object method assumes that there are some pixels in any given scene whose reflectances are quite stable. A linear relation for each band based on the reflectance of these "invariant objects" can be used to normalize images acquired at different times. It is a relative normalization. If there are simultaneous ground reflectance measurements available or some assumptions about surface properties are made, it can be an absolute correction procedure. This method is simple and straightforward, but it is essentially a statistical method and performs only a relative correction. Another major limitation is its difficulty in correcting heterogeneous aerosol scattering.

- **Histogram matching**: in the histogram matching method, it is assumed that the surface reflectance histograms of clear and hazy regions are the same. After identifying clear sectors, the histograms of hazy regions are shifted to match the histograms of their reference sectors (clear regions).

  The idea behind this method is quite simple and it is also easy to implement. This method has been incorporated into ERDAS Imagine image processing software package. The PCI image processing software package is also based on a similar principle. However, the major assumption is not valid when the relative compositions of different objects and their spectral reflectances are different. This method also does not work well if the spatial distribution of aerosol loadings vary dramatically. If the scene is divided into many small segments to deal with the variable aerosol loadings, it is most likely that the major assumption of this method will be violated.

- **Dark object**: this method has a long history, as we have shown in the description of the algorithms for MERIS and MODIS, and is probably the most popular atmospheric correction method. If a scene contains dense vegetation, ETM+/TM band 7 (around 2.1 m) can be used to identify dense vegetation pixels whose reflectances have strong correlations with band 1 (blue) and 3 (green) reflectances. However, this method does not work well if the dense vegetation is not widely distributed over the hazy regions. The required existence of dense vegetation canopies is a serious limitation to many land surface imagery acquired over the winter season in the northern hemisphere. The empirical relations between band 7 reflectance and blue (band 1) and green (band 3) reflectances may also vary under different vegetation conditions.

- **Contrast reduction**: for regions where surface reflectance is very stable, the variations of the satellite signal acquired at different times may be attributed to variations of the atmospheric optical properties. Aerosol scattering reduces variance of the local reflectance. The larger the aerosol loading is, the smaller the local variance becomes. Thus, the local variance can be used for estimating the aerosol optical depth. This method has been successfully applied to desert dust monitoring. Its assumption of invariant surface reflectance limits its global applications because under general conditions surface reflectance changes in both space and time.

Apart from the previous classification, a well-known method for the atmospheric correction of Landsat ETM+ data was proposed by Liang et al. [2001]. The key feature of this new algorithm is the automatic estimation of heterogeneous aerosol distribution from the imagery itself. Information for the retrieval of water vapor may be insufficient in ETM+ bands, so water vapor transmission is calculated from climatology data or other satellite products. To calculate aerosol effects accurately, not only aerosol optical depth is needed, but also single scattering albedo and phase function. The last two variables can be determined from aerosol climatology data, although determining them from other satellite products in the near future is foreseen.

A flat Lambertian surface is assumed, with a plane-parallel atmosphere above, mathematically represented by Eq. 1.4.47. The terms ρ_0, $T(\mu_s)T(\mu_v)$ and S are stored in LUTs. By considering a constant amount of water vapor and solar zenith angle, the only variable is aerosol optical depth.

Surface reflectance of the visible bands in clear regions are determined by the knowledge of minimum surface reflectance. This step may introduce uncertainty whose magnitude depends on the surface brightness. If there exist low-reflectance surfaces in a scene, such as vegetation,water, or wet soil, the error is very small. A simpler approach is used quite often as well. By assuming a visibility value for a clear region (e.g., 50 km), we can retrieve surface reflectance very accurately.

This algorithm takes advantage of histogram matching methods. However, instead of matching histograms of two regions (clear and hazy), it is assumed that the average reflectance of each cover type is the same under different atmospheric conditions (from clear to hazy). Thus, the assumption that the landscape has the same percentage composition between the hazy and clear regions can be avoided. Because bands 4, 5, and 7 imagery are much less contaminated by most aerosols, these three bands are used to classify all pixels into specific cover types. Mean reflectance matching is performed in the first three visible bands separately. A smoothing process is followed for each band to determine the final aerosol optical depth.

The surface adjacency effects are treated by defining an "effective" surface reflectance ρ_e, so that the classic plane-parallel formulae can be exactly applied. If the surface is not homogeneous, the plane-parallel formula is not valid. This is a typical 3-D radiative transfer problem. The purpose is to develop an empirical formula for calculating the effective reflectance of a heterogeneous Lambertian surface, so that Eq. 1.4.47 is valid for a heterogeneous surface apart from that the reflectance is replaced by the effective reflectance. The basic approach employed was to run a 3-D radiative transfer code over a step-function surface and fit an empirical formula of effective reflectance. An empirical weighting function g whose convolution with the step-function produces the effective reflectance is defined:

$$\rho_e = \frac{\sum_i^N \sum_j^N g_{ij}\rho_{ij}}{\sum_i^N \sum_j^N g_{ij}}. \tag{2.5.1}$$

The fitted empirical function is

$$g(s) = f_1(\tau)exp(-1.424s) + f_2(\tau)exp(-12916s), \tag{2.5.2}$$

where s is the distance from the central location. The functions f_1 and f_2 are expressed in terms of τ by polynomial functions. The first term of the right side of Eq. 2.5.2 represents the contribution from the background pixels, and the second term represents the contribution from the current pixel and its nearest neighboring pixels.

After estimating the aerosol optical depth, the retrieval of surface reflectance is straightforward. Eq. 1.4.47 is solved, where all quantities related to the atmospheric conditions are determined by searching in look-up tables. The retrieved surface reflectance is actually the effective reflectance. The real reflectance of each pixel can be determined from Eq. 2.5.1. Theoretically, it has to be an iterative procedure since ρ_{ij} must be real reflectance, but preliminary results indicate no need for iterations because there will be generally very small improvements under most circumstances.

Part II

Atmospheric Correction Algorithm for MERIS Data over Land

Chapter 3

Algorithm Theoretical Background

The atmospheric correction algorithm for MERIS data over land presented in this thesis is described in this chapter. It has been named SCAPE-M, that stands for Self-Contained Atmospheric Parameters Estimation from MERIS data. The fundamental basis for the retrieval of AOT, CWV and surface reflectance are detailed in the first section of the chapter. The procedures developed for cloud masking and correction of topographic effects are also presented. The second section deals with the development of the Look-Up Table (LUT) which is used in all the radiative transfer calculations that are performed along the atmospheric correction process. The optimization of MODTRAN4 for the application to atmospheric correction and the selection of the LUT input parameters, their dimension and the breakpoints positions are discussed. Finally, the robustness of the different algorithm approaches and assumptions is assessed in the third section of the chapter. The impact of different factors, such as the atmospheric state, the target elevation or the surface roughness, on AOT, CWV and surface reflectance retrievals is investigated by a sensitivity analysis using synthetic MERIS data sets. Errors estimated for AOT, CWV and surface reflectance retrievals are given in the last place. An early version of the method presented in this chapter and some of the results discussed in the Chapter 4 were reported in Guanter et al. [2006b].

3.1. Algorithm Description

3.1.1. Generalities

From a formal point of view, atmospheric correction can be divided into two separated phases. The first one would is to the estimation of the atmospheric parameters needed to quantify the atmospheric influence on the measured radiation. Then, the second phase deals with decoupling surface and atmosphere radiative transfer effects. Surface reflectance images free from atmospheric effects will be obtained as final output. The SCAPE-M atmospheric correction algorithm for MERIS data over land presented in this work is intended to be a full atmospheric correction processor, able to convert from radiometrically corrected TOA radiance images to georegistered surface reflectance images. All the steps needed in this conversion are covered in an automatic manner, without making use of ancillary inputs. For this purpose, modules for cloud masking, AOT and CWV retrieval have been designed to work sequentially. The information retrieved by them is in turn applied to the derivation of final reflectance images, where the correction of topographic and adjacency effects is also addressed.

It was discussed in Section 1.1 that three atmospheric contributors should be treated specifically in the spectral range covered by MERIS: ozone, water vapor and aerosols. The stratospheric ozone principally absorbs in the green-red wavelengths, leading to line transmittances of around 0.92 in MERIS bands 5 and 6 (560 and 620 nm, respectively) [Santer et al., 1999]. However, default climatology values are usually applied for the ozone column content due to its low temporal and spatial variability. The integrated ozone column content provided by the European Center for Medium–Range Weather Forecasting (ECMWF) [European Centre for Medium-Range Weather Forecasts, 2006] is attached to MERIS images, and could be used in those cases where a refinement of the default values was necessary.

For aerosols and water vapor the situation is different, as they vary strongly in small spatial and temporal scales. Coincidence of this atmospheric information with the image to be processed is needed. The most efficient way to achieve this coincidence is the retrieval of the atmospheric parameters from the image itself. Since the radiative transfer effects of aerosols and water vapor are spectrally decoupled, two separate strategies have been designed for the retrievals. The resulting AOT and CWV maps are put together to produce the final surface image. For this purpose, accurate modelling of the atmospheric radiative transfer is needed. The MODTRAN4 code has been selected, as it provides precise calculation of the atmospheric scattering and absorption processes. The way it has been modified and optimized for its application to atmospheric correction is described in Appendix C.

Another factor to be taken into account in the retrieval of surface reflectance are the illumination effects appearing in rough terrains. It may also be an important error source on the retrieved target reflectance, as surface orientation and slope contribute to modify the ratio between the direct and diffuse irradiance arriving at the target. Due to MERIS images cover hundreds of kilometers, rough terrain regions are likely to appear in them. For this reason, topographic effects are included in the mathematical formulation transferring from surface reflectance to TOA radiance, or, equivalently, in the inversion of TOA radiance to derive surface reflectance. Inserting the topographic correction inside the atmospheric correction itself is more accurate than performing the topographic normalization over the surface reflectance image, because the separation between direct and diffuse fluxes can be addressed properly.

A simple model correction for adjacency effects in the target reflectance has been implemented as well. It is applied to MERIS full spatial resolution (FR) images (pixel size about 300 m) while adjacency is considered negligible at reduced spatial resolution (RR) images (pixel size about 1.2 km). The adjacency correction performs a first-order removal of the environment influence on the calculated surface reflectance. All the steps followed by SCAPE-M to derive surface reflectance images from the Top-Of-Atmosphere (TOA) radiances measured by MERIS will be described in the remaining of this section.

3.1.2. Radiative transfer calculations

The retrieval of atmospheric constituents and surface reflectance involves modelling the radiative transfer across the atmosphere. The signal measured by the sensor is predicted by means of a suitable formulation of the interactions between surface and atmosphere in the spectral range covered by the sensor. Thus, a simple but accurate formulation of the TOA signal in terms of surface reflectance and atmospheric optical parameters is necessary.

Since MERIS does not provide multiangular measurements, as long as multitemporal series of images are not available, the usual Lambertian approach for the surface reflectance is assumed. This approach is justified in Section 1.4.5. Lambert's Cosine Law holds that the radiation per unit solid angle from a flat surface varies with the cosine of the angle subtended between the surface normal and a given direction. In other words, intrinsic surface reflectance does not depend on illumination and observation angles. Neglecting directional effects in the target reflectance provides a simple formulation of the radiative transfer, which leads to an important decrease in the computation time and modelling effort. It has been demonstrated that the Lambertian approach can work well in the general case where the acquisition geometry is not in the retro–dispersion hot spot direction [Lee and Kaufman, 1986], and so if the observation is close to nadir. Thome et al. [1998] state that the percentage difference between the Lambertian case and typical non-Lambertian cases is less than 1% in the near nadir viewing range. This Lambertian assumption leads to the well–known equation already described in Section 1.1 (Eq. 1.4.48):

$$L_{\mathrm{TOA}} = L_0 + \frac{1}{\pi}\frac{\rho_s(E_{\mathrm{dir}}\mu_{\mathrm{il}} + E_{\mathrm{dif}})T_{\uparrow}}{1 - S\rho_s} \tag{3.1.1}$$

where L_{TOA} is the TOA radiance, L_0 is the atmospheric path radiance; μ_{il} is the cosine of the illumination zenith angle θ_{il}, measured between the solar ray and the surface normal; $E_{\mathrm{dir}}\mu_{\mathrm{il}}$, E_{dif} are the direct and diffuse fluxes arriving at the surface, respectively; S is the atmospheric spherical albedo, reflectance of the atmosphere for isotropic light entering it from the surface; $T_{\uparrow}$ is the total atmospheric transmittance (for diffuse plus direct radiation) in the observation direction, and ρ_s is the surface reflectance. Eq. 3.1.1 must be computed constantly within the atmospheric correction process, either in forward mode, to reproduce the signal measured by the sensor given the atmospheric state and the surface reflectance, or in inverse mode, in order to calculate surface reflectance from the at-sensor radiance. The atmospheric optical parameters L_0, E_{dir}, E_{dif}, $T_{\uparrow}$ and S must be provided by a radiative transfer code that receives the atmospheric conditions and scene geometrical parameters as input.

An optimized version of the MODTRAN4 atmospheric radiative transfer code [Berk et al., 2003, 1998] was used for the generation of a Look-Up Table (LUT) that provides the atmospheric parameters from interpolation. This code is based on a rigorous resolution of the radiative transfer equation, coupling scattering and absorption processes. For this reason it is relatively slow in the calculations. However, thanks to its high accuracy and fine spectral resolution, MODTRAN4 is a reference code in remote sensing applications. The faster Second Simulation of the Satellite Signal in the Solar Spectrum (6S) radiative transfer code [Vermote et al., 1997c] was initially tested, but it was discarded because of the decoupling of scattering and absorption events, which make it inconvenient for the evaluation of the radiative transfer inside absorption bands, as it is necessary for the CWV retrieval. The use of a LUT allows to speed up the calculation of the atmospheric parameters, as linear interpolations substitute running a RTC. As it will be detailed in Section 3.2, the LUT depends on 6 free input parameters: View Zenith Angle (VZA), Solar Zenith Angle (SZA), Relative Azimuth Angle (RAA), surface elevation (ELEV), horizontal visibility (VIS) and columnar water vapour (CWV). The original MODTRAN4 code was modified so that the atmospheric optical parameters needed for the atmospheric correction in Eq. 3.1.1 were provided as output, as they are not in the original MODTRAN4 code. Two runs of MODTRAN4 for each combination of inputs were needed in order to calculate those parameters.

The fast linear interpolation in the LUT enables the atmospheric parameters in Eq. 3.1.1 be calculated on a per-pixel basis so that the effects of target elevation and topography are properly corrected. The need for this correction will be justified in Section 3.3. The Global Earth Topography And Sea Surface Elevation at 30 arc second resolution (GETASSE30) Digital Elevation Model (DEM) provided jointly with the Basic ERS & Envisat (A)ATSR and MERIS (BEAM) Toolbox [Fomferra and Brockmann, 2005] is used. The dependence of L_0, $E_{\mathrm{dir}}\mu_{\mathrm{il}}$ and E_{dif} on the surface elevation is plotted in Fig. 3.1. It can be stated that L_0 and E_{dif} decrease with the surface elevation, as they are mostly caused by multiple scattering which grows with the atmospheric path. On the contrary, $E_{\mathrm{dir}}\mu_{\mathrm{il}}$ increases with the surface elevation, as the higher the surface is the smaller the extinction from the line of sight becomes. Note also the influence of the surface roughness on the direct irradiance.

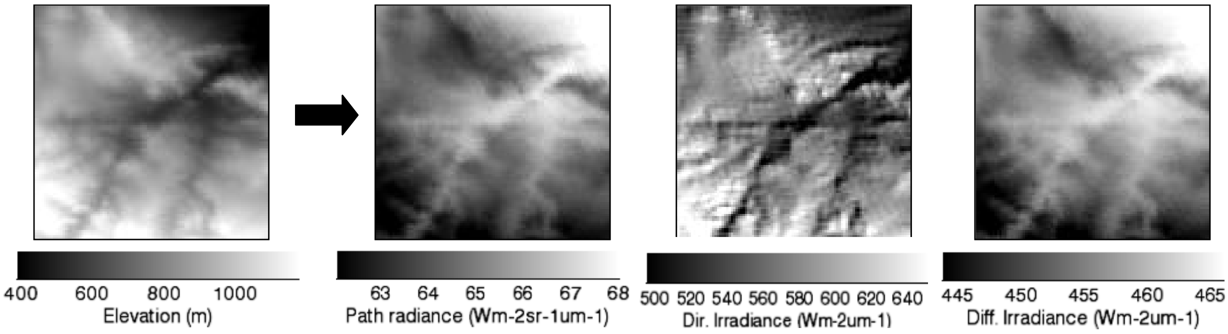

Figure 3.1: DEM and the subsequent atmospheric parameters at the 1st MERIS band (412 nm) calculated by interpolation from the LUT. Images correspond to a 30×30 km^2 area, extracted from a MERIS FR image centered at 39.3°N, 2.4°W over the Iberian Peninsula.

3.1.3. Masking non-land pixels

The initial step of the atmospheric correction algorithm is masking out all but cloud-free land pixels. Pixels with surface elevation higher than 2500 m, which is the upper limit for elevation in the atmospheric LUT, pixels labelled as `Invalid` in MERIS Level-1b flags, and pixels with self-shadowing effects are also discarded.

The most difficult contribution to be separated from land pixels is that coming from clouds over continental areas. A cloud mask to eliminate pixels totally or partially affected by clouds, whatever their optical thickness or height is, must be generated prior to the estimation of aerosol loading and water vapor content. Utilizing the `Cloud Probability Processor` implemented in the BEAM Toolbox [Fomferra and Brockmann, 2005] as a plug-in in the atmospheric correction software was considered in the first place. It calculates the cloud probability (0-100%) for every pixel. However, similar cloud probabilities were found in cloudy pixels and in bright cloud-free bare soils. Then, the large data set of images acquired over the Iberian Peninsula (which was one of the main data sources to test the algorithm) could hardly be processed with that method, as an important contribution from bright soils is found.

Thus, a simpler but more robust cloud masking method based on static thresholds in the reflectance and its spectral slope has been designed. In its current status, two sets of thresholds are used. The first of them, `cloud mask #1`, is very restrictive in order to ensure AOT retrieval is only performed over cloud-free and non-bright pixels. This is done because even the thinnest cloud may affect considerably aerosol retrievals, leading to a large AOT overestimation. The second set of thresholds, `cloud mask #2`, is designed to discriminate pixels in which the contamination by clouds is ensured. It is intended to be applied in the CWV and surface reflectance retrieval, over which thin clouds do not have such a large impact. However, even though the normal operation of the algorithm makes use of cloud masks `#1` and `#2` in the way that is described above, that sequence can be controlled by the user through an input flag named `Cloud_flg` to be set in the input file (the reader is referred to Appendix D for detailed instructions about the launch of SCAPE-M). This flag can have three different values: `Cloud_flg`= 0 corresponds to the normal operation as described above, with `cloud mask #1` being applied in aerosol retrieval and `cloud mask #2` in CWV and surface reflectance retrieval. When `Cloud_flg`= 1, the relaxed mask `cloud mask #2` is used along the entire procedure. It should be used when high aerosol loadings (fire events, polluted areas...) are expected in the observed area, which would probably be removed by the restrictive `cloud mask #1`. Finally, only `cloud mask #1` is used if `Cloud_flg`= 2. Surface reflectance would only be retrieved over areas with the minimum risk of being affected by clouds. It is recommended when the emphasis is put on the best accuracy in surface reflectance, rather than on counting on the largest amount of pixels.

Static thresholds are applied over TOA apparent reflectances rather than over TOA radiances in order to normalize by the incoming radiation, which varies with time and geographic location. The thresholds have been selected ad-hoc after evaluating a number of images with different cloud types and conditions. TOA apparent reflectances are calculated by dividing TOA radiances by the extraterrestrial solar irradiance arriving at the external atmospheric layer following Eq. 1.4.40.

According to their optical thickness, clouds can be separated into thick and thin clouds. The detection of the first ones is relatively easy, as they are much brighter than the surfaces below, apart from snow or ice covers. Moreover, thick clouds eliminate completely the influence of the surface underneath, which makes its reflectance pattern nearly flat in the visible wavelengths. For this reason, TOA reflectances in the visible region are selected as a reliable indicator of thick clouds presence. Mistaking snow and ices surfaces for cloudy pixels is not a problem, as the atmospheric correction algorithm is intended to be applied to land surfaces with presence of vegetation and bare soil pixels. An average TOA reflectance ρ_{TOA}^{av} at visible wavelengths is calculated as the average reflectance in channels 1 to 8 (412.4-681.3 nm), and static thresholds are applied to classify pixels as either `cloud mask #1`, `cloud mask #2` or none of them.

The second type of clouds is thin clouds, which are not so bright, as well as semi-transparent to the radiation reflected by the surface. This causes the detection of this type of clouds to be substantially more difficult than in the case of the thick ones. In order to mask thin clouds, thresholds are applied over the first MERIS band ρ_{TOA}^{1}, which measures high radiation levels when thin clouds are present, independently of the brightness of the surfaces below. Moreover, to enhance the fact of the cloud spectral flatness, the last classification criterion is given by comparing the apparent reflectance in the first band with that in either band 8 (`cloud mask #1`) or 9 (`cloud mask #2`). The two threshold sets are:

- `cloud mask #1`: $\rho^{av}_{\mathrm{TOA}} > 0.27$, $\rho^{1}_{\mathrm{TOA}} > 0.2$, $\rho^{1}_{\mathrm{TOA}} > \rho^{8}_{\mathrm{TOA}}$
- `cloud mask #2`: $\rho^{av}_{\mathrm{TOA}} > 0.3$, $\rho^{1}_{\mathrm{TOA}} > 0.23$, $\rho^{1}_{\mathrm{TOA}} > \rho^{9}_{\mathrm{TOA}}$

The cloud masking method performance is illustrated in Fig. 3.2. The two threshold sets were applied to a MERIS FR image acquired last 15 May 2003 over Toulouse, France. The subset shown in Fig. 3.2(a) corresponds to an area of about 120 × 120 km where thin clouds were present. Fig. 3.2(b) is derived with the threshold set labelled as `cloud mask #2`, while Fig. 3.2(c) results from `cloud mask #1`. It can be stated that the thickest clouds are well detected in both cases, but it does not happen the same for the thinnest ones, that are only masked by `cloud mask #1`. However, some cloud-free pixels are also masked as clouds when `cloud mask #1` is used. These results reinforce the use of `cloud mask #1` for masking any pixel with certain probability of being affected by clouds, while `cloud mask #2` is applied in the derivation of CWV and surface reflectance images, as most of the clouds are masked without eliminating bright cloud-free pixels in addition. The adaptation of a more sophisticated method based on classification using different absorption features as well as brightness criteria [Gómez-Chova et al., 2005] is foreseen for future versions of SCAPE-M.

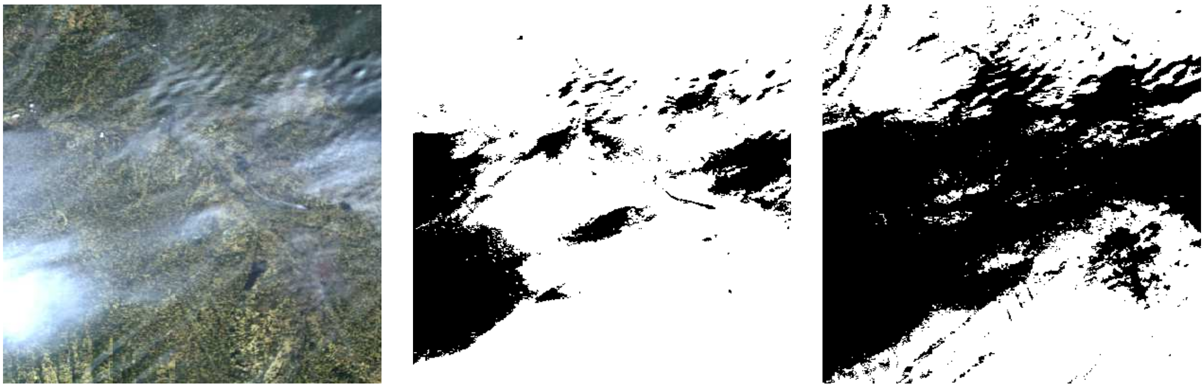

(a) RGB composite (b) `cloud mask #2` (c) `cloud mask #1`

Figure 3.2: Example of the cloud masking technique performance. The true color composite in (a) corresponds to a subset extrated from a MERIS FR image acquired over Toulouse, France (latitude= 43.6°N, longitude= 1.4°W, mean elevation= 150 m) on 15 May 2003. Threshold sets `cloud mask #2` and `cloud mask #1` lead to (b) and (c), respectively.

Even though SCAPE-M is intended to work over land surfaces, water pixels located close to land surfaces are also processed. In particular, inland water bodies up to 400 km^2

and coastal pixels separated up to 10 km from the coast line are also processed, as the atmospheric parameters derived from land pixels can be extended to those areas. Water pixels are detected as those with $\rho_{\mathrm{TOA}}^{13} < 0.08$, taking advantage of the dark reflectance of water at the NIR. The largest water bodies are removed by discarding all the closed regions labelled as water with an area higher than 400 km^2, but keeping the pixels in a 10 km distance from the coast line provided by the MERIS Level-1b `Coastline` flag. The `Land/Sea` flag can not be used for the classification of inland water bodies because some of them are missing. An example of inland and coastal waters mask derived by this procedure is displayed in Fig. 3.3

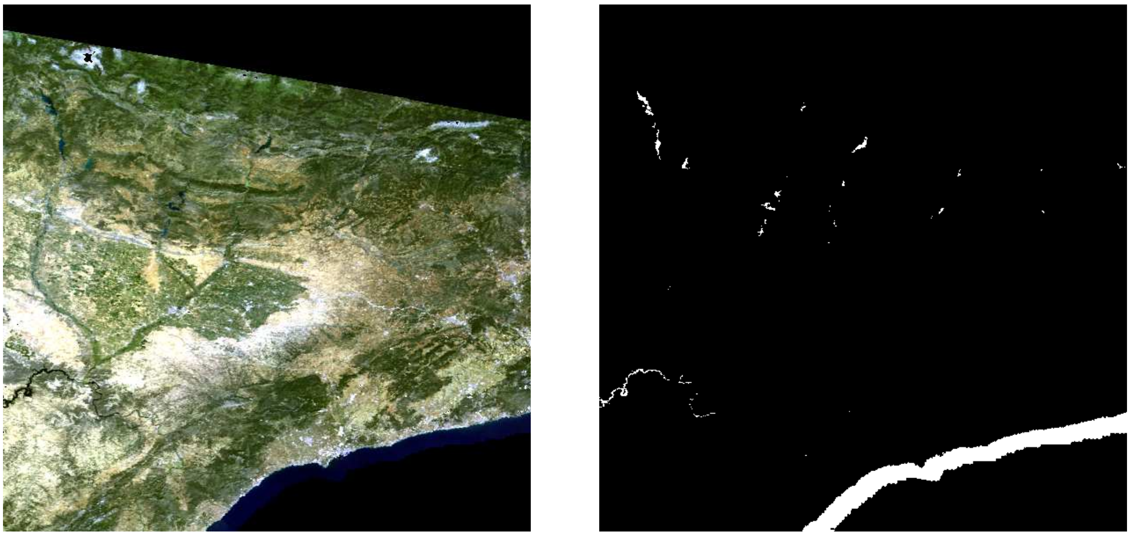

(a) RGB composite

(b) Inland and coastal waters mask

Figure 3.3: Example of detection of inland and coastal waters.

3.1.4. Accounting for topographic effects

Topographic effects may modify the distribution of direct and diffuse irradiance fluxes arriving at the target with respect to those calculated for flat surfaces. This would affect the direct and diffuse fluxes in the denominator of Eq. 3.1.1, and the simulated L_{TOA} as a result (or, equivalently, the retrieved surface reflectance ρ_s if Eq. 3.1.1 is inverted). The magnitude of this influence is partially coupled to the atmospheric state.

The area covered by MERIS scenes usually ranges from 350 to 1100 km, depending on the scene type. This means that rugged surfaces usually appear within the images. Techniques aimed to accounting for topographic effects in remote sensing images have been developed by a number of authors. Most of them [Civco, 1989; Colby, 1991; Franklin and Giles, 1995; Riaño et al., 2003; Teillet et al., 1982] perform a simple topographic correction prior to the atmospheric correction, so a proper separate correction of the direct and diffuse fluxes at the surface is not achieved. The dependence of the global flux at the surface on varying terrain slopes and orientations is related to the atmospheric state, as the ratio between direct and diffuse terms is weighted by the atmospheric transmittance. For this reason, atmospheric correction must be coupled to an accurate formulation of topographic effects [Richter, 1997, 1998].

The dependence of the direct flux on the illumination angle, defined as the angle between solar rays and the surface normal vector, is already parameterized in Eq. 3.1.1. However, the influence of the surface slope and orientation over the diffuse flux is neglected. This deficiency can be corrected by adding a term which modulates the diffuse irradiance as a function of angles and atmospheric transmittance. Following Richter [1997, 1998], Hay's model [Hay, 1979] can be implemented in Eq. 3.1.1 to account for the anisotropic distribution of the diffuse irradiance. According to Hay's model, the diffuse irradiance on a tilted plane $E^t_{\mathrm{dif}}(x, y, z)$ at height z and horizontal position (x, y) is given by

$$E^t_{\mathrm{dif}}(x,y,z) = E_{\mathrm{dif}}(z)\left[t_{\mathrm{dir}}(z)\mu_{\mathrm{il}}(x,y) + [1 - t_{\mathrm{dir}}(z)\mu_s]\frac{1+\mu_n(x,y)}{2}\right], \tag{3.1.2}$$

where $E_{\mathrm{dif}}(z)$ is the isotropic diffuse flux arriving at a surface at height z, $t_{\mathrm{dir}}(z)$ is the transmittance for direct radiation from the Sun to the target, μ_s the cosine of the SZA θ_s, and $\mu_n(x, y)$ the cosine of the surface normal zenith angle θ_n. The diffuse solar flux at the surface in Eq. 3.1.2 is estimated as a linear combination of two contributions, one coming from the circumsolar diffuse irradiance from the solid angle near the Sun and the other isotropically from the remaining sky dome [Richter, 1997, 1998]. It can be stated that $E^t_{\mathrm{dif}}(x, y, z) \simeq E_{\mathrm{dif}}(z)$ if the surface tilt angle is small, with the limit case $E^t_{\mathrm{dif}}(x, y, z) = E_{\mathrm{dif}}(z)$ for flat surfaces. The three zenith angles to be considered in the topographic correction of the diffuse term are plotted in Fig. 3.4. The azimuth angles of the Sun (ϕ_s) and the plane (ϕ_n), which are also involved in the calculation of μ_{il}, are not depicted.

The diffuse irradiance dependence on $t_{\mathrm{dir}}(z)$ causes the need to know in advance the atmospheric state, especially the aerosol loading. A priori, other contributions to $t_{\mathrm{dir}}(z)$ which may vary significantly from climatology values are water vapor and surface elevation. It is assumed that the first one can be replaced by a default value in all the MERIS bands except for that in 900 nm, while the impact of surface elevation is properly addressed by the interpolation from the DEM, as it is shown in Fig. 3.1. However, aerosols do affect the entire spectral region, and are not known in advance. Therefore, the diffuse solar flux is assumed to be isotropic ($E^t_{\mathrm{dif}}(x, y, z) = E_{\mathrm{dif}}(z)$) for the simulation of TOA radiances in the aerosol retrieval module. This is not a big shortcoming, as most of the information in AOT estimation comes from the atmospheric path radiance, and slight errors in the diffuse irradiance computation do not have a major impact. For the retrieval of CWV and surface reflectance, the AOT map has already been derived. This map is used jointly with the

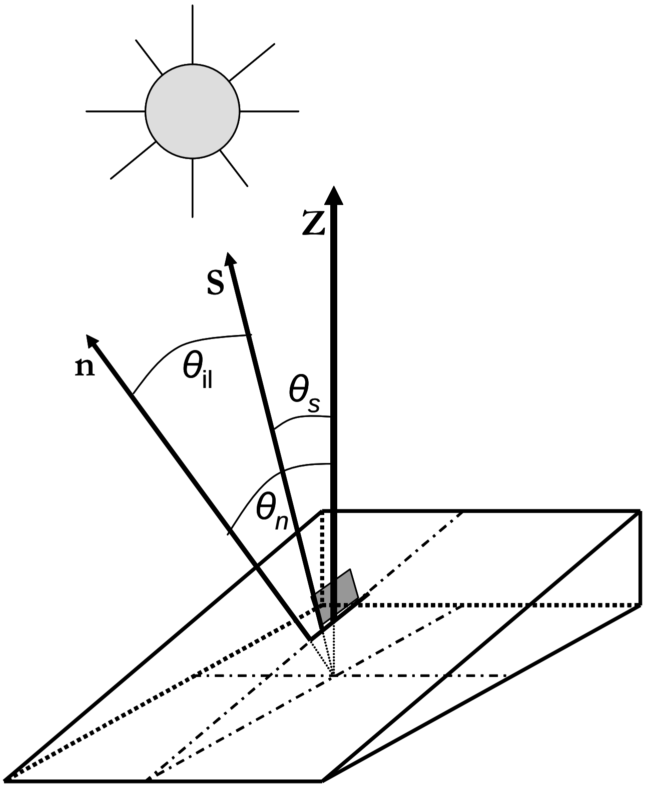

Figure 3.4: Schematic view of the three zenith angles θ_{il}, θ_n and θ_s to be considered in the topographic correction. **S** is the surface-to-Sun vector, and **n** the surface normal vector. The solar azimuth angle and the azimuth angle accounting for the plane orientation, which are also involved in the calculation of μ_{il}, are not depicted for the sake of clarity.

DEM and a default CWV value of 2 g·cm^{-2} to calculate $E^t_{\text{dif}}(x, y, z)$ by means of Eq. 3.1.2.

The angles θ_{il} and θ_n are calculated from the GETASSE30 DEM overlapped to each MERIS image. The illumination angle θ_{il} is calculated as the angle between the normalized surface-to-Sun vector **S** and the surface normal vector **n**, i.e. $\mu_{\text{il}} = \mathbf{n} \cdot \mathbf{S}$. For flat surfaces, $\mu_{\text{il}} = \mu_s$. **S** is easily calculated by using spherical coordinates and the solar zenith and azimuth angles provided attached to MERIS images, while **n** is calculated by a least square regression of the plane equation $ax + by + cz + d = 0$ to the 9 elevation points given in a 3×3 square grid centered at the pixel. The resulting $[a, b, c]$ vector generates **n**, which in turn leads to μ_n by $\mu_n = \cos \mathbf{n}_z$. A similar approach was adapted for the processing of Scanning Force Microscopy data at a nanometer scale [Palacios-Lidón et al., 2006].

An example of μ_{il} variations within a MERIS FR image acquired over the Iberian Peninsula (latitude= 39.5°N, longitude= 4.0°W) on 26 July 2003 is displayed in Fig. 3.5. The derived μ_{il} image is compared with the DEM of the same area. Sun position at the image center is SZA= 27.2° and SAA= 131.7° ($\mu_s = 0.89$, South-East illumination). It can be observed that illumination angles are highly variable in rugged surfaces, as illuminated and shadowed areas can be easily identified. The negative gradient in the illumination from South-East to North-West due to μ_s variations across the images can also be detected. Most of the actual illumination angles vary from 0° to 40° in the images, while SZA is between 23.4 and 30.9°. It will be shown that neglecting the variations of the illumination angle with the surface topography could lead to higher errors that the ones due to a mis-estimation of the atmospheric constituents or the assumption a Lambertian surface in many combinations of geometrical configurations and atmospheric states.

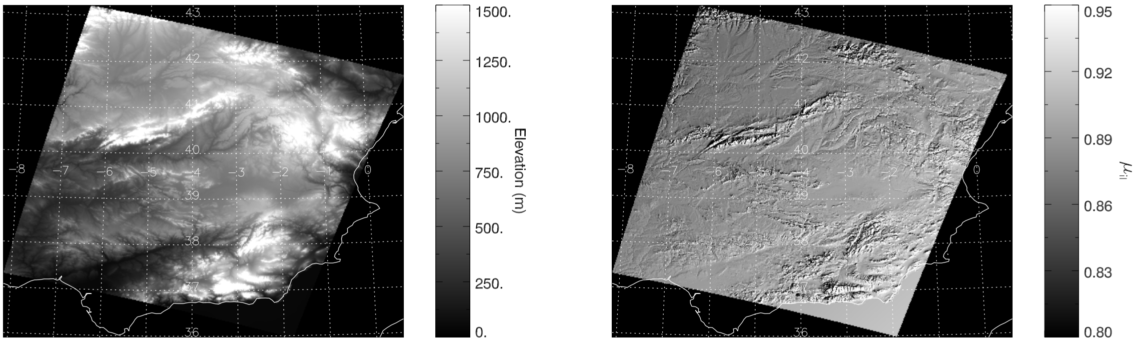

(a)

(b)

Figure 3.5: Actual illumination angles within a MERIS FR image acquired over the Iberian Peninsula (latitude= 39.5°N, longitude= 4.0°W) on 26 July 2003. The solar position at the image center is SZA= 27.2° ($\mu_s = 0.89$) and SAA= 131.7°. Left (a), elevation of the area provided by GETASSE30. Right (b), μ_{il} image calculated from the DEM on (a) and the SZA image following the procedure described above.

3.1.5. Retrieval of Aerosol Optical Thickness

It was described in Section 1.1 that aerosols are the main perturbation agent in the spectral range covered by MERIS. The fact that aerosols are highly variable in spatial and temporal terms, and that they can be originated by different processes, causes a proper modelling of the interaction between radiation and aerosols a difficult task. This is the first step for the aerosol retrieval from remote sensors. The concept of dark targets [Kaufman and Sendra, 1988] is widely extended in aerosol retrieval [Kaufman et al., 1997; Santer et al., 1999; Vermote et al., 1997a]. It is based on the assumption that only a small amount of the photons reaching the sensor comes from the surface if it is dark, because the main contribution to the registered radiance in the visible spectral region comes from the radiation reflected by the atmosphere. If the surface reflectance is set to a default value previously selected according to the type of dark target, the atmospheric contribution becomes the only unknown variable in the reproduction of the measured TOA radiance. As the Rayleigh contribution depends mainly on the surface elevation, which can be provided by a DEM at the same resolution and projection than the image to be processed, and ozone does not present important temporal or spatial variations either, aerosols are assumed to be the only remaining variable to be determined in the radiative transfer problem. However, the dark target method is very restrictive, because it can only be applied to areas with a uniform distribution of dark surfaces, such as dense vegetation in the visible bands or water bodies in the NIR.

The approach proposed in this work allows the estimation of atmospheric parameters from a wider range of land targets, with the only restriction that the surface reflectance can be represented by a linear combination of two pure green vegetation and bare soil endmembers. AOT is retrieved by means of a multiparameter inversion of a set of 5 TOA radiance spectra, assuming the atmospheric state is constant above them. A version of this methodology for the AOT retrieval from CHRIS/PROBA data has also been developed [Guanter et al., 2005b].

Aerosols are parameterized by the horizontal visibility and the rural model [Shettle and Fenn, 1979]. The first one provides the aerosol total loading, normalized at 550 nm, while the rural model specifies the AOT spectral slope. Horizontal visibility is used because it is the original MODTRAN4 input accounting for aerosol loading. The conversion to AOT at 550 nm (τ_{550}) is performed afterwards. Concerning aerosol type, early versions of the method tried to derive information on the aerosol model characterizing the extinction spectral behavior, but it was concluded that there is not enough information on MERIS data over land (that is, bright targets at the NIR wavelengths, one single view angle and a reduced spectral range from 400-900 nm) to achieve a reliable estimation of the aerosol model. The difficulties to estimate the aerosol model from MERIS data were also reported in Santer et al. [2005] and Ramon and Santer [2005].

The aerosol retrieval in SCAPE-M is based on the assumption that the atmospheric state is invariant inside 30×30 km cells. Aerosols are estimated sequentially from all the 30×30 km cells in the image by means of a sliding window with given mean VZA, SZA, RAA and surface elevation. The 30 km size is chosen as a trade-off between the largest area in which the atmosphere can be considered constant and the smallest one providing enough variability in the surface. The first step is masking out all the pixels affected by cloud contamination. Making use of `cloud mask #2`, those pixels which are sure to be cloudy are removed. Visibility from a given cell is calculated as long as it contains more than 35% of cloud-free pixels. If the cloud-free pixels is lower than 35% it is assumed that the cell is too contaminated by clouds for a reliable aerosol retrieval. The lowest radiance values in each spectral band within the cell are found then. The resulting spectrum is employed somehow similarly to a dark target. It provides the highest limit for the aerosol content: an iterative procedure looks for the visibility value leading to the atmospheric path radiance which is closest to the radiance in the dark spectrum, not allowing path radiance to be higher than the dark spectrum in any of the visible bands (from 412.5 to 681.25 nm). The lowest the radiance in the dark spectrum is, the closest the estimated visibility value will be to the real value. If no spectrum with relatively dark values is found, the retrieved aerosol loading will overestimate the real conditions. To avoid this situation, a lower limit of 45 km (τ_{550} about 0.2) is arbitrarily chosen: if the estimated visibility is lower than 45 km, the dark pixel estimation for that cell is discarded.

The next step is refining that initial visibility estimation with a more sophisticated method involving the inversion of TOA radiances in combinations of green vegetation and bare soil pixels. This is performed only over the pixels which are classified as land pixels by `cloud mask #1`. The brightest land pixels might be classified as clouds by this mask, because `cloud mask #1` was designed to seek for any potential cloudy pixel, including those with possible thin clouds. These are a major error source in aerosol retrieval, as they lead to extreme AOT values.

The visibility in each of the cells is retrieved from 5 pixels with high spectral contrast inside this window, by means of a multiparameter inversion of the TOA spectral radiances. To provide an estimation of the surface reflectance each of the 5 reference pixels is represented by a linear combination of two vegetation and soil spectra, which act as endmembers:

$$\rho_s = C_v \rho_{veg} + C_s \rho_{soil} \qquad C_v, C_s > 0 \tag{3.1.3}$$

The proportions of vegetation and soil $C_{v,s}$ are allowed to be larger than 1.0, covering those cases in which the surface reflectance is brighter than the endmembers. The constraint is that the generated surface reflectance must be in the range $[0, 1]$. The ten coefficients $C_{v,s}$ (2 for each of the 5 pixels) are free parameters in the inversion. It must be remarked that the vegetation and bare soil endmembers are not real endmembers characterizing every single scene, but they are only used to represent the average surface reflectance contribution by means of its linear combination. Thus, there is no need for the retrieval of endmembers from the image, but it is enough if the a priori selected spectra can be combined to reproduce the actual spectral shape of the reference pixels. A similar idea using linear combinations of endmembers to be inverted inside an AOT retrieval scheme, although on a per-pixel basis, was also proposed by von Hoyningen-Huene et al. [2003].

The selection of 5 as the number of pixels to serve as reference for the atmospheric retrievals comes from a balance between the computation burden and the representative sampling in the 30 × 30 km window: a higher number would increase the number of free parameters in the inversion, without adding much information to the sampling. The 5 reference pixels must have as much spectral contrast as possible (ranging from pixels with high vegetation content to high bare soil content). The reason is that this contrast in the surface, while assuming a constant atmosphere above, is used in the discrimination of the radiative transfer contribution of surface and atmosphere to the TOA signal. A perfect choice for the set of reference pixels would be a pure vegetation pixel, a pure bare soil pixel, and three intermediate ones, mixture of vegetation and soil. In the operative procedure, the selection is based on the definition of three categories of land pixels, using the Normalized Difference Vegetation Index (NDVI) [Tucker, 1979]. It is calculated from TOA reflectances instead of from radiances, in order to normalize the effect of varying illumination. Pure bare soil pixels are those with a NDVI value between 0.1 and 0.15, mixed pixels are between 0.15 and 0.45, and pure vegetation pixels have a NDVI in the range 0.4–0.9. The DEM overlapped to the image is used to ensure the selected pixels do not present variations larger than ±20% in the surface elevation and ±10% in the illumination angle μ_{il}, calculated from the normal vector to the surface. In both cases larger variations would add errors to the retrievals. Variations in the surface elevation might cause differences in the Rayleigh contribution, while the changes in the illumination angle would modify the amount of radiation in the system.

The inversion is performed by means of the minimization of a Merit Function δ^2 specifically designed for this problem,

$$\delta^2 = \sum_{\mathrm{pix}=1}^{5} \omega_{\mathrm{pix}} \sum_{\lambda_i} \frac{1}{\lambda_i^2} \left[L^{\mathrm{SIM}}|_{\mathrm{pix},\lambda_i} - L^{\mathrm{SEN}}|_{\mathrm{pix},\lambda_i} \right]^2 \tag{3.1.4}$$

where L^{SIM} is the set of simulated TOA radiances using Eq. 3.1.1, L^{SEN} stands for the TOA radiance measured by the sensor, λ_i corresponds to the center wavelength of the i band, and ω_{pix} is a weighting factor equals to 2 for pure vegetation pixels, 1.5 for mixed pixels and 1 for bare soil pixels. The Merit Function is weighted by λ_i^{-2} to drive the inversion towards the smaller wavelengths, where the aerosol effect is much larger than the reflectance of most of the natural surfaces. The higher sensitivity of vegetation targets to the aerosol loading is enhanced in δ^2 by ω_{pix}. MERIS channels 11th and 15th are avoided in the computation of δ^2 because they are affected by strong gaseous absorptions that might be an error source in the aerosol retrieval. There are 11 free parameters for each cell, 1 for the visibility and 10 for the $C_{v,s}$ abundances in the 5 reference pixels. The water vapour column content is set to 2 g·cm^{-2}, as its influence on the aerosol retrieval is negligible, as it will be shown in Section 3.3. L^{SIM} is generated by means of Eq. 3.1.1 without correcting for the topographic effects in the diffuse terms which are presented in Eq. 3.1.2. A prior knowledge of the atmospheric state is needed for the calculation of $E^t_{\mathrm{dif}}(x, y, z)$, which is not available until the aerosol map is generated. In any case, the contribution of this term can be neglected if it is compared with the atmospheric path radiance in the visible region, which provides most of the information for aerosol retrieval. To prevent the AOT estimation from unexpected reflectance patterns in the set of reference pixels, the inversion of δ^2 is repeated if the partial $\delta^2|_{\text{pix}}$ value for a pixel exceeds ±2 times the value of δ^2. This feature is useful in removing pixels affected by very thin clouds which are not filtered by the cloud mask or by the NDVI thresholds.

The accuracy of AOT retrieval in SCAPE-M can be tuned according to the user requirements. The user can select two options which provide a better accuracy in AOT retrieval than the basic operation mode, with the penalty of larger computation times. The first of them is intended to correct errors associated to the simple formulation of ρ_s in Eq. 3.1.3. In order to minimize possible biases due to a bad representation of the actual surface reflectance by endmember combinations, three different vegetation spectra are combined with one bare soil spectrum. The vegetation spectra correspond to a green vegetation crop, a typical forest spectrum and a dark vegetation target. The aerosol loading is calculated independently for each of the three pairs of vegetation and soil endmembers. The AOT value leading to the minimum δ^2 value in the inversion, is selected for the cell. The vegetation and bare soil endmembers are displayed in Fig. 3.6. The reason for having 3 vegetation spectra accounting for different vegetation types and only one for bare soil is that vegetation is considered to have a wider range of spectral patterns than bare soils. These are less variable in spectral terms, while they may have important variations in brightness, which is already modulated by C_s.

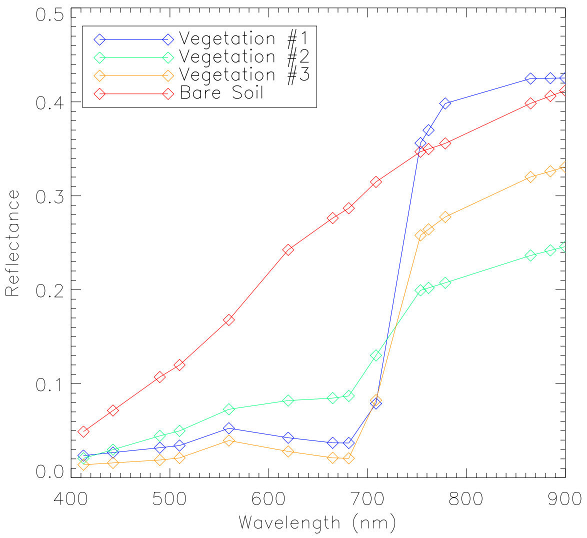

Figure 3.6: Vegetation and bare soil reflectance spectra used as endmembers in the aerosol retrieval module. The vegetation spectra correspond to a green vegetation crop (Vegetation #1), a typical forest spectrum (Vegetation #2) and a dark vegetation target (Vegetation #3).

The second option which should improve the aerosol retrieval is intended to reduce possible errors arising from using only one set of 5 reference pixels. If the corresponding flag is activated, AOT retrieval is not performed over one set of reference pixels, but up to 10 sets, depending on the availability of suitable pixels in the cell, are used to estimate aerosols. The final AOT value is calculated by averaging all the individual results. These two options are controlled by a variable named `AOT_time_flg` to be set by the user in the input file. It can have 3 different values: if `AOT_time_flg` is equal to 0, neither the endmember correction nor multiple sets of reference pixels are applied; if it is 1, only the endmember correction is applied; finally, if it is 2, both refinements are used. After trying the method against a large data set varying the 3 options, it was found that `AOT_time_flg`= 1 is the best choice in the general case, as the computation time is not very affected and considerable improvements are reached. Running the method for different sets of reference pixels did not lead to important changes, as most of the retrievals were in a narrow range.

The minimization of the Merit Function in Eq. 3.1.4 is performed by the Powell's Minimization Method [Press et al., 1986], based on a 1–D minimization separately in each direction of the parameters space, without the need for the analytical expression of the function derivatives. An appropriate initialization of the Powell's algorithm is needed in order to reduce the convergence time. Visibility is set to 45 km (AOT at 550 nm about 0.2), while for the vegetation and soil proportions a linear correlation between the NDVI and the coefficients $C_{v,s}$ was found from several simulations. A more efficient strategy for the inversion was also tried. It lied on the high linear dependence of TOA radiances in Eq. 3.1.1 on the surface reflectance: if the approach $S\rho_2 \ll 1$ is made, $L_{\text{SEN}} = f(\rho_s)$ becomes a linear model. The inversion of L_{SEN} could then be performed in a coupled procedure, where 10 of the parameters were retrieved by an analytical inversion based on the least squares method [Whittaker and Robinson, 1960], and the best-fitting visibility value was calculated afterwards. However, in practice the linear inversion fell in negative errors or meaningless values in some occasions, which could not be solved by common weighting procedures as it is done in usual multiparameter inversion techniques. In any case, the computation time associated to AOT retrieval is about one order of magnitude lower than that for water vapor and surface reflectance, so utilizing the Powell non-linear inversion is justified.

When a visibility value is derived for each of the cells in which the retrieval is successful, the resulting mosaic is smoothed in order to reproduce the smooth variations expected in the atmospheric distribution. Blank cells (namely those with a proportion of land pixels smaller than 35%) are filled by means of interpolating with the surrounding ones. If there were no neighbors with data to perform the interpolation for a certain cell, visibility would be set to the mean value calculated from all the occupied cells. A cubic convolution interpolation method is used to convert from cell to pixel scale. The final visibility map is generated after masking the visibility image per-pixel with `cloud mask #2`.

The last step is the conversion from horizontal visibility to τ_{550}. Once the aerosol model and the atmospheric vertical profile are fixed, the AOT integrated over the entire atmospheric column is given by visibility and surface elevation. This dependence is illustrated in Fig. 3.7. τ_{550} is plotted as a function of visibility and surface elevation in Fig. 3.7(a). The 7 visibility and the 3 surface elevation values are those tabulated in the atmospheric LUT. It can be observed that τ_{550} does not vary linearly with visibility, while it does with the target elevation, as it will be shown in Section 3.2. This may cause errors if linear interpolation is applied to calculate τ_{550} for a given visibility value. In order to correct for this effect, 3 transfer functions are generated to convert from visibility to τ_{550}, each one of them accounting for one of the 3 elevation values in the LUT. They are parameterized as

$$\tau_{550}(z, \mathrm{VIS}) = \exp[a(z) + b(z)\ln(\mathrm{VIS})], \tag{3.1.5}$$

because it was found that $\ln(\tau_{550})$ is highly linear with $\ln(\mathrm{VIS})$. The free parameters $a(z), b(z)$ are calculated by linear fitting of the 7 pairs $\{\ln(\mathrm{VIS}), \ln(\tau_{550}(z_i, \mathrm{VIS}))\}$ for each of the 3 elevation breakpoints z_i in the LUT. In order to generate the τ_{550} map from the visibility and surface elevation maps, linear interpolation on z and the visibility to τ_{550} transfer functions are applied sequentially: for a given z value, $a(z), b(z)$ are calculated through linear interpolation of $a(z_i), b(z_i)$ generated from the breakpoints. Then, τ_{550} is calculated by means of Eq. 3.1.5. A comparison of linear interpolation with the use of the transfer function in Eq. 3.1.5 for $z = 0$ km is displayed in Fig. 3.7(b). Errors in τ_{550} associated to linear interpolation can be up to 0.03. An example of the conversion of the visibility map before the smoothing process into the final τ_{550} map is shown in Fig. 3.8.

3.1.6. Retrieval of Columnar Water Vapor

The water vapor retrieval module in SCAPE-M is based on a differential method which evaluates the radiances inside and outside a given water vapor absorption feature. It is run after the aerosol estimation in order to eliminate errors in CWV which would arise if the aerosol loading is not known, as it would be justified in Section 3.3. Similar approaches were presented by other authors (Kaufman and Gao [1992], Bennartz and Fischer [2001], Chylek et al. [2003]). In the case of MERIS, it is shown in Fig. 1.2 that band 14 (centered at 890 nm) is free from water vapor absorption, while band 15 (centered at 900 nm) is affected by one of the wings of the water vapor absorption feature centered at 940 nm. The influence of that water vapor absorption feature at MERIS bands 14 and 15 is shown in Fig. 3.9. A radiance spectrum simulated with MODTRAN4 at a spectral resolution of 1 cm^{-1} is resampled to MERIS reference band configuration.

The basis of the method is to invert the ratio R of the radiance at MERIS bands 15 to

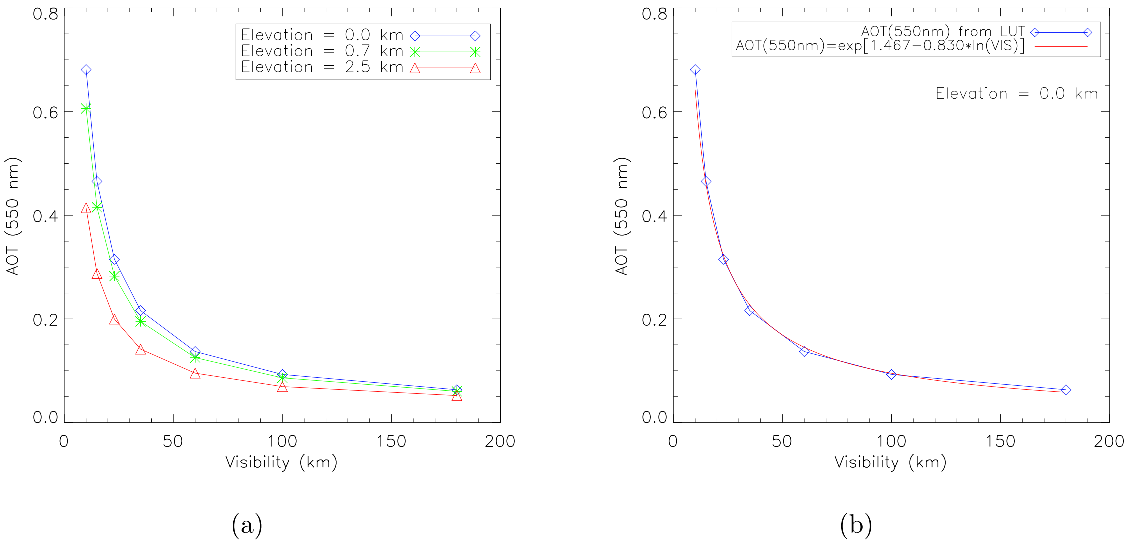

(a) (b)

Figure 3.7: Dependence of τ_{550} with visibility and surface elevation. Left (a), τ_{550} is plotted as a function of visibility for the 3 surface elevation breakpoints in the LUT. Right (b), comparison of τ_{550} calculated from linear interpolation between visibility breakpoints with the τ_{550} calculated from the transfer function in the legend.

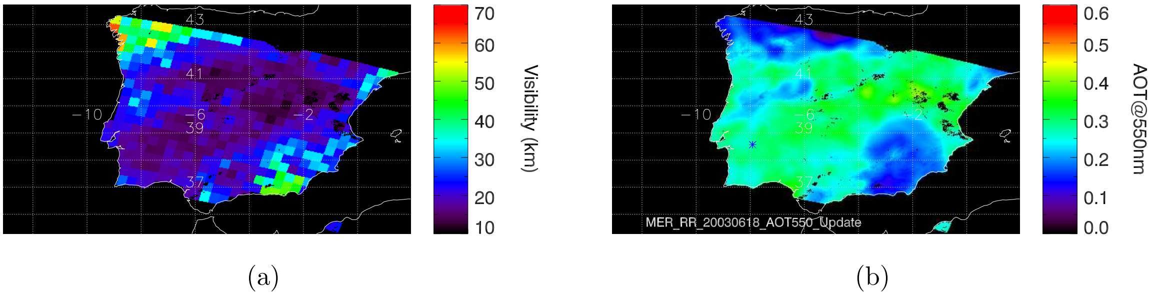

(a) (b)

Figure 3.8: Conversion from visibility (“per-cell basis”) to τ_{550} (“per-pixel basis”) for a MERIS RR image acquired over the Iberian Peninsula on 18 June 2003.

the one at 14 (L_{14}, L_{15}, respectively),

$$R = \frac{L_{15}}{L_{14}} \tag{3.1.6}$$

CWV being the only free parameter in the inversion. With this purpose, a simulated ratio R^{SIM} is generated so that it fits the actual ratio R^{SEN} measured by MERIS. The Merit Function $\chi(\mathrm{CWV})$ to be minimized is

$$\chi(\mathrm{CWV}) = R^{\mathrm{SEN}}(\mathrm{CWV}) - R^{\mathrm{SIM}}(\mathrm{CWV}) \tag{3.1.7}$$

The function χ may have either positive or negative values. Then, the minimization of $\chi(\mathrm{CWV})$ consists in finding the root of a 1-D function. This fact allows to apply the fast

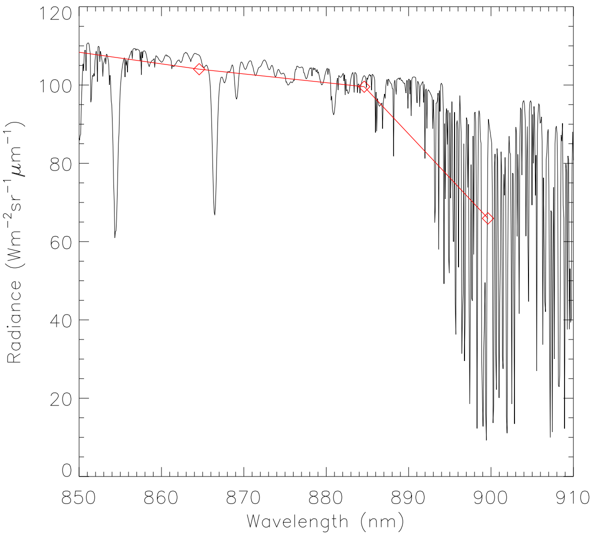

Figure 3.9: MODTRAN4 1 cm^{-1} TOA radiance spectrum resampled to MERIS nominal band configuration. MERIS bands 13, 14 and 15 are pointed out by diamonds.

Brent's method [Press et al., 1986] to estimate the water vapor content with a low time penalty.

Given the angular configuration, the AOT and the surface elevation for each pixel, the water vapor content is varied by an iterative procedure to find the R^{SIM} which best matches the actual R^{SEN} measured by MERIS. The dependence of R^{SEN} on the aerosol content (Bennartz and Fischer [2001], Chylek et al. [2003]) is taken into account by using the value of the AOT derived in the AOT retrieval module. Eq. 3.1.1 is applied to simulate the TOA radiances. Since an estimation of the aerosol loading is already available, Hay's model in Eq. 3.1.2 is used to account for the correction of the diffuse irradiance term in tilted surfaces. For the simulation of the radiance at bands 14 and 15 the value of the surface reflectance at those channels must be known. However, surface reflectance can not be estimated until information about the CWV is available. This interdependence is sorted out by assuming a default CWV value for the reflectance retrieval at bands 13 and 14, which are used in the estimation of the reflectance at band 15. In the case of bands 13 and 14, at-sensor radiances are atmospherically corrected setting the water vapor to a default value of 2 g·cm^{-2}; band 15 is calculated from linear extrapolation using bands 13 and 14. The absence of absorptions in the surface constituents and the linear spectral response of land targets in this reduced spectral range between 865 and 900 nm are assumed to justify the extrapolation. Several reflectance spectra of land targets are displayed in Fig. 3.10 to validate this approach. CWV map is generated on a per-pixel basis by inverting Eq. 3.1.7 for all the land pixels which have not been masked as clouds by `cloud mask #2`.

Although only a residual contribution of water vapor is found in MERIS band 14, it

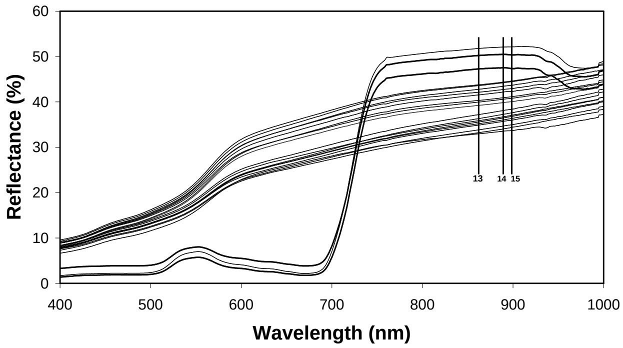

Figure 3.10: Reflectance spectra of vegetation and bare soil targets. MERIS bands 13, 14 and 15 (centered at 865, 890 and 900 nm, respectively) are marked in order to show the linearity of reflectance with wavelength in that spectral range for most of land targets.

can still affect the retrieved surface reflectance used as a basis for the inversion of Eq. 3.1.7, especially in the case of high water vapor loadings. This problem is solved by an iterative procedure that can be activated by the user. The CWV value derived after the assumption of CWV= 2 g·cm^{-2} for the estimation of surface reflectance is used as input in a new iteration so that the CWV applied to the reflectance retrieval in bands 13 and 14 is much closer to the actual value that the default 2 g·cm^{-2}. This option is selected if the flag `CWV_time_flg` in the SCAPE-M input file is set to 1.

Finally, it must be remarked that no correction of the “smile effect” [Mouroulis et al., 2000] over CWV retrievals is performed. Optical aberrations in pushbroom systems may cause the spectrometer entrance slit to be projected as a curve on the rectilinear detector array [Mouroulis et al., 2000; Qu et al., 2003]. This causes a combination of bending of spectral lines across the spatial axis and of the spatial lines across the spectral axis. The first effect, known as “smile”, causes a non-linear variation in the bands spectral position with the across-track position of the different detectors compounding the sensor. Spectral shifts of up to 1 nm have been reported for the 5 MERIS cameras [European Space Agency, 2006]. Even though such shift is negligible in the radiance measured out of absorption bands, it may become important inside them. For example, in the case of the water vapor band centered at 940 nm, plotted in Fig. 3.9, any small change in the channel wavelength may lead to different radiance measurements. An algorithm for the correction of the smile effect is implemented in the BEAM software, but it is not applied in SCAPE-M because it only corrects the extraterrestrial solar irradiance at band 15, what results in very subtle modifications from the original data.

Then, CWV retrievals are also conditioned by the pixel position because of the MERIS varying spectral configuration. However, no correction for this effect has been performed for computational reasons: the proper correction of the smile effect in CWV retrievals should be based on resampling the atmospheric optical parameters to the actual band positions on a per-column basis, instead of to the reference wavelength. This would mean that a huge atmospheric LUT at a very fine spectral resolution should be available, in order to resample the atmospheric parameters to the particular band configuration in each of the image columns before addressing the CWV retrieval. Such a procedure would lead to unaffordable computation times for the present version of the algorithm. Errors in CWV associated to the smile effect will be quantified in Section 3.3.

3.1.7. Retrieval of Surface Reflectance

Once the atmospheric state has been properly characterized, the analytical inversion of Eq. 3.1.1 is used to retrieve surface reflectance from the TOA radiance image provided by the sensor, in those pixels masked as land by `cloud mask #2`. The justification for avoiding directional effects in the target reflectance was discussed in Section 1.4.5. The correction of topographic effects in both the direct and diffuse irradiance terms are included in the retrieved surface reflectance.

TOA radiance images are corrected from atmospheric effects in 12 of the 15 MERIS bands in this way. The bands treated with a different strategy are 2, 11 and 15. On one hand, calibration problems are found in band 2 (centered at 442.5 nm), as a spike in reflectance spectra usually appears after atmospheric correction. Since no absorption feature is located around 442.5 nm, this might be caused by problems in the corresponding gain coefficient, which might be optimized for the medium reflectance levels in water bodies, that are brighter than most of land surfaces at the blue spectral region. No reported information has been found about this issue. On the other hand, bands 11 and 15 are affected by oxygen and water vapor absorptions. If those two bands are processed following the same scheme as the others, errors in reflectance are likely to appear due to either slight errors in radiative transfer calculations or in the sensor spectral calibration [Green, 1998; Guanter et al., 2006c]. Therefore, with the aim of "making-up" the final reflectance spectra, reflectance at bands 2, 11 and 15 are calculated by either interpolation or extrapolation with the adjacent bands. The validity of this approach is again justified in Fig. 3.10.

The final step in the atmospheric correction algorithm is the correction of errors in reflectance due to the adjacency effect. A tradicional statement of the problem can be found, for instance, in Dave [1980]; Deschamps et al. [1980]; Mekler and Kaufman [1980, 1982]; Santer and Schmechtig [2000]; Tanré et al. [1981]. The adjacency effect is caused by photons reflected by the surroundings of the observed target which appear to be coming directly from the target itself because of atmospheric multiple scattering. It leads to a loss of contrast in heterogeneous areas: dark surfaces look brighter because photons coming from the adjacent brighter surfaces enter into the sensor line of sight, while the bright surfaces appear darker because the photons escaped from the observer's line of sight are not counterbalanced by those coming into. The magnitude of this effect depends directly on the atmospheric turbidity and the surface heterogeneity. For mean atmospheric and observation conditions, the spatial range in which the influence of the adjacent surfaces over the imaged pixel is noticeable have been set arbitrarily to 1 km by some authors (e.g., Jianwen et al. [2006]; Richter [1997]). Under this assumption, adjacency effects can be neglected in the case of sensors with spatial resolution coarser than 1 km, when the observed area is not very heterogeneous or when the atmospheric aerosol loading is low. For those reasons, adjacency is negligible in MERIS RR (pixel size about 1.2 km) images, while it still may have some impact on FR ones (pixel size about 300 m). Then, the correction of adjacency effects is only performed over MERIS FR images if the user selects `ADY_flg`= 1 in the SCAPE-M input file.

The simple formulation for the correction of adjacency effects proposed in this work for MERIS FR data is similar to that presented by, e.g., Richter [1997]; Vermote et al. [1997a]. It consists in modelling the radiance at the sensor as a linear combination of the photons coming directly from the target and those coming from areas adjacent to the target and scattered to the sensor direction. Defining the global flux E_g as $E_g = E_{\mathrm{dir}}\mu_{\mathrm{il}} + E_{\mathrm{dif}}$, we can rewrite Eq. 3.1.1 (following Vermote et al. [1997a] notation) as

$$L_{\mathrm{TOA}} = L_0 + \frac{1}{\pi}\frac{[\rho_s t_{\mathrm{dir}} + \bar{\rho}_s t_{\mathrm{dif}}]E_g}{1 - S\bar{\rho}_s} \tag{3.1.8}$$

where t_{dir}, t_{dif} are the transmittances for direct and diffuse radiation in the upward direction ($T_{\uparrow} = t_{\mathrm{dir}} + t_{\mathrm{dif}}$), respectively, ρ_s the actual target reflectance and $\bar{\rho}_s$ the background reflectance. If ρ_s^u is the surface reflectance neglecting the adjacency effect (assumption of a infinite uniform target) which appears in Eq. 3.1.1, and we assume $S\rho_s \ll 1$, the product $\rho_s^u T_{\uparrow}$ can be associated to the linear combination

$$\rho_s^u T_{\uparrow} = \rho_s t_{\mathrm{dir}} + \bar{\rho}_s t_{\mathrm{dif}} \tag{3.1.9}$$

by comparing Eq. 3.1.1 and Eq. 3.1.8. The surface reflectance free from the adjacency effect is then calculated as

$$\rho_s = \rho_s^u + \frac{t_{\mathrm{dif}}(\mu_v)}{t_{\mathrm{dir}}(\mu_v)}[\rho_s^u - \bar{\rho}], \tag{3.1.10}$$

The background contribution is formally given by

$$\bar{\rho}_s = \int_{-\infty}^{\infty}\int_{-\infty}^{\infty} f(r(x,y))\ \rho(x,y)\ dx\ dy \tag{3.1.11}$$

where $r(x,y)$ indicates the distance of a given background pixel at (x,y) to the observed pixel, located at $(0,0)$, and $f(r)$ is the atmospheric point spread function, which establishes the contribution of the environment to the registered TOA radiance. It depends on the atmospheric state and the observation configuration (angles, surface elevation, sensor inside or outside the atmosphere...). For operational purposes, the assumption of the background contribution being negligible for pixels further then 1 km will be made. In the case of MERIS FR, this leads to consider a 5 × 5 pixels window centered at the observed pixel as representative of the environment contribution. Five are the possible distances r from the observed pixel to the other 24 in the window: $[1, \sqrt{2}, 2, \sqrt{5}, \sqrt{8}] \times 300$ m, if we take 300 m to be MERIS FR pixel size. Eq. 3.1.11 is converted into

$$\bar{\rho}_s = \sum_{i=-2}^{2} \sum_{j=-2}^{2} f(r_{ij})\ \rho^u_{s_{ij}} \tag{3.1.12}$$

For the sake of simplicity, the atmospheric spread function $f(r_{ij})$ has been designed so that no dependence on the atmospheric state is considered, but the environment contribution is only given by the distance to the observed pixel. This dependence is illustrated in Fig. 3.11. Diamonds mark the value of $f(r_{ij})$ at the set of possible distances in the 5 × 5 pixels window. The curve is normalized to have a unity area. A Gaussian dependence has been chosen in order to reproduce the smooth variations of the background contribution with the distance that have been presented by other authors. The assumption of $f(r_{ij})$ being given by a Gaussian function is also an approximation to the real case, in which Rayleigh and aerosol scattering influences superpose. Rayleigh scattering coupling scale has broader spatial influence than aerosols, so that the actual function should be a smooth one with a bell-like shape in the middle (aerosols) and wide wings in the edges (Rayleigh). The width and height of the center peak would change with the aerosol loading, while the wings would be more stable because no important variations are expected in Rayleigh scattering (mainly driven by the target elevation). Those criteria could be also fulfilled by an exponential adjacency distance-dependence, as it was proposed by Kaufman [1989].

The final surface reflectance image free from adjacency effects is retrieved by applying Eq. 3.1.10 with $\bar{\rho}_s$ given by Eq 3.1.12. As last step of the atmospheric correction in SCAPE-M, the reflectance image, as well as the other atmospheric correction outputs, can be geometrically corrected if the user selects the corresponding option in the input file (`GC_flg`= 1). The "mapproj" processor, supplied with the BEAM software, is automatically launched in order to obtain the images geo-rectified according to the latitude/longitude projection.

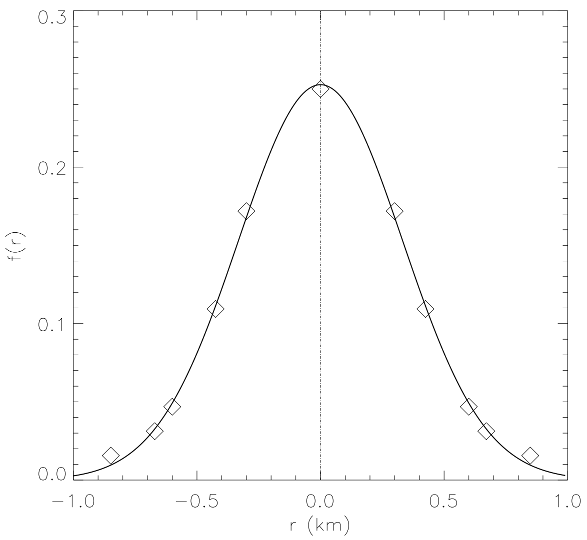

Figure 3.11: Atmospheric spread function $f(r_{ij})$ as a function of the distance to the observed pixel.

3.2. Generation of LUTs with MODTRAN4

3.2.1. MODTRAN4 & atmospheric correction

As it has been exposed in Section 3.1, the atmospheric optical parameters needed for the computation of Eq. 3.1.1 are retrieved from a LUT generated off-line by means of the MODTRAN4 radiative transfer code (see Section 1.5). In particular, atmospheric path radiance, transmittances for direct and diffuse radiation, direct and diffuse fluxes and spherical albedo are read from the LUT.

The MODTRAN4 code [Berk et al., 2003, 1998] is one of the most widely used RTCs in accurate simulations of atmospheric radiative transfer. It is a general-purpose atmospheric simulator, which reproduces the radiance at the sensor level with up to 1 cm^{-1} of spectral resolution. The rigorous coupling of absorption and scattering events makes it an accurate code for the simulation of multi- or hyperspectral optical remote sensing data sets. However, two major problems appear when MODTRAN4 is to be applied to the atmospheric correction of remotely sensed imagery. On one hand, it is a “forward” RTC, which means that it is intended to generate TOA radiances from given atmospheric and surface configurations. Applying it to the retrieval of surface reflectance from TOA radiances is not straightforward, because the necessary atmospheric functions are not included in the standard MODTRAN4 output, but have to be computed separately. On the other hand, the mathematical coupling between scattering and absorption in every atmospheric path originates prohibitive computation times when a large number of runs is necessary, as it is usually the case of image processing applications. This situation is more critical when the DISORT [Stamnes et al., 1988] algorithm implemented in MODTRAN4 must be used, normally when a high accuracy in the computation of off-nadir observation angles is required. For these reasons, other efficient but less accurate RTCs are often preferred for atmospheric correction purposes, such as the 6S code [Vermote et al., 1997c] described in Section 1.5.

The LUT to be utilized in the frame of the algorithm presented in this work must cover a wide range of geometrical and atmospheric conditions in order to be applied on an operational basis. As it will be described in this section, the designed LUT consists of 6 parameters, 3 for the angular configuration, one for the surface elevation, one for the aerosol loading and one for the CWV, each of them parameterized by a number of 3 to 7 breakpoints set within given variation ranges. This means that tens of thousands of radiative transfer simulations in the wavelength range from 400 to 900 nm must be performed. As it is, MODTRAN4 can not be applied to the generation of such a LUT. On one hand, computation time would become prohibitive, especially if the high accuracy provided by DISORT is required. On the other hand, the atmospheric parameters provided by MODTRAN in the original output files are not decoupled from the multiple scattering between atmosphere and surface, what results in “surface-dependent” path radiance and fluxes. I.e., those are not defined only by the atmospheric state but also for the reflectance of the surface underneath. The easiest solution would be the use of the 6S code instead of MODTRAN4. Output parameters are conveniently decoupled from the surface influence, and computation times are orders of magnitude lower than in MODTRAN4. However, some of the radiative transfer simulations that must be carried out in the different modules and applications of the present algorithm involve high precision calculations inside gaseous absorption bands. The 6S code was discarded because it computes scattering and absorption separately, what leads to a loss in accuracy especially inside absorption bands.

The final solution consisted in adapting the MODTRAN4 original code to make it suitable for remote sensing applications. Other authors, most of them mostly working on atmospheric correction of hyperspectral data, have applied the standard MODTRAN4 version to infer the atmospheric optical functions [Adler-Golden et al., 1999; Miesch et al., 2005; Miller, 2002; Richter and Schlaepfer, 2002; Staenz and Williams, 1997], which are normally stored in pre-calculated LUTs. The application of MODTRAN4 for the accurate simulation of TOA radiances is also described in Verhoef and Bach [2003]. The modifications of the original code are done on the source code level, generating a faster executable file providing directly the atmospheric functions. For the same reason, some MODTRAN4 subroutines have been modified so that the retrieval of the spectral radiances and fluxes needed for the calculation of the atmospheric parameters are not written to an external file, but they are internally passed to a driver subroutine in charge of the management of the data. Both hard disk space and computation time are saved which is a critical issue for applications that need a large amount of runs. Another convenient feature that has been added to the standard MODTRAN4 version is the calculation of the AOT by integrating the aerosol extinction coefficient along the vertical path. Only the total optical thickness (aerosol plus Rayleigh plus ozone) at 550 nm can be directly accessed in the radiance mode of the original MODTRAN4. This modified code has been named ATLUT, in order to distinguish it from MODTRAN4 original code. It was developed in collaboration with Rudolf Richter from DLR - German Aerospace Center. The mathematical background supporting those modifications is described in Appendix C.

3.2.2. Design of the LUT

The designed LUT consists of 6 free parameters: VZA, SZA, RAA, ELEV, VIS and CWV. ATLUT generates the LUT from nested runs which have the breakpoint combinations as input. Each of them is tabulated with a varying number of breakpoints (3 to 7) distributed along the expected variation range. Output variables are:

- Atmospheric path radiance
- Direct irradiance at the ground
- Diffuse irradiance at the ground
- Atmospheric spherical albedo
- Direct transmittance for radiation in the upward direction
- Ratio of direct to diffuse transmittance in the upward direction
- AOT at 550 nm

All these parameters are resampled to MERIS reference band configuration, with MERIS filter functions modelled as rectangular functions with width equal to the nominal bandwidth. This is justified by the band binning used in the design of MERIS channels [European Space Agency, 2006; Rast et al., 1999]. Apart from the 6 free parameters {VZA, SZA, RAA, ELEV, VIS, CWV}, other input variables defining radiative transfer calculations must be set in advance. The selected atmospheric model is the mid-latitude summer, because summer is the season when the maximum number of cloud-free images is expected to be available for processing. Multiple scattering is computed making use of the DISORT scaling option under 8 fluxes, as it was discussed in the previous section. Ozone and CO_2 are set to default values, 7.08 $\mathrm{g \cdot m^{-2}}$ and 330 parts per million by volume (ppmv), respectively. The columnar ozone content provided by ECMWF is attached to MERIS images for the acquisition time, and could be added as a free parameter in the LUT. This was discarded as ozone low spatial and temporal variability do not lead to a significant impact on the signal, while adding an extra parameter to the LUT would have caused an increase in computation times. The rural aerosol model is also set in advance, as it provides the best representation of the atmospheric conditions expected in continental areas. The calculations are performed using the default 5 cm^{-1} atmospheric data base, which provides a sufficient spectral sampling at the scale of MERIS typical bandwidths.

The distribution of the breakpoints has been set so that they cover the maximum variation range in the parameters. Given a certain set of inputs, the values of the atmospheric parameters are calculated through linear interpolation in the 6 directions of the parameter space. It must be remarked that possible errors due to deviations from linearity at any combination of optical parameters and input values tend to compensate along the whole atmospheric correction process. For example, if a small bias in path radiance is introduced by linear interpolation during the estimation of AOT, it is cancelled off to a large extent when the resulting AOT value is re-inserted in the process to calculate surface reflectance, as the same LUT and interpolation technique are used in forward and reverse modes.

The optimum breakpoint positions for the 6 input parameters are presented in Table. 3.1. The number of breakpoints describing each dimension in the LUT is selected as a tradeoff between sufficient sampling and LUT size. For this purpose, radiative transfer simulations have provided the dependencies of physical magnitudes on the 6 free parameters. Basic input parameters for those simulations were VZA = 30°, SZA = 20°, RAA = 120°, ELEV = 0 km, VIS = 23 km and CWV = 2 $\mathrm{g{\cdot}cm}^{-2}$. Only the parameter under study was modified within the selected range, the rest of inputs staying constant in those basic inputs. A number from 3 to 7 provides a sufficient sampling of the parameter space without leading to unaffordable computation times or LUT size. For the selection of the breakpoint positions, their influence on scattering and absorption processes have been analyzed. Atmospheric path radiance at the MERIS shortest wavelength (412.5 nm) is selected to describe scattering, while the ratio between pairs of absorption/reference bands describes absorption.

Both scattering and absorption aspects have been considered for the VZA, and are displayed in Fig. 3.12. VZA is allowed to vary from 0 to 45°. MERIS FOV of 68.5° provides a maximum at-satellite VZA of 34.25°. This value is extended to 45° to cover all possible variations in VZA due to variations in platform roll angle or Earth ellipsoidal shape. Path radiance dependence on VZA is shown in Fig. 3.12(a), and the same is in Fig. 3.12(b) for absorption. Markers point out the final breakpoint positions selected from the analysis. The variations are smooth enough within all the range to allow linear interpolation, especially in what respects to water vapor and oxygen absorption. The largest error in linear interpolation would appear for the largest VZA. However, MERIS reduced angular sam-

Table 3.1: Breakpoint positions in the LUT for the 6 input variables.

	#1	#2	#3	#4	#5	#6	#7
VZA (°)	0	9	18	27	36	45	–
SZA (°)	0	10	20	35	50	65	–
RAA (°)	0	25	50	85	120	155	180
ELEV (km)	0	0.7	2.5	–	–	–	–
VIS (km)	10	15	23	35	60	100	180
CWV ($g{\cdot}cm^{-2}$)	0.3	1	1.5	2	2.7	5	–

pling enables linear interpolation to be used in all the range. The same conclusions can be extracted from Fig. 3.12(c) and Fig. 3.12(d), which show the dependence of path radiance and absorptions on SZA, respectively. Note that the angular range in SZA is larger than in VZA. The maximum SZA considered is 65°, which is the MODTRAN4 upper limit for the illumination angle. Much larger SZA are not expected in the real case. If such conditions were found, SZA would be reset to 65° in the beginning of the processing. This is likely to occur in images acquired in winter at high latitudes.

The dependence of atmospheric path radiance at MERIS band 1 on RAA is plotted in Fig. 3.13. Seven breakpoints are selected to described path radiance variations within the 0 to 180° range. The step is 25° in the edges, where a higher variation rate is found, and 35° in the center, where the variation rate is more relaxed. Path radiance is the only optical parameter depending on RAA. Thus, errors due to linear interpolation in RAA only affect scattering events, and not fluxes or absorption calculations. These are mainly a function of VZA and SZA.

The dependence of both scattering and absorption processes with surface elevation is close to linearity, as it can be checked in Fig. 3.14. The linear interpolation is fully justified in this case, and so it is the selection of only 3 points to describe the entire range from 0 to 2.5 km. Higher altitudes are not considered because the good performance of the method is not guaranteed for them: difficulties in radiative transfer calculations could appear when all the atmospheric layers inside the planetary boundary layer (up to 1-2 km) do not appear. Moreover, snow or ice surfaces are likely to be present in a high proportion of the targets above 2500 m altitude.

Finally, the breakpoints set for visibility and CWV are displayed in Fig. 3.15. Visibility drives atmospheric path radiance, as it is plotted in Fig. 3.15(a). The dependence of AOT at 550 nm with visibility is plotted in the right axis. It can be stated that it follows the same variation pattern than path radiance. Validity of linear interpolation is assumable in the whole range from 10 to 180 km (or, equivalently, from AOT at 550 nm about 0.06 to 0.9).

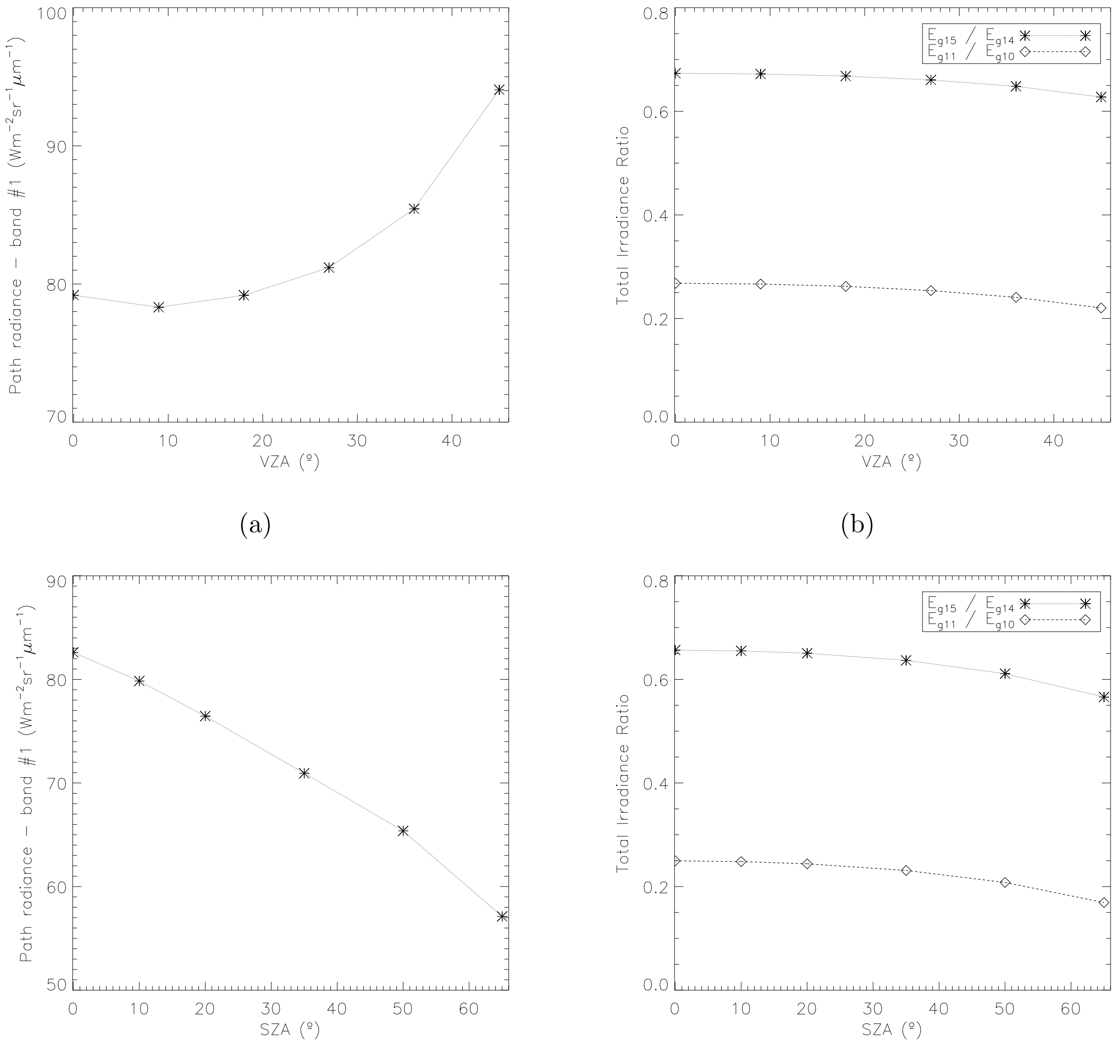

(a) (b)

(c) (d)

Figure 3.12: Path radiance at the 1st MERIS band and ratio of total irradiance inside and outside gaseous absorptions as a function of observation and illumination zenith angles. Upper left (a), atmospheric path radiance at 412.5 nm plotted as a function of VZA. Upper right (b), the same as (a) for the ratio of total irradiance inside and outside water vapor (E_{g15} / E_{g14}) and oxygen absorptions (E_{g11} / E_{g10}). Equivalent plots to (a) and (b) for the dependence on the SZA are in (c) and (d), respectively.

In any case, a more sophisticated non-linear interpolation is applied for the conversion of visibility into AOT at 550 nm (see Fig. 3.7(b)), because no-compensation of errors between forward and backward calculations occurs in this case. On the other hand, Fig. 3.15(b) shows the variation of the depth of the water vapor absorption measured at band 15 with the CWV. Again, the most important errors could appear for CWV values below 0.7-0.8 g·cm^{-2}, which are extremely dry conditions. Linear interpolation should work well in

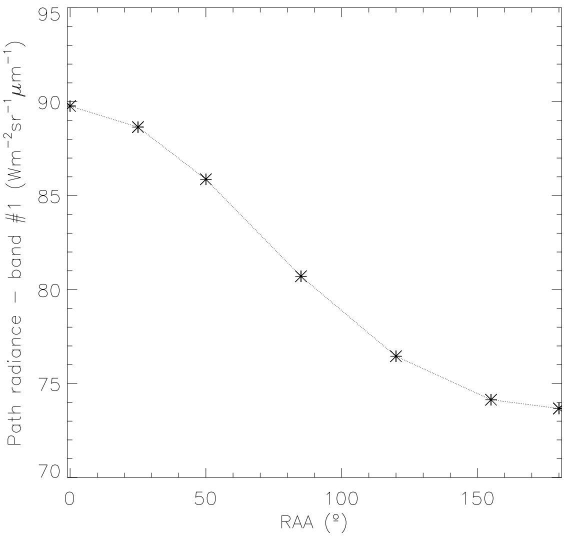

Figure 3.13: Atmospheric path radiance at 412.5 nm plotted as a function of RAA.

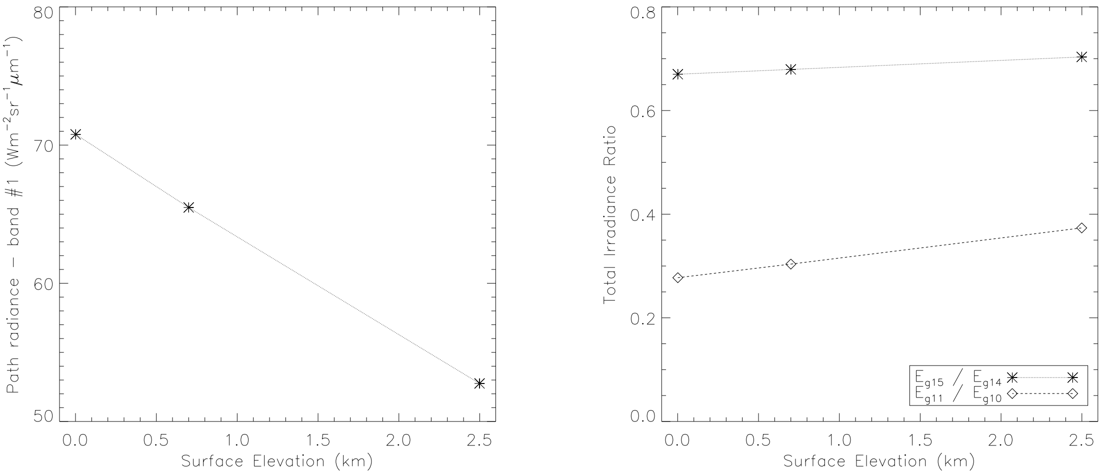

(a) (b)

Figure 3.14: Path radiance at the 1st MERIS band and ratio of total irradiance inside and outside gaseous absorptions as a function of surface elevation. Left (a), atmospheric path radiance at 412.5 nm plotted as a function of surface elevation. Right (b), the same than (a) for the ratio of total irradiance inside and outside water vapor (E$_{g15}$ / E$_{g14}$) and oxygen absorptions (E$_{g11}$ / E$_{g10}$).

the rest of the considered range.

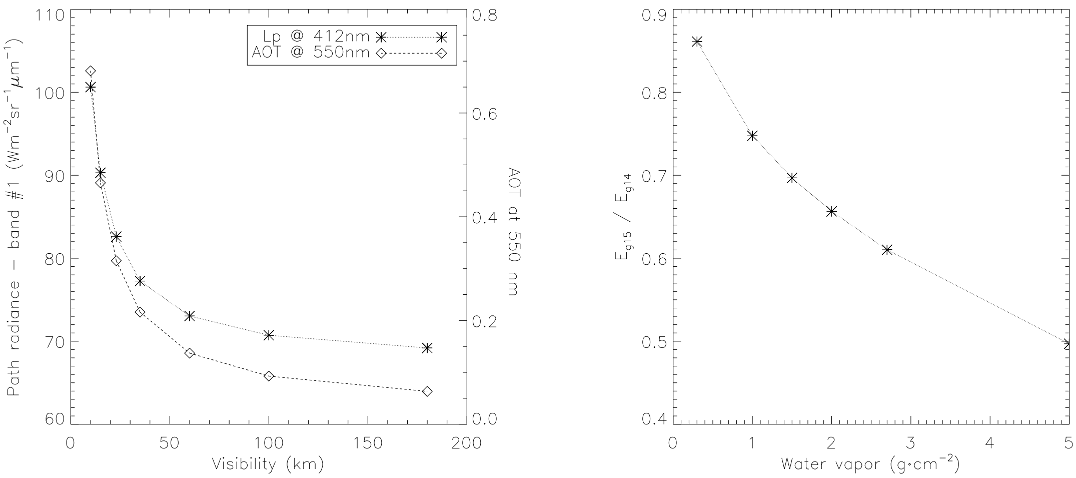

(a) (b)

Figure 3.15: Breakpoint positions for visibility and CWV. Left (a), atmospheric path radiance at 412.5 nm and AOT at 550 nm as a function of horizontal visibility. Right (b), ratio of total irradiance inside and outside water vapor absorption as a function of water vapor.

3.2.3. Interpolation

As it has been said before, data are extracted from the LUT by means of linear interpolation in a 6–D space. The technique applied for the 6–D linear interpolation is a generalization of interpolation on a 2–D space to the case of a 6–D one. Each of the tabulated data points are weighted by the hyper-area spanned by the point of interpolation and the diametrically opposite grid point. Similar approaches are discussed by other authors in different disciplines (see, for example, Kraaijpoel [2003]; Pluim et al. [2003]). Illustration of this model for the 2–D case is shown in Fig. 3.16. The extension to a N–D space is straightforward.

Following Kraaijpoel [2003] notation, the interpolation scheme displayed in Fig. 3.16 can be mathematically expressed as:

$$\begin{aligned} &I[f(x,y)](x,y;x_0,y_0,x_1,y_1) = \\ &\quad \frac{(y_1-y)(x_1-x)}{(y_1-y_0)(x_1-x_0)} f(x_0,y_0) + \frac{(y-y_0)(x_1-x)}{(y_1-y_0)(x_1-x_0)} f(x_0,y_1) + \\ &\quad \frac{(y_1-y)(x-x_0)}{(y_1-y_0)(x_1-x_0)} f(x_1,y_0) + \frac{(y-y_0)(x-x_0)}{(y_1-y_0)(x_1-x_0)} f(x_1,y_1) \end{aligned} \tag{3.2.1}$$

where $I[f(x,y)](x,y;x_0,y_0,x_1,y_1)$ is the interpolated value at point (x,y) surrounded by vertices (x_0,y_0), (x_0,y_1), (x_1,y_0) and (x_1,y_1). Each of the fractions in Eq. 3.2.1 can be interpreted as a the normalized area spanned by the point of interpolation and the opposite

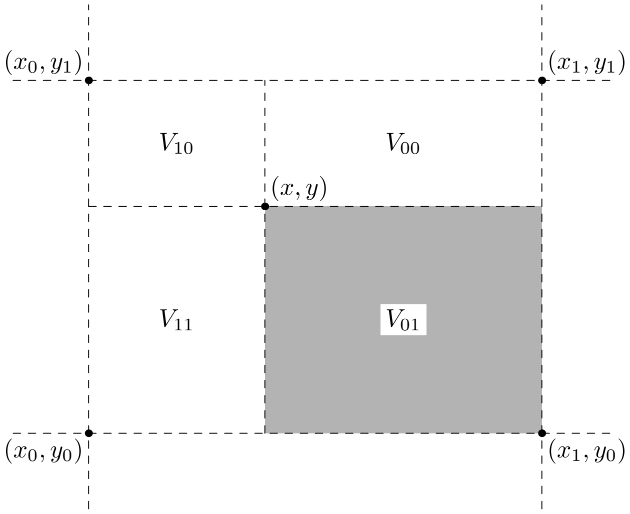

Figure 3.16: Bilinear interpolation: area weighted average (after Kraaijpoel [2003]). Labels $V_{i,j}$ indicate the area weighting the data point at (x_i, yj).

vertex. If we define

$$\begin{aligned} V_{00} &= (y_1 - y)(x_1 - x) \\ V_{10} &= (y_1 - y)(x - x_0) \\ V_{01} &= (y - y_0)(x_1 - x) \\ V_{11} &= (y - y_0)(x - x_0) \\ V &= V_{00} + V_{10} + V_{01} + V_{11} \qquad (3.2.2) \end{aligned}$$

we can re-write Eq. 3.2.1 as

$$I[f(x, y)](x, y; x_0, y_0, x_1, y_1) = \qquad (3.2.3)$$

$$\frac{V_{00}}{V} f(x_0, y_0) + \frac{V_{10}}{V} f(x_1, y_0) + \frac{V_{01}}{V} f(x_0, y_1) + \frac{V_{11}}{V} f(x_1, y_1) \qquad (3.2.4)$$

The use of this formula is very convenient in computational terms, as it is easily implementable and does not involve a high computation burden. A recursive algorithm performing 1-D linear interpolation for each of the 6 dimensions was also tried, but it was discarded because it was neither as robust nor as efficient as the one with the weighting areas. The procedure starts looking for which of the $6 \times 6 \times 7 \times 3 \times 7 \times 6 = 31752$ hyper-cells contains the interpolation point. The data points to be used in the 6–linear interpolation are the $2^6 = 64$ vertices of the hyper-cell. As different physical magnitudes are contained in the LUT, the dynamic ranges of each of the dimensions are normalized to $[0, 1]$ (i.e., $V = 1$). A matrix compounded by the 7 optical parameters in the 15 MERIS bands is returned as interpolation result.

3.3. Sensitivity Analysis

3.3.1. Sensitivity of Aerosol Optical Thickness Retrieval

The performance of the AOT retrieval method described in Section 3.1 is tested by means of a synthetic data set of MERIS radiance spectra. The input parameters are controlled in the generation of the radiance data sets, so the impact of different factors on the retrieved AOT can be assessed, quantifying possible biases that may appear. It is assumed that the forward model which generates TOA radiance is error-free, so that all error sources are associated to wrong input values or bad performance of the AOT retrieval module. General theory about sensitivity analysis can be found in Saltelli et al. [2004].

The set of MERIS radiance spectra has been generated using MODTRAN4 in forward mode trying to reproduce representative conditions of MERIS acquisitions. The VZA was set to 20°, SZA to 28°, RAA to 150° (measured from North to East), the surface was tilted 10° towards the sun and was located 300 m ASL. The water vapor column content was 2 g·cm^{-2}. The surface reflectance was generated by linear combinations of green vegetation and bare soil endmembers, which were grouped in sets of 5 spectra to simulate the 5 reference pixels. Twelve different green vegetation spectra are combined to check the sensitivity of the AOT retrieval module to the target spectral response. The widest range of vegetation types has been extracted from atmospherically corrected MERIS images, in order to ensure the maximum sampling of real cases in nature. They are displayed in Fig. 3.17. Only 1 bare soil spectrum is used because of the relatively smaller contribution of bare soils to the merit function in Eq. 3.1.4 and the less variation in spectral patterns (apart from overall brightness). In each of the 5 spectra clusters, the abundances for the vegetation endmember were taken from a typical case of $\{0.9, 0.8, 0.65, 0.6, 0.2\}$, while abundances for bare soils were set to one minus the vegetation abundance. The atmospheric turbidity was varied from hazy to clear, with 9 AOT values of $\{0.62, 0.45, 0.36, 0.31, 0.27, 0.22, 0.20, 0.16, 0.12\}$, which correspond to visibility values of $\{14, 20, 25, 30, 35, 40, 50, 70, 90\}$ km. The resulting data set consists of 12 × 9 sets of 5 reference pixels.

The AOT retrieval module was run over the 12 × 9 sets of reference pixels under 4 different set of inputs. It is assumed that the observation and illumination angles are known. Initially, all the inputs are equal to the ones used in the forward simulations. This situation enables the detection of possible biases in the method itself, such as problems in convergence or systematic AOT overestimation or underestimation. For the other parameters:

1. The surface elevation at the target position is set to either 0 m, which corresponds to neglecting altitude effects in aerosol retrieval, or to 600 m, which simulates errors in the elevation data.

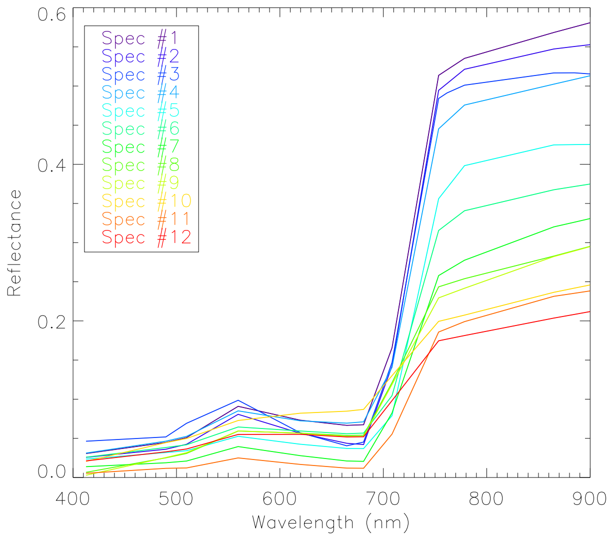

Figure 3.17: Green vegetation reflectance spectra used in the generation of the synthetic data set for the assessment of the AOT retrieval module performance.

2. The terrain slope at the target position is modified to either 0°, which corresponds to neglecting topographic effects in aerosol retrieval, or to 20° towards the sun direction, which simulates errors in the slope estimation.
3. The CWV is set either to 1 g·cm^{-2} or to 3 g·cm^{-2}, to confirm the residual water vapor continuum absorption does not affect substantially the aerosol retrieval.

The sensitivity to the target spectral response in vegetation pixels is presented in the first place. A comparison of the retrieved τ_{550} with the input τ_{550} values for 4 selected representative cases are displayed in Fig. 3.18. The labels in the legend refer to the same labels in Fig. 3.17. Different trends are found in the results:

- Label `Spec #1` corresponds to a very good performance of the method, despite the fact that the vegetation spectrum is not equal to any of the vegetation endmembers in Fig. 3.6.
- Label `Spec #3` corresponds to the worst performance among the 12 cases, with large Root Mean Square Error (RMSE) of 0.106. Even though this uncertainty in AOT is larger than what could be admitted for most of studies, it can be stated that the vegetation spectrum #3 presents an unusual spectral shape, nearly flat in the visible wavelengths with unreliable reflectance levels in the blue and the red and a sharp peak in the green. One could conclude that such a spectrum could be partially associated to errors in the atmospheric correction performed over the pixel, and that is not probable to find similar cases in nature.

- Label `Spec #5` corresponds to a case where the input green vegetation spectrum coincides with one of the vegetation endmembers. A perfect match with RMSE equal to 0 is found as expected.
- `Spec #11` is associated to a case in which RMSE is around the 0.026 that is calculated as mean RMSE for the 12 cases. It represents the most likely case.

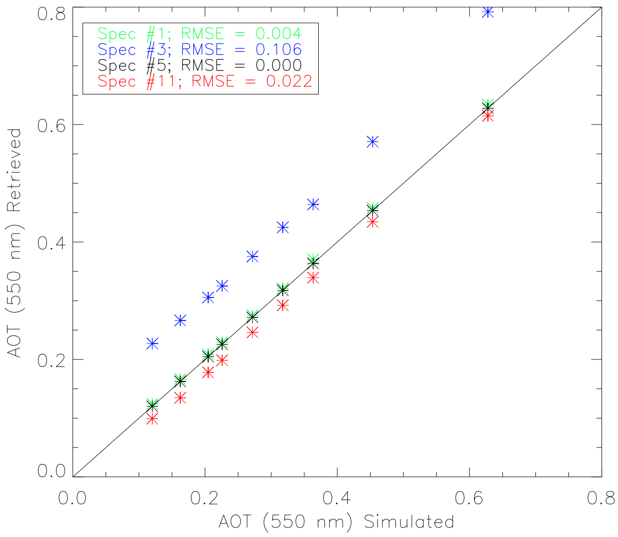

Figure 3.18: Comparison between retrieved and input AOT values for representative sets of reference pixels selected from the synthetic data set.

RMSE values for all the 12 green vegetation types are displayed in Table. 3.2. It can be stated that RMSE is smaller than 0.03 in 75% of the cases, what reinforces the validity of the approach proposed in this work. The mean RMSE calculated from the 12 cases is 0.026. If we assume that all possible vegetation reflectance spectra are represented by those in Fig. 3.17, and also the AOT at 550 nm range from 0.12 to 0.6 covers most of the situations in a real atmosphere, we can adopt 0.026 (rounded to 0.03) as the uncertainty associated to each AOT retrieval because of ignoring the target true spectral reflectance.

Concerning factors 1-3 in the list, the set of reference pixels generated from the vegetation spectrum labelled by #5 is utilized. As it is one of the endmembers applied in the AOT retrieval, only the biases associated to those parameters are evaluated in this way. Elevation effects on the AOT retrieval for the conditions described above are displayed in Fig. 3.19. Hereinafter, the Δ variable in the legend is calculated as

$$\Delta x = x - x_{\texttt{input}}, \tag{3.3.1}$$

$x_{\texttt{input}}$ being the input elevation value used in the forward simulations. The first conclusion from Fig. 3.19 is the good performance of the method when the inputs defining the scene

Table 3.2: RMSE in τ_{550} calculated from the 12 sets of reference pixels.

n	RMSE	n	RMSE
1	0.004	7	0.003
2	0.003	8	0.056
3	0.106	9	0.065
4	0.004	10	0.000
5	0.000	11	0.022
6	0.020	12	0.029

for the aerosol retrieval are the same than those used in the forward simulations (ΔELEV = 0 m). The retrieved AOT values match exactly the input ones all over the covered AOT range. This confirms no intrinsic bias, neither from the mathematical basis nor from the computational one, is associated to the method. Possible convergence problems in the optimization procedure or coding errors are discarded. Concerning the influence of the elevation itself, setting the surface at the sea level, ΔELEV = -300 m, leads mainly to the overestimation of the Rayleigh contribution to the atmospheric path radiance, as the atmospheric path is longer both in the downward and upward directions. Assuming the atmospheric path radiance can be built as the sum of the Rayleigh and particles intrinsic path radiance, overestimating the Rayleigh contribution results in the underestimation of the aerosol content which reproduce the TOA signal. It can be observed in the plot that all the points calculated with ΔELEV = -300 m are below the 1:1 line. The contrary is true for the ΔELEV = $+300$ m case: the underestimation of the Rayleigh path radiance is compensated by the overestimation in the aerosol loading. However, the deviations in the two cases are not symmetrical for the same absolute altitude difference, the RMSE being larger when altitude is overestimated. This fact can be explained by non linear effects in multiple scattering in the different atmospheric layers.

The role of the other factors considered in this study are summarized in Fig. 3.20. The effects of varying the slope of the target on the AOT retrieval are depicted in Fig. 3.20(a). It is shown that the impact of this factor is smaller than neglecting the target altitude, and that it manifests nearly symmetrically for either the underestimation (RMSE $\sim$ 0.011) or the overestimation (RMSE $\sim$ 0.013) of the surface slope. From Eq. 3.1.1, it is stated that the surface slope modifies the direct irradiance arriving at the target, but it has little influence on the path radiance. This explains the low contribution of the surface slope, as the path radiance, rather than the irradiance at the surface, is the key variable driving the aerosol retrieval. On the other hand, the dependence on the CWV is plotted in Fig. 3.20(b). The response to the sign of Δ is rather different in this case. While no impact

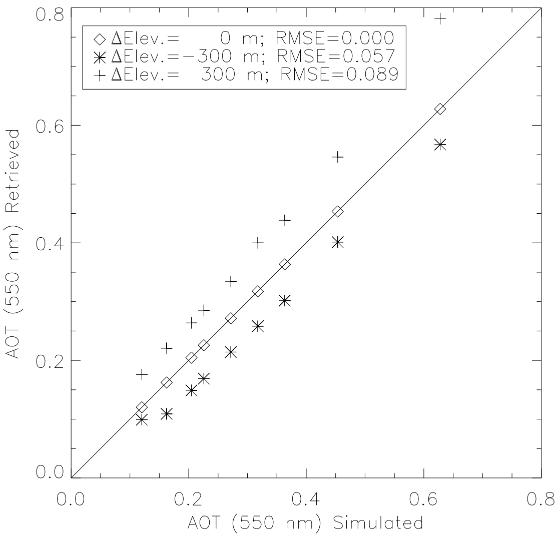

Figure 3.19: Dependence of AOT retrieval on target elevation.

on the retrieved AOT is registered when the CWV is underestimated (CWV $= 1$ g·cm^{-2}), non-negligible RMSE of 0.03 appears when CWV $= 3$ g·cm^{-2}. Again, these trends may be justified by non-linear multiple scattering effects, as the water vapor continuum absorption occurs also in the visible wavelengths. Those effects do not have a linear behavior with the CWV amount, leading to the different RMSE found for equal absolute errors in CWV. In any case, even when CWV $= 3$ g·cm^{-2}, errors in the retrieved AOT are not important on average AOT loadings, namely from 0 to 0.35 at 550 nm. This reinforces the atmospheric correction scheme presented in Section 3.1, where AOT is calculated before CWV.

The consequences of fixing the aerosol type to the rural model have not been addressed in this study. It is difficult to give accurate numbers about the errors caused by deviations in the aerosol model in the real case, because the number of possible atmospheric states may be infinite, and the generation of a "typical" situation is not realistic. It was discussed in Section 1.1 that aerosols in the atmosphere may come from different sources, and are highly influenced by wind regimes carrying particles from different origins and properties which combine at a given location. Since the reduced MERIS spectral sampling hardly allows a reliable estimation of the aerosol model in the general case, the rural model was chosen as the most representative one of the atmospheric conditions over land targets. Errors associated to each combination of aerosol types should be estimated separately. For example, it is shown in Fig. C.5(a) that the assumption of a rural model when a major proportion of maritime aerosols is present would probably lead to underestimating the AOT in the NIR wavelengths due to differences in the extinction coefficient spectral slope.

All the factors presented before have been put together in order to calculate an average error associated to AOT retrieval. Errors in surface elevation, slope, and CWV are

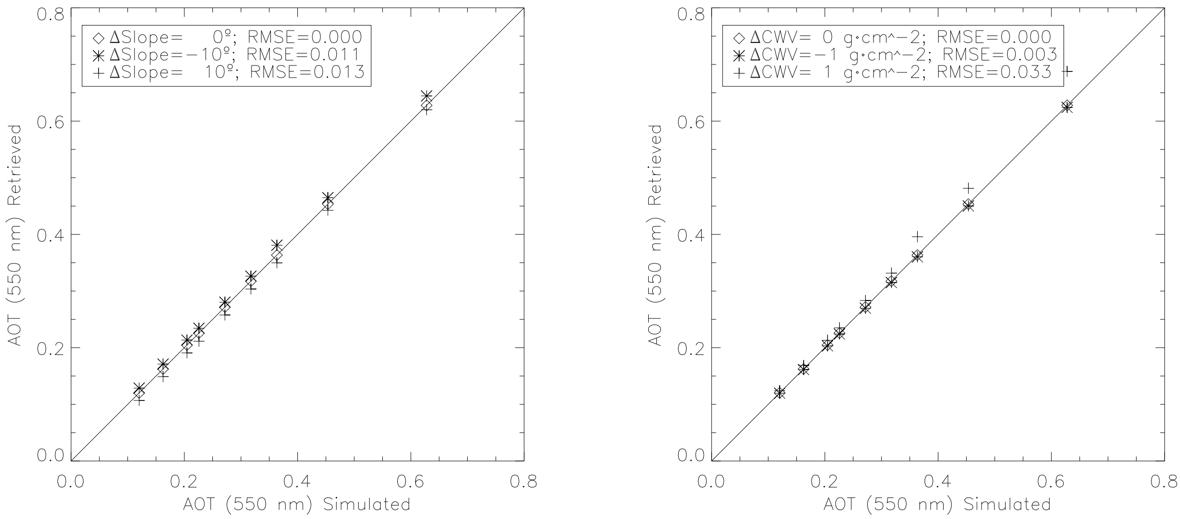

(a)

(b)

Figure 3.20: Dependence of AOT retrieval on (a) surface slope, and (b) on columnar water vapor content.

simulated, with reflectance given by vegetation spectra chosen from those in Fig. 3.17. All the other inputs are the ones mentioned at the beginning of this section. Running the AOT retrieval module over the simulated data provides an estimation of mean AOT errors associated to the method. The sign of those errors is selected so that their effect over AOT retrieval occurs in the same direction, either overestimation or underestimation. This means all errors tend to sum up, instead of cancelling off. As remarked before, the most important contribution comes from surface reflectance. In order to calculate errors in the average case, reflectance spectrum with RMSE about the 0.026 calculated as mean RMSE are selected. This is, `Spec #6` (RMSE= 0.02) represents a positive bias in AOT retrieval, while `Spec #11` (RMSE= 0.022) accounts for the negative bias. For surface elevation, the variation limits for the selection of reference pixels, ±20% from the mean elevation in each cell, is selected as representative error. Also for surface slope the ±10% is chosen as error. For water vapor, ±0.5 $g \cdot cm^{-2}$ is selected as representative deviation from the 2 $g \cdot cm^{-2}$ used as input. Then, the resulting groups of inputs representing positive and negative bias in AOT retrieval are:

- Overest. conditions: `Spec #6`, elevation= 360 m, slope= 16.8° and CWV= 2.5 $g \cdot cm^{-2}$.
- Underest. conditions: `Spec #11`, elevation= 240 m, slope= 1.9° and CWV= 1.5 $g \cdot cm^{-2}$.

It can be stated that the overall RMSE is close to 0.03, both for the positive and negative bias. This reinforces that mis-matches between real vegetation patterns and the endmembers are a major error source in the AOT retrieval module, as around 70% of

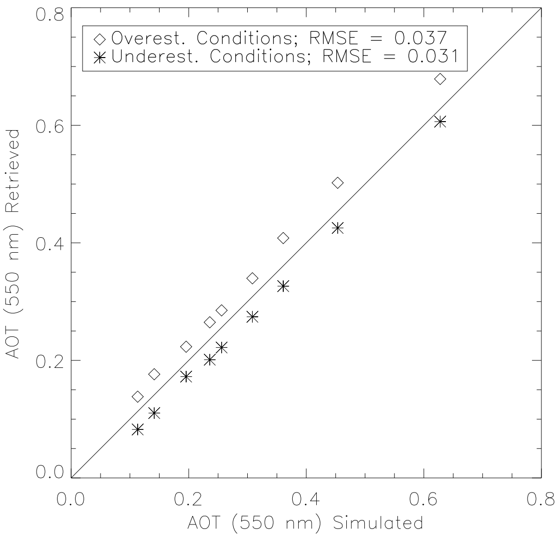

Figure 3.21: Positive and negative mean errors in AOT retrieval estimated from accumulative errors in surface elevation, slope, CWV and particular vegetation spectra.

the total error is associated to this factor. Thus, ±**0.03** can be assumed as the intrinsic error associated to AOT retrievals with the method presented in this work. Errors due to deviations from the rural aerosol model are not represented by that figure.

3.3.2. Sensitivity of Columnar Water Vapor Retrieval

An analog study is performed to analyze the factors to be considered in CWV retrievals. A MERIS TOA radiance synthetic data set is generated from forward simulations. The synthetic spectra are inverted using the CWV retrieval module described in Section 3.1. The same conditions selected for the AOT test are utilized here (VZA =20°, SZA =28°, RAA =150° surface slope tilted 10° towards the sun, and elevation ASL of 300 m). The horizontal visibility is set to 25 km (AOT at 550 nm of 0.36), and the CWV is varied with in 11 values $\{0.4, 0.8, 1.2, 1.6, 2.0, 2.4, 2.8, 3.2, 3.6, 4.0, 4.4\}$ g·cm^{-2}. For the target spectral response, 20 reflectance spectra are generated by the linear combination of a green vegetation spectrum and a bare soil one. The weighting factors in the linear combination range from 0 to 100%, leading to 20 spectra from pure vegetation to pure bare soil, with 18 intermediate cases in different proportions. This variation in the target type enables quantifying the method's sensitivity to the target spectral response. The resulting data set consists of 11 × 20 spectra.

The improvements achieved with the iteration over the CWV to minimize errors caused by assuming CWV= 2 g·cm^{-2} in the retrieval of the reflectance at bands 13 and 14 are illustrated in Fig. 3.22. All the input values are the same than those used in the simulations.

It can be stated that the RMSE decreases considerably in the second iteration. However, the method performance is satisfactory for CWV up to 3 g·cm^{-2}, which is about the higher limit for CWV in typical conditions. Thus, the option `CWV_time_flg`= 1 in the SCAPE-M input file driving the iteration over CWV should only be used when high values of the CWV are expected, as it is the case of tropical latitudes. In any case, this option will be used in the remaining of this analysis to make sure uncertainties are only associated to the factors that are being varied in each of the cases. Again, mis-formulations of the algorithm or coding errors can be discarded due to the perfect match between simulated and retrieved CWV values in Fig. 3.22.

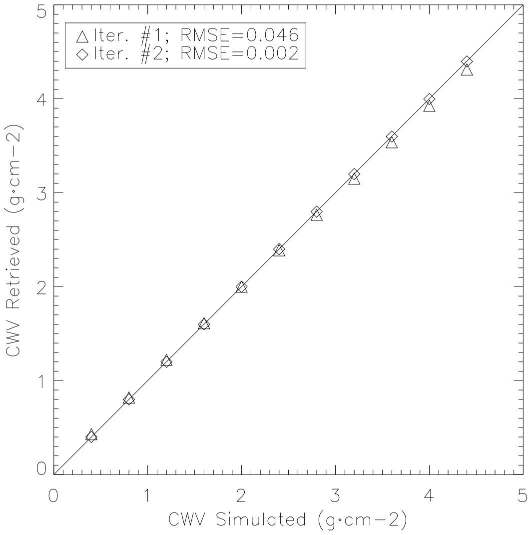

Figure 3.22: Comparison of CWV retrievals with simulated data for 1 and 2 iterations in the retrieval scheme.

As in the case of AOT, the influence of target elevation and surface slope on CWV retrievals is assessed. The aerosol content and the target spectral response are the other analyzed factors. Small errors are associated to the surface slope and to the target spectral response, less than 0.5% in both cases. In particular, surface slope does not contribute to modify the water vapor absorption depth. As it is modelled in the radiative transfer equation in Fig. 3.1.1, it appears as a multiplicative factor on the direct irradiance term. This term is much larger than the diffuse irradiance or the path radiance terms in the NIR wavelengths in which the water vapor absorption takes place. Then, the ratio between bands 15 and 14 to be used in the CWV retrieval is mostly driven by the ratio between the direct terms, and it is nearly independent of the surface slope. Concerning the target spectral response, errors in CWV are usually associated to non linear features in the target reflectance around the wavelengths affected by water vapor absorptions, such as liquid water absorption in plants or iron oxides in bare soils. However, these are not present in the reduced range from 890 to 900 nm used in MERIS for CWV estimations. Errors caused by the reflectance spectral slope are also minimized, as there is not an important change in reflectance in such a narrow spectral range.

The maximum impact on CWV retrievals is found to be associated to the target elevation and to the aerosol loading, as it is shown in Fig. 3.23. Errors in CWV retrievals due to a bad compensation of altitude effects are displayed in Fig. 3.23(a). CWV is underestimated when the target is assumed to be at sea level. This is due to water vapor concentration is larger in the lowest atmospheric layers for the standard midlatitude summer profile which is selected. Thus, if the target is at the sea level less columnar water vapor is needed to reproduce the same absorption than the one generated with the target located at a given altitude above the sea level. The same rationale applies to the overestimation appearing when CWV is retrieved setting the surface elevation above the real one. Average errors at the reference CWV value of 2 g·cm^{-2} are 0.06 g·cm^{-2} when the target altitude is overestimated by 300 m, and 0.05 g·cm^{-2} when it is underestimated by the same height. The non-linearity in the water vapor vertical profile causes the deviation to be symmetrical with the sign of ΔELEV. On the other hand, noticeable errors appear in CWV retrievals for mis-estimations of AOT at 550 nm of ± 0.15. When input CWV is 2 g·cm^{-2}, errors are 0.12 g·cm^{-2} for ΔAOT $= 0.15$, and 0.13 g·cm^{-2} for ΔAOT $= -0.15$. This dependence of CWV retrieval on the aerosol loading is due to the different magnitude of radiation multiple scattering inside and outside the water vapor absorption: inside the absorption, absorptive regime dominates against the scattering one, as photons are likely to be absorbed without much interactions. Increasing the aerosol loading makes multiple scattering contribution larger, producing a more efficient absorption inside the band. This transmission decrease is not counterbalanced by an equal decrease outside the absorption. This causes aerosols do not have the same influence on radiation in the band 14 than in the 15, what makes the water vapor absorption depth changes with the aerosol loading. In particular, the absorption depth (as measured from the band outside the absorption) is decreased when the aerosol loading is decreased, while larger AOT leads to deeper absorption bands. In CWV terms, when the input aerosol loading set for CWV retrieval is overestimated, less water vapor is needed to generate the same depth in the absorption, leading to the underestimation of CWV. This trends can be observed in Fig. 3.23(b). Retrieved CWV overestimates the true value when the AOT at 550 nm is underestimated, and the same happens on the contrary. This reinforces the calculation of AOT before the CWV, as it is done in the algorithm presented in this work.

Apart from those scene-dependent factors, errors introduced by spectral calibration variations in the instrument are also analyzed. It has been already mentioned that the MERIS instrument is composed of 5 cameras, each equipped with its own CCD sensor. Each CCD covers the spectral range with a nominal 1.25 nm spectral sampling interval

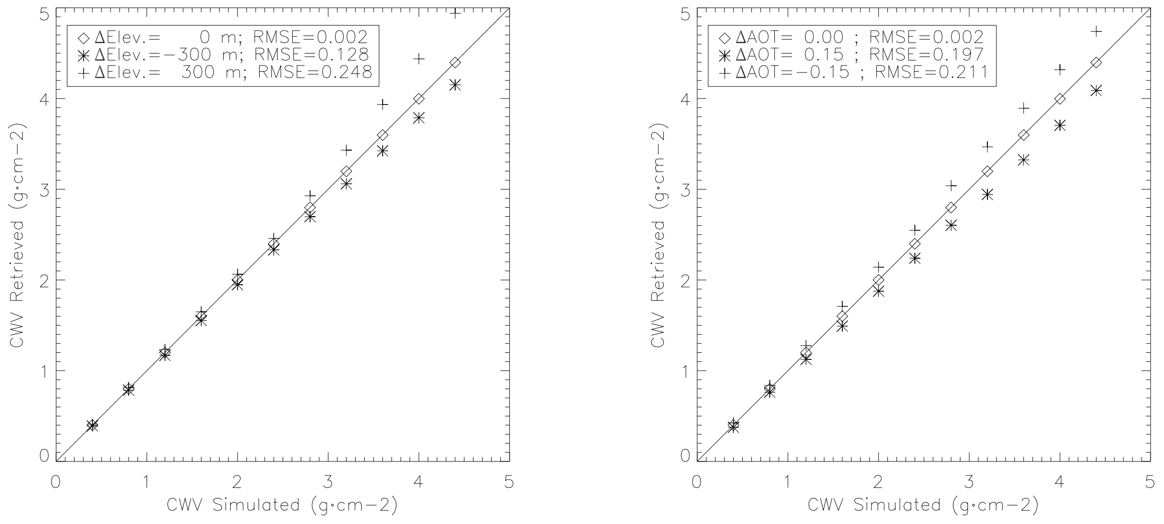

(a)

(b)

Figure 3.23: Dependence of CWV retrieval on the target altitude (a) and on the AOT at 550 nm (b).

[European Space Agency, 2006]. The exact spectral band positions change along the CCD across-track direction because of the smile effect. The tabulated spectral shifts at band 15 in the 5 MERIS cameras are displayed in Fig. 3.24 for the 3700 MERIS across-track pixels. It can be seen that spectral shifts vary linearly within the CCD spatial dimension, and that it is not larger than 1 nm in absolute terms. The same pattern is found for the other MERIS bands. Although this shift does not affect the radiance measured out of absorption bands, it may do inside them. In complex absorption bands, such as the oxygen A-band or the water vapor band centered in 940 nm, any small change in the band position may lead to different effective transmittance values, as it is shown in Fig. 3.9. One can observe that small changes in the center wavelength would produce non-negligible changes in the measured radiation in the MERIS band 15. Since only one reference wavelength is used to simulate MERIS measurements in the retrieval algorithms, the sensitivity to deviations between the reference wavelength and the actual ones must be explored.

In order to investigate the impact of the smile effect in CWV retrievals, 3 TOA radiance spectra at 1 cm^{-1} spectral resolution were simulated with the MODTRAN4 code. Input CWV values were 1, 2 and 3 $\text{g}\cdot\text{cm}^{-2}$. Those high spectral resolution spectra were resampled to MERIS channels varying the center wavelength according to the wavelength positions in Fig. 3.24. After resampling, a set of 3700 MERIS-equivalent radiance spectra with band spectral centers varying up to 1 nm are available. In order to translate from spectral shift to CWV, the ratio between channels 15 over 14 is calculated. The same CWV retrieval algorithm described in Section 3.1 is applied to all the ratios. The results for CWV equals to 1, 2 and 3 $\text{g}\cdot\text{cm}^{-2}$ are plotted in Fig. 3.25 as a function of the spectral shift from the

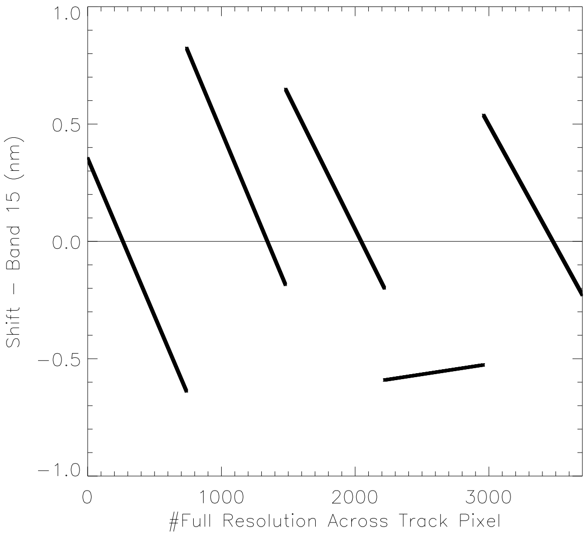

Figure 3.24: Spectral shift from the reference band setting at band 15 for the 5 MERIS cameras.

reference wavelength in band 15.

Curves in Fig. 3.25 are the envelope of the initially retrieved curves. A smoothing process is applied to retain only the spectral dependence, which is expected to be smooth and continuous. Some small step-like trends were found in the original curve, because the spectral resolution of the spectra to be convolved (1 cm^{-1}, i.e. around 0.08 nm at 900 nm) is coarser than the MERIS wavelength grid (step of the order of 0.0015 nm at 900 nm). The first conclusion is that the absolute error in CWV associated to the spectral shift depends on the total CWV, as a noticeable dependence on water vapor amount is still found after calculating relative errors. Peak errors are around +8% for 3 $\mathrm{g{\cdot}cm^{-2}}$, +4% for 2 $\mathrm{g{\cdot}cm^{-2}}$ and +2% for 1 $\mathrm{g{\cdot}cm^{-2}}$. Moreover, the dependence is not symmetrical around 0 nm shift, but CWV errors are larger when the shift is positive. This is explained by the fact that the longer the wavelength in the 900 nm region is the deeper the water vapor absorption feature becomes, which is compensated by higher CWV. By converting from relative to absolute errors it can also be stated that maximum CWV variations in the along track direction are around 0.15 $\mathrm{g{\cdot}cm^{-2}}$ for CWV= 2 $\mathrm{g{\cdot}cm^{-2}}$, or 0.25 $\mathrm{g{\cdot}cm^{-2}}$ for CWV= 3 $\mathrm{g{\cdot}cm^{-2}}$. These variations can be easily seen in the camera transitions in the derived water vapor maps. For those reasons, the correction of the smile effect should be addressed prior to CWV retrievals if a maximum accuracy is sought. The natural solution would be counting on a set of fine spectral resolution LUTs, which are resampled on a per-column basis. However, the computational complexity of this procedure would lead to huge calculation times, which would be unaffordable for any operational algorithm. Thus, errors in CWV due to the smile effect are assumed to be intrinsic to the MERIS instrument.

For a final estimation of the mean error to be associated to each single CWV retrieval a

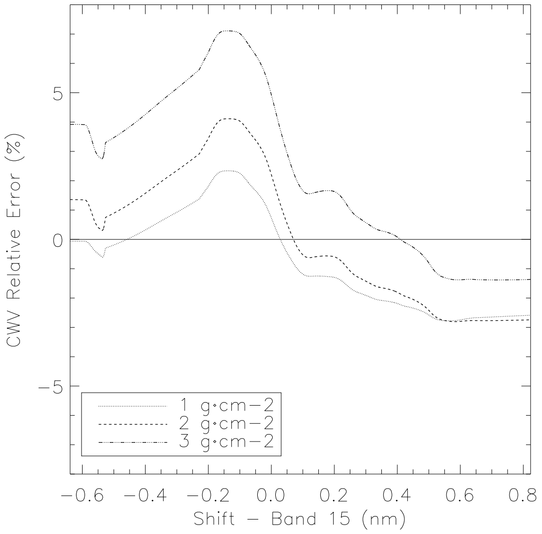

Figure 3.25: Impact of the smile effect in MERIS band 15 on CWV retrievals, for input CWV of 1 g·cm^{-2}, 2 g·cm^{-2} and 3 g·cm^{-2}.

similar scheme to that presented in Fig. 3.21 should be followed. All the factors leading to either underestimating or overestimating the CWV content would be clustered to generate a set of TOA radiance spectra. Running the CWV retrieval module on them would provide an idea of the error magnitude. However, by comparing Figs. 3.22-3.23 with Fig. 3.25 it can be stated that CWV errors are mainly driven by the spectral shift if values similar to those in the previous section, and AOT variations of 0.03, are assumed. For this reason, an overall relative error in CWV of **4%**, peak error for the reference 2 g·cm^{-2} value, is chosen as representative of all CWV retrievals.

3.3.3. Sensitivity of Surface Reflectance Retrieval

The sensitivity of surface reflectance to the factors presented previously is addressed in the last place. The analysis is based on comparing surface reflectance spectra derived from the atmospheric correction of a MERIS synthetic data set with known surface reflectance spectra which were used as input in the simulations. The input angular configuration, the AOT and CWV grids, and the surface altitude (± 300 m from 300 m) and slope (± 10° from 10°) are the same than those described in the previous sections.

Surface reflectance spectra derived from the atmospheric correction of simulated TOA radiances are displayed in Fig. 3.26(a). Errors of 0.0 and ±0.15 in AOT at 550 nm were introduced in the atmospheric correction step. The relative errors corresponding to the vegetation spectrum for all the MERIS bands and grided AOT are plotted in Fig. 3.26(b). It can be observed that errors are larger in the visible wavelengths, where aerosol scattering contribution is maximum. Errors decrease smoothly with wavelength, but they grow again inside MERIS bands 11 and 15, located inside oxygen and water vapor absorptions, respectively. This is due to the different contribution of radiation multiple scattering inside absorption bands than outside them. As it was discussed when analyzing the influence of AOT in CWV retrievals, radiation multiple scattering tends to increase the absorption efficiency inside absorption bands, as photons have larger atmospheric paths. The contrary occurs if the aerosol loading is underestimated: absorptions become larger than those simulated for atmospheric correction, resulting in reflectance underestimations. In any case, those errors in reflectance in bands 11 and 15 are not representative of the real case in SCAPE-M, as reflectance is calculated from interpolation or extrapolation from the neighboring bands. It must be remarked that errors in Fig 3.26(b) depend on the aerosol model, that is not taken into account in this study.

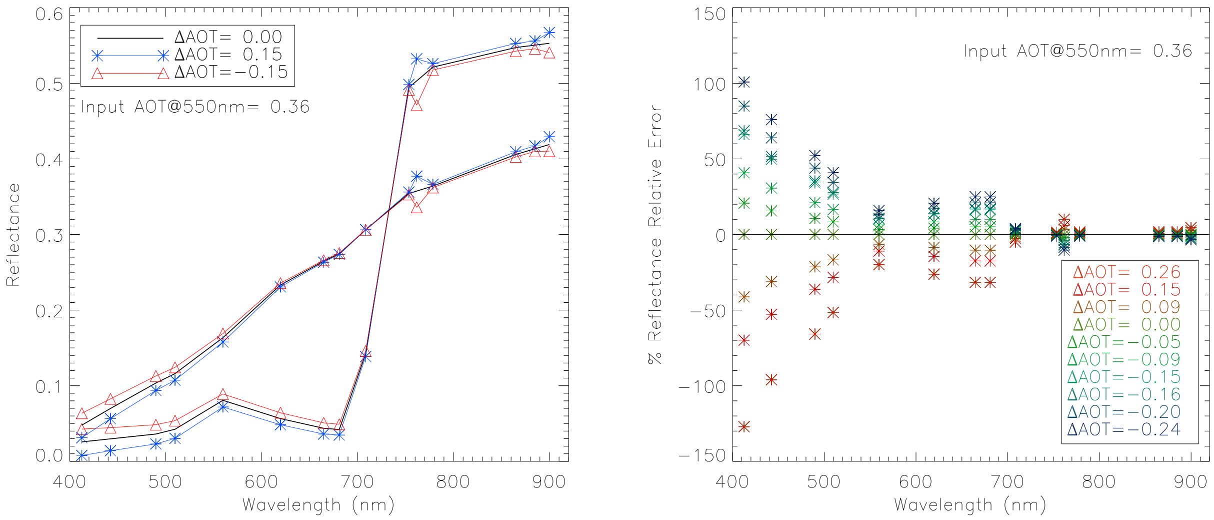

(a)

(b)

Figure 3.26: Reflectance errors associated to errors in the estimated AOT. Left (a), green vegetation and bare soil reflectance spectra derived from atmospheric correction with errors in AOT at 550 nm of 0 and ±0.15 externally added. Right (b), reflectance relative error in the atmospheric correction of the vegetation target in (a) for all the tested AOT values.

An analog representation for the dependence on water vapor is depicted in Fig. 3.27. Surface reflectance spectra derived from atmospheric correction setting CWV to either 1.2 g·cm^{-2} and 2.8 g·cm^{-2} are compared to the input spectra, generated with CWV of 2 g·cm^{-2}, in Fig. 3.27(a). It can be stated that the largest reflectance errors appear in bands 9 and 15, which are the ones where water vapor has the largest contribution. In relative terms, reflectance errors are presented in Fig. 3.27(b). Errors around 20% are associated to the shortest wavelengths. This is due to a combination of the low reflectance in the visible region for green vegetation targets with the water vapor continuum absorption, which becomes noticeable for extreme CWV deviations. However, the most important reflectance errors appear in bands 9 and 15 when the error in CWV does not exceeds 1 g·cm^{-2}, which is the general case. In the present atmospheric correction scheme, only the former one must be considered, as surface reflectance in band 15 is calculated from linear extrapolation of the reflectance in bands 13 and 14, as it was justified in Fig 3.10.

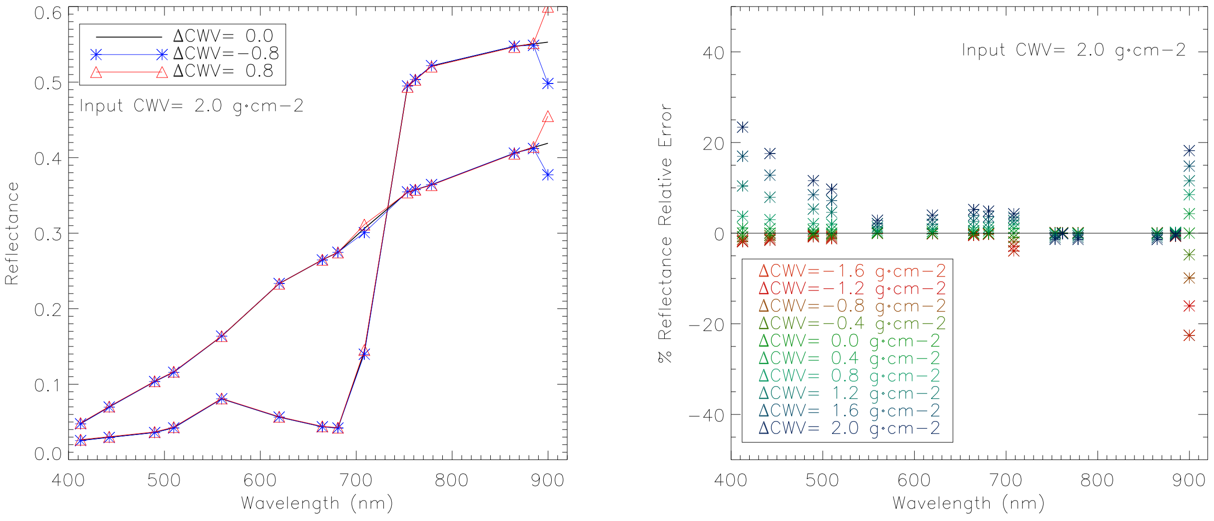

(a) (b)

Figure 3.27: Reflectance errors associated to errors in the estimated CWV. Left (a), green vegetation and bare soil reflectance spectra derived from atmospheric correction with errors in CWV 0 and ±0.8 g·cm^{-2} externally added. Right (b), reflectance relative error in the atmospheric correction of the vegetation target in (a) for all the tested CWV values.

Errors in surface reflectance due to unbalanced values of the target slope and surface elevation are presented in Fig. 3.28. The contribution of surface slope is shown in Fig. 3.28(a) and 3.28(b). An important impact at the NIR wavelengths of up to 15% is observed. This is explained by the fact that the surface slope mainly acts modifying the direct irradiance arriving at the target, that has its maximum values in the NIR region. The large errors associated to this factor reveal that any atmospheric correction algorithm should take topographic effects into account somehow. However, those errors are calculated by taking Eq. 3.1.1 and Eq. 3.1.2 as a reference. Therefore, the contribution from opposite slopes and valleys is not considered. Ray tracing techniques should be employed for an accurate error analysis. Concerning the dependence on the surface altitude, the corresponding plots are displayed in Fig. 3.28(c) and Fig. 3.28(d). A major impact occurs at the shortest wavelengths. This is due to the mis-estimation of the surface elevation leads to errors in the computation of the Rayleigh path radiance, which affects mainly the shortest wavelengths. Reflectance relative errors up to 30% are again associated to the low reflectance levels of vegetation in those wavelengths.

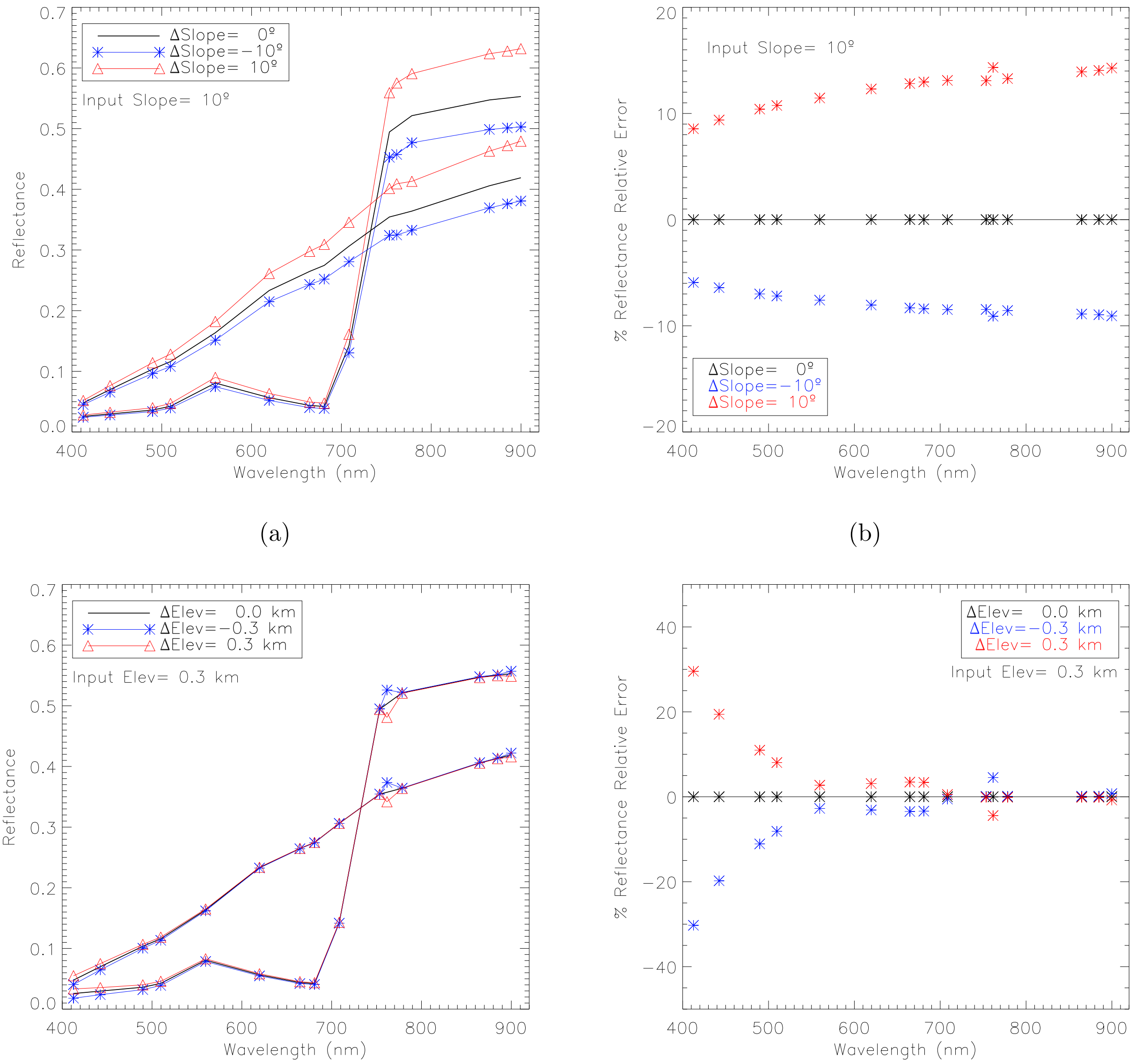

(a) (b)

(c) (d)

Figure 3.28: Reflectance errors associated to errors in elevation and surface slope. Upper left (a), the same than in Fig. 3.26(a) for errors of 0° and ±10° in the surface slope. Upper right (b), the same than in Fig. 3.26(b) for errors of 0° and ±10° in the surface slope. Lower part, the same than in the upper part for errors of 0 km and ±0.3 km in the surface elevation.

In order to associate an error to atmospherically corrected reflectances, simulated radiance spectra with typical atmospheric and reflectance inputs have been generated. Surface reflectance is retrieved after adding errors to the input parameters, which were AOT, CWV, surface elevation and terrain slope. Two opposite values are selected for each of them, so that one leads to overestimating the subsequent surface reflectance and the other works in the opposite direction. Two sets of input conditions are built, one with the parameters that lead to overestimating surface reflectance and the other with those which have the opposite effect. Input values were AOT= 0.35, CWV= 2 g·cm^{-2}, elevation= 300 m and surface slope= 10°. The same target elevation and slope variation range applied to the estimation of AOT error is employed here: ±20% for elevation and ±10% for terrain slope. The estimated ±0.03 for AOT and ±4% for CWV account for uncertainties in atmospheric retrievals. For surface reflectance, 5 MERIS reflectance spectrum are generated by means of 5 straight lines with 5 different slopes and intercepts. These are plotted in Fig. 3.29(a). The 5 points in each observation wavelength are selected so that they cover most of the reflectance values to be found in land targets, from 5% in the darkest targets at the first band to 60% at 900 nm which could be found in some dense vegetation or bright soil targets.

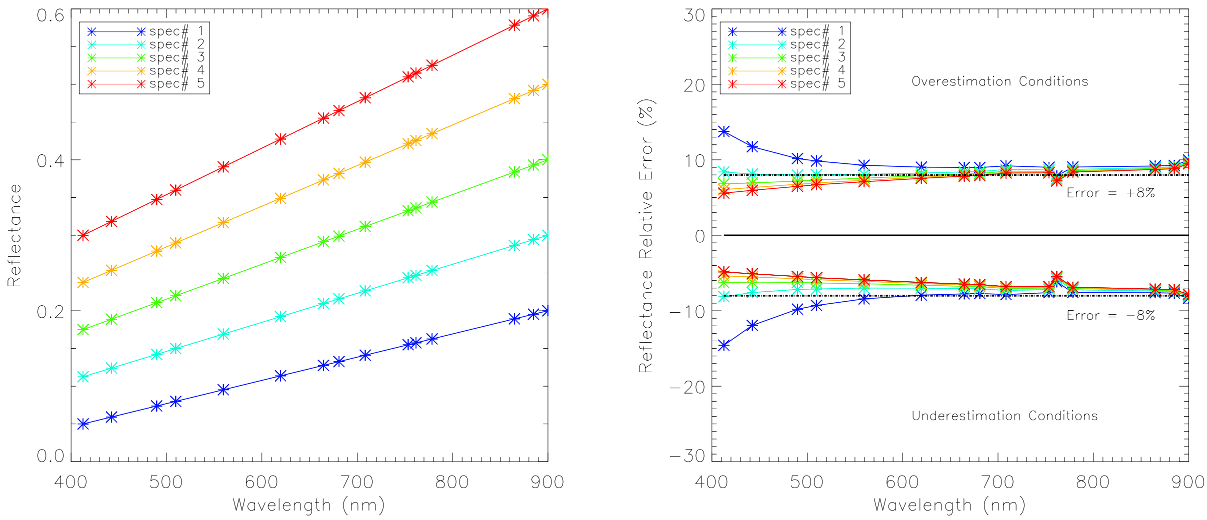

(a)

(b)

Figure 3.29: Reflectance errors calculated by taking into account different error sources. Left (a), MERIS reflectance spectra simulated so that most of the reflectance range expected in land targets is covered. Right (b), reflectance relative errors calculated from performing atmospheric correction with input "overestimation" (elevation= 360 m, slope= 16.8°, AOT= 0.32 and CWV= 2.08 g·cm^{-2}) and "underestimation" conditions (elevation= 240 m, slope= 1.9°, AOT= 0.38 and CWV= 1.92 g·cm^{-2}). Dotted lines mark constant 8% errors selected as representative of the whole MERIS spectral range.

The estimated reflectance relative error is displayed in Fig. 3.29(b). "Overestimation conditions" are elevation= 360 m, slope= 16.8°, AOT= 0.32 and CWV= 2.08 g·cm^{-2}, while "underestimation conditions" are elevation= 240 m, slope= 1.9°, AOT= 0.38 and CWV= 1.92 g·cm^{-2}. Dotted horizontal lines mark 8% error. When atmospheric correction is performed under overestimation conditions, the resulting relative error calculated between input and retrieved spectra fluctuates from 5-15%. The same trend is found for the underestimation case, with relative errors from -5 to -15%. Such fluctuation range is reduced to 5-9% if the first spectrum with the lowest reflectance values is not considered.

Moreover, error becomes nearly constant with wavelength for spectra from 2 to 5. For spectrum #1, with the lowest spectral reflectance ranging from 0.05 to 0.15, relative errors grow up to 15% in the blue wavelengths, and non-linear dependencies in the spectral domain are found. From all those considerations, the relative error to be associated to retrieved surface reflectance is assumed to be **8%**, which is representative of most of the spectral reflectance values that are expected in land targets.

Apart from all the contributions discussed within this section, directional effects in the target reflectance may also be a non-negligible error source that must be considered. Nevertheless, no dedicated error analysis is devoted to that contributions because it is not included in the present atmospheric correction algorithm, as it has been remarked in Section 3.1. The reader is referred to the literature (e.g., Hu et al. [1999]) for further information about those topics.

Chapter 4

Validation of Atmospheric Correction Products

The validation of the aerosol optical thickness, water vapor and surface reflectance products derived by SCAPE-M from MERIS data is detailed in this chapter. The validation exercise has relied on comparing SCAPE-M retrievals with reference data sources. These are either ground-based measurements or other equivalent MERIS-based products. Concerning the validation of the atmospheric products, AERONET[1] [Holben et al., 1998] sunphotometer measurements distributed all over the world have been a useful tool in the assessment of the method performance under different environments and atmospheric conditions. In addition, the extensive field campaigns carried out in the Barrax study site have been an appreciated data source, as both atmospheric and surface reflectance measurements were taken simultaneously to MERIS acquisitions. SCAPE-M results have also been cross-checked against other MERIS products coming from ESA-sponsored algorithms, in order to test SCAPE-M with other methods already validated against independent sources.

4.1. Sources of Reference Data for Validation

The validation of the atmospheric products is based on the comparison of MERIS-derived τ_{550} and CWV retrievals with ground-based measurements. Two major data sources have been utilized: extensive field campaigns at the Barrax study site and AERONET. The first one provides a complete data base of localized atmospheric and surface reflectance measurements, while AOT and CWV in different environmental conditions are provided by AERONET stations located all over the world.

A series of field campaigns has been carried out from 2003 to 2005 at the Barrax study

---

[1] http://aeronet.gsfc.nasa.gov/

site (La Mancha, Spain, 39.05°N, 2.09°W), as part of the ESA's Earth Observation Envelope Programme to support geophysical algorithm development, calibration/validation activities and the simulation of future Earth Observation missions. In particular, the SPectra bARrax Campaigns (SPARC)[2] took place in July 2003 and 2004, in the frame of the Phase-A Preparations for the Surface Processes and Ecosystem Changes Through Response Analysis (SPECTRA) mission [Rast, 2004], while the SENtinel-2 and FLuorescence EXperiment (SEN2FLEX)[3] was held during June and July 2005. It involved different activities in support of initiatives related both to fluorescence experiments (for modelling and detection of solar induced fluorescence) and to Global Monitoring for Environment and Security (GMES) Sentinel-2 initiative (for prototyping of spectral bands, spectral widths, and spatial/temporal resolutions to meet mission requirements).

The Barrax study site is a flat continental area with an average elevation ASL of around 700 m. The area is characterized by a flat morphology and large, uniform land-use units, which make it very suitable for remote sensing calibration and validation activities. The most frequent meteorological situation over central Spain in summer consists of a surface thermal low daily developed due to the intense solar heating, with a high pressure system located over the Azores islands and a thermal low over northwest Africa. This synoptic situation is associated with cloudless skies, weak winds and high temperatures, hindering the air renovation at low levels and driving an increase of the atmospheric turbidity and water vapor content, reaching maximum values in summer. Moreover, the Inter Tropical Convergency Zone movement to higher latitudes in summer makes more feasible the arrival of air masses of Saharan origin, characterized by higher burdens of mineral particles and consequently, higher AOT. These dust layers usually arrive over the aerosol mixing layer, at 2000-3000 m ASL, and can be recognized by their flat AOT spectral behavior as measured by ground based sunphotometers and by the vertical profile of the aerosol extinction coefficient as retrieved by an atmospheric lidar. Their origin and nature can also be pointed out by a detailed analysis of air mass backtrajectories and atmospheric transport models (V. Estellés, University of Valencia, personal communication, 2006).

A wide range of remote sensing and ground-based measurements were taken during the SPARC and SEN2FLEX campaigns. Apart from many other data, AOT and CWV measurements were determined from every campaign date with an automatic CIMEL CE318-NE sunphotometer. This version of the sunphotometer employs 9 filters at nominal wavelengths 340, 380, 440, 500, 670, 870, 940, 1020 and 1600 nm. Measurements at 940 nm are used for retrieving the CWV by applying the method from Bruegge et al. [1992]. The other channels (except 1600 nm) are used for AOT retrieval. Details on the method used for retrieving AOT can be found elsewhere [Estellés et al., 2006]. For the comparison with

---

[2] `http://www.uv.es/leo/sparc2004/`

[3] `http://www.uv.es/leo/sen2flex/`

MERIS derived τ_{550}, the AOT at VIS channels was interpolated following the Ångström law. During the field campaign, measurements were made in a 5-10 minutes basis instead of the by default 15 minutes, in order to better track the AOT and CWV evolution during the airborne sensor acquisitions, and therefore estimate their temporal variability. Further atmospheric information was obtained by two radio-soundings per day, spectral radiance measurements with three different instruments (Licor 1800 and Optronic 754-O-PMT spectroradiometers, Microtops II sunphotometer). In addition, a ground-based lidar mobile laboratory with autonomous power system was operated on site by a team from the Atmospheric Pollution Unit of the Spanish Research Centre for Energy, Environment and Technology (CIEMAT).

Concerning AERONET, it is an optical ground based aerosol monitoring network and data archive supported by NASA's Earth Observing System and expanded by federation with many non-NASA institutions. The network hardware consists of identical automatic sun-sky scanning spectral radiometers owned by national agencies and universities. More than 500 stations located all over the world provides globally distributed near real time observations of aerosol spectral optical thickness, aerosol size distributions, and precipitable water in diverse aerosol regimes. The data undergo preliminary processing (real time data), reprocessing (final calibration around 6 months after data collection), quality assurance, archiving and distribution from NASA's Goddard Space Flight Center master archive and several identical data bases maintained globally. The data provide algorithm validation of satellite aerosol retrievals and characterization of aerosol properties that are unavailable from satellite sensors. The CIMEL Electronique 318A spectral radiometer is again the radiometer performing the atmospheric measurements. It makes two basic measurements, either direct sun or sky, both within several programmed sequences, which provide the final AOT and CWV products after the corresponding calibration and processing. Three levels of data are available: Level 1.0 (unscreened), Level 1.5 (cloud-screened), and Level 2.0 (cloud-screened and quality-assured). The location of the Barrax study site and most of the AERONET stations used in the validation of the atmospheric products are plotted in Fig. 4.1. The latter ones have been selected so that a wide range of atmospheric conditions are found, due to the variety of surface conditions and environmental factors (surface elevation, topography, maritime influence...) from one site to another.

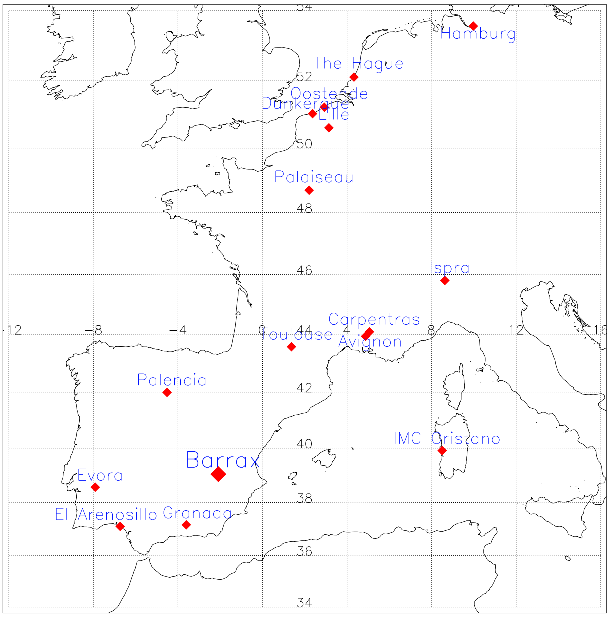

Figure 4.1: Location of the Barrax study site and all the European AERONET stations used in the validation of the atmospheric products.

4.2. Results from Aerosol Optical Thickness Retrieval

AOT maps derived from MERIS RR images acquired during the SPARC campaigns 2003 and 2004 are displayed in Fig. 4.2. The three maps are plotted with the same color scale and color ranges for comparative purposes. Different atmospheric conditions were found those dates. A typical summer situation in the Iberian Peninsula is registered on 14 July 2003 and 17 July 2004, with high atmospheric turbidity in both of them. Moreover, an intrusion of Saharan dust in the upper atmospheric layers was detected on 17 July 2004 by both sunphotometer and lidar ground-based measurements [Martínez-Lozano et al., 2006]. The aerosol loading on 14 July 2004 was lower than in the other two days. Extreme τ_{550} values higher than 0.4 are probably caused by sub-pixel clouds that have not been properly masked. In any case, the border between aerosols and thin clouds is somewhat diffuse, and it may turn out to be very difficult to distinguish from thin clouds to high aerosol loadings at the time of detection. Tighter reflectance thresholds in the cloud mask would enable to remove even the thinnest clouds, but important proportions of medium to bright land surface targets would also be masked as well. Thus, residual errors in τ_{550} due to non-masked clouds will be assumed.

The atmospheric conditions detected in Fig. 4.2 are confirmed by ground-based measurements. AOT spectra derived from irradiance measurements acquired by a LICOR 1800 device are plotted in Fig. 4.3. The original LICOR measurements were collected at 1 nm

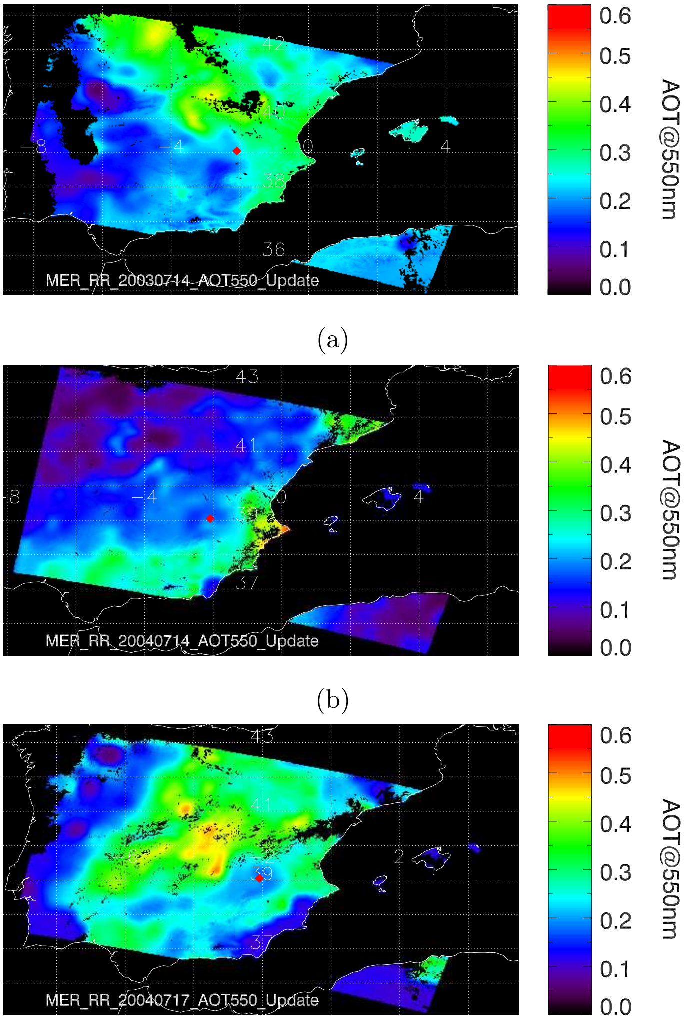

(a)

(b)

(c)

Figure 4.2: AOT at 550 nm calculated from the 3 MERIS RR images acquired during the SPARC campaigns in July 2003 and 2004. The location of the Barrax site is marked by a diamond.

spectral resolution, and were resampled to the MERIS band configuration for comparison. A spectrally-constant absolute AOT error of 0.02 is assigned to the *in situ* measurements. The high and low aerosol regimes on 14 July 2003 and 2004, respectively, are well reproduced by the ground measurements. The flat spectral shape in the AOT spectrum from 17 July 2004, typical in Saharan dust intrusions, can also be observed. Gaseous absorptions are not corrected in the AOT spectra. A good comparison is found with the absolute τ_{550} values that can be read from the MERIS maps. However, such comparison is not that good if the spectral aspect is taken into account: as it was discussed in Section 3.1, the aerosol model was fixed to the rural model, whatever the real conditions are. This leads to important errors in AOT, especially at the longest NIR wavelengths, when deviations from standard continental conditions are predominant in the atmosphere. This is the case of air masses coming from the desert or the ocean. As a result, deviations about 0.1 at the NIR are calculated from comparison between MERIS and ground-based measurements.

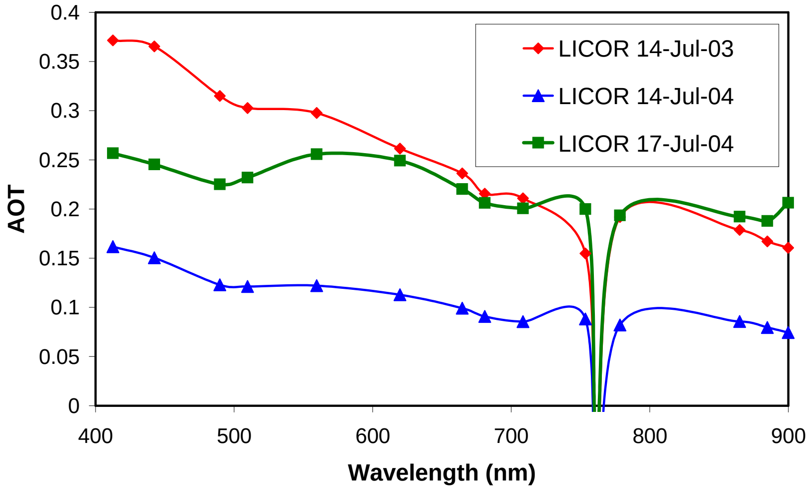

Figure 4.3: AOT spectra acquired during the SPARC campaigns 2003 and 2004 by a LICOR 1800 device [Martínez-Lozano et al., 2006], after resampling to MERIS band configuration.

The method performance has been compared with that of the BAER algorithm [von Hoyningen-Huene et al., 2005a, 2003]. With this purpose, both methods have been run over the three images displayed in Fig. 4.2. Results for the two MERIS acquisitions during the SPARC campaign 2004 are shown in Fig. 4.4 and Fig. 4.5. The main difference between the two methods is the spatial resolution of AOT calculations: SCAPE-M provides AOT maps calculated from a grid compounded by 30 × 30 km cells, which is smoothed in order to represent natural variations expected in a real atmosphere. However, this scheme is not enough to register possible variations in the atmospheric state at a finer scale. The BAER method, in turn, relies on a per-pixel AOT retrieval, so it is able to describe small AOT fluctuations. These points can be observed in Figs. 4.4-4.5: the same patterns are found in the AOT spatial distribution from the two methods, but sharp variations in AOT from pixel to pixel are only detected in BAER results. The shortcoming of a per-pixel parametrization is that some of the finest variations in AOT may come from errors in AOT retrieval as well as from intrinsic atmospheric dynamics. This trend leads to AOT maps having a salt-pepper appearance in some regions within the image that can hardly be justified only by atmospheric processes. Moreover, AOT retrieval is performed only over about 40% of the pixels in the case of the BAER method, what suggest applying some kind of interpolation to fill in the remaining gaps in order to build continuous AOT maps. Finally, it must be remarked that extreme τ_{550} values higher than 0.4 are found in the maps derived by the two methods. This situation is worse in the case of the BAER method, as it can be stated by checking Fig. 4.5(b). Such turbid conditions were not actually measured during the SPARC experiment by the many ground-based measurements. Therefore, those values are likely to be caused by unmasked cloudy pixels, which are very difficult to detect (especially in the RR configuration). A similar comparison with the MERIS Level2 aerosol product [Santer et al., 1999] was foreseen, but the fact that AOT is only calculated on DDV pixels makes too less pixels be available in the Iberian Peninsula for cross-checking, and the analysis was discarded.

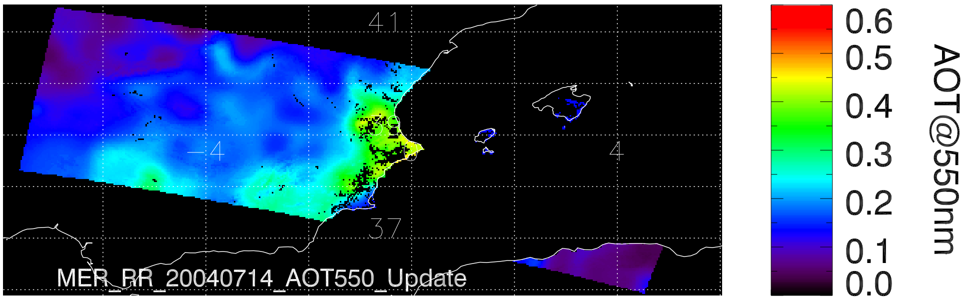

(a) SCAPE-M

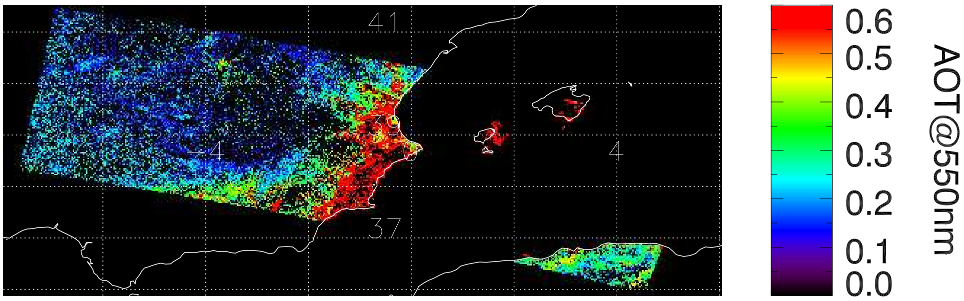

(b) BAER

Figure 4.4: Comparison of τ_{550} maps derived by SCAPE-M (a) and the BAER algorithm (b). The RR image acquired on 14 July 2004 during the SPARC experiment is used as input.

An especial atmospheric situation was present during the forest fires episodes in Portugal on August 2003[4], which destroyed more than 50,000 hectares of forest and bushes in the first weeks of August. From the point of view of aerosol retrieval, fire episodes must be handled carefully. On one hand, aerosols coming from biomass burning are usually much more absorbent than what is parameterized as "rural model", so the optical parameters (single scattering albedo, phase function, extinction coefficient profile) are far from the input values employed in the generation of the atmospheric LUT. On the other hand, fire smoke can be easily mistaken by thin clouds. In any case, the magnitude and temporal persistence of Portugal fires on 2003 enable they can be monitored from MERIS data, as it was reported by von Hoyningen-Huene et al. [2005a,b]. The τ_{550} map derived by SCAPE-M

---

[4] `http://earth.esa.int/ew/fires/portugal_aug_03/`

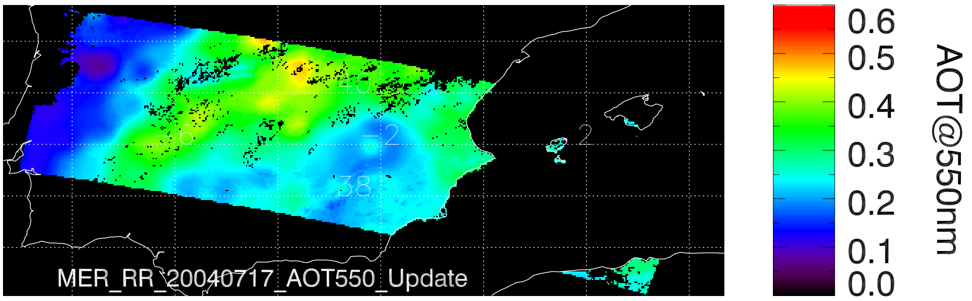

(a) SCAPE-M

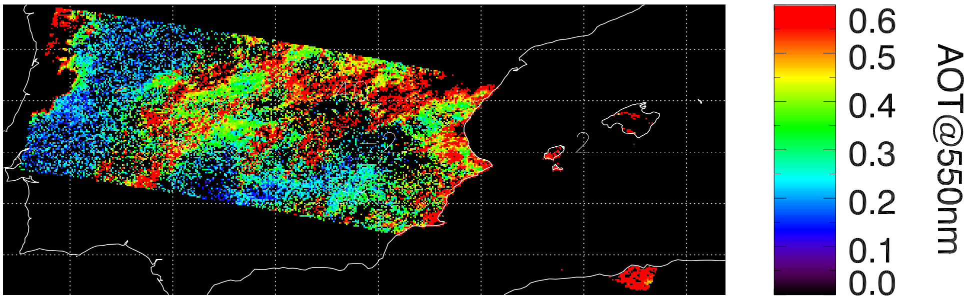

(b) BAER

Figure 4.5: The same as Fig. 4.4 for 17 July 2004.

from a MERIS RR image acquired on 11 August 2003 is displayed in Fig. 4.6. It has been derived making use of the relaxed cloud mask (`Cloud_flg`= 1) to prevent fire smoke from being classified as clouds. Large AOT values are detected in the Western half of the Iberian Peninsula, with the focus around 39°N, 8°W. The evolution of the smoke plumes towards Northern Europe can also be noted. It must be remarked that those high τ_{550} values close to 0.6 are around the upper threshold of detectable values, as higher aerosol loadings would probably be classified as clouds. This fact reinforces the need for a more sophisticated cloud masking algorithm able to discriminate high aerosol loadings form thin clouds.

The high aerosol loading associated to Portugal fires can be quantified by checking the Evora AERONET station archive. The Evora station is the closest one to the fire origin, as it is pointed out by a blue diamond in Fig. 4.6. AOT at 550 nm derived from a series of MERIS images is compared with AERONET data for the time period between July and December 2003 (data from January to June were not available) in Fig. 4.7. MERIS data come from a series of 133 MERIS RR images acquired over the Iberian Peninsula from January to December 2003. After cloud screening, 35 dates of concurrent MERIS and AEONET data are available. As it can be stated in Fig. 4.7, both AERONET and MERIS detect the highest aerosol loadings for the day-of-year (DOY) range from 211 to 242, that correspond to August. A general good agreement between MERIS and AERONET τ_{550} values, both in absolute terms and in the temporal evolution, is found all over the time period.

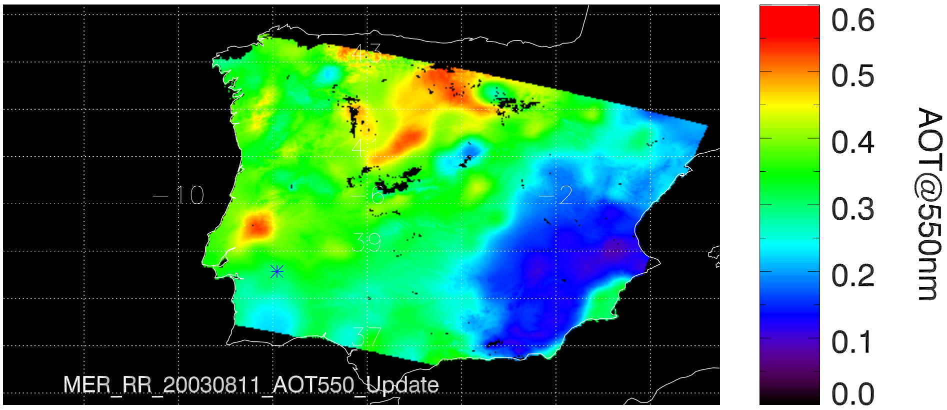

Figure 4.6: τ_{550} map derived from MERIS RR data showing the high aerosol loading due to forest fires in Portugal on August 2003. The location of the Evora aeronet site is marked by a diamond.

Highly polluted areas are another interesting test bench for aerosol retrieval algorithms. The τ_{550} map derived from a MERIS RR acquired over China on 1 May 2003 is shown in Fig. 4.8. Extreme τ_{550} values around 1.0 are constantly registered in the AERONET station located in the city of Beijing, which are mainly caused by human activities. This trend is confirmed by Fig. 4.8. The optical properties of urban aerosols are quite different from those represented by the rural model. Therefore, the τ_{550} in Fig. 4.8 derived under the assumption of aerosol properties being given by the standard rural model is biased by probable deviations from the real aerosol optical parameters. However, spatial patterns in the aerosol distribution and high aerosol concentrations are still well reproduced in MERIS. As in the case of the Portugal forest fires, it must be stated that such high aerosol loadings are in the limit of detectable aerosols by the method presented in this work, as the simplicity in the developed cloud masking algorithms causes high aerosol contents are classified as clouds, which are not considered in the aerosol retrieval. For this reason, the relaxed cloud mask was again selected by setting `Cloud_flg` to 1 in the SCAPE-M input file.

The robustness of the method against different surface and/or atmospheric conditions is assessed by comparing MERIS retrievals with concurrent AERONET data from different stations. With this purpose, more than 170 MERIS RR images have been processed. The reason for employing RR images instead of FR ones is that the former ones can be accessed more easily accessed thanks to the ESA MERIS Catalogue and Inventory (MERCI) database[5]. In addition, testing the method over RR images provides evidence of the method performance in the worst operating conditions, as the AOT retrieval lies on the availability of targets with the maximum spectral contrast, which is reduced as the spatial resolution coarsens. Moreover, more pixels contaminated by sub-pixel clouds are likely to escape from

---

[5] http://merci-srv.eo.esa.int/merci/

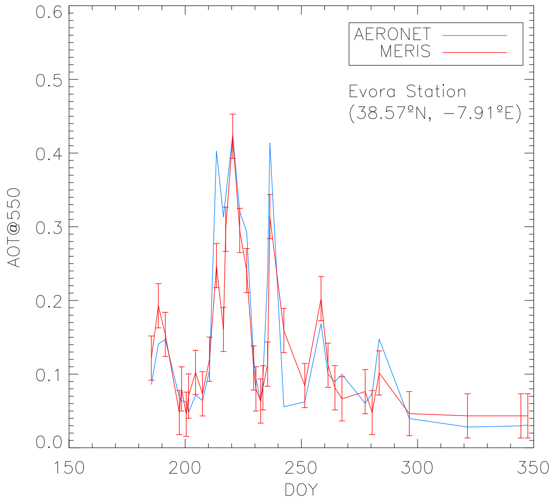

Figure 4.7: Comparison of τ_{550} time series for the Evora site between July and December 2003 derived from both MERIS and AERONET data. Vertical error bars correspond to the ±0.03 error in τ_{550} estimated for MERIS retrievals.

the cloud masking process in the RR mode. AOT from all the non-cloudy points with a temporal separation between MERIS and AERONET acquisitions lower then ±1 hour are plotted in Fig. 4.9 for those stations where the number of coincidences enable to calculate some statistics. It must be remarked that the scatter plots are automatically generated by a routine reading from AERONET files and MERIS images and finding concurrent points, and that only the points classified as cloudy have been removed. No other criterion for the discrimination of potential outliers has been applied, with the aim of being realistic in the analysis of the method potential and limitations.

The first conclusion from Fig. 4.9 is that the aerosol loading is well retrieved in the general case, as it is confirmed by the high linear correlation found from the comparison with most of the AERONET sites. In absolute terms, the comparison depends on the total aerosol loading, as very high correlation are found for low aerosol regimes, whereas some systematic underestimation is detected as AOT increases. A different modelling of the AOT variable in the different RTCs used in the inversion of radiance measurements, both in SCAPE-M and AERONET, is considered the most likely explanation for these deviations at the largest aerosol regimes. This trend is represented by regression lines slopes smaller than one, mostly caused by τ_{550} values larger than 0.4. In particular, slopes about 0.8 and square Pearson's correlation coefficient R^2 about 0.73 are obtained from the Avignon, Carpentras and Palencia stations. Correlation slopes are smaller in the Evora and Toulouse sites (0.703 and 0.597, respectively), leading to a larger underestimation of τ_{550} at the largest values. However, the high linearity in the comparison still holds ($R^2 = 0.817$

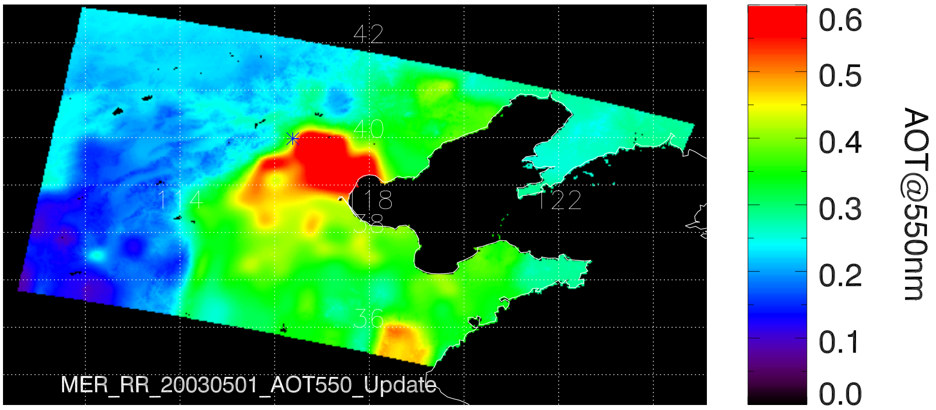

Figure 4.8: τ_{550} map derived from MERIS RR data showing the high polluted areas around the city of Beijing, marked by a blue asterisk.

in Evora, $R^2 = 0.728$ in Toulouse). Mean RMSE are about 0.05 in all those cases, which is close to the 0.03 estimated as the intrinsic uncertainty associated to the method. Finally, the worst situation comes from the comparison with the El Arenosillo site, where no linear correlation with MERIS retrievals is found ($R^2 = 0.337$, slope of 0.407, leading to a RMSE of 0.10).

The most probable reason to explain such bad results in the El Arenosillo site is the particular environment in which the station is located. El Arenosillo is in the South of the Iberian Peninsula, nearly in the Atlantic shore and less than 200 km from Northern Africa. Thus, it is strongly influenced by maritime or Saharan aerosols, which are not well parameterized by the rural aerosol model. This may lead to a bad characterization of the aerosol properties, which would vary with wavelength. This trend is illustrated in Fig. 4.10. MERIS retrievals at 440 and 870 nm reference wavelengths are compared with AERONET data from the El Arenosillo station. MERIS-derived AOT at wavelengths other than 550 are generated by applying the Ångström law with an exponential coefficient α of 1.243, which is estimated from the AOT spectra derived from MODTRAN4 for the rural model. A noticeable dependence of the correlation with the observation channel is found, changing from 0.41 at 440 nm to 0.156 at 870 nm. On the other hand, severe calibration problems in the Cimel instruments operating at El Arenosillo site in 2000-2001 have been reported by Cachorro et al. [2004]. No information about the calibration and processing algorithms of the El Arenosillo station on 2003 is available, so error that are intrinsic to the data acquisition and processing can not be discarded.

The improvements associated to the MERIS finest spatial resolution of 300 m is shown in Fig. 4.11. Seventeen MERIS FR images acquired from February to November 2003 over Toulouse were processed and validated against AERONET measurements. Scatter

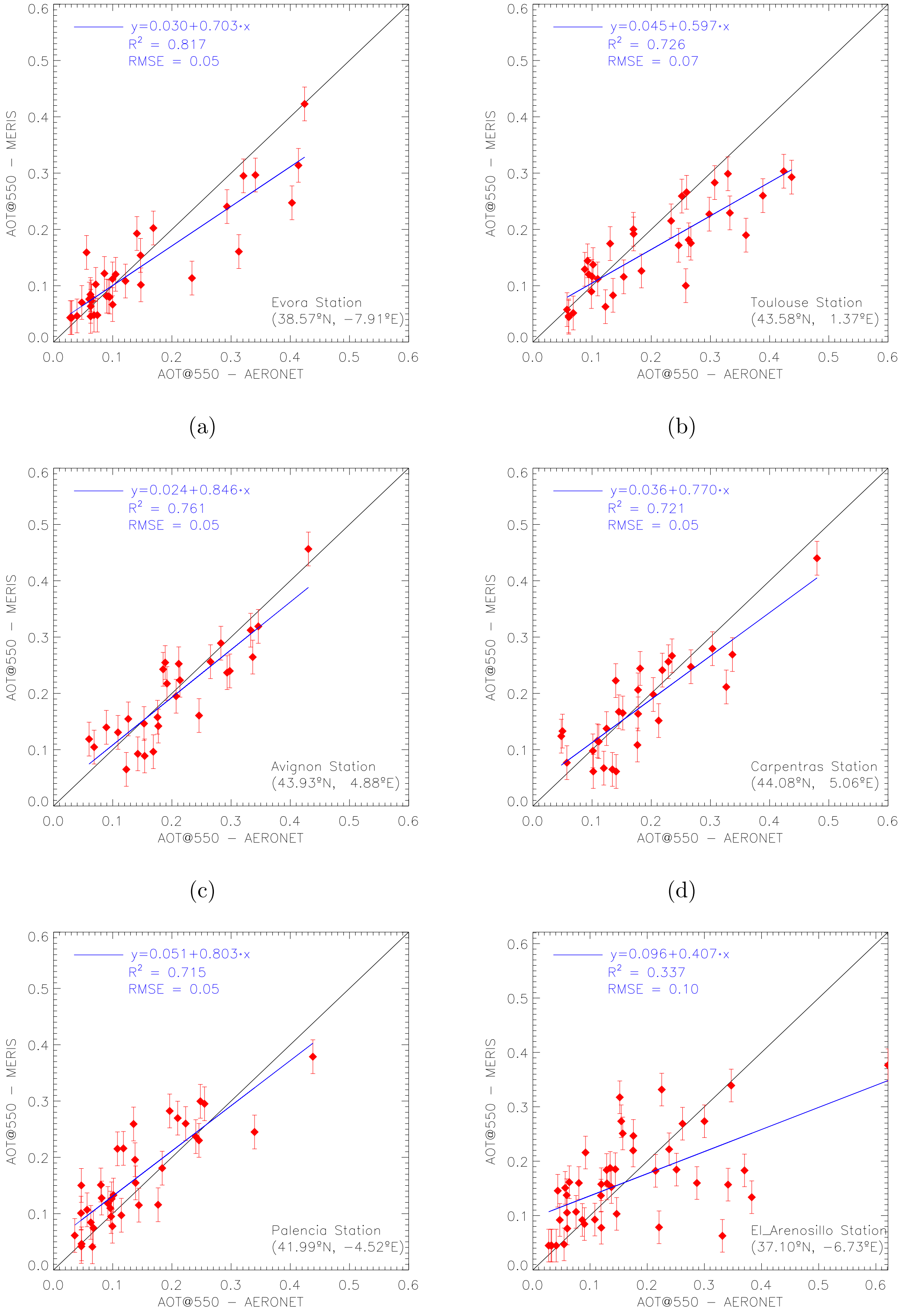

(a) (b)

(c) (d)

(e) (f)

Figure 4.9: Comparison of MERIS-derived estimates of τ_{550} with AERONET data.

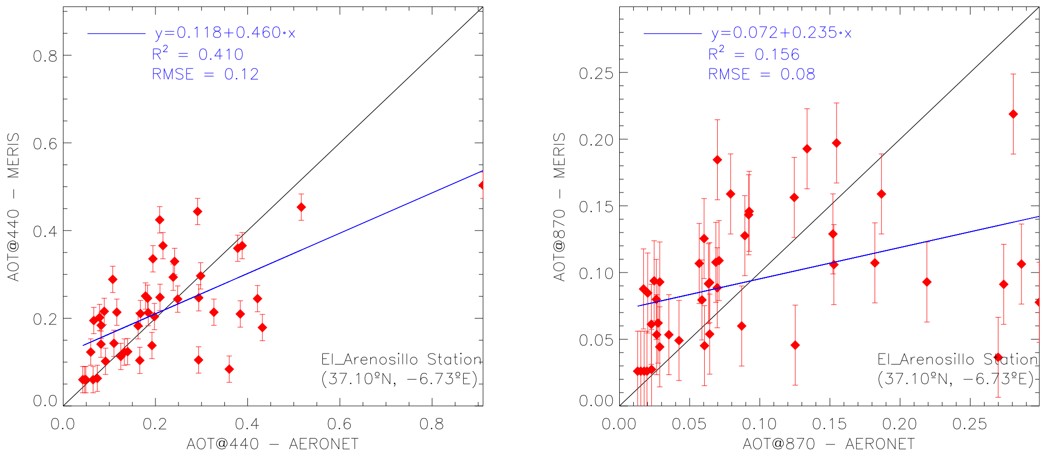

(a) (b)

Figure 4.10: Comparison of MERIS-derived estimates of AOT at 440 nm (a) and 870 nm (b) with AERONET data from the El Arenosillo station.

plots between MERIS and AERONET data for the three reference wavelengths 440, 550 and 870 nm are displayed. The good discrimination between clear and turbid atmospheric conditions is stated. Secondly, it can be observed that the linear correlation increases with respect to the RR case. The mean value of the slope also grows from 0.6 to about 0.7. These improvements are mostly due to the increase in spectral contrast (purer pixels can be selected as reference pixels for the aerosol retrieval) associated to the finer spatial resolution of FR images.

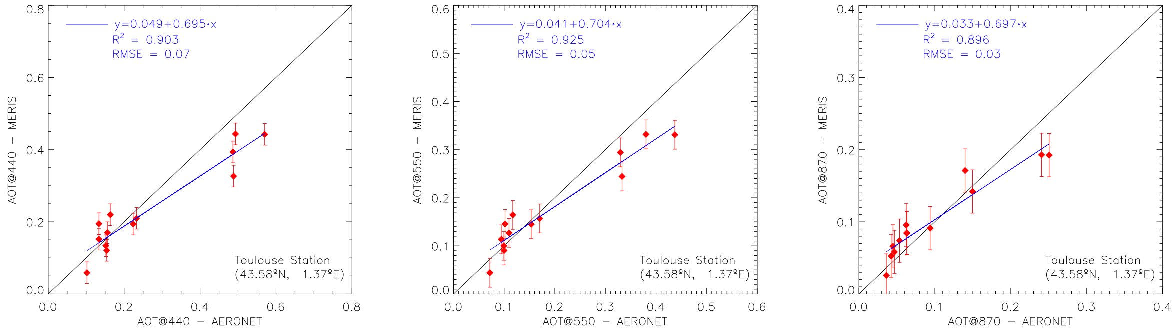

(a) (b) (c)

Figure 4.11: Comparison of MERIS FR-derived estimates of AOT at 440 nm (a), 550 nm (b) and 870 nm (c) with AERONET data from the Toulouse station.

Further validation of AOT retrievals with AERONET sites in other locations around the world is displayed in Fig. 4.12. The comparison of τ_{550} derived from MERIS FR data with several AERONET stations from Northern Europe is presented in Fig. 4.12(a). A good correlation in the comparison is found, independently of the station which is considered, although the underestimation of the highest aerosol contents is also detected. A considerable number of dates with high aerosol loadings, τ_{550} from 0.3 to 0.6, is found. The results from the comparison of 8 images acquired over the Amazon jungle with three AERONET sites in Brazil is shown in Fig. 4.12(b). Despite the reduced number of points, an evident linear correlation is observed, with $R^2 = 0.785$. Finally, the comparison of other AERONET stations in Southern Europe with the same set of MERIS RR images is displayed in Fig. 4.12(c). Although less points were available for the comparison, the linear correlation between MERIS and AERONET retrievals is observed within a wide range of τ_{550} from 0.07 to 0.4. This correlation increases considerably if the point with τ_{550}= 0.47, measured by the Ispra station the 17 September 2003, is not considered.

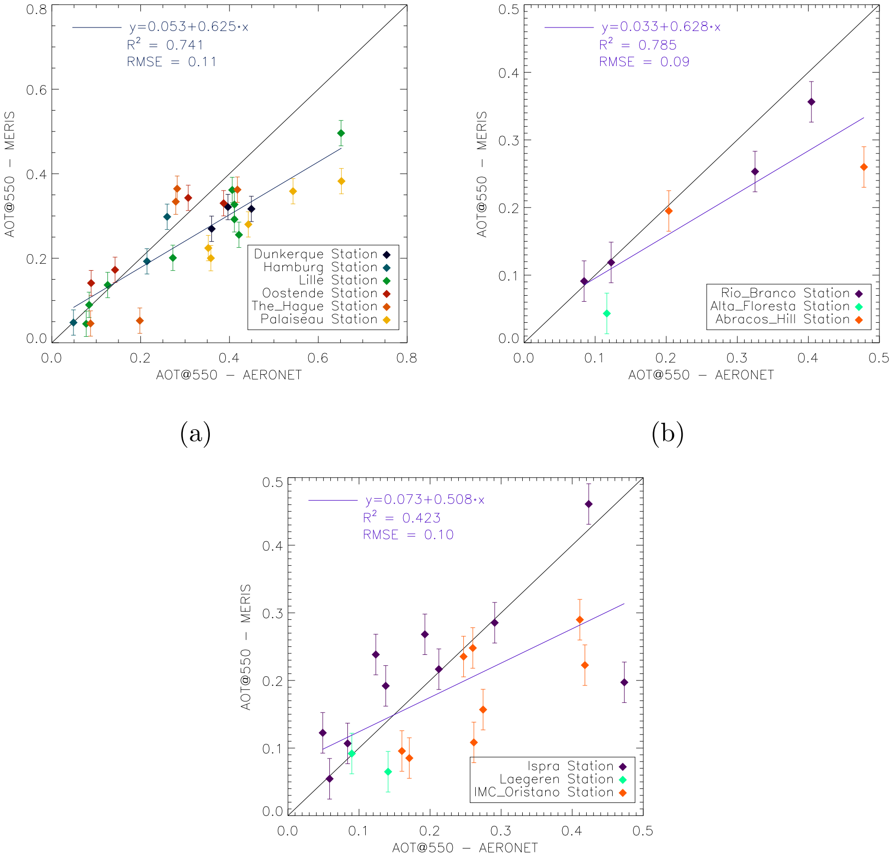

(a)

(b)

(c)

Figure 4.12: Comparison of MERIS-derived estimates of τ_{550} with AERONET data from several stations in Northern Europe, Brazil and Southern Europe.

The atmospheric situation in Southern Europe on 17 September 2003 was investigated into more detail. The τ_{550} horizontal distribution derived from MERIS is displayed in

Fig. 4.13. It can be observed that it was a very clear day all over the registered area, except for a plume of particles centered at the Po valley in Northern Italy. This is a very deep valley bordered by the Alps on the North, as it is shown in the DEM in Fig. 4.13(b). No information about the origin of that plume has been found, although it could be caused by foggy conditions inside the valley. The low aerosol loading detecting from MERIS data at the Carpentras and Avignon locations is confirmed by AERONET data. The Carpentras station measured an AOT at 440 nm around 0.16, and 0.20 was measured in Avignon. However, the AOT at 440 nm at the Ispra station grows up to 0.60, due to the plume observable in the image. The τ_{550} value calculated from the MERIS image exactly at the position of the Ispra AERONET station (45.803°N, 8.627°E) is around 0.2, but it can be seen that this value increases strongly some tens of kilometers southwards. Thus, it can be concluded that the method is describing well that unusual atmospheric situation. The mismatch between MERIS and AERONET measurements at the Ispra station may be simply justified by a bad spatial or temporal co-registration, or by the angular discrepancies in the acquisition of the original radiance data between MERIS and AERONET instruments.

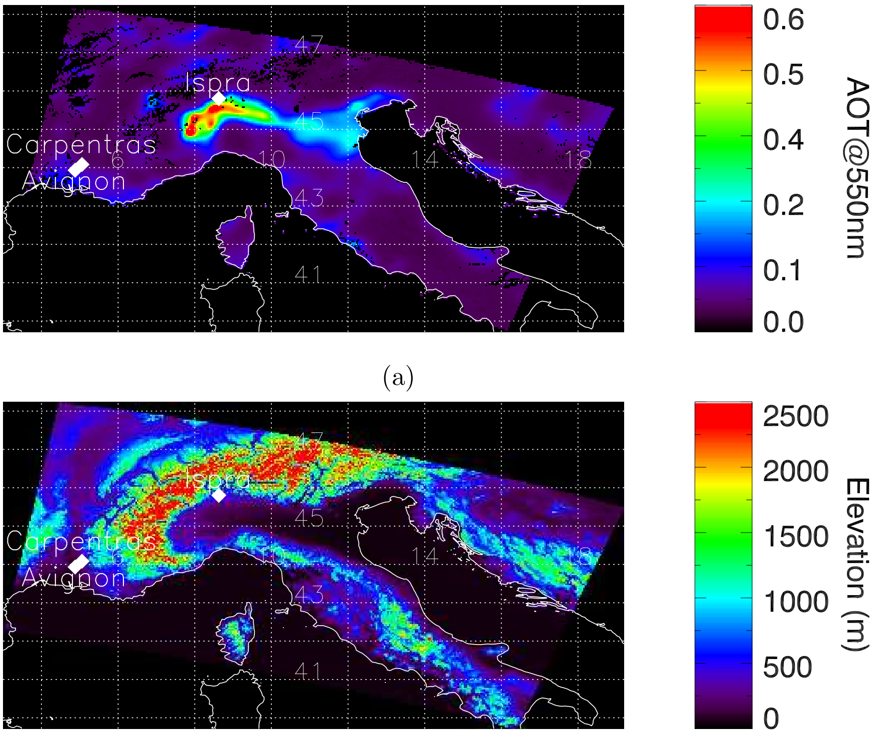

(a)

(b)

Figure 4.13: Atmospheric situation in Southern Europe on 17 September 2003. The MERIS-derived τ_{550} map is shown in (a), and the DEM from the same area is displayed in (b). AERONET stations with concurrent data available are pointed out.

Some sample τ_{550} maps calculated from either RR or FR MERIS images acquired over different sites around Europe and under different atmospheric conditions are displayed in Fig. 4.14. More than 200 equivalent maps are available after the processing of the entire MERIS data base used in the testing and validation of the methodology presented in this thesis. All the images processed along the development of this work are list in Appendix E.

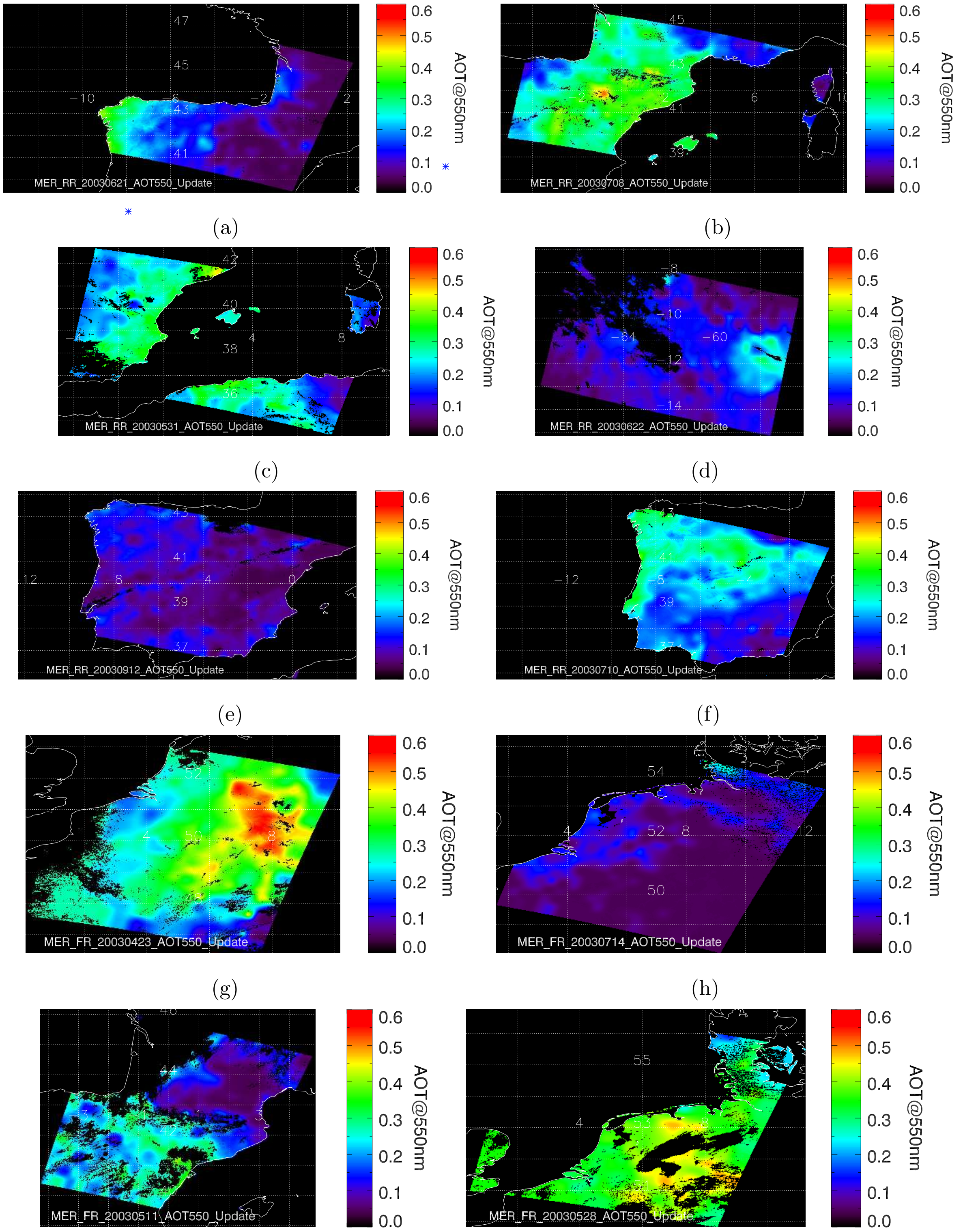

(a) (b) (c) (d) (e) (f) (g) (h) (i) (j)

Figure 4.14: Sample τ_{550} maps derived from MERIS FR/RR images.

4.3. Results from Water Vapor Retrieval

An analogous validation exercise has been carried out for SCAPE-M water vapor retrievals. The water vapor maps corresponding to the MERIS RR images acquired over the Barrax area during the SPARC 2003 and 2004 campaigns are shown in Fig. 4.15. Topographic effects on the total column content can be noted. Also some trends of the turbulent nature of the water vapor spatial distribution are present all over the area.

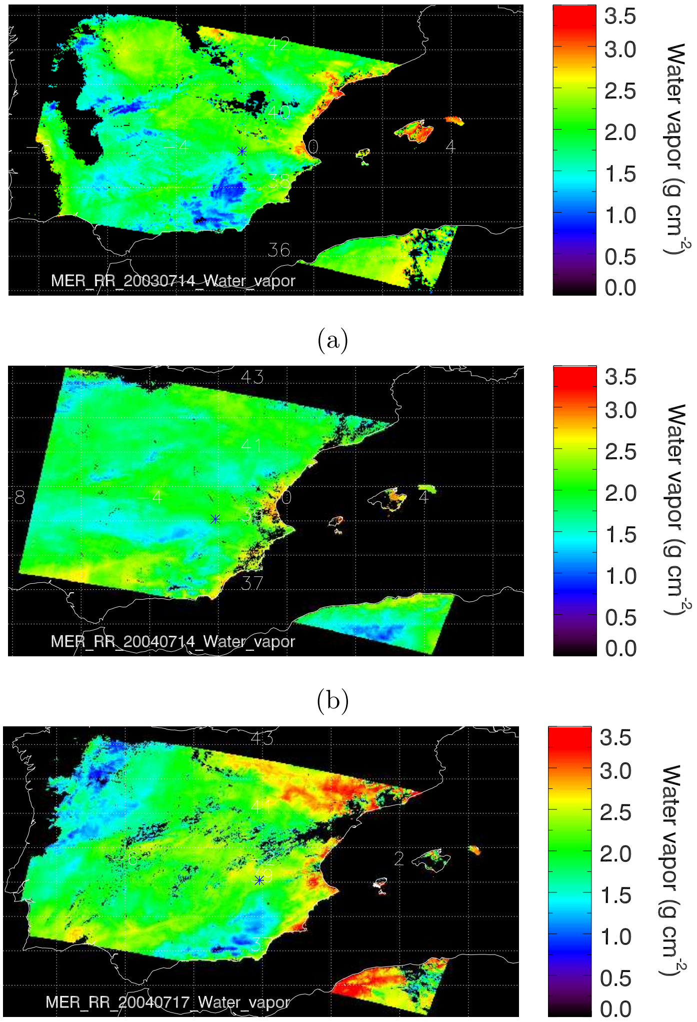

(a)

(b)

(c)

Figure 4.15: CWV calculated from the 3 MERIS RR images acquired during the SPARC campaigns in July 2003 and 2004. The location of the Barrax site is marked by an asterisk.

The CWV retrievals from MERIS data are firstly compared with the ground measurements taken during the SPARC campaigns and with the ESA MERIS Level 2 water vapor product [Bennartz and Fischer, 2001]. This product has been properly validated using concurrent microwave radiometer (MWR) and GPS measurements [Ciotti et al., 2003; Li et al., 2003]. The results from the two MERIS acquisitions during the 2004 SPARC campaign are depicted in Fig. 4.16. Mean values calculated from an area of 3 × 3 km around the Barrax site are plotted for SCAPE-M retrievals and the ESA Level 2 product, with the error bars indicating the spatial variability through the standard deviation of the samples. Direct extinction measurements were acquired by a MICROTOPSII sunphotometer. The result of the vertical integration of the water vapor profile measured by a radiosonde launched simultaneously to the ENVISAT overpass is also plotted. Some overestimation in the algorithm retrievals is found if we compare with the ESA product, from 1.98 g·cm^{-2} to 1.86 g·cm^{-2} on 14 July and from 2.32 g·cm^{-2} to 2.25 g·cm^{-2} on 17 July. However, the direct measurement by the MICROTOPSII device gives 1.94 g·cm^{-2} and 2.35 g·cm^{-2}, which are closer to the method estimation than to the ESA product results. The data from the radiosondes, although keeping the same temporal evolution than the other measurements, are out of range, perhaps due to the mis-calibration of the sonde.

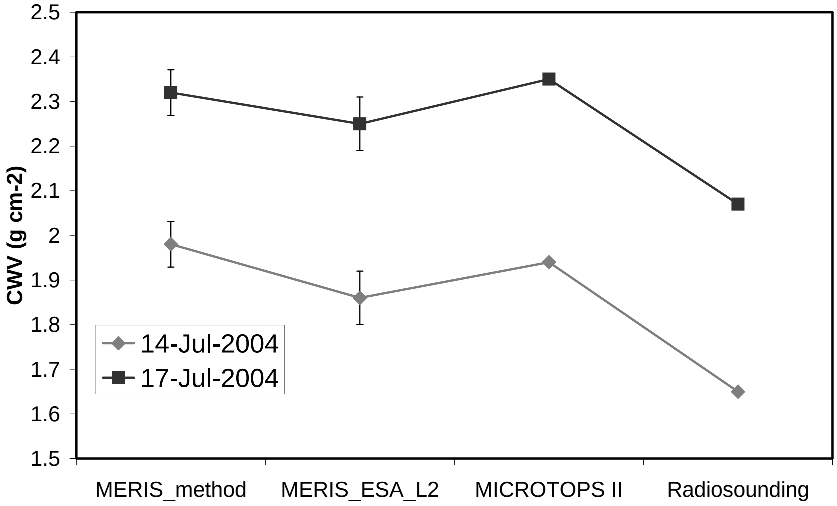

Figure 4.16: Simultaneous water vapor measurements by 4 different sources during 2 days in the 2004 SPARC campaign. Error bars show the CWV spatial variability in a 3 × 3 km window.

Again, AERONET measurements have been used as a reference to test the method against different atmospheric conditions over the Earth. The intercomparison between the CWV derived from MERIS RR with that from AERONET data is resumed in Fig. 4.17, as it was done for AOT in Fig. 4.9. Vertical error bars account for the 4% associated to CWV retrievals after the sensitivity analysis. A good correlation between MERIS and AERONET data is found in general, with slopes and R^2 close to 1 and RMSE around 0.2 g·cm^{-2}, although a small overestimation of 0.1-0.2 g·cm^{-2} is detected in most of the cases. However, the goodness of the comparison shows to be dependent on the AERONET site, as either very good or quite bad correlations are obtained in certain sites without a clear justification. In fact, the two extreme cases are Avignon and Carpentras, which are spatially separated by only tens of kilometers. In the first station, CWV retrieved from MERIS images matches very well AERONET measurements, with $R^2 = 0.973$, slope of 0.955 and RMSE of 0.14 g·cm^{-2} being calculated by a linear regression. However, this values are very different when MERIS results are compared with the data from the Carpentras station, where the regression results are $R^2 = 0.746$, slope of 0.754 and RMSE of 0.38 g·cm^{-2}. It is difficult to associate that bad comparison in Carpentras to the CWV retrieval technique, as there is not any a priori assumption on the target nature, as long as it is a land surface (not cloud or water body). I.e., there is not any reason to predict that the method will work well in Avignon and not in Carpentras. Thus, errors calculated from the comparison with the Carpentras station could be somehow related to the Carpentras station itself and the processing technique leading to the precipitable water vapor product, which are unknown. Moreover, the τ_{550} derived from MERIS data over Carpentras was well correlated with the station measurements (Fig. 4.9(d)), what leads to discard radiometric problems to a large extent. The same can be applied on the contrary: very poor correlations were obtained from the comparison of MERIS-derived τ_{550} with the data available in El Arenosillo station, while CWV retrievals from the same sources are highly correlated ($R^2 = 0.976$, slope of 0.948 and RMSE of 0.18 g·cm^{-2}). Therefore, errors in τ_{550} over El Arenosillo can be associated to atmospheric processes not considered in the method designed for MERIS rather than to problems in the AERONET measurements. The models for the conversion from the AERONET-measured radiance to AOT is the third possible factor.

Comparison between SCAPE-M retrievals and some other AERONET sites is depicted in Fig. 4.18. AERONET stations from Northern Europe, Brazil and Southern Europe are utilized. Except for the three points from the Dunkerque station, where SCAPE-M gives lower CWV values, AERONET and MERIS retrievals are very consistent, and the comparisons are even somewhat better than at the sites in Fig. 4.17, as smaller positive biases are observed. The applicability of the method to high CWV contents is stated in Fig. 4.18(b), where MERIS retrievals are compared with ground-based measurements in the Amazon jungle. The high water vapor contents expected in tropical atmospheres are well retrieved by SCAPE-M ($R^2 = 0.956$, slope of 1.114 and RMSE of 0.22 g·cm^{-2}). It must be reminded that 5 g·cm^{-2} is the maximum CWV tabulated in the LUT, so SCAPE-M can not deal with higher values.

Further analysis making use of the same data is performed by plotting SCAPE-M retrievals against the ESA Level2 water vapor product for 200×200 pixels subsets extracted from several MERIS images. Subsets were selected so that a variety of water vapor amounts, from dry to wet conditions, and topographic conditions, with flat or rough terrain at different elevation ASL, are considered. Four representative cases are shown in Fig. 4.19. The information on the terrain elevation and roughness is indicated in the plots by means of the elevation mean value and its standard deviation, respectively. The 200×200 CWV

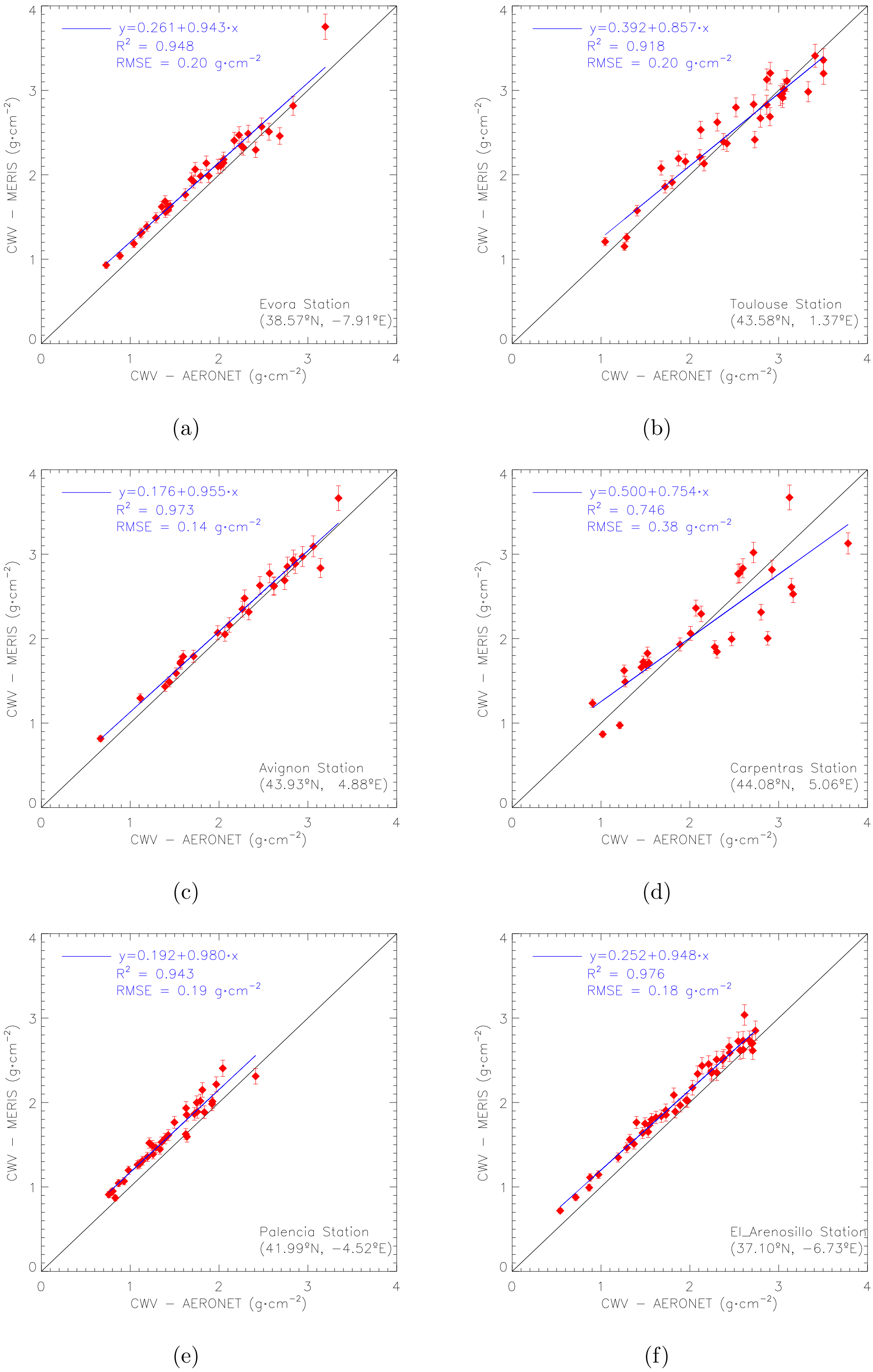

(a) (b) (c) (d) (e) (f)

Figure 4.17: Comparison of MERIS-derived CWV with AERONET data.

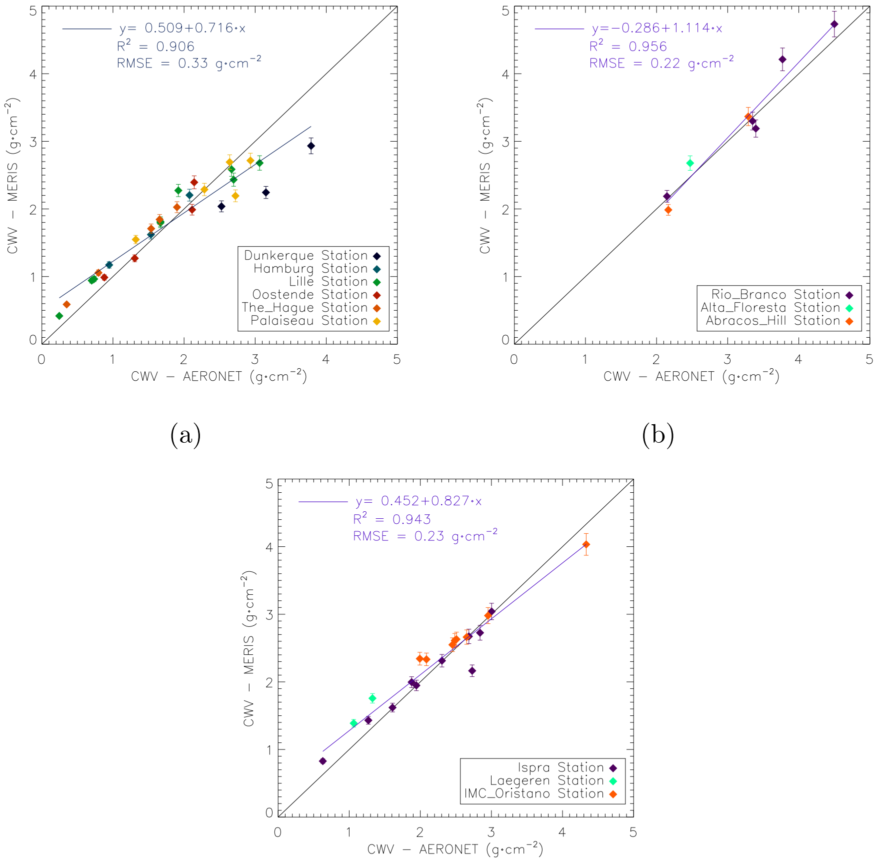

(a)

(b)

(c)

Figure 4.18: Comparison of MERIS-derived estimates of CWV with AERONET data from several stations in Northern Europe, Brazil and Southern Europe.

points are classified into bins representing the entire CWV variation range at a 0.02 g·cm^{-2} resolution. The color of the points informs about the number of occurrences in a given bin, growing from blue to red.

It can be stated that both the mean CWV in the area and the surface elevation have an impact on the correlation between the two methods, but it has not been possible to derive a universal functional dependence from all the analyzed subsets. The general rule is that SCAPE-M overestimates with respect to the ESA product when the surface elevation is medium-high (above 300-400 m ASL), while the tendency is on the contrary for lower elevations. The influence of the surface elevation on CWV retrievals for the two methods is illustrated in Fig. 4.20. The data come from a horizontal transect extracted from a RR MERIS image acquired on 13 June 2003. High variability in CWV was measured that day within the imaged area. The profiles were sorted out in order of increasing elevation, and smoothed in order to remove the high frequency component, which is mostly due to the water vapor horizontal evolution. The two curves cross each other for an elevation

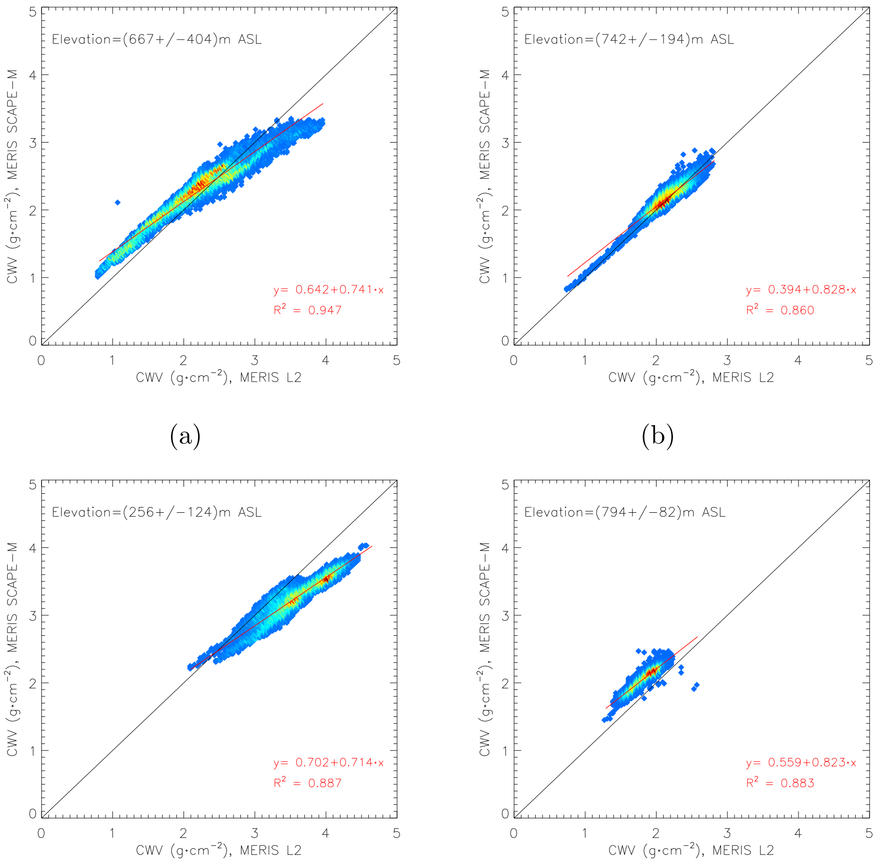

(a) (b)

(c) (d)

Figure 4.19: Comparison of the ESA Level2 water vapor product and SCAPE-M retrievals, for 4 different combinations of surface conditions and mean CWV content.

around 400 m. This trend is repeated in most of the cases, although the reference elevation at which CWV/elevation lines cross has been found to depend also on the mean CWV content in the area. The separation between the two curves also varies from one scene to the other.

Most of those conclusions are confirmed by the visual comparison displayed in Fig. 4.21. The CWV map derived by SCAPE-M (Fig. 4.21(a)) from the same MERIS RR image acquired on 13 June 2003 is compared with that from the ESA Level2 water vapor product (Fig. 4.21(b)). The topographic influence on CWV retrievals is illustrated by comparing with the DEM of the same area in Fig. 4.21(c). Only pixels in which both methods provide a CWV value are displayed. Thus, CWV retrievals over water bodies are masked out, as they are provided by the ESA product but not by SCAPE-M, which is restricted to land targets. The main conclusion to be remarked is that both maps show similar water vapor distributions. However, some slight deviations are found in some areas. These mostly correspond to surfaces with extreme elevation values, either nearly at sea level or above

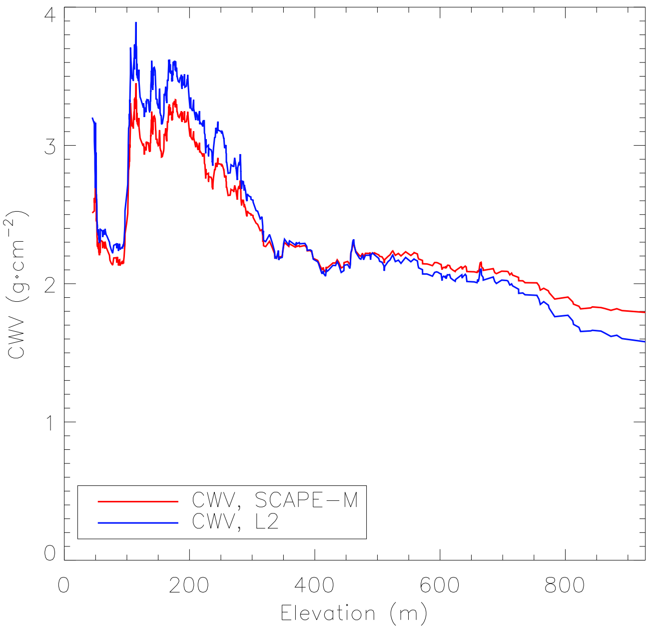

Figure 4.20: Water vapor content from ESA and SCAPE-M plotted as a function of the surface elevation.

1500 m. In the first case, the ESA product calculates larger CWV values than SCAPE-M (see the left hand side of the image), while it happens on the contrary for the most elevated targets (although this is less visible in the displayed image). Thus, the different response to elevation changes by the two methods illustrated in Fig. 4.20 is also detected in Fig. 4.21.

This trend is clearly reflected in Fig. 4.19(a). The large standard deviation of 404 m indicates that important topographic variations were present in the area contained in that subset, which is located at 667 m ASL on average. Thus, a wide range of surface elevation conditions were covered. The resulting scatter plot shows that most of the points are over the 1:1 line, which means that SCAPE-M overestimates, but that there are also an important proportion of pixels in which the CWV calculated by SCAPE-M is lower than that of the ESA product. It has been checked that the latter ones correspond to the pixels with the lowest elevation. That behavior is confirmed in Fig. 4.19(c) and Fig. 4.19(d), where SCAPE-derived CWV under- or overestimates the one from the ESA product, respectively, depending on the mean surface elevation. However, some exceptions to this dependence have also been detected. Fig. 4.19(b) corresponds to a situation in which both the mean water vapor content and the surface elevation are relatively similar to those in Fig. 4.19(d). The expected CWV overestimation is not found, but an almost perfect matching is achieved. The reason for this high correlation is not clear. Perhaps other external factors, such as the aerosol loading, the illumination or acquisition angles or topographic effects may explain that differences between the two cases. The impact of unbalanced AOT or surface slope

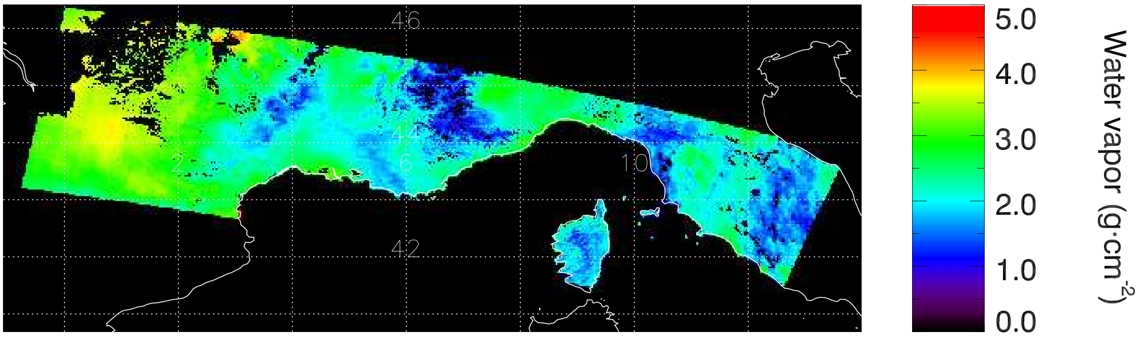

(a) SCAPE-M

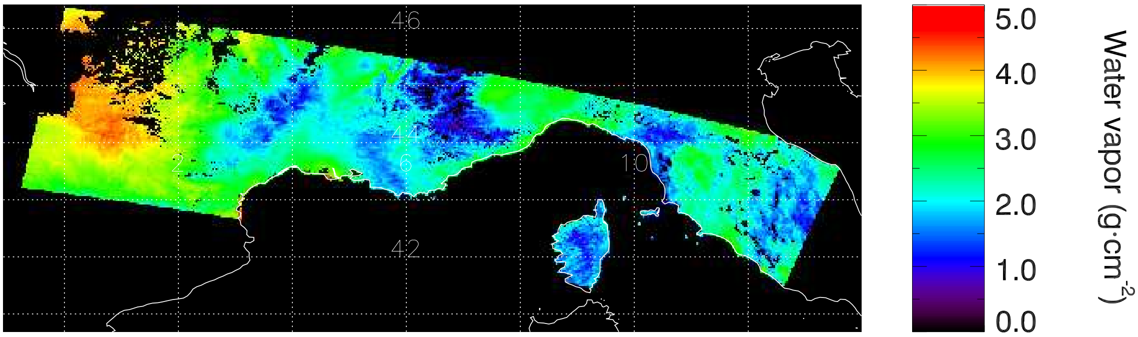

(b) ESA Level2

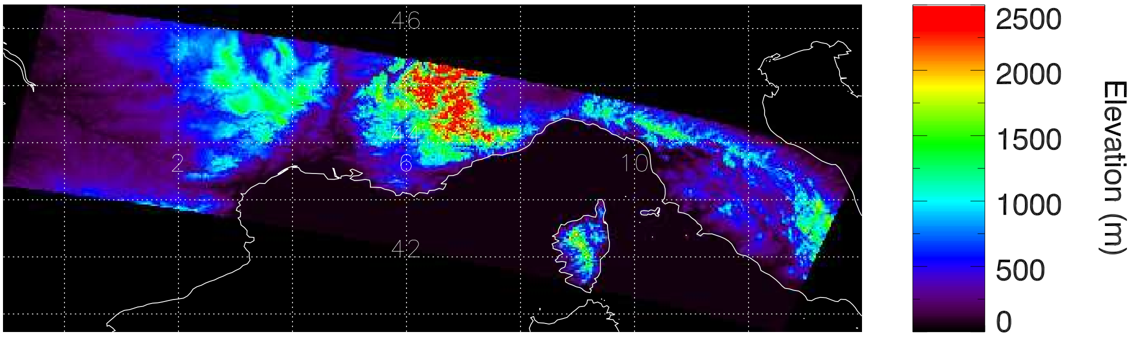

(c) DEM

Figure 4.21: Comparison of the CWV maps derived by SCAPE-M (a) and the ESA Level2 water vapor product (b) with the GETASSE30 DEM at the same resolution and projection (c). A MERIS RR image acquired on 13 June 2003 is used as input.

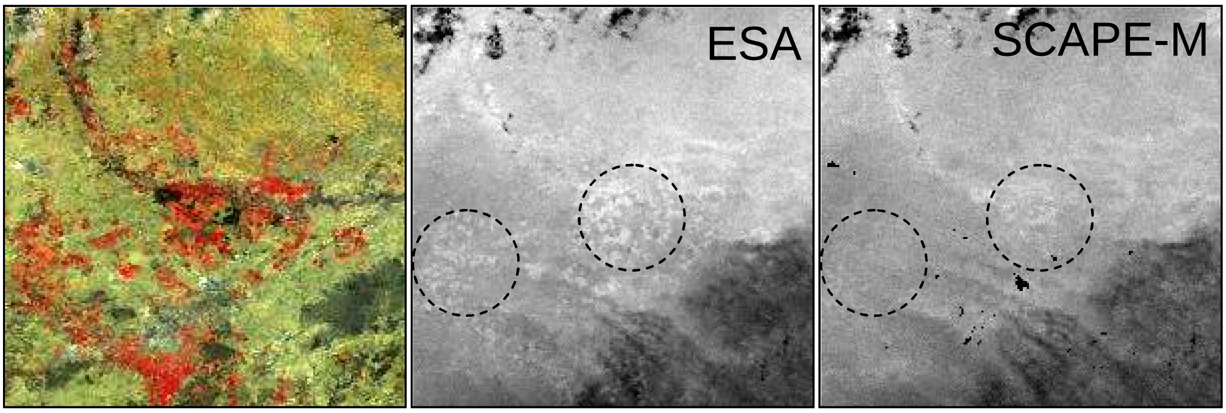

Figure 4.22: False color composite (left) and water vapor subsets (center and right) extracted over the Barrax site from the maps provided by ESA and SCAPE-M. Dashed circles point out areas where residual effects of the surface reflectance are noticeable. Images correspond to a $15{\times}15$ km^2 area, extracted from a MERIS FR image centered at 39.3°N, 2.4°W acquired over the Iberian Peninsula last 14 July 2004.

on CWV retrievals was quantitatively estimated in Section 3.3. Those factors are not considered by the ESA CWV retrieval algorithm, what may lead to errors under certain conditions. In any case, it must be remarked that a positive bias was found when SCAPE-M CWV retrievals were compared to some AERONET measurements in Fig. 4.17. In particular, 5 of the 6 stations are below 300 m ASL, the Palencia station being the only which is located at a considerable altitude (750 m). If the overestimation of the ESA product with respect to SCAPE-M retrievals that has been shown in Fig. 4.19 and Fig. 4.20 holds, the ESA product would give CWV substantially higher than AERONET sites.

Apart from this assessment of the mean water vapor content, the robustness of CWV retrievals against the surface reflectance pattern is checked. Because of the turbulent dynamics of water vapor in the lower atmospheric layers, water vapor maps should not show a dependence on the type of surface which is underneath those layers. The water vapor map derived from a MERIS FR image acquired on 14 July 2004 by means of SCAPE-M is compared to the equivalent ESA water vapor product. Windows of 200 × 200 pixels extracted from SCAPE-M and ESA water vapor maps are displayed in Fig. 4.22. A false color composite is also displayed for visual comparison. The mean water vapor content is around 2 g·cm^{-2}. Areas showing residual errors due to an unbalanced surface contribution are pointed out by dashed circles. In this case SCAPE-M seems to have a better performance than the ESA algorithm, as the effects of the surface are less apparent. It must be reminded that the sensitivity of CWV retrievals to the spectral reflectance slope in NIR wavelengths was not presented in the sensitivity analysis in Section 3.3, as that contribution was found to be negligible against other factors. The existence of a residual contribution from surface reflectance to SCAPE-M water vapor maps can be partially explained by the fact that the Barrax region is a very flat area with large spectral contrast in the targets, from cultivated fields to dry bare soils. Those are possibly the worst conditions for the removal of the surface influence from the derived maps.

Examples of CWV maps derived by SCAPE-M are displayed in Fig. 4.23, for the same MERIS images than those in Fig. 4.14. Wet and dry atmospheric conditions are detected from MERIS FR and RR images acquired all over the world. Two observations can be made from the maps. The first one is the sensitivity of CWV retrievals to the smile effect associated to MERIS measurements. Camera transitions are visible in most of the maps. This situation worsens as CWV increase, as it was analyzed in Fig. 3.25. The dependence of the error in CWV caused by the smile effect in the sensor with the total water vapor content is confirmed in Fig. 4.23(d). Note that the CWV range in the color scale has been increased in that image. Water vapor steps around 0.2 $g{\cdot}cm^{-2}$ are found between the two sides of a camera transition. The correction of this effect is very difficult from the technical point of view, and it would lead to unaffordable computation times, so it has not been considered.

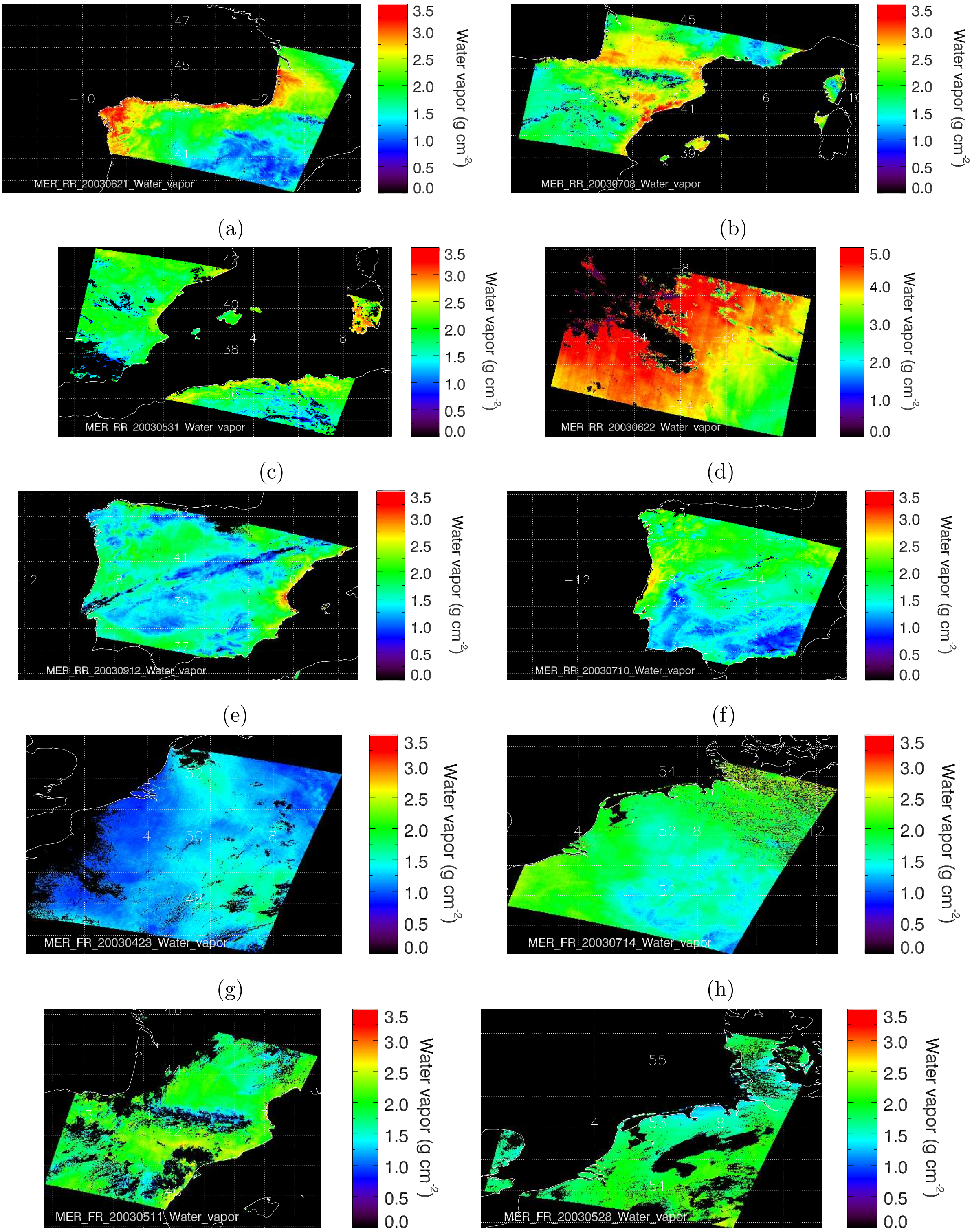

(a) (b) (c) (d) (e) (f) (g) (h) (i) (j)

Figure 4.23: Sample CWV maps derived from MERIS FR/RR images.

4.4. Results from Surface Reflectance Retrieval

The validation of atmospherically corrected images is conditioned by the availability of reliable ground truth. In the case of MERIS, the spatial resolution of 300 m or 1000 m causes the direct comparison with *in situ* reflectance measurements to be hardly representative of MERIS measurements. Therefore, as long as a robust physical model is applied to the conversion from TOA radiance to surface reflectance, much of the validation of the final reflectance product must rely on the validation of the intermediate atmospheric products. Thus, the accuracy in the MERIS surface reflectance images derived by SCAPE-M is supported by the comparison of AOT and water vapor retrievals with reference ground-based measurements, as well as with a proper model able to deal with contributions such as the topographic factor or the adjacency effect. Neglecting the directional effects in the target reflectance is considered the only deficiency in the signal modelling. The reasons for the assumption of a Lambertian target were already discussed in Section 3.

Nevertheless, reflectance images derived by SCAPE-M have been compared to independent sources in order to detect possible errors up to a first-order approximation. In particular, a MERIS FR image processed by SCAPE-M which was acquired over the Barrax study site on 14 July 2003 during the SPARC experiment has been compared to a CHRIS-PROBA image acquired on the same date. The coupled CHRIS-PROBA system [Barnsley et al., 2004], launched on 22th October 2001, provides high spatial resolution hyperspectral/multiangular data. CHRIS measures over the VNIR bands from 400 nm to 1050 nm, with a minimum spectral sampling interval ranging between 1.25 (@400 nm) and 11 nm (@1000 nm). It can operate in different modes, reflecting a necessary compromise between spatial resolution and the number of spectral channels, caused by limits to on–board storage. The data presented in this work were acquired using operation Mode–1, with 62 spectral bands at a spatial resolution of 34 m, and an approximate swath of 15 km. The PROBA platform provides pointing in both across–track and along–track directions. In this way, the CHRIS-PROBA system has multiangular capabilities, acquiring up to 5 consecutive images from 5 different view angles in the same satellite overpass. CHRIS-PROBA data were processed following the procedure described in Guanter et al. [2005a,b]. In short, CHRIS images were firstly cleaned from drop-outs and vertical striping. Single values of AOT and CWV were retrieved as representative of the 15 km side area registered by CHRIS. The final surface reflectance images were retrieved by correcting the reflectance errors related to wrong CHRIS' gain coefficients, especially at the NIR observation channels. For a better comparison with MERIS data, the CHRIS-PROBA image acquired from the smallest VZA (around 27°) is used in this study. The Red-Green-Blue (RGB) composition generated from the CHRIS image is displayed in Fig. 4.24(a). A subset of 400 × 400 pixels extracted from the corresponding MERIS FR image is depicted in Fig. 4.24(b). The red box in Fig. 4.24(b) marks the approximate region covered by the CHRIS image.

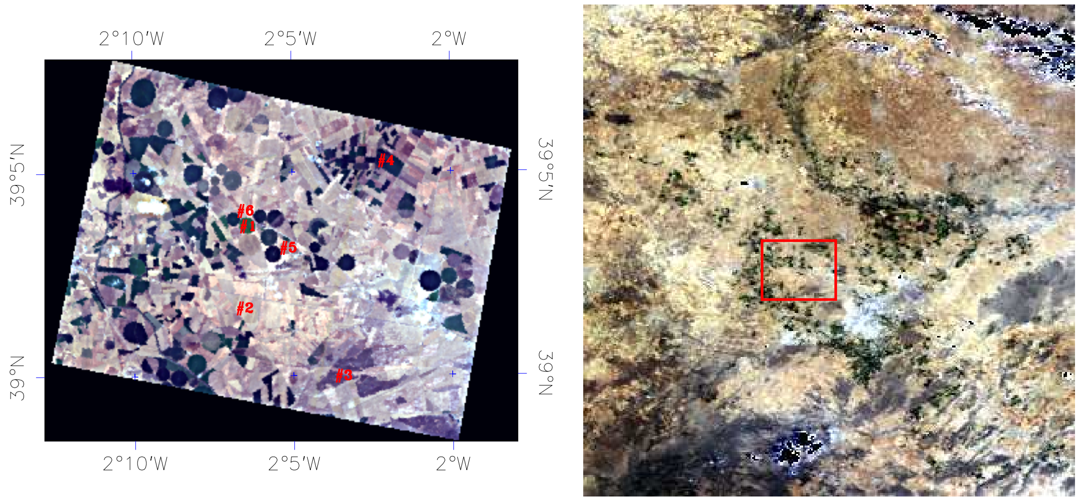

(a) CHRIS-PROBA (b) MERIS

Figure 4.24: CHRIS-PROBA and MERIS images acquired over the Barrax study site on 14 July 2003. The numbers in (a) point out the targets that have been superposed to MERIS data, and the red box in (a) mark the approximate area covered by CHRIS.

Some reflectance spectra have been manually extracted from the CHRIS image to compare with MERIS-derived reflectance spectra. A more systematic analysis based on the degradation of the CHRIS-PROBA image up to 300 m per pixel and the co-registration with the MERIS image was considered at first, but it was discarded afterwards because errors in resampling and geometric correction were not negligible against those associated to the atmospheric correction itself, especially at the scale of heterogeneity of the Barrax study site. The use of the freely available Moderate Resolution Imaging Spectroradiometer (MODIS) [Justice et al., 1998] catalogue, which was employed by other authors for atmospheric correction validation purposes [Grey et al., 2006], was not considered for the same reason.

The numbers in Fig. 4.24(a) point out the targets where those spectra have been extracted from. Representative targets of vegetation and bare soil pixels have been chosen. The purest pixels have been selected in the case of MERIS, in order to reduce sub-pixel effects. Six sample reflectance spectra are plotted in Fig. 4.25. The reflectance data from the CHRIS-PROBA image was validated by cross-checking against *in situ* measurements carried out by an Analytical Spectral Devices (ASD) FieldSpect Pro FR Spectroradiometer (footprint around 0.8 m, 2 nm of spectral resolution) simultaneously to CHRIS acquisitions [Guanter et al., 2005b]. CHRIS spectra are calculated as the mean value of all the pixels inside a 300 × 300 m window simulating a MERIS FR pixel, and the error bars correspond to the standard deviation in that window. The error bars around MERIS spectra come from the 8% relative error in reflectance which was estimated for SCAPE-M retrievals in Section 3.3. Despite the very different spatial resolution in both sensors, as well as different illumination and observation geometrical configurations, a good matching between MERIS and CHRIS surface reflectance spectra is found overall. It can be noted that pure green vegetation pixels can be still found despite the 300 m resolution in MERIS, partly thanks to the width and homogeneity of the Barrax crops. In particular, the spectrum labelled by #1 corresponds to a potato crop. The high reflectance levels in the NIR, as well as the sharp peak around the green region, are associated to extreme values of the Leaf Area Index (LAI) around 6 which were measured during the campaign. The spectra in #6 are from a alfalfa crop. The low reflectance values in #3 represent a forest canopy, #2 is a bare soil target, and #5 a senescent wheat crop. The target in #4 is from an unclassified vegetation target. It is confirmed that MERIS spectra are mostly within the reflectance range marked by the error bars in the CHRIS spectra, accounting for the uniformity of the target. It must also be remarked that worse correlations would be found in some other targets, which are assumed to be strongly driven by the surface heterogeneity. In any case, the existence of pixels were a high correlation is found somehow reinforces the validity of the SCAPE-M retrievals.

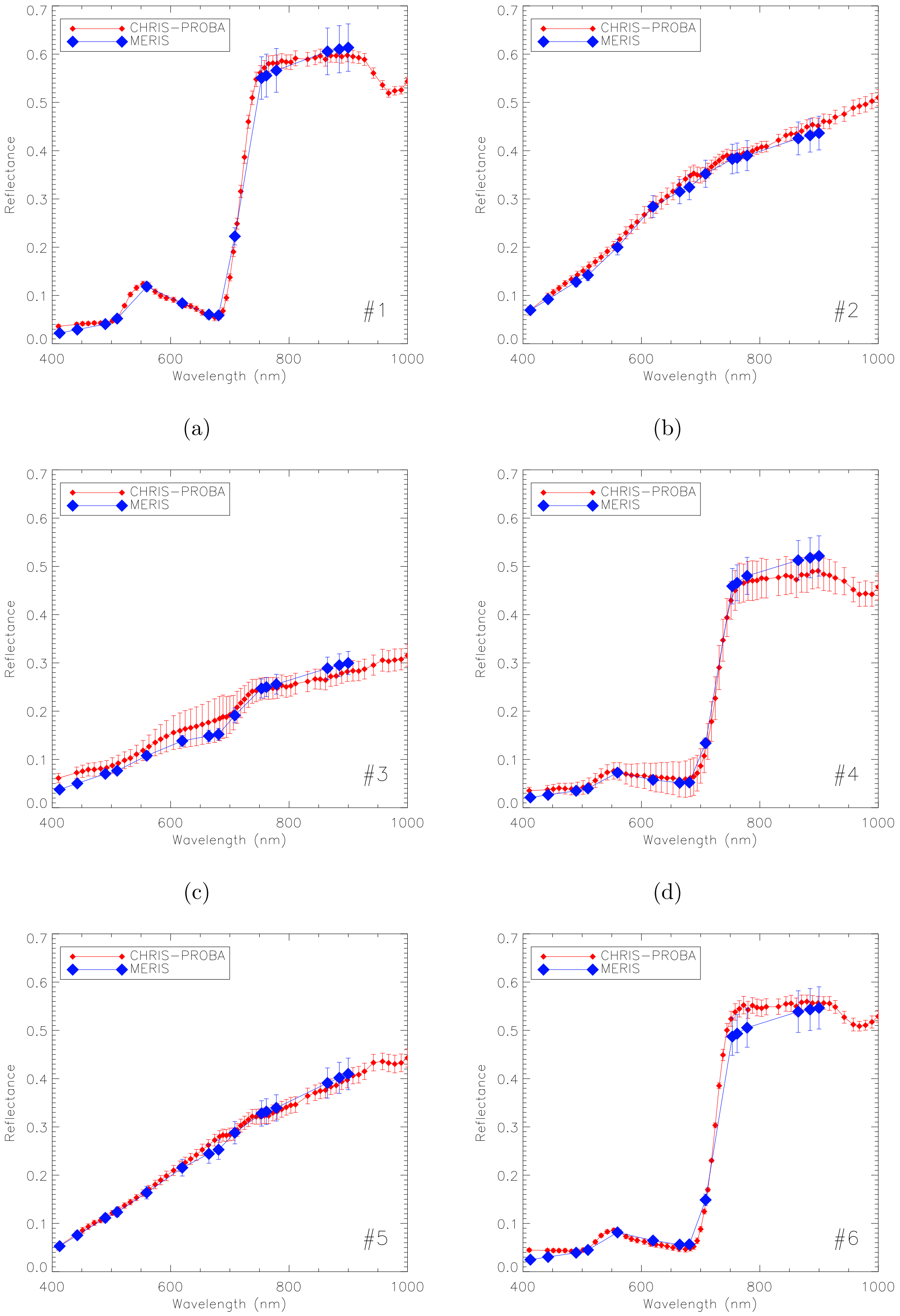

(a) (b)

(c) (d)

(e) (f)

Figure 4.25: Comparison of CHRIS-PROBA and MERIS derived surface reflectance spectra extracted from the targets marked in Fig. 4.24(a).

A comparison with the ESA surface reflectance product has also been performed, in a similar way than it was done with AOT and CWV retrievals. The surface reflectance map derived by the BAER algorithm after processing the MERIS FR image acquired over Barrax on 14 July 2003 is compared to the equivalent map as derived by SCAPE-M. The RGB composites generated from the outputs of the two methods are displayed in Fig. 4.26. It can be observed that the proportion of pixels where the correction failed is much larger in the case of BAER. This is due to BAER only calculates surface reflectance in those pixels in which a successful aerosol retrieval was achieved. As AOT estimation is only performed over those surface were a certain proportion of green vegetation is detected, large areas in the image, mostly consisting of dry bare soils and senescent vegetation, are not processed. This explains the black regions all over the image in the BAER output. On the other hand, the interpolation and smoothing of the atmospheric retrievals which is carried out by the SCAPE-M method enables to obtain continuous surface reflectance image, with only cloudy pixels and water bodies being masked out.

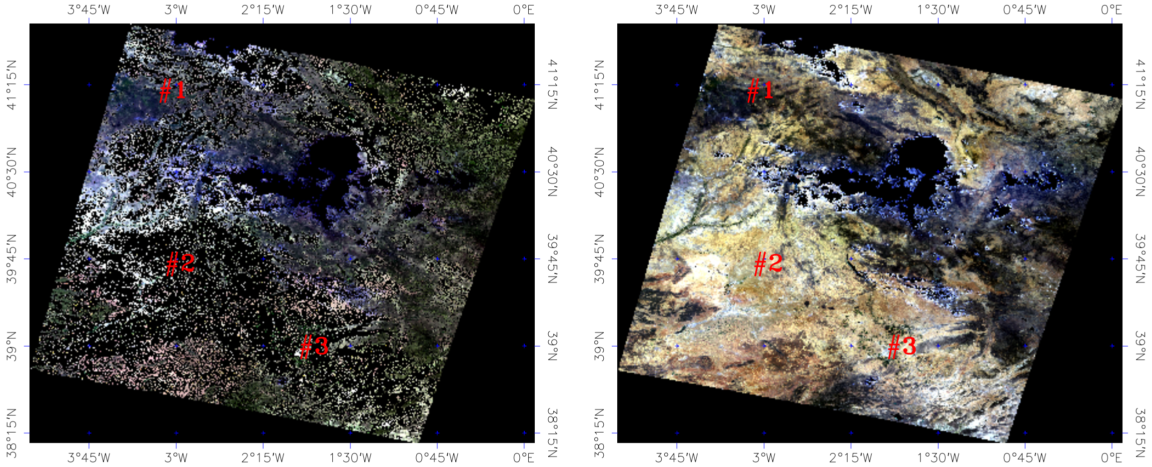

(a) BAER

(b) SCAPE-M

Figure 4.26: Surface reflectance maps derived by the BAER and SCAPE-M methods from the MERIS FR image acquired on 14 July 2003 over the Barrax area. Red labels mark the areas used in the quantitative comparison of the two methods.

For a quantitative analysis of the surface reflectance values retrieved by the two methods, subsets of 400 × 400 pixels centered at the labels in Fig. 4.26 are extracted. The scatter plots for the three areas and three spectral channels are presented in Fig. 4.27. Only those pixels where both BAER and SCAPE-M provided a surface reflectance value are plotted. The scatter plots are built by classifying all the reflectance values into 0.005-width bins. Colors range from blue for the less populated categories to the red for the one with the highest number of occurrences. It can be stated that the correlation between BAER and SCAPE-

M retrievals is nearly independent on the area, as the point distribution patterns and the numbers characterizing the linearity of the comparison are repeated for the three regions #1, #2 and #3. However, those correlations are strongly influenced by the spectral band. Low correlations are found in the case of the blue channel, while they become higher as the observation wavelength is increased. In the case of band 1, the categories with the largest number of pixels are located close to the 1:1 line, although there is a high proportion of categories showing a low correlation. This leads to R^2 being of the order of 0.7, with slopes higher than 1.5 and negative biases. The low reflectance values around 0.03 are caused by the fact that AOT retrievals in BAER are only calculated over vegetated areas, whose reflectance in the visible wavelengths is very low. In the case of the red band centered around 681 nm, the linear correlation is very high in the three regions, with R^2 higher than 0.97, slopes around 1 and small positive biases around 0.01. The mean reflectance value is around 0.1, which is also characteristic of pixels with a major contribution of green vegetation. Those results improve slightly in the band 12, as the R^2 coefficient and the slope of the fit are again close to 1, but the bias around 0.01 is relatively smaller than in the red band due to the larger reflectance values. This dependence on the wavelength may be explained by the impact of residual errors in the atmospheric correction in dark targets: a bad characterization of the atmospheric state, which can be associated to errors in aerosol or water vapor retrieval, to neglecting elevation or topographic effects or even to adjacency or directional effects, may lead to noticeable errors in the subsequent surface reflectance when these ones are relatively low. The same conclusion was reached in the sensitivity analysis after checking Fig. 3.29. Some of the factors listed above are considered by the SCAPE-M model, but not by BAER. Moreover, the τ_{550} mean value calculated from the maps derived jointly to the surface reflectance images are 0.35 for SCAPE-M and 0.45 for BAER, which also contributes to explain the overestimation in the surface reflectance derive by SCAPE-M respecting to BAER.

A final test of SCAPE-M atmospheric correction is carried out by analyzing surface reflectance of water bodies. It was discussed in Section 3.1 that the retrieval of AOT is performed using land pixels as a basis, but the estimated aerosol loading in the 30×30 km^2 cells could be applied for the processing of inland and coastal waters inside those cells. The CWV is retrieved on a per-pixel basis over land pixels, so a default value of 2 g·cm^{-2} is applied over water targets. Results obtained from the processing of a FR image acquired on 2 June 2004 over the Rosarito study site (Iberian Peninsula, 40°06'06"N, 5°16'47"W) are presented in Fig. 4.28. The Rosarito site is one of the core sites in the calibration and validation activities of the CHRIS-PROBA mission over inland water surfaces. One spectrum from a green vegetation target and three from water targets are displayed in Fig. 4.28. The spectral patterns in the water spectra are consistent with the expected patterns in water targets. The peaks at the green (water pigments absorption) and far-red (particulate matter scattering) spectral regions vary from one spectrum to the other.

Ground-based measurements are used again for the assessment of the retrieved reflectance. Since less variability is expected in water bodies than in land surfaces, a direct comparison of *in-situ* reflectance measurements with MERIS-derived spectra is performed. A field campaign directed by the Centro de Estudios y Experimentación de Obras Públicas (CEDEX) on 19 June 2003 collected reflectance spectra from several reservoirs at the North-West side of the Iberian Peninsula. A cloud-free MERIS FR image was acquired that day. The comparison of MERIS-derived reflectance spectra with ground-based measurements over the Tremp (“TR”, 42.19ºN, 0.93ºE), Terradets (“TD”, 40.07ºN, 0.89ºE), Rialb (“RL”, 41.96ºN, 1.20ºE) and Caselles (“CA”, 42.00ºN, 0.62ºE) is displayed in Fig. 4.29. A general good correlation is found from the comparison, despite the different spatial and temporal resolution of the two data sources: MERIS-derived spectra are extracted from the center of the reservoir and not from the exact position where the ground measurement was taken, in order to reduce the most sub-pixel effects caused by land surfaces in the surroundings. Moreover, MERIS acquisition was at 10:20 a.m., while field measurements were taken in a wide time range from 8:55 a.m. to 4:10 p.m. In any case, both the spectral shape and the average brightness are reliable enough for the application of algorithms for the retrieval of water features from satellite data, which is the final objective of this work.

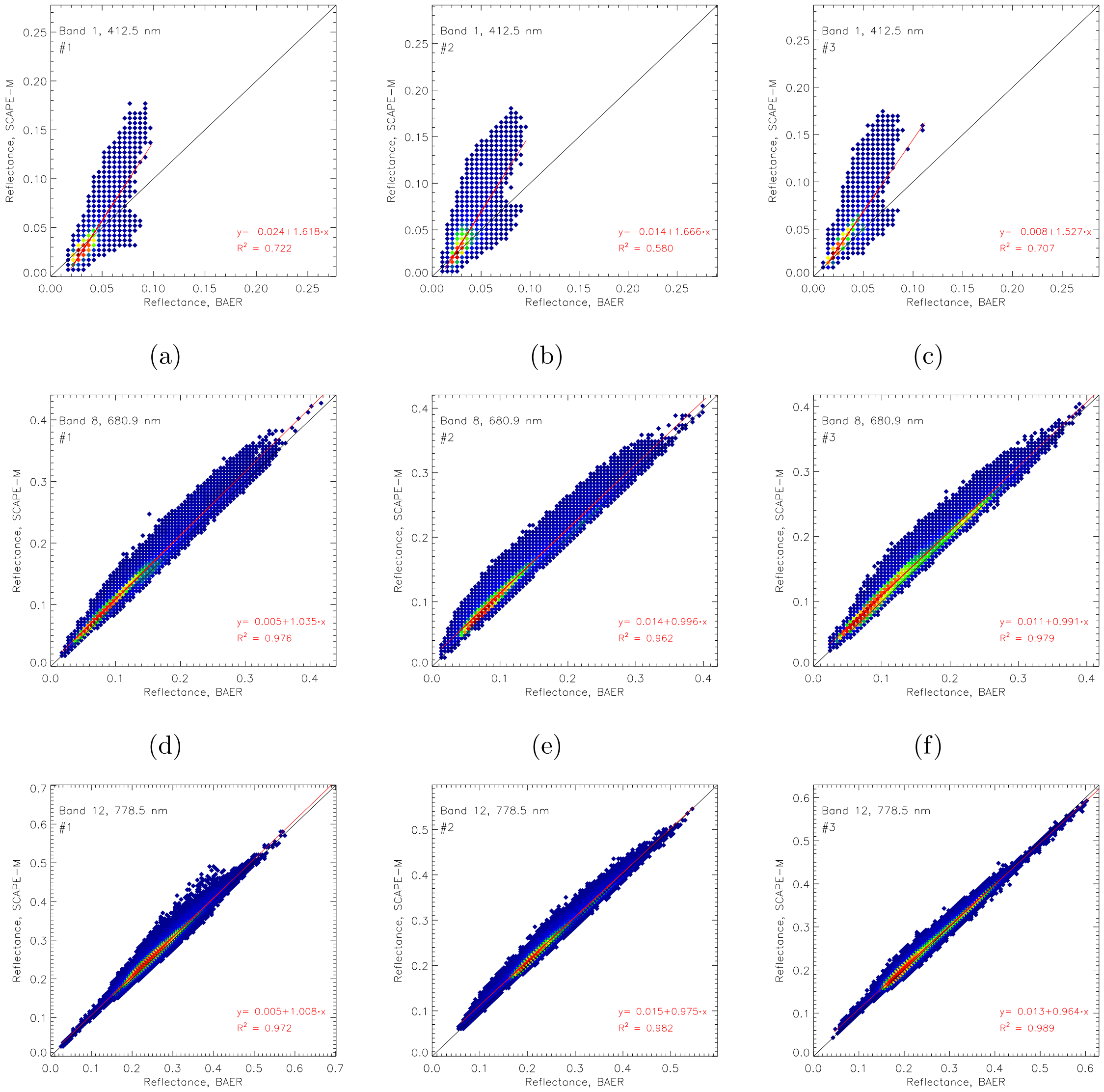

(a) (b) (c)

(d) (e) (f)

(g) (h) (i)

Figure 4.27: Comparison of the BAER surface reflectance product and SCAPE-M retrievals, for the three areas marked in Fig. 4.26 and three MERIS bands.

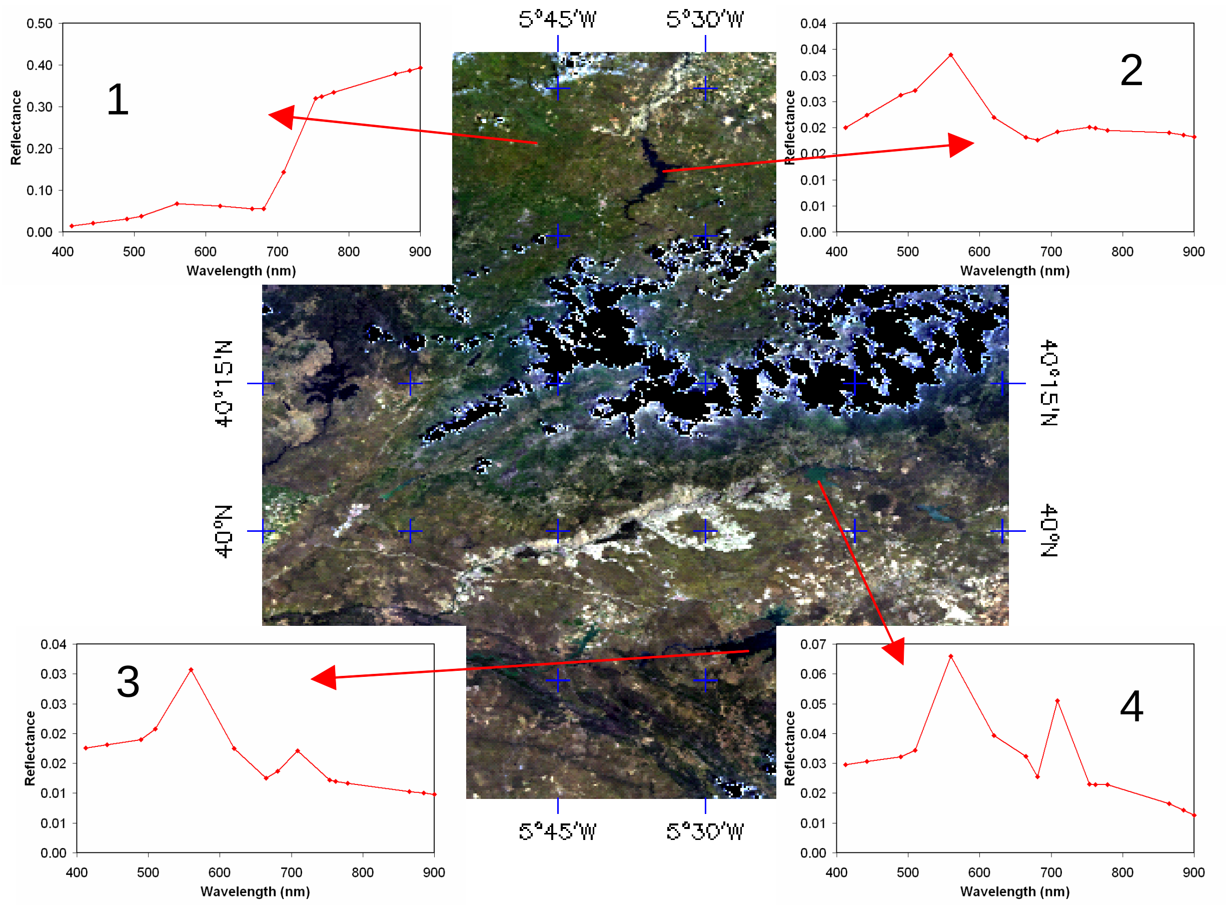

Figure 4.28: Sample vegetation (1) and inland water (2-4) reflectance spectra derived from a MERIS FR image acquired on 2 June 2004 over the Rosarito site (40°06'06"N, 5°16'47"W).

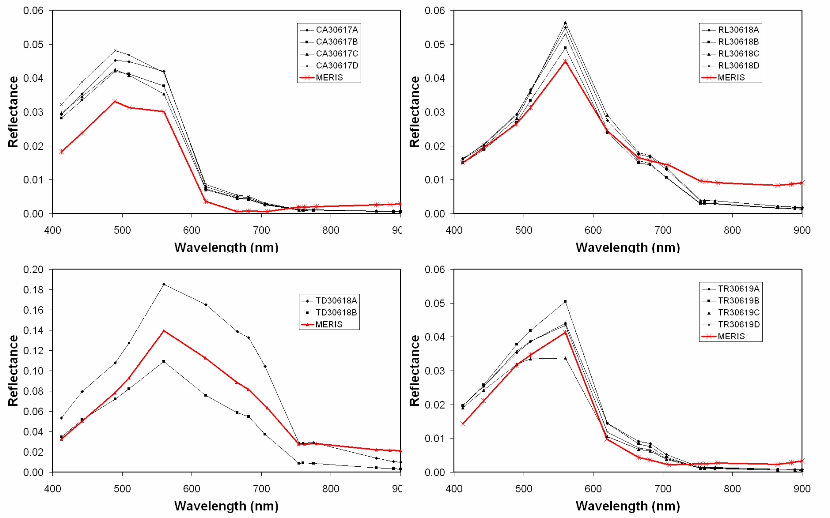

Figure 4.29: Comparison of MERIS-derived water reflectance spectra with ground-based measurements over North-West Iberian Peninsula on 19 June 2003.

Chapter 5

Application: Estimation of Chlorophyll Fluorescence from MERIS data

A weak electromagnetic signal is emitted by vegetation chlorophyll under excitation by solar radiation. This emission, known as solar-induced chlorophyll fluorescence, occurs in the red and far-red spectral regions (namely, from 650 to 800 nm). The low intensity of this signal with respect to the reflected solar radiation makes the decoupling of the two contributions from the measured at-sensor radiance a challenging problem. A widely used approach for the estimation of chlorophyll fluorescence from remote measurements is the Fraunhofer Line Discriminator principle. It consists in measuring the upwelling radiation inside absorption bands, where the solar radiation is partly extinguished so that the fluorescence contribution is enhanced. As a consequence, the fluorescence signal acts in-filling the superposed absorption bands. However, apart from the fluorescence signal there are other factors affecting the depth of the absorption bands, such as aerosols or surface elevation, that must be taken into account into the fluorescence retrieval scheme. In this framework, the fluorescence signal is included in the atmospheric radiative transfer scheme presented in this thesis, so that chlorophyll fluorescence and surface reflectance are retrieved consistently from the measured at-sensor radiance. This methodology is tested on MERIS imagery taking advantage of its good characterization of the atmospheric O_2-A absorption band, leading to the possibility of estimating chlorophyll fluorescence from a spaceborne sensor. Validation of those retrievals will be achieved by applying the method to data acquired by the airborne sensor CASI-1500 concurrently to MERIS acquisitions. The intercomparison between the fluorescence derived from the two types of remotely sensed data and with ground-based measurements shows a good consistency.

5.1. Remote Sensing of Chlorophyll Fluorescence

Vegetation photosynthesis is a key factor driving the different biochemical cycles and CO_2 exchanges occurring between biosphere and atmosphere. For this reason, the monitoring of vegetation state and biological activity is one of the major goals of remote sensing. This has traditionally relied on vegetation indices that characterize the amount and spatial distribution of vegetation [Baret and Guyot, 1991; Price, 1992; Tucker, 1979], although some effort has been devoted to design indices able to estimate potential levels of canopy photosynthesis and net primary productivity [Choudhury, 2001; Peñuelas and Filella, 1998; Verma et al., 1993]. However, most of the published vegetation indices fail to detect dynamic variations of photosynthesis rates, like those occurring during the day or under certain stress conditions, because they have no direct link to photosynthetic functioning beyond their sensitivity to canopy structure or pigment concentrations [Dobrowski et al., 2005; Evain et al., 2004].

Looking for a deeper view into vegetation biochemical processes, the Photochemical Reflectance Index (PRI) [Gamon et al., 1992] was intended for estimating changes in xanthophyll cycle pigments as they vary together with changes in photosynthetic light use efficiency (LUE), and it has been proved to be one of the few indices able to reproduce fast changes in the plant photosynthetic activity [Gamon et al., 1992, 1997; Nichol et al., 2002; Peñuelas et al., 1995, 1997; Trotter et al., 2002]. PRI takes advantage of the reflectance changes at 531 nm associated with the xanthophyll cycle and the related thylakoid energisation. It is derived from narrow band reflectance at 531 and 570 nm, as

$$\mathrm{PRI} = \frac{\rho_{531} - \rho_{570}}{\rho_{531} + \rho_{570}} \tag{5.1.1}$$

The reflectance at 570 nm partly corrects for the complicated changes in reflectance due to illumination angle, leaf orientation and canopy architecture. It can be directly calculated from reflectance measurements taken with the sufficient spectral resolution, and due to the good correlation with LUE, PRI is considered one of the most useful indices in the characterization of the plant photosynthetical activity in laboratory conditions. However, Barton and North [2001] demonstrated that PRI is very sensitive to factors such as canopy structure, LAI or Leaf Angle Distribution (LAD). Thus, the application of PRI to the vegetation monitoring from remote sensors must be carefully handled due to the PRI dependence on the factors described above. A prior estimation of LAI and LAD should be available before the analysis of the results, and some functional dependence on the illumination and observation geometries should also be calculated for each type of crop in order to normalize the angular dependence. Otherwise, the assessment of the vegetation photosynthetical activity the index is intended for may turn out to be masked out by other external factors. Similar difficulties in the application of PRI at spatial areas larger than the leaf were already pointed out by Peñuelas et al. [1997].

An alternative indicator of the actual plant physiological status is the solar induced chlorophyll fluorescence (CF). The CF signal has been widely reported to be directly linked to plant photosynthesis (e.g., Krause and Weis [1984]; Papageorgiou [1975]; Scheiber and Bilger [1987]), and the PRI index [Amorós-López et al., 2006; Dobrowski et al., 2005; Evain et al., 2004; Liu et al., 2005]. Chlorophyll is the photosynthetic pigment underlying the processes of primary production and it is probably the only constituent of the biosphere to fluoresce in the red and far-red, what makes red fluorescence (RF) and far-red fluorescence (FRF) a specific signature of vegetation. The emission of light as fluorescence is produced after absorption of light by a mechanism directly in competition with the photochemical conversion [Moya and Zerovic, 2004]. In addition to CF, the UV part of the solar spectrum induces a blue-green fluorescence emission (BGF) of vegetation that originates from various phenolic compounds. BGF has been found not to be directly linked to chlorophyll or to photosynthesis [Moya et al., 2003]. A schematic view of the process leading to RF/RFR and BGF emissions is displayed in Fig. 5.1: part of the electromagnetic radiation absorbed by the plant is re-emitted at longer wavelengths as a residual of energetic exchanges inside the leaf.

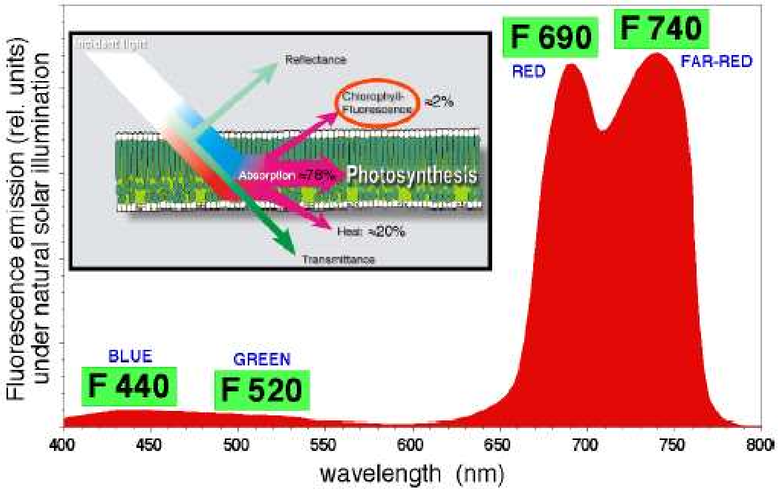

Figure 5.1: Schematic view of the process leading to vegetation fluorescence emission.

CF emission varies over time as a function of the plant photosynthetic activity [Kautzky and Hirsch, 1931]. This fact enables the monitoring of plant functioning, stress and vitality using passive remote sensing strategies. Even though the remote measurement of CF is still in very early stages of development, some advances have been published both for small (leaf) and large (canopy) spatial scales. The main problem for the detection of the CF signal is its low intensity when it is compared with the radiation reflected by the plants. Recent studies established CF in the 750 nm region to be about 2%, on average, of the plant reflectance in such spectral region [Campbell et al., 2002; Zarco-Tejada et al., 2003b]. Zarco-Tejada et al. [2000a,b] reported that CF can be detected by reflectance calculations and optical indices under both laboratory and natural conditions, but the Fraunhofer Line Discriminator (FLD) principle is the most widely used in the detection of fluorescence [Amorós-López et al., 2006; Liu et al., 2005; Moya et al., 2004, 2003; Moya and Zerovic, 2004; Sioris et al., 2003]. The FLD principle is based on enhancing the emitted fluorescence signal against the reflected solar radiance by measuring inside the solar Fraunhofer or atmospheric absorption lines. The incoming solar radiation is obscured inside those lines, while the plant emission is not affected, so the ratio emitted-to-reflected radiation is increased. The fluorescence signal acts in-filling the Fraunhofer line, reducing the apparent depth with respect to a non-fluorescent target. This rationale can be extended to the absorption lines due to the molecular oxygen in the terrestrial atmosphere. In the case of a sensor located in a platform at a given altitude inside the atmosphere, or even at the TOA, both the solar radiation and the CF radiation would be significatively affected by the atmospheric absorption, but this would have a different impact on the two contributions, as the emitted radiation is only attenuated in the path from the target to the TOA, while the incoming solar radiation also interacts with the atmosphere in the downward path from the TOA to the target.

The solar Fraunhofer line Hα and the atmospheric oxygen lines A and B (centered at 760 and 687 nm, respectively), are quite pronounced on a high spectral resolution radiance spectrum, as shown in Fig. 5.2. A typical CF spectrum is also depicted. The three lines could be used for the estimation of CF by the FLD principle, as they largely overlap the emission spectrum. However, the O_2 absorption lines can characterize the CF emission better than Hα, as they are closer to the CF emission peaks. As it is discussed by Moya et al. [2004], the signal-to-noise ratio yield by each absorption band also depends on their depth and shape and on the plant reflectance, which is 5–10 times higher at 760 than at 656 or 687 nm for a typical green leaf. All these factors (absorption strength, reflectance response, proximity to emission peaks) are depicted in Fig. 5.2. It can be stated that the position of the O_2-B band is closer to a CF emission peak than the O_2-A one, but the absorption is around 70% lower than in the 760 nm line, which receives nearly 50% of the emitted radiation. The spectral response of vegetation target is nearly linear around the 760 nm region, while the curvature due to the proximity of the red-edge is usually noted around the 690 nm region. This linearity in the target reflectance response is an advantage for the proper modelling, which relies on linear interpolations. For these reasons, it is concluded that the O_2-A band offers the best conditions for the detection of chlorophyll fluorescence. Other fluorescence researchers working on the detection of CF at near-canopy levels have also focused their research on the 760 nm O_2 band [Amorós-López et al., 2006; Liu et al., 2005; Pérez-Priego et al., 2005].

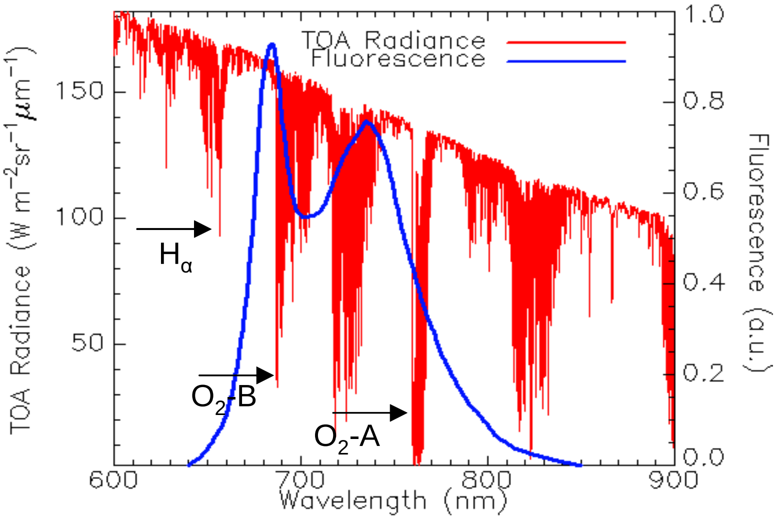

Figure 5.2: Superposed spectra of TOA radiance and chlorophyll fluorescence. The Fraunhofer line Hα and the atmospheric O_2-A and B lines are pointed out.

Although the feasibility of the detection of CF from space was already postulated more than 30 years ago [Plascyk, 1975], no decisive advances have been achieved in this field. At the airborne scales, Maier et al. [2002]; Zarco-Tejada et al. [2003a] found evidence of the CF detection in apparent reflectance derived from commercial hyperspectral airborne sensors based on the in-filling of fluorescence in the 760-nm atmospheric oxygen absorption band. A prototype called AIRFLEX, which is referenced in Moya et al. [2004] at earlier development states, was designed to measure solar-induced fluorescence at the 760 and 687 nm O_2 bands. This instrument was located at an airplane flying at more than 2000 m ASL during the SENtinel-2 and FLuorescence EXperiment (SEN2FLEX)[1] which was held during June and July 2005 in the Barrax study area. It involved different activities in support of initiatives related to fluorescence experiments for the modelling and detection of solar-induced fluorescence under natural conditions. After the first data processing, it was found that the signature of the vegetation is evident in the filling-in of the O_2 bands, as well as a good correlation between the CF signals at the two wavelengths.

Several modelling aspects must be taken into account when the fluorescence signal is to be detected by a sensor on board an airplane or a satellite, measuring inside the O_2 absorptions. Factors such as the illumination and observation angles, target elevation and orientation or atmospheric turbidity do have a crucial impact on the depth of absorption features. Therefore, any attempt of estimating CF from remote sensors should rely on a solid atmospheric/surface interaction model, where most of those issues are properly addressed.

---

[1] `http://www.uv.es/leo/sen2flex/`

The estimation of CF from MERIS data is presented in this chapter. The MERIS spectral configuration enables a good characterization of the O_2-A absorption feature. A high spectral resolution irradiance spectrum resampled to the MERIS reference band setting displayed in Fig. 5.3. The dotted box includes MERIS bands 10 (centered at 753.5 nm, bandwidth of 7.5 nm), 11 (centered at 761.6 nm, bandwidth of 3.75 nm) and 12. Bands 10 and 11 offer an optimal configuration as reference/measuring channel pair to be used by the FLD technique: the O_2-A absorption is well defined by band 11, centered around the bottom of the absorption feature (apart from intrinsic instrumental spectral shifts) with a small bandwidth of 3.75 nm, and band 10 is separated only by 7-8 nm, and it is nearly free from absorption. No other space-borne instrument presents such a good spectral resolution around the O_2 absorption at a spatial scale finer than the 300 m per pixel of MERIS FR mode. This size is a reasonable upper limit for the pixel dimensions to which the interpretation of the fluorescence signal is feasible, as pure vegetation targets can be detected. At coarser spatial resolutions, the appearance of non-fluorescent targets at the sub-pixel level would lead to weakening the fluorescence signal, so that the estimation of CF could become impossible. In addition to the spectral configuration, MERIS presents a reliable radiometric and spectral calibration after a number of specific calibration and validation activities. All these features make MERIS a unique instrument for the remote sensing of fluorescence from a satellite platform.

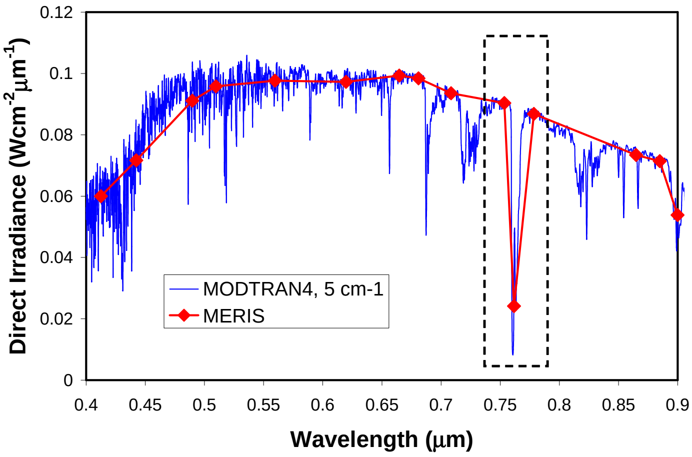

Figure 5.3: Direct irradiance spectrum at sea level calculated by MODTRAN4 and resampled to the MERIS reference spectral setting. The dotted box marks the O_2-A absorption feature.

In this framework, the design of a method for the estimation of CF from MERIS data fits perfectly into the contents covered by this thesis. In this methodology, the fluorescence signal is added to the radiative transfer equation as an extra source function, what enables the quantification of CF in physical units (i.e., radiance). All the considerations made for the retrieval of surface reflectance from the TOA radiance images acquired by MERIS (estimation of the atmospheric components, consideration of target elevation ASL, correction of topographic effects...) are equally applied to the CF retrieval which is performed consistently with the surface reflectance retrieval. As a result, maps of CF from space in radiance units are generated, what is a new type of information in the field of remote sensing of vegetation fluorescence.

5.2. Sensitivity Analysis

As it has been discussed, the CF signal to be measured is directly related to the O_2-A absorption feature. In order to define the factors affecting the depth of the O_2-A absorption a sensitivity analysis have been carried out. With this purpose, a synthetic data set of TOA radiance spectra at MERIS band configuration has been simulated with Eq. 5.3.1 and different combinations of surface reflectance, atmospheric inputs (AOT and CWV), target elevation and terrain slope (this one parameterized by the cosine of the illumination angle μ_{il}).

A typical MERIS acquisition configuration has been selected, given by VZA= 0°, SZA= 28° and RAA= 150° (measured from North to East). The default setup consisted of a surface tilted 10° towards the sun, with an elevation ASL of 300 m, the AOT at 550 nm was 0.32, the water vapor column content was 2 $\mathrm{g{\cdot}cm^{-2}}$, and a typical green vegetation spectrum (the one labelled as "Vegetation #1" in Fig. 3.6) was selected for the surface reflectance. These inputs were independently varied to analyze their individual impact over the TOA signal. The CF contribution was also varied according to typical variation ranges from 1 to 10 $\mathrm{Wm^{-2}sr^{-1}\mu m^{-1}}$ at 760 nm (see, for example, Amorós-López et al. [2006]; Liu et al. [2005]). The 10 CF spectra used in the simulations are displayed in Fig. 5.4.

The depth of the O_2-A absorption is measured from the bottom of the absorption feature at band 11 (L^{11}) to the radiance at the same wavelength calculated by linear interpolation between bands 10 and 12 (L^{11}_{int}). These variables are shown in the scheme in Fig. 5.5. The *Normalized Difference at O_2-A absorption Index* (NDOI) has been designed for quantifying the O_2-A absorption. It is given by

$$\mathrm{NDOI} \equiv \frac{L^{11}_{int} - L^{11}}{L^{11}_{int} + L^{11}} \tag{5.2.1}$$

The variation of the NDOI with the fluorescence signal is estimated from the default setup and the 10 CF spectra in Fig. 5.4. The surface reflectance is also varied between 5 different reflectance levels, from 0.5 to 1.5 times the "Vegetation #1" reflectance spectrum in Fig. 3.6. The variation of the NDOI as a function of F_s^{11} and the ρ_s^{11} are plotted in Fig. 5.6. The main conclusion to be outlined is that the fluorescence emission does have a noticeable

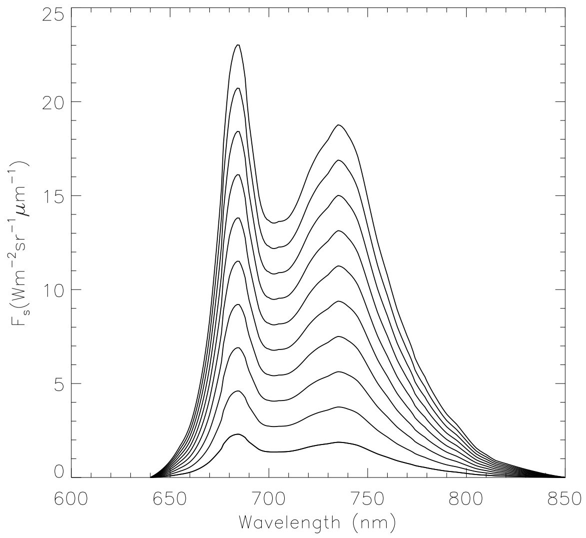

Figure 5.4: CF spectra used for the generation of the synthetic data set.

impact on the O_2-A absorption, as the in-filling of the absorption band by fluorescence leads to a NDOI decrease of up to 3% in the F_s^{11} range from 0 to 10 $\mathrm{Wm^{-2}sr^{-1}\mu m^{-1}}$. It is also noticeable that the darker the target is, the more detectable fluorescence becomes. This is explained by the larger relative contribution of the emitted signal against the reflected one. This suggest that the same fluorescence signal would be more easily estimated in forest canopies, usually darker ($\rho_s^{11} \simeq 0.25 - 0.35$), than in healthy green crops ($\rho_s^{11} > 0.35$). In any case, the response of NDOI against changes in the fluorescence emission enables its detection to be attempted.

However, it must be remarked that the numbers in Fig. 5.6 depend on the particular configuration selected for the simulations. This means that changes in the observation or illumination angles, atmospheric conditions or target elevation and orientation could modify slightly those results, as they all affect the atmospheric transmittance. Also, the value of NDOI for the different reflectance values is different even if CF= 0. The variation of the O_2-A absorption depth with some of those parameters is summarized in Fig. 5.7. The calculations have been performed with the default input configuration and no fluorescence being added to the reflected radiation. Very different dependencies are found from one parameter to another.

On one hand, the O_2-A absorption depth shows to be very sensitive to changes in the target elevation, in the aerosol loading and in the reflectance at 760 nm. This statement was already reached when the sensitivity of CWV retrievals to external factors was assessed in Section 3.3. The O_2-A absorption decreases with the target elevation, as less atmospheric path is being crossed by the radiation when the target is at a certain distance from the sea level. It happens on the contrary with the aerosol loading. This is due to the decrease in

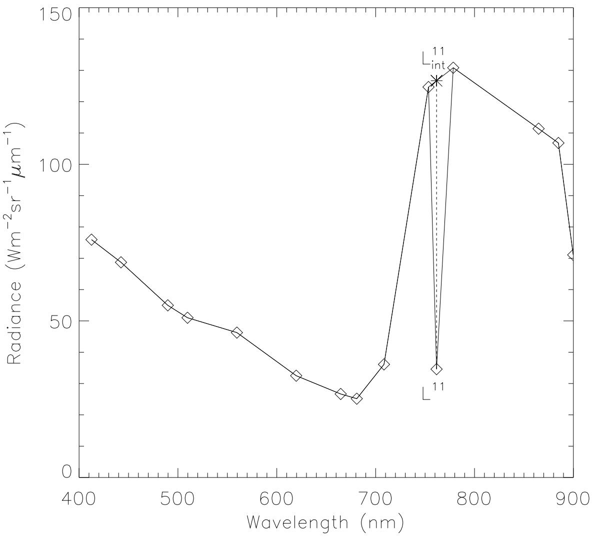

Figure 5.5: TOA green vegetation radiance spectrum resampled at MERIS band configuration. The variables L^{11} and L^{11}_{int} used in the calculation of the NDOI are pointed out.

transmittance inside the band due to a higher aerosol loading is not counterbalanced by an equal decrease outside. As it was discussed for the water vapor absorption in MERIS band 15, increasing the aerosol loading makes multiple scattering contribution larger, producing a more efficient absorption inside the band. Outside the absorption band, the increase of the aerosol loading also contributes to make the extinction more efficient, but not with the same magnitude that inside the band. This transmission decrease is not counterbalanced by an equal decrease outside the absorption. For this reason, aerosols do not have the same influence on the radiation in the bands 10 and 12 than in the 11, what makes the O_2 absorption depth changes with the aerosol loading. In particular, the absorption depth (as measured from the band outside the absorption) is decreased when the aerosol loading is decreased, while larger AOT leads to deeper absorption bands. The reflectance around 760 nm also influences the NDOI due to nonlinear effects which are not considered in the definition of the index.

On the other hand, the impact of CWV and terrain slope on the NDOI is much smaller than that of surface elevation and AOT. Only a residual absorption is due to water vapor at the 760 nm region, which becomes noticeable only for the largest water vapor contents (> 3 g·cm^{-2}). Concerning the terrain slope, it contributes as a constant multiplicative factor over all the spectrum, so it has not a noticeable impact on the absorption depth.

Finally, the dependence of the O_2-A absorption on changes in the sensor spectral calibration has been investigated. As it was discussed in Section 3.3, MERIS is compounded of 5 cameras consisting in CCD arrays which cover the 400-900 nm range with a nominal spectral sampling interval of 1.25 nm [European Space Agency, 2006]. MERIS spectral

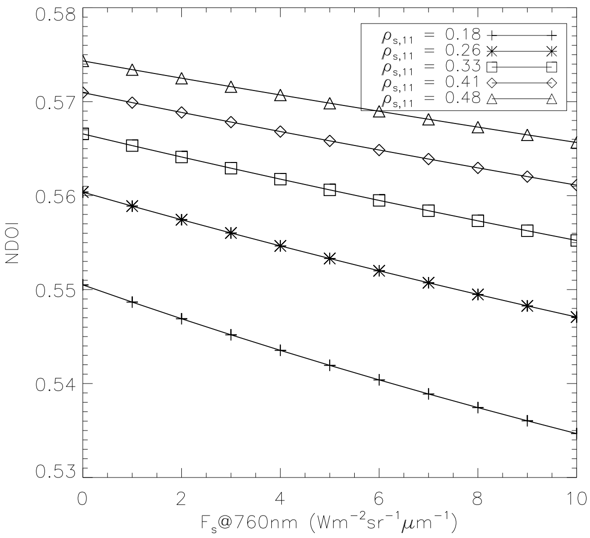

Figure 5.6: NDOI as a function of F_s^{11} and ρ_s^{11}.

calibration is well-characterized, and the exact band positions for every imaged pixel are available. The tabulated band 11 center wavelengths in the 5 MERIS cameras is displayed in Fig. 5.8 for the 3700 MERIS across track pixels. As it was the case of band 15 in Fig. 3.24, band spectral positions vary linearly with the across-track position in the CCD, and they do not separate more than 1 nm from the reference wavelength at 761.6 nm. This shift is not noticeable outside absorption bands, but it may lead to significative changes in the measured radiance inside absorption bands. This different impact outside and inside absorption band causes spectral shift to be another factor affecting the O_2-A absorption depth.

This fact is analyzed in Fig. 5.9. The variation in the O_2-A absorption depth with the exact band positions is displayed. The NDOI has been calculated from a high spectral resolution radiance spectrum resampled to all the spectral configurations reported for the 3700 detector indices in the across-track direction. The high spectral resolution radiance spectrum was generated with MODTRAN4 and the default combination of inputs described previously, and is output at a 1 cm^{-1} resolution. The 3700 MERIS-like spectra at the 760 nm region (bands 10, 11 and 12) are plotted in Fig. 5.9(a). It is confirmed that spectral shifts of the order of 1 nm do not change significantly the radiance levels outside absorption bands, although changes inside the O_2-A absorption are noticeable. Those changes in the measured radiance are converted into NDOI variations along the CCDs across-track direction in Fig. 5.9(b). The step-like shapes are caused by the use of a step-function to model MERIS bands, while the spectral resolution of the spectra to be convolved (1 cm^{-1}, i.e. around 0.057 nm at 760 nm) is coarser than the MERIS wavelength grid (step of the order of 0.0007 nm at 760 nm). The calculated variation of the NDOI is much larger

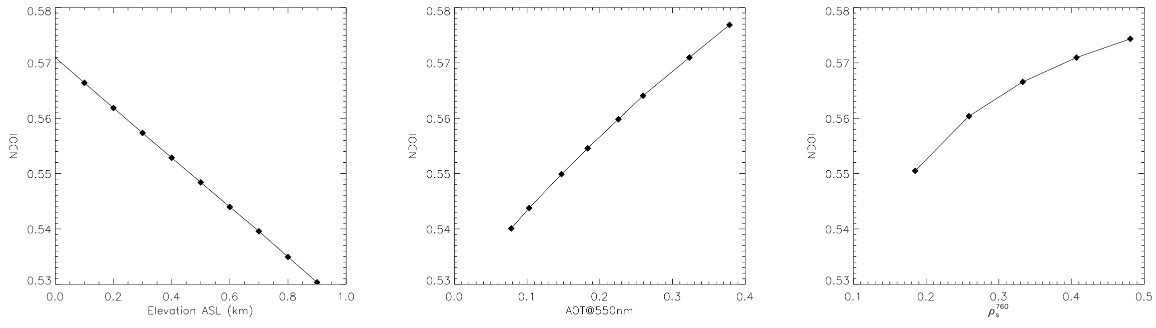

(a) Surface elevation (b) AOT at 550 nm (c) ρ at 760 nm

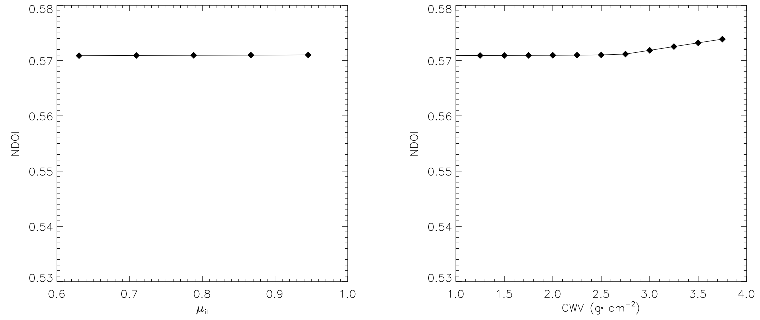

(d) μ_{il} (e) CWV

Figure 5.7: NDOI as a function of surface elevation (a), AOT at 550 nm (b), reflectance at 760 nm (c), surface slope (d) and CWV (e).

than that due to the other parameters studied before, with a peak-to-peak change in the absorption depth up to 20%. This makes the sensor spectral calibration a major issue in the fluorescence retrieval. Since only the reference wavelength at 761.6 nm has been considered, errors due to the “smile effect” must be assumed. A new version of the algorithm based on a per-column processing is under investigation. Meanwhile, only those parts of the detectors in which a nearly-flat variation in the NDOI should be used. In particular, the fourth MERIS camera is an optimum candidate for the fluorescence retrievals, while the large NDOI variations found within the first camera make it should be discarded for this purpose. It must be noted that the suitability of detector areas for fluorescence retrieval is not related to the magnitude of the shift from the reference wavelength of 761.6 nm, but to the shift influence over the O_2-A band. For example, the same wavelength change of around 0.13 nm occurs between detectors 400 and 500 and detectors 800 and 900, but it leads to very different changes in the NDOI (0.11% and 1.8%, respectively).

Overall, it must be concluded that the fluorescence signal, although detectable, has a smaller contribution to the O_2-A absorption than spectral shifts, surface elevation, AOT and surface reflectance. This means that the CF retrieval is strongly conditioned by those parameters. The surface elevation can be accurately provided by a suitable DEM, but

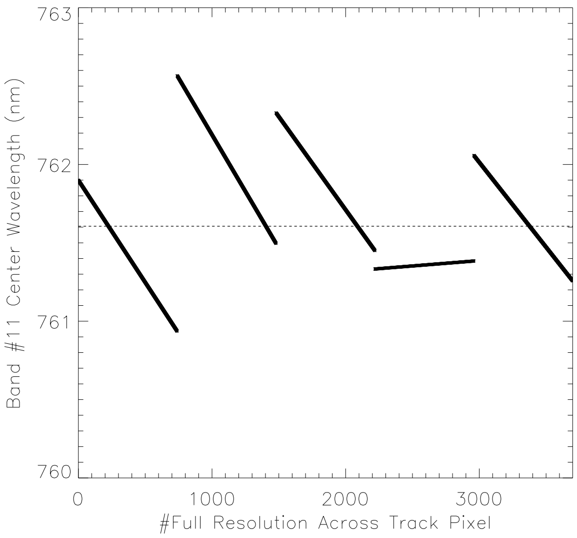

Figure 5.8: Spectral position of MERIS band 11 for the 5 MERIS cameras. The dashed line represents the wavelength 761.6 nm at which band 11 is referenced.

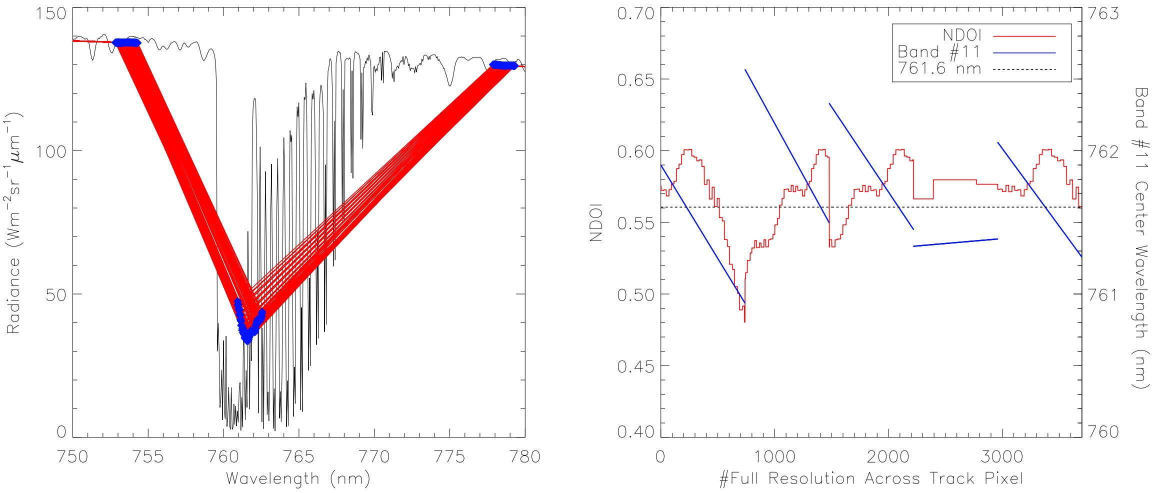

(a) (b)

Figure 5.9: Impact of changes in the sensor spectral calibration over the O_2-A absorption band. Left (a), MODTRAN4-derived TOA radiance spectrum convolved to the 3700 spectral configurations in the MERIS across-track direction. Right (b), the NDOI in the MERIS across-track direction derived from the spectra in (a).

it is not so easy to have a reliable estimation of the aerosol loading. From Fig. 5.6 and Fig. 5.7(b) it is estimated that an error of 0.05 in AOT at 550 nm may have a similar impact on the O_2-A absorption as a CF emission around 4 Wm^{-2}sr^{-1}μm^{-1}. This means that a huge effort must be put on a proper estimation of the aerosol loading. The same is true for the surface reflectance. In the case of the spectral calibration, a minimum variation of the band position in the across-track direction must be guaranteed. Working inside detector areas where spectral shifts are small and constant or correcting this shift by resampling the atmospheric parameters with the proper spectral positions for each column are possible solutions.

From all those results, it is concluded that the best estimation of fluorescence can be achieved if the CF retrieval method is coupled to an atmospheric correction scheme, where surface elevation, aerosols, surface reflectance and even the sensor spectral calibration are properly modelled. Including fluorescence in the radiative transfer problem also enables to derive results in radiance units, rather than in arbitrary units, which is an advantage for the interpretation of results.

5.3. Methodology Description

The CF signal is included in the whole radiative transfer scheme as an additive term adding up over the reflected flux at the target level in Eq. 3.1.1. If the CF emission is assumed to be isotropic [Moya et al., 2004], the at-sensor radiance is given by

$$L_{\mathrm{TOA}} = L_0 + \frac{\left[(E_{\mathrm{dir}}\mu_{\mathrm{il}} + E_{\mathrm{dif}})\frac{\rho}{\pi} + \mu_v F_s\right] T_{\uparrow}}{1 - S\rho_s} \tag{5.3.1}$$

where F_s stands for the spectral CF emission (F_s and CF will be used indistinctly hereinafter). Once the aerosol and water vapor contents have been estimated from the corresponding modules of the atmospheric correction procedure, all the atmospheric functions in Eq. 5.3.1 are known. This leads to a problem of 2 unknowns, ρ_s and F_s, and one equation.

The FLD principle is used to decouple the emitted and reflected contributions. MERIS bands 10 and 11 are used as reference/measuring band, as it has been discussed previously. Theoretically, any other pair of bands in the red and NIR spectral regions could be used in order to provide the necessary information for the separation of ρ_s and F_s, but the low weight F_s would have in the radiance outside a strong absorption band would cause the fluorescence signal too low to be separated from the reflected radiation. Writing the spectral dependence explicitly, the system to be solved is

$$\left.\begin{aligned} L^{10}_{\mathrm{TOA}} &= L^{10}_0 + \frac{\left[(E^{10}_{\mathrm{dir}}\mu_{\mathrm{il}} + E^{10}_{\mathrm{dif}})\frac{\rho^{10}_s}{\pi} + \mu_v F^{10}_s\right] T^{10}_{\uparrow}}{1 - S^{10}\rho^{10}_s} \\ L^{11}_{\mathrm{TOA}} &= L^{11}_0 + \frac{\left[(E^{11}_{\mathrm{dir}}\mu_{\mathrm{il}} + E^{11}_{\mathrm{dif}})\frac{\rho^{11}_s}{\pi} + \mu_v F^{11}_s\right] T^{11}_{\uparrow}}{1 - S^{11}\rho^{11}_s} \end{aligned}\right\} \tag{5.3.2}$$

The problem consists then of two equations being defined by 4 variables, ρ^{10}_s, F^{10}_s, ρ^{11}_s, and F^{11}_s. The problem is closed-up by assuming a linear spectral dependence in ρ_s and F_s

between bands 10 and 11, which are thus related by

$$\left.\begin{aligned} \rho_s^{11} &= A\rho_s^{10} \\ F_s^{11} &= BF_s^{10} \end{aligned}\right\} \tag{5.3.3}$$

This simplistic modelling is justified by the spectral proximity of MERIS bands 10 and 11, which is around 8 nm. It is a refinement against just assuming $\rho_s^{11} \simeq \rho_s^{10}$ and $F_s^{11} \simeq F_s^{10}$, as it was done in an earlier version of the method. The A coefficient is calculated on a per-pixel basis, using ρ_s^{10}, ρ_s^{11} as provided by the atmospheric correction module neglecting the fluorescence contribution (ρ_s^{10} was calculated directly from the TOA radiance as one of the 13 MERIS bands nearly-free from atmospheric absorptions, while ρ_s^{11} was derived from interpolation between ρ_s^{10} and ρ_s^{12}). On the other hand, a universal value is selected for the B coefficient. A typical fluorescence spectrum from a green canopy is displayed in Fig. 5.10. Most of the variability in the emission spectrum due to external parameters is expected in the 670-740 nm range, while the shape of the two wings at the sides of this interval remains constant for a wide range of canopy conditions and vegetation types. In particular, the literature shows that a value around -0.8 for the spectral slope of the CF emission at the 760 nm region can be adopted as representative of a wide range of those cases.

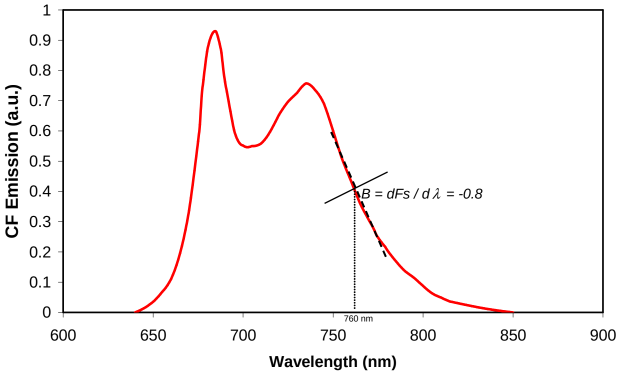

Figure 5.10: Typical CF emission spectrum from a green canopy. The estimated $B = -0.8$ around 760 nm is depicted.

From Eq. 5.3.2 and Eq. 5.3.3 and a little algebra, the analytical expression for the fluorescence emission at 760 nm is given by

$$F_s^{11} = \frac{B}{\mu_v}\left[\frac{X^{11}(E^{10} + X^{10}S^{10}) - AX^{10}(E^{11} + X^{11}S^{11})}{B(E^{10} + X^{10}S^{10}) - A(E^{11} + X^{11}S^{11})}\right] \tag{5.3.4}$$

where

$$X^i = \frac{L^i_{\mathrm{TOA}} - L^i_0}{T^i_\uparrow}, \qquad i = 10, 11 \tag{5.3.5}$$

and

$$E^i = \frac{1}{\pi}[E^i_{\text{dir}}\mu_{\text{il}} + E^i_{\text{dif}}], \qquad i = 10, 11 \tag{5.3.6}$$

All the variables in Eq. 5.3.4 are calculated along the atmospheric correction process, so the obtainment of CF can be considered a direct by-product of the atmospheric correction itself, which returns surface reflectance and fluorescence maps simultaneously. However, the use of the FLD principle for the CF retrieval implies an accurate computation of the O_2-A absorption, which is a complex task:

1. Radiative transfer calculations inside deep and narrow absorptions are sensitive to many factors, such as the particular formulation of the radiative transfer problem and the method applied for the solution. As it was described in Section 3.2, the LUT employed in the atmospheric simulations was generated by running MODTRAN4 under the DISORT-scaling option with 8 fluxes, with the default 5 cm^{-1} atmospheric data base. A finer spectral resolution or the application of the original DISORT algorithm could not be afforded because of the huge computation burden associated. Moreover, small errors in the inputs (aerosols, water vapor, geometry...) or in the interpolation process could also lead to noticeable errors in the calculated atmospheric parameters.

2. The "smile effect" intrinsic to the instrument causes spectral shifts from the reference band setting in the across-track direction [Mouroulis et al., 2000]. The absolute value of those shifts depends on the spectral band, but not variation pattern in the across-track direction, and they are not higher than 1 nm in MERIS (Fig. 5.8). Such a shift does not have a meaningful impact on channels measuring out of absorption bans, but it is noticeable inside them. As it was shown in Section 5.2, the effective transmittance values calculated in complex absorption bands depends strongly on the exact position and shape of the convolution function used to simulate the channel. In the generation of the atmospheric LUT, a rectangular function centered at 761.6 nm with a width of 3.75 nm was applied to simulate MERIS band 11 in the convolution of the MODTRAN4 output.

One of the consequences of a bad evaluation of the O_2-A absorption at MERIS band 11 is that errors in surface reflectance at that band occur after the atmospheric correction of the original radiance data. Those errors are visible as spikes and dips in the reflectance spectra, which are smooth in natural targets. This effect is illustrated in Fig. 5.11. Three typical land surface reflectance spectra extracted from an atmospherically-corrected MERIS image are plotted. It can be observed that no smooth transition is found between bands 10 and 12, but a spike occurs at MERIS band 11 in the three spectra. This spike is larger in the case of the green vegetation spectrum because of the in-filling contribution of CF, which is not expected in the bare soil and in the senescent vegetation spectra. Thus, a linear spectral dependence can be assumed for the reflectance patterns of non-fluorescent targets, especially in those surfaces with no red-edge features in the reflectance spectra.

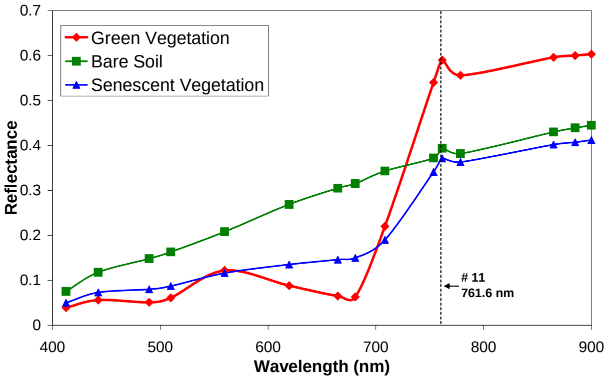

Figure 5.11: Reflectance patterns of typical land targets extracted from MERIS data. The dashed line points out reflectance errors at MERIS band 11.

With this assumption of linear reflectance in the red-NIR regions for non-fluorescent targets, a technique called *transmittance correction* has been designed to refine the atmospheric optical parameters at MERIS band 11 in the LUT. It is based on calculating an effective transmittance function T_{eff} which corrects the path radiance and upward transmittance in the LUT so that errors in the subsequent surface reflectance at band 11 are reduced. The new path radiance $L_0'^{11}$ and upward transmittance $T_\uparrow'^{11}$ to be used in Eqs. 5.3.4-5.3.6 are given by

$$L_0'^{11} = L_0^{11} \cdot T_{eff} \tag{5.3.7}$$

$$T_\uparrow'^{11} = T_\uparrow^{11} \cdot T_{eff} \tag{5.3.8}$$

The T_{eff} function is calculated from targets that are considered non-fluorescent inside the same 30 × 30 km cells (100 × 100 pixels in MERIS FR mode) that are used in the AOT retrieval. It is assumed that the atmospheric conditions are constant within each cell. No important variations in the spectral calibration are expected either, as the spectral shift in a 100-elements array can be neglected. A NDVI threshold of 0.45 is arbitrarily set to separate non-fluorescent pixels from those with potential fluorescent activity. All the pixels in the non-fluorescent category are in turn classified according to their elevation ASL in steps of 20 m, in order to minimize the dependence of the O_2-A absorption depth with the target elevation. Then, T_{eff} is calculated for all the non-fluorescent pixels, by means of an inversion procedure that searches for the T_{eff} leading to the most linear reflectance pattern when applied to the optical parameters in the LUT during the atmospheric correction. The reference reflectance at band 11 used for the inversion is calculated by linear interpolation of the reflectance at bands 10 and 12. The mean value of T_{eff} from all the non-fluorescent pixels in a given elevation category is adopted for all the fluorescent pixel in the same category.

5.4. Results

5.4.1. Results from MERIS data

The Barrax study site offers a unique case for testing the performance of the fluorescence retrieval algorithm described before. Extensive green vegetation fields are present in different phenological states and stress levels, either irrigated or not. The flatness of the terrain practically avoids the influence of surface elevation, as it is nearly constant around 700 m ASL. Moreover, a large MERIS FR data set has been acquired along the last years over the Barrax study site, with a number of images in coincidence with dedicated field campaigns. For the analysis of the results, a 90 km-side square area centered at the Barrax site is chosen. Possible errors associated to changes in the MERIS spectral calibration and in the atmospheric state are minimized by working in a reduced area. The analyzed area is shown in Fig. 5.12.

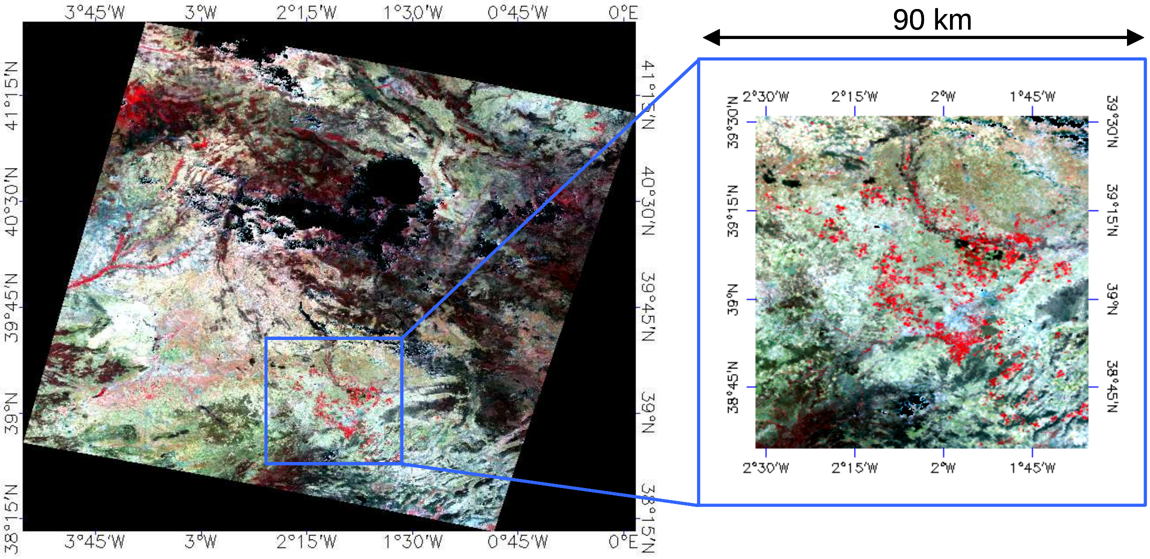

Figure 5.12: False color composite of the MERIS FR image acquired over the Iberian Peninsula on 14 July 2003. The analysis area around the Barrax study site is zoomed up.

Four CF maps of the area depicted in Fig. 5.12 are shown in Fig. 5.13. The four subsets are extracted from MERIS FR images acquired, respectively, on 14 July 2003, 14 July 2004, 17 July 2004 and 3 June 2005. Then, the first three subsets were acquired during equivalent summer periods in the middle of July, while the forth one was taken about one month and a half before. Different environmental conditions (temperature, humidity...) and vegetation growing stages are expected in those time lapses. This trend is confirmed in the different CF levels measured on 3 June 2005 with respect to those on 2003 and 2004. For example, the CF signal of about 2-4 $Wm^{-2}sr^{-1}\mu m^{-1}$ which was estimated from the July images in the cluster of vegetation pixels centered at 38.9°N, 2.0°W nearly disappeares in 2005. The same occurs around 38.6°N, 2.4°W, although the fluorescence signal was already very low on 2003 and 2004. These changes in CF are a potential indication of the link between fluorescence and plant state, although variations due to changes in the vegetation cover from one year to the other can not be discarded either. It must be remarked that the fluorescence intensity estimated from MERIS data compares well with the approximated range of variation published in the literature for the chlorophyll fluorescence emitted under natural conditions [Amorós-López et al., 2006; Liu et al., 2005].

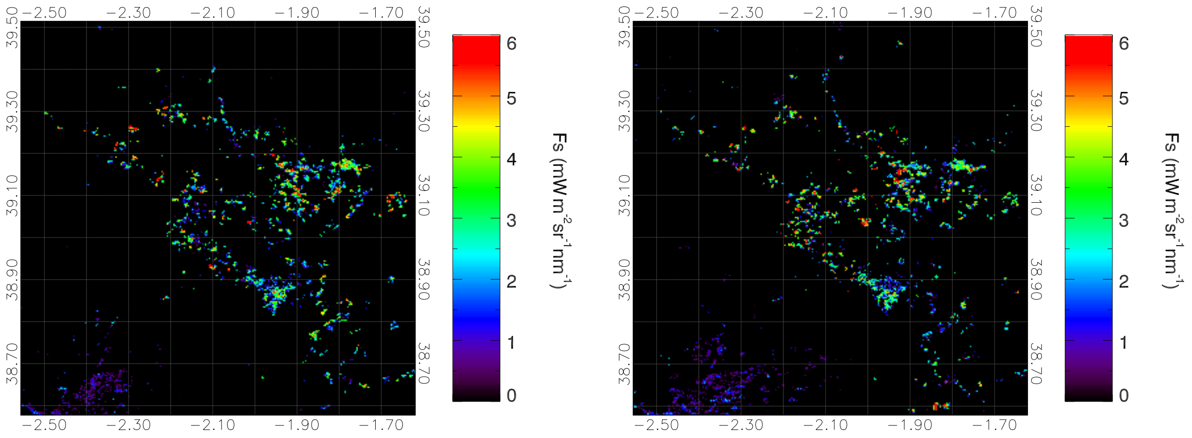

(a) MERIS FR, 14 July 2003

(b) MERIS FR, 14 July 2004

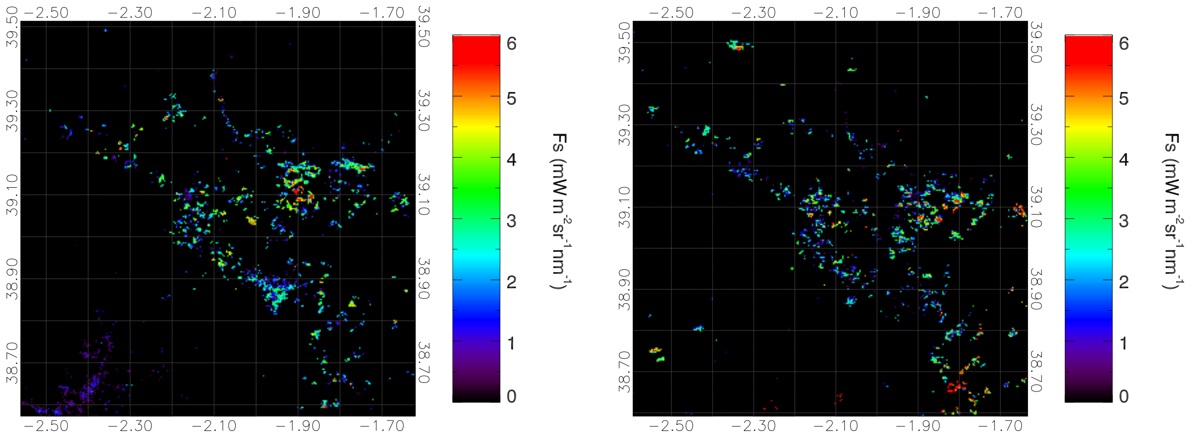

(c) MERIS FR, 17 July 2004

(d) MERIS FR, 3 June 2005

Figure 5.13: Maps of F_s at the Barrax study site in for different dates.

The CF map generated from the image acquired on 14 July 2003 has been compared with other biophysical products derived from MERIS data. In particular, maps of fractional vegetation cover (fCover), LAI, LAI times the leaf chlorophyll content (LAI×C_{ab}) and fraction of photosynthetically active radiation absorbed (fAPAR) were calculated using the `TOA-VEG` processor [Baret et al., 2006] implemented in the BEAM Toolbox [Fomferra and Brockmann, 2005]. The results are displayed in Fig. 5.14. The comparison with the corresponding CF map in Fig. 5.13(a) does not lead to solid conclusions about the correlation between fluorescence and the other biophysical parameters. Although the same vegetation patterns can be recognized within the different products, the 300 m per pixel spatial resolution is too coarse for a quantitative analysis.

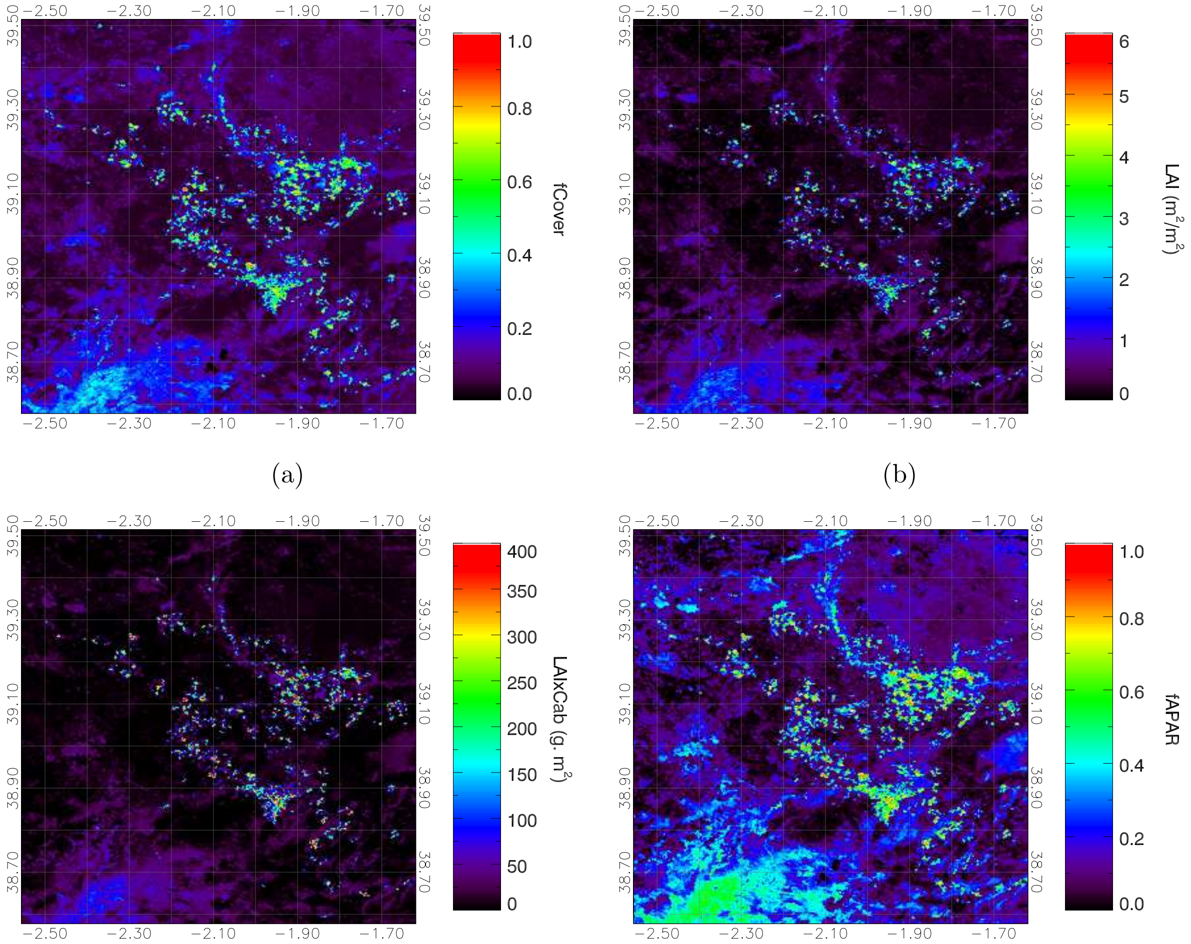

(a) (b)

(c) (d)

Figure 5.14: Maps of fCover, LAI, LAI×C_{ab} and FAPAR derived from the MERIS FR image acquired on 14 July 2003 by the `TOA-VEG` processor implemented in the BEAM Toolbox.

Further information of those potential correlations is gained by plotting the different biophysical products against the fluorescence signal. Only the pixels with NDVI higher than 0.45 are plotted in order to separate the purest vegetation pixels. The scatter plots for each parameter are displayed in Fig. 5.15. Two variables have been added to those in Fig. 5.14 because of their possible correlation with the measured fluorescence. These are the reflectance at 760 nm (ρ_s^{11}) and the MERIS Terrestrial Chlorophyll Index (MTCI) [Dash and Curran, 2004]. In the first case, it was demonstrated in Section 5.2 (Fig. 5.7(c)) that non-linear effects in the radiative transfer between surface and atmosphere may cause the depth of the O_2-A absorption feature biased by the surface reflectance at the same wavelength. Concerning the MTCI, it is a vegetation index specifically designed for the band setting of MERIS with the purpose of evaluating the vegetation chlorophyll content. Thus, some degree of correlation between each of the variables in Fig. 5.15 and the fluorescence signal was a priori expected. However, it is found that the chlorophyll-related products, LAI$\times$C$_{ab}$ and MTCI, do not present a clear correspondence with F_s, although this seems to be higher than for the other parameters. This fact would suggest that the fluorescence emission is more related to the pigment concentration than to the amount of vegetation, what indicates the link between fluorescence and vegetation photosynthetic activity. Secondly, CF and ρ_s^{11} are totally independent. This proves the good performance of the atmospheric correction scheme in which the retrieval of CF is included.

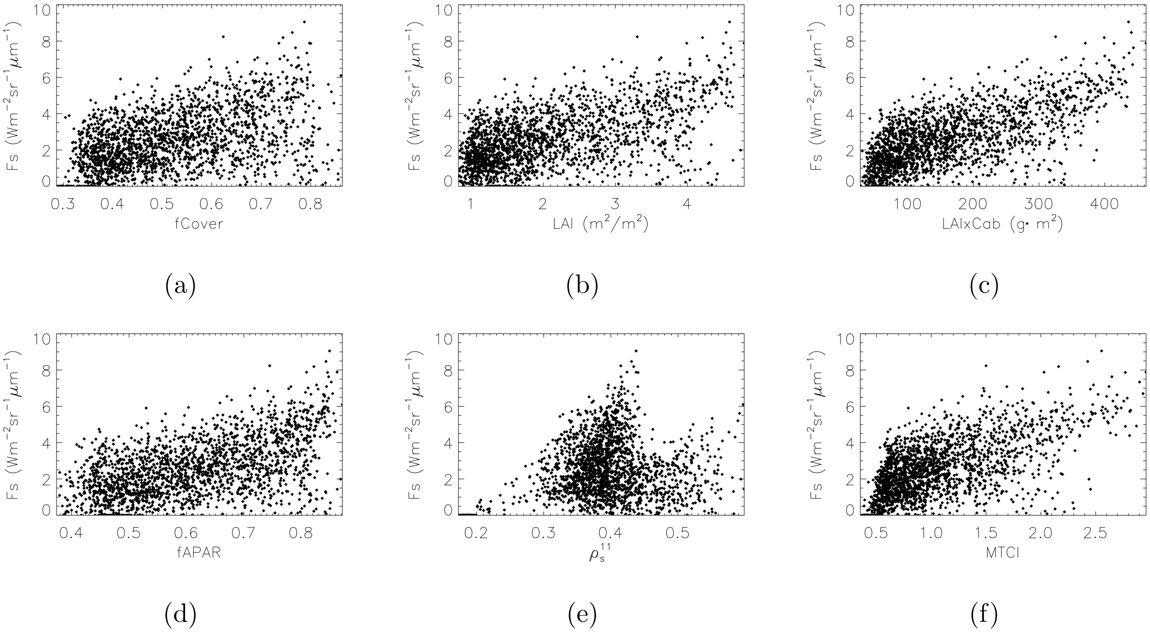

(a) (b) (c)

(d) (e) (f)

Figure 5.15: Scatter plots between the estimated CF signal in Fig. 5.13(a) and different vegetation parameters.

These results support the ability of the proposed methodology to estimate vegetation fluorescence from MERIS FR data. However, it is difficult to attempt a robust quantitative validation of the results at a 300 m per pixel resolution, as the crops where ground truth is available can not be clearly distinguished, nor pure vegetation pixels be isolated. For this reason, the same methodology has been applied to data acquired at the time of MERIS acquisitions by the airborne sensor CASI-1500 during the SEN2FLEX campaign. The *in situ* measurements of solar-induced fluorescence taken during the campaign enable the quantitative assessment of the CF signal retrieved from remote sensing data.

5.4.2. Results from CASI-1500 data

The Compact Airborne Spectrographic Imager (CASI) 1500 [Itres Research Ltd., 2006] is a pushbroom sensor acquiring hyperspectral images in the 370 to 1050 nm spectral region with a spectral resolution up to 2.2 nm (288 bands). The nominal spatial resolution is 3 m per pixel. Sample vegetation and bare soil spectra acquired by CASI-1500 (hereinafter, CASI) are displayed in Fig. 5.16. A comparison of the CASI band configuration in the 288 bands operation mode with a set of typical Airborne Visible/Infrared Imaging Spectrometer (AVIRIS) [Green et al., 1998] response functions is also plotted. It can be stated that CASI provides a nearly-continuum spectrum in the entire spectral range, with very fine observation channels that are able to reproduce any small absorption feature due to surface or atmospheric components. A detailed characterization of the O_2-A absorption band at 760 nm is also provided. These features enable the use of CASI for the estimation of the CF signal at a much finer spatial resolution than MERIS.

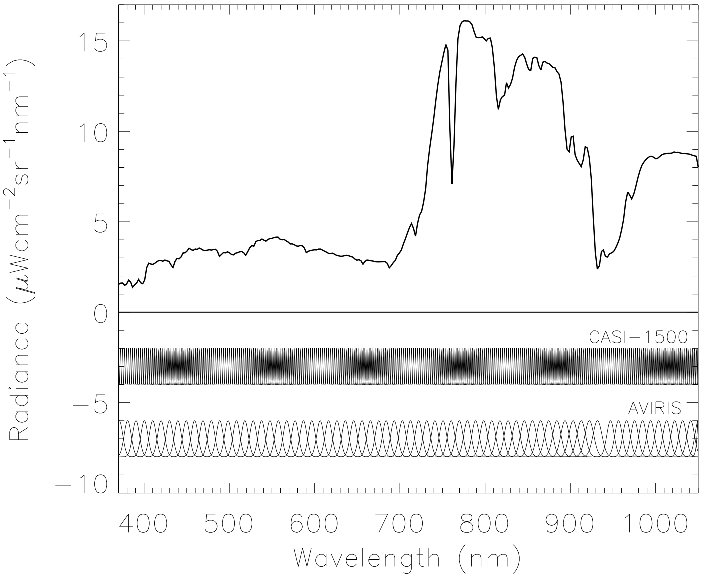

Figure 5.16: Up, green vegetation spectrum acquired by CASI-1500 in the 288 bands operation mode. Below, CASI-1500 response functions are compared to AVIRIS ones in the 370 to 1050 nm spectral region.

As in the case of MERIS, the fluorescence retrieval is coupled to an accurate atmospheric correction algorithm. It is specifically designed for ultra-fine spectral resolution (bandwidth from 2 to 10 nm) and spatial resolution (pixel size less than 10 m) imaging spectrometers [Guanter et al., 2006a]. The assessment of the spectral calibration is coupled to the removal of the atmospheric distortion so that maps of surface reflectance are derived, as well as CWV maps, estimations of AOT and updated sensor gain coefficients and spectral calibration. The F_s term is included in the atmosphere/surface radiative transfer according to Eq. 5.3.1, and the same steps for the estimation of the fluorescence signal as in the case of MERIS are carried out.

This methodology has been applied to the CASI images acquired over the Barrax study site during the SEN2FLEX experiment. In particular, 12 lines of CASI data were acquired in morning (around 10:00 a.m. Local Time) and noon (around 14:00 p.m Local Time) flights, at an altitude around 2000 m above the ground level. CASI provided images in the VNIR ranges (from 370 to 1050 nm) working under two different operation modes: one measured in 288 channels with bandwidths of 2.2 nm and Field Of View (FOV) equal to 23.6°, and the other measured in 144 channels with bandwidths of 4.4 nm and FOV of 39.3°. The instrument operation, the radiometric calibration and the geometric correction was carried out by Itres Research Ltd., Calgary, Canada. The original spatial resolution was 3 m per pixel, although the images were also resampled to 13 m per pixel in order to reduce the noise detected in some channels due to the low signal levels.

The final surface reflectance maps and the intermediate products, both atmospheric parameters and calibration coefficients, were validated using ground-based measurements and data provided by the CASI operators. The τ_{550} and the spectral shift from the laboratory calibration are the most relevant ones according to the sensitivity analysis in Section 5.2. Those are plotted in Fig. 5.17. The comparison between the AOT at 550 nm estimated from CASI data and the same retrieved from ground measurements is depicted in Fig. 5.17(a). Points correspond to 4 different days, June 1, 2, 3 and July 14, either from 288 or 144 bands modes. Horizontal error bars correspond to the standard deviation in the ground measurements in a 2-hours window centered at the time of CASI acquisition, while the uncertainty estimated for each single measurement is 0.02. No error budget is calculated for the AOT retrievals from CASI data. It can be concluded that variations in the aerosol loading are well registered by the method in general, both for low and high concentrations, although there are some deviations in absolute terms leading to a square Pearson correlation coefficient r^2 of 0.519. This increases to 0.714 if the acquisition on 14 July is removed from the analysis. An intrusion of Saharan dust was detected that date. This intrusion mostly occurs at atmospheric layers above the plane. Thus, it does not affect the radiation in the target-to-sensor path, what explains the underestimation of AOT from CASI data. On the other hand, the characterization of the "smile" effect in CASI is displayed in Fig. 5.17(b). The across track spectral shift for the 144 bands configuration is plotted. It can be checked that the deviation from the laboratory calibration is around the ±1 nm claimed by the CASI operators (J. Howse, ITRES Research Ltd., personal communication, 2005). This characterization of the instrument in the across-track direction enables the correction of the smile effect. This is done by resampling the atmospheric parameters provided by MODTRAN4 at a high spectral resolution with the CASI band configuration updated on a per-column basis. The impact of spectral shifts on the measured O_2-A absorption is then minimized.

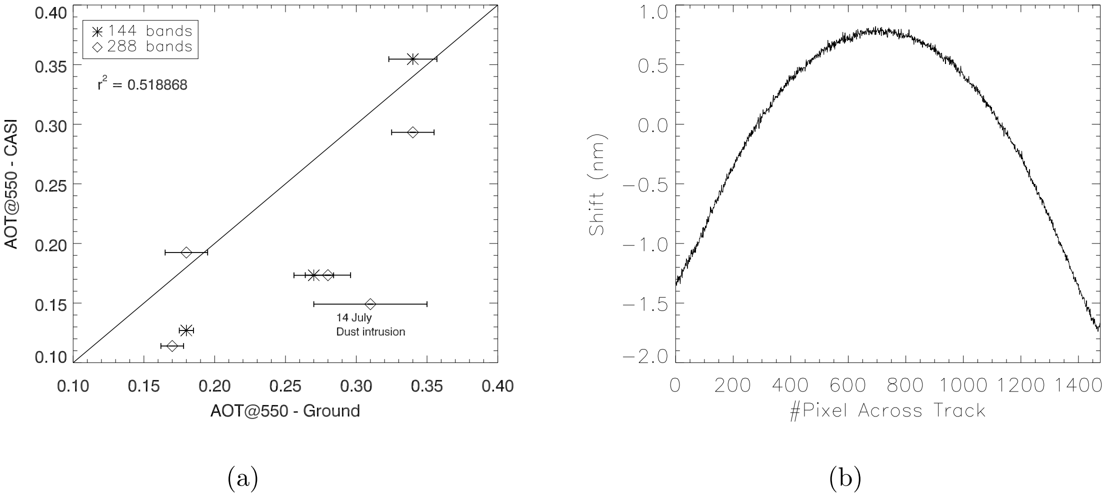

(a) (b)

Figure 5.17: Results from the reflectance/fluorescence retrieval scheme applied to CASI data from SEN2FLEX campaign. Left (a), comparison between AOT derived from CASI data with AOT calculated from ground-based measurements. Right (b), calculated spectral shift in the across-track direction for CASI under the 144-bands mode.

Reflectance and fluorescence images were obtained as final product. The reflectance images were used, in turn, for the derivation of NDVI and PRI. RGB composites showing the imaged area and NDVI, PRI and F_s images are plotted in Fig. 5.18. The circular shapes of some fields are due to the irrigation system consisting in a pivot system spinning around the crop. It can be observed that different information is provided by the three vegetation indicators. For example, the NDVI normally presents a low variation within the same field, while PRI and CF show noticeable variations. Indeed, CF shows spatial patterns within the fields in areas where the NDVI looks homogeneous. This is a new proof of the decoupling between the green vegetation amount, as given by the NDVI, and the actual plant photosynthetic activity, indicated by the fluorescence signal. Indeed, the correlation between PRI and CF reported by some authors working at the laboratory level [Amorós-López et al., 2006; Dobrowski et al., 2005; Evain et al., 2004; Liu et al., 2005] has not been proved, as the PRI decreases gradually towards the edges of the image in vegetation targets. This may be explained by the large dependence of the PRI on the canopy structural parameters, and so on the view angle, described by Barton and North [2001]. The variation in the VZA from the center to the edge of the line is about 11° in the 288-bands mode and 20° in the 144-bands mode. Thus, if the large variations in PRI with the across-track position are actually due to the varying VZA, its application to the analysis of vegetation from remote sensing data must be carefully considered, as the information about the plant physiological status that the PRI is intended to provide might be drastically biased by the acquisition geometry.

On the other hand, the range of F_s values compares well with those reported by some authors working at the canopy level [Amorós-López et al., 2006; Liu et al., 2005], and so with those estimated from MERIS data. For a quantitative validation of the retrieved CF signal it has been compared with ground-based fluorescence measurements taken simultaneously to CASI acquisitions. The radiance measured by an ASD spectroradiometer at different crops over the Barrax study site was converted into chlorophyll fluorescence at 760 nm by applying the FLD principle. Four representative cases from different surfaces are displayed in Fig. 5.19. The labels BS, F, C and W correspond to bare soil, festuca (a kind of grass), corn and wheat, respectively. The red marks point out the transects along which the ASD measurements were taken. The resulting CF signal from each target type along those transects is compared to the NDVI. Very different trends can be observed from one surface to another. In the wheat crop, both CF and NDVI present high values along the transect. It is noticeable that the NDVI is almost constant around 0.9, while CF varies up to ± 1 $\mathrm{Wm^{-2}sr^{-1}\mu m^{-1}}$ around a center value of about 2.5 $\mathrm{Wm^{-2}sr^{-1}\mu m^{-1}}$. This fact is a new proof of the non-correlation between CF and NDVI. This situation is confirmed in the festuca field, where the high amount of green vegetation given by NDVI values from 0.7 to 0.8 does not correspond to high values of CF. In the case of bare soil, both CF and NDVI are very low, as expected. The negative CF values can be adopted as zero-error of the method. Finally, low fluorescence levels are also found in the corn crop. It is a young crop still in growing stages. Large spaces are seen between plants, what explains the high-frequency NDVI variations along the transect.

These ground-based fluorescence measurements are compared with CASI-derived F_s signal in Fig. 5.20. A high linear correlation between the two CF estimations can be noted. However, results still deviate from the 1:1 correspondence. Further investigation is needed about this topic, both at ground-based and remote measurements. Firstly, more points would be needed for a detailed statistical analysis. Concerning ASD-derived F_s, it is taken as reference because it is assumed to be free from possible errors due to instrument calibration or aerosol loading, but some other error sources must be assessed. For example, no correction of fluorescence due to variation between neighboring bands are performed over ASD retrievals, while they are done over the remote F_s estimations (Eq. 5.3.3). On the

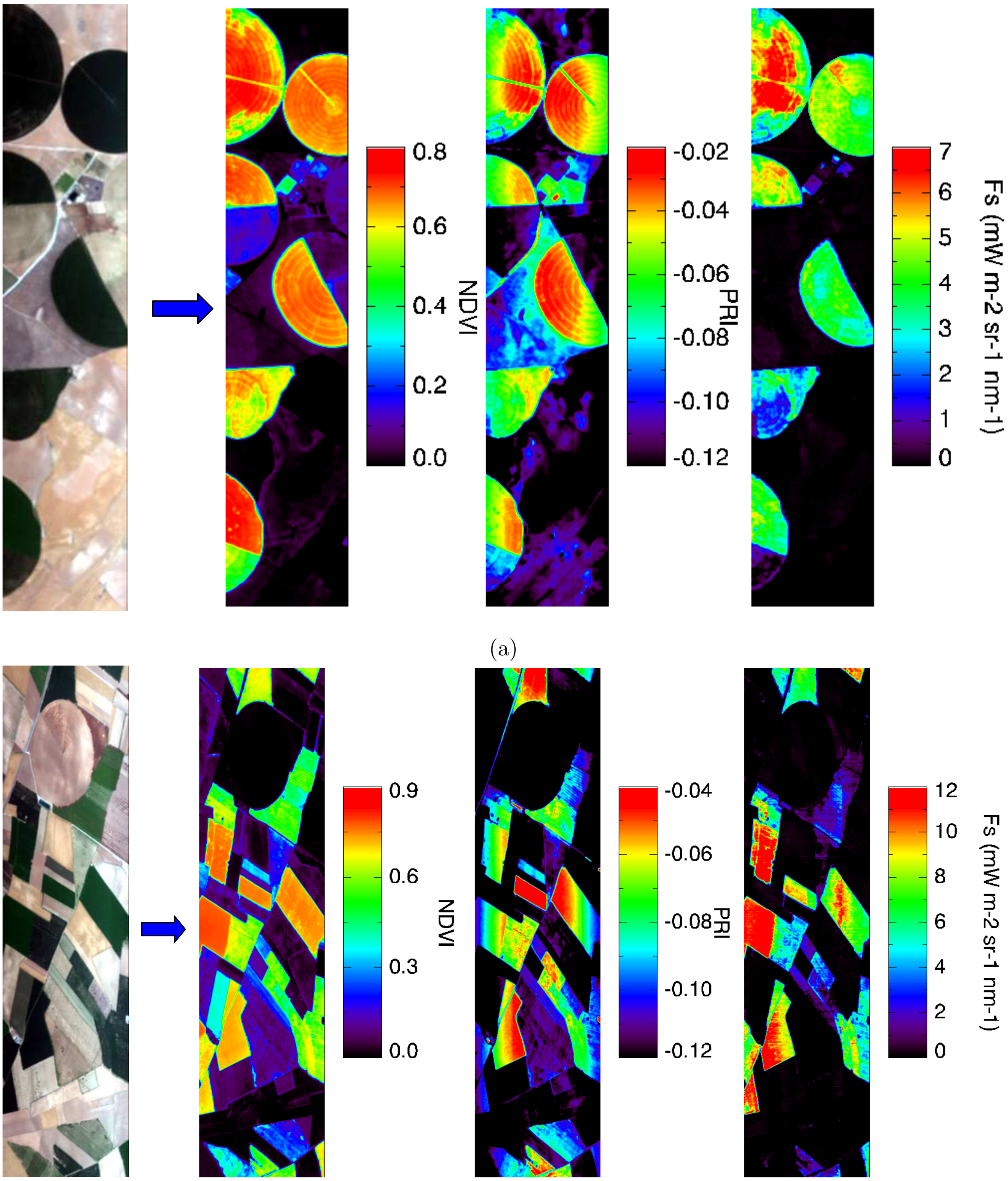

(a)

(b)

Figure 5.18: RGB composite and NDVI, PRI and F_s images derived from CASI data acquired during the SEN2FLEX campaigns in the 288-bands mode (a) and 144-bands mode (b).

other hand, ASD-derived fluorescence may be closer to the 0-3 $\text{Wm}^{-2}\text{sr}^{-1}\mu\text{m}^{-1}$ published in the literature, so the CASI-derived F_s would overestimate the actual fluorescence signal. In any case, the demonstrated method ability for the remote discrimination of high and low

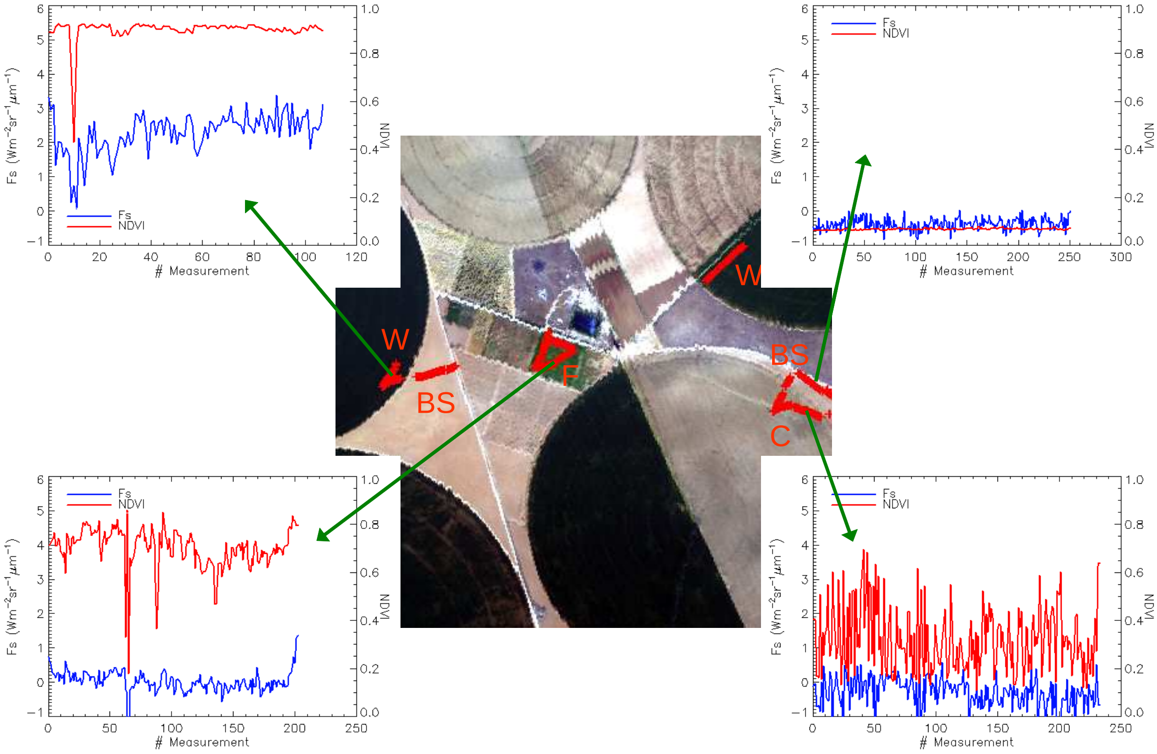

Figure 5.19: Ground-based fluorescence measurements at the Barrax site during the SEN2FLEX campaign. The red lines mark the transects where ASD measurements were taken. The labels BS, F, C and W correspond to bare soil, festuca (a kind of grass), corn and wheat surfaces, respectively.

levels of fluorescence emissions, and so of plant photosynthetic activity, can be considered an unprecedent step in the field of monitoring vegetation activity from space.

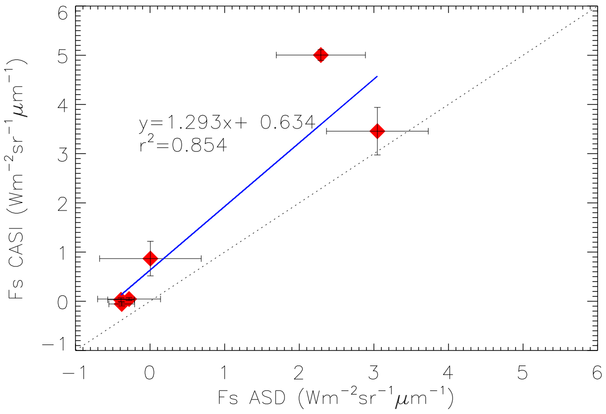

Figure 5.20: Comparison of F_s retrievals at ground-level with those derived from CASI data.

Part III

Summary and Conclusions

Summary and Conclusions

Under the title *New algorithms for atmospheric correction and retrieval of biophysical parameters in Earth Observation. Application to ENVISAT/MERIS data* a new methodology for the processing of MERIS Level 1b data over land targets has been presented. The aim of the work was developing an operational algorithm for the conversion from the calibrated radiance provided by MERIS to robust atmospheric and surface products. In particular, maps of aerosol optical thickness, columnar water vapor, surface reflectance and chlorophyll fluorescence are automatically generated. This autonomous working is summarized in the name chosen for the corresponding computer code *Self-Contained Atmospheric Parameters Estimation from MERIS data* (SCAPE-M). How those parameters are derived and the validation with external data sources has been discussed along this thesis.

The document is divided into 5 separate chapters. The first two chapters are used to establish the environment in which the work is framed. The other three refer explicitly to the description and validation of the methodology implemented in SCAPE-M. Going into more detail:

Chapter 1

It sets the physical and mathematical basis of atmospheric radiative transfer. The main atmospheric species and their optical activity are detailed, with a especial emphasis put on aerosols, as it may be the most complicated atmospheric component, in terms of modelling and retrieval, in the spectral range covered by MERIS. A careful description is also devoted to the statement of the radiative transfer equation, its boundary conditions and proper parameterizations for its application to remote sensing. Finally, some pages deal with the computational issues of atmospheric radiative transfer, through the description of MODTRAN4 [Berk et al., 1998] and 6S [Vermote et al., 1997c], two computer codes widely used in the simulation of the interaction between radiation and the surface/atmosphere system.

Chapter 2

The implementation of those aspects into atmospheric correction algorithms is described in Chapter 2. Some state-of-the-art atmospheric correction algorithms have been presented. The chapter is started with the two methods applied by ESA to the processing of MERIS data. One was proposed by Santer et al. [1999], and is implemented in the MERIS ground segment to derive the Level 2 reflectance product. However, this method failed in the estimation of the AOT over land surfaces, as only few pixels were found to be valid for the retrieval. As a result, the MERIS Level 2 reflectance product is still affected by the aerosol contribution. The BAER method [von Hoyningen-Huene et al., 2003] was selected to complete the aerosol correction. Apart from those two methods, the reference algorithms applied to MODIS [Vermote et al., 1997a], MISR [Martonchik et al., 1998], AATSR [Grey et al., 2006] have been described. A final review of several "classical" methods applied to Landsat TM/ETM have been also addressed.

Chapter 3

A full description of the atmospheric correction scheme for MERIS data presented in this work is given. All the steps in the conversion from TOA radiance to surface reflectance and atmospheric products are described. Those include a cloud masking technique, which is based on sets of static thresholds to be selected by the user as a tradeoff between the number of masked pixels and the probability of cloud contamination. The correction of topographic effects is discussed then. The direct and diffuse irradiance arriving at the target are weighted by the actual illumination angle, which is calculated from a DEM overlapped to the MERIS image. AOT, CWV and surface reflectance retrieval methods are reported after.

The AOT retrieval module is the most complex one. AOT retrieval is performed on cells of 30×30 km in which the image is divided. For each cell, an initial AOT estimation is obtained from the darkest pixel, assuming that all the radiance measured at that point is due to atmospheric multiple scattering. A further refinement is performed at those cells with sufficient green vegetation and bare soil pixels. The TOA radiances at 5 land pixels (mix of vegetation and bare soil, with as mush spectral contrast as possible) are inverted assuming the surface reflectance can be provided by a linear combination of two endmembers, pure vegetation and bare soil spectra. The endmember abundances and the AOT at 550 nm are retrieved concurrently. No attempt of aerosol type retrieval is performed, because not enough information about aerosol optical properties is found in MERIS data over land. A rural aerosol model is set instead. Both the number of 5-pixels clusters and the number of vegetation endmembers to be tried in the inversion are set by the user, according to computation time criteria. The final step is the closing of gaps and smoothing of the resulting mosaic-like AOT map.

The CWV retrieval is performed afterwards. It relies on the inversion of the ratio of MERIS band 15 to 14, which gives information about the depth of the left wing of the water vapor absorption feature centered at 940 nm. An estimation of surface reflectance is necessary for the inversion. This is achieved by assuming a default CWV value of 2 g·cm^{-2} for the atmospheric correction of bands 13 and 14, which are nearly free of water vapor absorptions, and the reflectance at band 15 is retrieved by extrapolation from 13 and 14. CWV is retrieved then by a 1-D inversion. This procedure can also be refined by iterating over the retrieved CWV value, which is applied to the estimation of a new surface reflectance instead of the default 2 g·cm^{-2} value. The alternative use of this loop is chosen by the user.

Surface reflectance is directly computed from the atmospheric parameters which provided the final CWV in the inversion procedure in 12 of the 15 MERIS bands. Linear interpolations are used for MERIS 2, 11 and 15, as reflectance errors are usually found due to either radiometric calibration errors (band 2) or inaccurate radiative transfer calculation inside absorption bands (11 and 15).

In the same chapter, the design of the atmospheric LUT which provides the atmospheric parameters for radiative transfer computations is detailed. The most suitable breakpoint numbers and positions for each of the free parameters in the LUT (i.e., VZA, SZA, RAA, surface elevation, AOT and CWV) are chosen by means of the simulation of scattering and absorption processes. An optimized version of MODTRAN4 (Appendix C) is utilized for the large number of radiative transfer calculations needed in the development of the LUT.

Finally, a sensitivity study providing approximate errors in the retrieved parameters have been carried out. The method has been tested against a number of input combinations and atmospheric situations. It has been found that the most important dependence on AOT retrieval is the particular spectral pattern of the reference pixels used for the inversion. CWV is mostly affected by MERIS spectral calibration, through spectral shifts from the band setting at which the LUT is generated. Overall errors in AOT of ±0.03 and ±4% in CWV have been estimated. For surface reflectance, a mean relative error of ±8% is associated in the whole 400–900 nm range.

Chapter 4

The validation of the atmospheric and reflectance products is carried out in this chapter. The validation exercise have relied on the comparison with external reference data, either from AERONET stations all over the world, local field campaigns in the Barrax study site (SPARC 2003/2004 and SEN2FLEX) or comparison with other satellite products.

AOT retrievals are compared in first place with ground-based measurements taken by a sunphotometer during the SPARC campaigns. A good agreement is found in the aerosol loading, although errors in the AOT spectral slope are found when an episode of Saharan dust intrusion is detected, due to the actual aerosol model separates from the rural model selected for the generation of the LUT. A qualitative comparison with BAER AOT retrievals is also presented. Similar AOT spatial distributions are retrieved by the two methods, although higher mean AOT values are registered by BAER, possibly due to a bad cloud masking. SCAPE-M has also been tested under extreme turbid conditions, such as the Portugal fires in 2003 and Beijing pollution. High AOT patterns were well reconstructed in the derived maps. Finally, a quantitative validation comparing SCAPE-M AOT retrievals from more than 200 MERIS images with AERONET data from stations around the world is presented. Mean R^2 values were around 0.7–0.8, although some case with very low R^2 (0.337, El Arenosillo station) or very high (0.925, Toulouse, FR data) are also found. A systematic underestimation of MERIS-derived AOT with respect to AERONET measurements for the highest aerosol loadings must be investigated.

A similar analysis is done over CWV retrievals. These are firstly compared with ground measurements taken during the SPARC campaigns. Good correlation with sunphotometer measurements and radiosoundings were obtained, although only two dates were available for comparison. AERONET data were used again in order to have more spatial and temporal sampling. Very good correlation were generally found, with $R^2 > 0.9$ in most of the cases. Those include stations located around the Amazon jungle, where high water vapor concentrations were measured (up to 4.8 $\mathrm{g\cdot cm^{-2}}$). The final study was based on comparing the SCAPE-M retrievals with the ESA official Level 2 water vapor product. Even though a general agreement was found, some deviations mainly associated to elevation was detected. In particular, SCAPE-M gave higher CWV than the ESA product for mean/high elevations (around 300 m or higher), while it happened on the contrary for targets at sea level. Less dependence on the target spectral response was found in SCAPE-M.

Finally, surface reflectance retrievals were compared with different sources. The first one was a CHRIS/PROBA image acquired over the Barrax site at the same time than a MERIS image. The 34 m per pixel CHRIS spatial resolution enabled comparison with ground measurements, so it was used as an intermediate step between MERIS and ground-based reflectance measurements. Good correspondence in the derived reflectance patterns was found in homogeneous targets. On the other hand, SCAPE-M reflectance retrievals are also compared with BAER-derived reflectance maps. The correlation between the two products improved by wavelength, and R^2 higher than 0.96 were calculated at the red and NIR wavelengths. These values were considerably lower (around 0.6) in the case of the first MERIS band, possibly due to the high contamination by aerosols. Finally, MERIS-derived water reflectance from inland water bodies were compared with concurrent ground-based measurements. A good correspondence in both the average reflectance leves and the spectral shapes was found.

Chapter 5

This final chapter deals with the estimation of chlorophyll fluorescence from MERIS data. MERIS band 11 centered at the bottom of the O_2-A absorption feature, together with band 10 used as reference, provide the basic information to separate the contribution of the emitted fluorescence from the reflected solar radiation. It has been justified that several factors, both environmental (aerosol loading, surface elevation, reflectance) and technical (instrument spectral calibration) affect the O_2 absorption depth measured by MERIS. Thus, fluorescence retrieval must be coupled to an atmospheric correction scheme providing a proper account of those factors. The CF maps generated from MERIS data showed a good correspondence with the typical variation ranges published in the literature. The CF signal is not redundant with other vegetation indicators, although it seems to have a better correlation with indices indicating pigment concentrations rather than vegetation amount. Quantitative validation was achieved by comparing MERIS CF retrievals with those from airborne CASI-1500 data. The latter were taken at a 3 m spatial scale, so the intercomparison with ground-based fluorescence measurements is meaningful. A extremely linear correlation of $R^2 = 0.976$ was found, although only 5 points were used. A systematic overestimation of CASI retrievals against ground-based measurements must be investigated.

Many statements and conclusions have been highlighted within the different topics addressed along this work. Some of them can be outlined here as the main concluding remarks.

- A new tool for the processing of MERIS Level 1b data is available for the remote sensing community. Automatic atmospheric and geometric correction are performed over the original MERIS images. Surface reflectance, aerosol optical thickness, columnar water vapor and chlorophyll fluorescence maps are obtained as a result.
- The retrieval of AOT over land is a complex task affected by many factors:
    1. The most important one may be the availability of an adequate model accounting for the contribution of surface reflectance to the TOA radiance. It must enable the decoupling between the radiation reflected by the surface and the one reflected by the atmosphere.
    2. A proper estimation of the aerosol model is also a challenging topic, especially in the case of MERIS (400-900 nm and one single view angle). The inclusion

of parameters describing the aerosol model adds extra free parameters to the inversion of TOA radiance, and MERIS spectral/angular configuration seems not sufficient to achieve robust values for all the parameters. For this reason, the rural aerosol model was adopted for the generation of the LUT. However, this may lead to inaccurate AOT retrievals when other aerosol types are present.

3. The spatial variation of aerosols must be investigated. The method proposed in this thesis performs AOT retrievals based on 30×30 km cells, in which the atmospheric state is assumed to be laterally homogeneous. This strategy provides important advantages, such as the availability of a whole area from which reference pixels can be selected and the reduction of the computational burden. However, no finer information about the aerosol distribution is obtained. This means that pixel-to-pixel variations within the cell are not detected. Whether those local variations in atmospheric conditions are likely to happen or not is not clear, but they are possibly relevant in topographically complex areas.
4. Unmasked cloudy pixels lead to out-of-range AOT values. This may be an important problem in the case of thin cirrus clouds, which are very difficult to detect. Some effort on developing robust cloud-masking techniques applicable to MERIS data would lead to better AOT estimations.

- The retrieval of CWV does not require such an important modelling effort. The main constraint has been found to be in the associated computational time, as retrievals on a per-pixel basis may be very time consuming for the largest images. The main error source in the case of MERIS is the variation of the band spectral positions in the along track direction of the CCD, which result in errors up to 0.2 $g{\cdot}cm^{-2}$ in camera transitions.

- Apart from AOT and CWV, other factors must be considered in the retrieval of surface reflectance. It is affected by both surface elevation and topographic effects, which are normally neglected in atmospheric correction methods. SCAPE-M takes them into account. The adjacency effect is also included by a simple model, but directional effects are not considered. No adequate modelling of the surface directional reflectance has been found which could be plugged into an operational procedure. Therefore, errors associated to the Lambertian approach are assumed to be intrinsic to the method, although it has been shown that the Lambertian assumption can provide accurate results in those cases where a principal plane geometry is not present.

- The chlorophyll fluorescence signal is a promising indicator of the vegetation conditions, closer to photosynthesis than other vegetation indices. Even though that signal is very weak respecting to other contributions, a first step towards its quantitative detection has been presented in this thesis. Further research in that direction could open a new line in the monitoring of vegetation from the space.

Part IV

Appendices

Appendix A

Acronyms

AATSR Advanced Along Track Scanning Radiometer

AERONET AErosol RObotic NETwork

AOT Aerosol Optical Thickness

ASD Analytical Spectral Devices

ASL Above Sea Level

BAER Bremen AErosol Retrieval

BEAM Basic ERS & Envisat (A)ATSR and MERIS

BRDF Bidirectional Reflectance Distribution Function

BRF Bidirectional Reflectance Factor

CASI Compact Airborne Spectrographic Imager

CCD Charge Coupled Device

CF Chlorophyll Fluorescence

CHRIS Compact High Resolution Imaging Spectrometer

CWV Columnar Water Vapor

DDV Dense Dark Vegetation

DEM Digital Elevation Model

DISORT DIScrete Ordinate Radiative Transfer

ELEV ELEVation

ENVISAT ENVIronmental SATellite

ESA European Space Agency

fAPAR Fraction of Absorbed Photosynthetically Active Radiation

fCover Fractional Vegetation Cover

FLD Fraunhofer Line Discriminator

FOV Field Of View

FR Full Resolution

FWHM Full Width at Half Maximum

IFOV Instantaneous Field Of View

LAD Leaf Angle Distribution

LAI Leaf Area Index

LUT Look-Up Table

MERIS MEdium Resolution Imaging Spectrometer

MTCI MERIS Terrestrial Chlorophyll Index

MODIS Moderate Resolution Imaging Spectroradiometer

MODTRAN MODerate Resolution TRANsmittance

NDVI Normalize Difference Vegetation Index

NIR Near InfraRed

NDOI Normalized Difference at Oxygen-A absorption Index

PRI Photochemical Reflectance Index

PROBA PRoject for On-Board Autonomy

RAA Relative Azimuth Angle

RGB Red-Green-Blue

RR Reduced Resolution

RTC Radiative Transfer Code

RTE Radiative Transfer Equation

RMSE Root Mean Square Error

SCAPE-M Self-Contained Atmospheric Parameters Estimation from MERIS data

6S Second Simulation of the Satellite Signal in the Solar Spectrum

SAA Sun Azimuth Angle

SEN2FLEX SENtinel-2 and FLuorescence EXperiment

SPARC SPectra bARrax Campaign

SZA Sun Zenith Angle

TOA Top Of Atmosphere

VIS VISible/VISibility

VNIR Visible and Near InfraRed

VZA View Zenith Angle

Appendix B

MERIS Instrument Description

Medium Resolution Imaging Spectrometer (MERIS) [European Space Agency, 2006; Rast et al., 1999] was launched by the European Space Agency (ESA) onboard its polar orbiting ENVISAT Earth Observation Satellite in March 2002. MERIS is a programmable, medium-spectral resolution, imaging spectrometer operating in the VNIR reflective spectral range. The ENVISAT/MERIS system is depicted in Fig B.1.

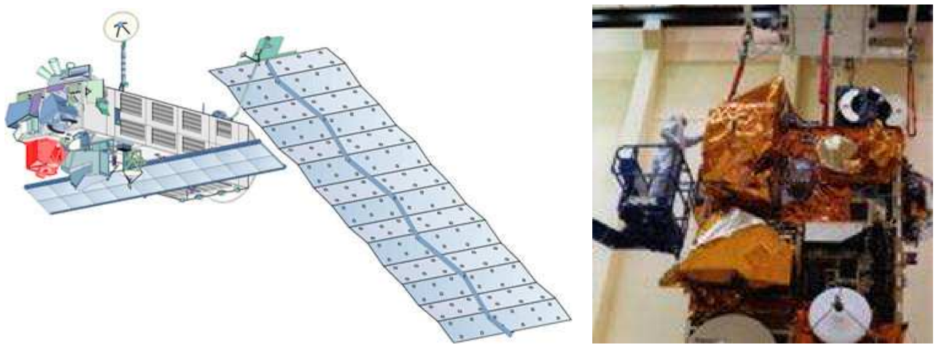

(a) (b)

Figure B.1: ENVISAT/MERIS system. Left (a), location of MERIS on ENVISAT. Right (b), MERIS instrument (from European Space Agency [2006]).

The instrument scans the Earth's surface by the so called "push-broom" method. Linear CCD arrays provide spatial sampling in the across-track direction, while the satellite's motion provides scanning in the along-track direction. MERIS is designed so that it can acquire data over the Earth whenever illumination conditions are suitable (illumination angles below 80°) with high radiometric (1 to 5%) and spectrometric (1 nm) performance. The calibration of MERIS is performed at the orbital south pole, where the calibration diffuser is illuminated by the Sun by rotating a calibration mechanism. In the calibration mode, correction parameters such as offset and gain are generated, which are then used to

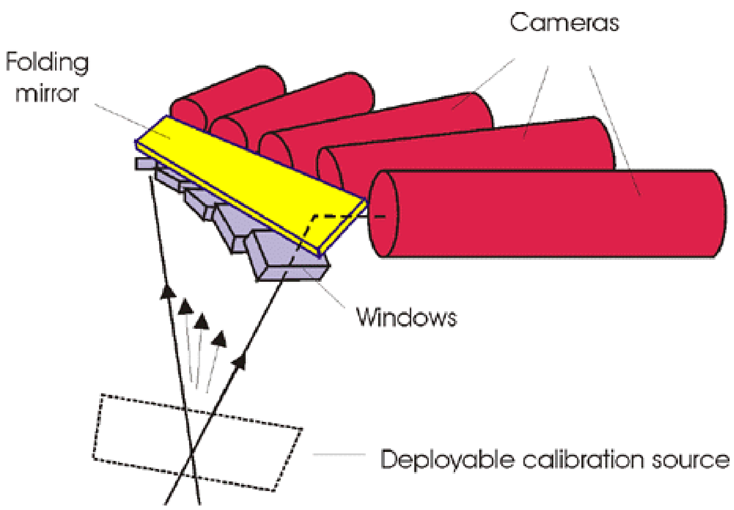

Figure B.2: Arrangement of MERIS optical modules, folding mirror and Earth viewing windows (from European Space Agency [2006]).

correct the recorded spectra. This correction can be carried out either on-board or on the ground.

The MERIS' 68.5° FOV around nadir covers a swath width of 1150 km at a nominal altitude of 800 km. It allows global coverage of the Earth in 3 days. The IFOV is divided into five segments, each of which is imaged by one of the corresponding five cameras, as shown in Fig. B.2. A slight overlap exists between the FOVs of adjacent optical cameras. An area CCD detector is used, with an instantaneous detector element FOV of 1.149 arcmin.

Fifteen spectral bands can be selected by ground command, each of which has a programmable width and a programmable location in the 390 nm to 1040 nm spectral range. However, a fixed set of bands was recommended by the Science Advisory Group (SAG) and frozen before launch. It is presented in Table B.1. The level 2 ESA products are being developed and will be validated for this set of bands. It is possible to use alternative band sets for experimental campaigns of a few weeks duration.

The scene is imaged simultaneously across the entire spectral range, through a dispersing system, onto the CCD array. Signals read out from the CCD pass through several processing steps in order to achieve the required image quality. These CCD processing tasks include dumping of spectral information from unwanted bands, and spectral integration to obtain the required bandwidth. Onboard analogue electronics perform pre-amplification of the signal and correlated double sampling and gain adjustment before digitization. The onboard digital electronics system has three major functions: it completes the spectral integration, performs offset and gain corrections in full processed mode, and creates the

Table B.1: MERIS fixed set of bands.

n°	Band centre (nm)	Band width (nm)	Application
1	412.5	10	Yellow substance and detrital pigments
2	442.5	10	Chlorophyll absorption maximum
3	490	10	Chlorophyll and other pigments
4	510	10	Suspended sediment, red tides
5	560	10	Chlorophyll absorption minimum
6	620	10	Suspended sediment
7	665	10	Chlorophyll absorption and fluorescence reference
8	681.25	7.5	Chlorophyll fluorescence peak
9	708.75	10	Fluorescence reference, atmosphere corrections
10	753.75	7.5	Vegetation, cloud
11	760.625	3.75	O_2 R- branch absorption band
12	778.75	15	Atmosphere corrections
13	865	20	Vegetation, water vapor reference
14	885	10	Atmosphere corrections
15	900	10	Water vapor, land

reduced-resolution data when required.

MERIS provides either full spatial resolution data (RR) or reduced spatial resolution data (FR). These two spatial resolutions, for the nominal orbit are:

- Full spatial resolution: 260 m across track, 290 m along track. Full FR scenes have 2241×2241 pixels and cover 582 km (swath) by 650 km (azimuth). Quarter scenes have 1153×1153 pixels and cover 300 km (swath) by 334 km (azimuth).
- Reduced spatial resolution: 1040 m across track, 1160 m along track. A reduced spatial resolution pixel is obtained by averaging the signal of 16 full spatial resolution pixels. More precisely, 4 adjacent pixels across-track for 4 successive pixel lines along-track are used. Resolution scenes have 1121×1121 pixels and cover 1165 km (swath) by 1300 km (azimuth).

Appendix C

Optimization of MODTRAN4 for the generation of LUTs: the ATLUT code

C.1. Mathematical background supporting MODTRAN4 optimization

The path radiance $L_p(\rho)$ and the total radiance $L_{total}(\rho)$ at the sensor level for a surface with reflectance ρ are given in MODTRAN4 [Richter, 1996] by

$$L_p(\rho) = L_p(0) + t_{dif} E_g(\rho)\rho/\pi \tag{C.1.1}$$

and

$$L_{total}(\rho) = L_p(\rho) + t_{dir} E_g(\rho)\rho/\pi, \tag{C.1.2}$$

where t_{dif} and t_{dir} are the spectral transmittances for diffuse and direct radiation, respectively, travelling upwards from the surface to the sensor, E_g is the global flux reaching the surface, equal to the direct plus diffuse fluxes $E_{dir}\mu_s + E_{dif}(\rho)$, μ_s being the cosine of the solar zenith angle. The multiple scattering between the atmosphere and the surface is computed in Eqs. C.1.1 and C.1.2 by means of the diffuse flux $E_{dif}(\rho)$ component, which is coupled to the surface reflectance. Since the aim of the ATLUT program is to obtain the intrinsic atmospheric parameters, independently of the surface below, Eq. C.1.2 must be rewritten to eliminate the dependence of the atmospheric parameters on ρ. In spectral regions where scattering is noticeable, it can be expressed as

$$L_{total}(\rho) = L_p(0) + \frac{T E_g(0)\rho/\pi}{1 - \rho S}, \tag{C.1.3}$$

where S is the atmospheric spherical albedo and T is the total transmittance $t_{dir} + t_{dif}$. This equation is formally identical to Eq. 3.1.1. It can be stated that ρ can be analytically inverted from L_{total} in Eq. C.1.3 which is the aim of atmospheric correction, as all the variables are independent of ρ. Thus, $L_p(0)$, t_{dir}, t_{dif}, E_{dir}, E_{dif}, and S must be calculated as the initial step in the atmospheric correction procedure.

The term t_{dir} is directly given by MODTRAN4. Concerning the fluxes, the explicit separation of the direct and diffuse fluxes in E_g is highly useful if the effects of topography are to be taking into account in the atmospheric correction [Richter, 1998; Richter and Schlaepfer, 2002]. The cosine of the local incident sun angle μ_s changes from pixel to pixel according to the terrain slope and its orientation, and must be provided externally as an input in the retrieval of the surface reflectance. The fluxes can be retrieved either from the radiance calculations or from MODTRAN4's flux file. Nevertheless, since the fluxes directly calculated by the `spcflx.f` subroutine may be inaccurate in spectral regions with strong gaseous absorptions, they are retrieved from the radiances in routine `trans.f`, using

$$E_{dir} = \frac{\pi L_{r,dir}}{\mu_s t_{dir} \rho} \tag{C.1.4}$$

$$E_{dif}(\rho) = \frac{\pi L_{r,total}}{t_{dir} \rho} - \mu_s E_{dir} \tag{C.1.5}$$

where $L_{r,dir}$ and $L_{r,total}$ are the direct and total reflected radiances, respectively, reaching the sensor after being reflected by the target surface.

Concerning $L_p(0)$, t_{dif} and S, it can be shown from Eqs. C.1.1 to C.1.3 that they can be computed from two MODTRAN4 runs, with two different values of the surface reflectance, ρ_1 and ρ_2. With a little algebra:

$$L_p(0) = \frac{L_p(\rho_2)\rho_1 E_g(\rho_1) - L_p(\rho_1)\rho_2 E_g(\rho_2)}{\rho_1 E_g(\rho_1) - \rho_2 E_g(\rho_2)}, \tag{C.1.6}$$

$$t_{dif} = \frac{\pi [L_p(\rho_1) - L_p(0)]}{\rho_1 E_g(\rho_1)} \tag{C.1.7}$$

and

$$S = \frac{E_g(\rho_2) - E_g(\rho_1)}{\rho_2 E_g(\rho_2) - \rho_1 E_g(\rho_1)} \tag{C.1.8}$$

Apart from the variables appearing in Eq. C.1.3, aerosol optical thickness τ is the natural optical parameter for the quantification of the aerosol loading. It is not accessible in the original MODTRAN4 neither as input nor as output. The AOT is defined as the integration of the aerosol extinction coefficient β_{ext} over the vertical path from the surface to the TOA:

$$\tau(\lambda) = \int_{z=0}^{z=TOA} \beta_{ext}(z, \lambda) dz \simeq \sum_{i=0}^{N_l} \beta_{ext}(z_i, \lambda) \Delta z_i \tag{C.1.9}$$

where z is the altitude above the ground surface, and N_l the number of atmospheric layers in the aerosol profile. According to Kneizys et al. [1996], the extinction coefficients are generated in MODTRAN4 as a product of an altitude dependent aerosol concentration $s(z_i)$, and a wavelength dependent aerosol extinction $k_{ext}(\lambda)$:

$$\beta_{ext}(z_i, \lambda) = s(z_i) k_{ext}(\lambda) \tag{C.1.10}$$

Both $k_{ext}(\lambda)$ and $s(z_i)$ are given in 4 separate height levels, with different aerosol models. Nominally, there are boundary layer aerosols (0–2 km), tropospheric aerosols (2–10 km), stratospheric aerosols (10–30 km) and volcanic aerosols (30–100 km). The $s(z_i)$ density profile is given by `aernsm.f`, while the routine `aerext.f` interpolates aerosol extinction, absorption and asymmetry coefficients for a given wavelength from the MODTRAN4 aerosol database in `extdta.f`. Thus, the aerosol loading is not only parameterized in ATLUT by the horizontal visibility or the aerosol plus Rayleigh plus ozone optical thickness at 550 nm, which are the standard variables in MODTRAN4, but also by the spectral AOT, which is the most widely used magnitude in the quantification of aerosol content.

In order to achieve the maximum accuracy in the calculation with the minimum time penalty, the scaled DISORT option of MODTRAN4 is used. It performs a set of DISORT runs to scale the results obtained from the faster but less accurate Isaacs 2–stream algorithm [Isaacs et al., 1987]. However, the scaling is not performed by MODTRAN4 over E_{dif} for a black surface ($\rho = 0$), if the variables containing the fluxes in the code are used, leading to significant miscalculations of the spherical albedo that cause substantial errors in the TOA radiances expressed in Eq. C.1.3. Moreover, if $\rho = 0$ equations C.1.4 and C.1.5 can not be applied for the calculation of the fluxes from the TOA radiances. These reasons justify that $0 < \rho_{1,2} < 1$. Neither from the mathematical point of view nor from the physical one there is any constraint for the selection of $\rho_{1,2}$, so values of $\rho_1 = 0.5$ and $\rho_2 = 0.15$ have been selected representing high and medium reflectances of natural targets.

C.2. Results and Validation

Both the validity of the proposed mathematical scheme in Eq. C.1.3 and the consistency of the radiative transfer functions in Eqs. C.1.6-C.1.8 have been assessed comparing ATLUT with the original MODTRAN4 code running under DISORT with 8 streams. The simulations presented hereinafter have been done in the visible and near–infrared spectral regions (400–1000 nm), which is about the range covered by MERIS and where the role of multiple scattering is most relevant. The input parameters can be grouped into three categories: the first one comprises the atmospheric properties, e.g., water vapor and aerosol properties. For the validation, a midlatitude summer atmosphere with a water vapor column of 2 g·cm^{-2} has been selected, and a rural aerosol with a horizontal visibility of 23 km.

The second one describes the geometric configuration, i.e., VZA, SZA and RAA between the sensor line-of-sight and the solar azimuth. Here nadir and 30° VZAs are investigated, as well as 30° and 60° SZAs. The configuration with VZA= 30°, SZA= 60° and RAA= 0° (backscatter geometry) is assumed to be the critical ("worst") case. The geometry combination of a nadir view with a SZA= 30° is called the "favorable" case in this study. The last group describes the surface reflectance properties. Here, constant reflectances of 0.3 and 0.0 (black ground) are considered.

The relative errors in the TOA radiance associated to the ATLUT code (Eq. C.1.3) and to MODTRAN4 using the Isaacs' method calculated taking MODTRAN4 using the DISORT method with 8 streams as reference are plotted in Fig. C.1 at 5 cm^{-1} of sampling interval. For the favorable case, Fig. C.1(a), it can be seen that the errors in the Isaacs' method are larger than 4% in the shortest blue wavelengths. Outside the main absorption regions, the relative error becomes nearly constant around 0.8-0.9%. In the case of the ATLUT code, the error fluctuates around 0% even in the shortest blue wavelengths, outside the absorption regions. In those wavelengths affected by oxygen and water vapor absorptions, sharp error peaks up to 12% appear. However, the resampling of the output radiances to typical bandwidths of remote sensing instruments smoothes these errors considerably. For example, filtering the TOA radiances with a set of 1000 Gaussian functions with Full Width Half Maximum (FWHM) of 7.5 nm (with a regular step interval of 0.6 nm) leads to maximum relative errors of 4% (Isaacs method), and mean errors in the strongest absorptions bands of 2% (both methods, plots not shown here). Results for the "worst" case conditions are shown in Fig. C.1(b). Relative Isaacs errors are up to about 9% in the shortest blue region while ATLUT errors are below 0.5% outside the absorption regions. Again, if the TOA radiances are resampled to FWHM=7.5 nm the maximum relative errors are below 4% and mean errors in the strongest absorption bands are 2%.

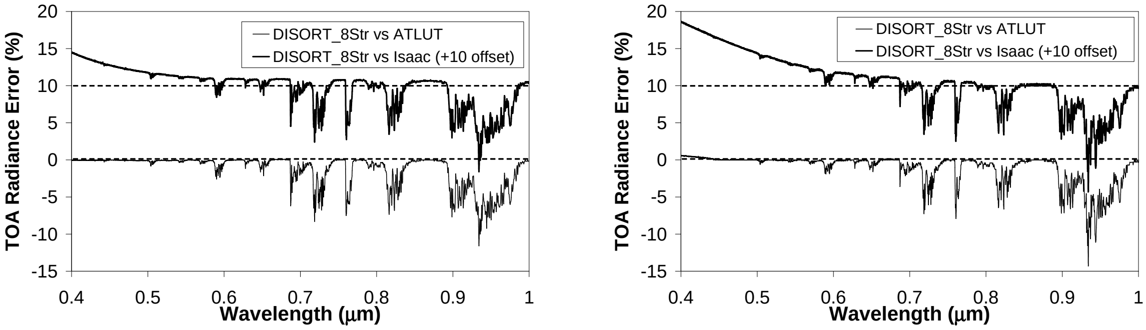

(a) (b)

Figure C.1: Relative error in the TOA radiances comparing the ATLUT code and Isaacs 2 stream algorithm in MODTRAN4 versus the DISORT algorithm with 8 streams (with an offset of +10% for clarity purposes) for the "favorable" geometry (a), the "worst case" geometry (b).

The TOA radiance signal simulated by MODTRAN4 with DISORT-8 and ATLUT around the 760 nm oxygen absorption band is displayed in Fig. C.2. In spite of the deep absorption band, a very good agreement is found between the two curves. The relative error inside the band is around 8%, but becomes smaller than 3% if the resampling to 7.5 nm is used, as plotted in the figure.

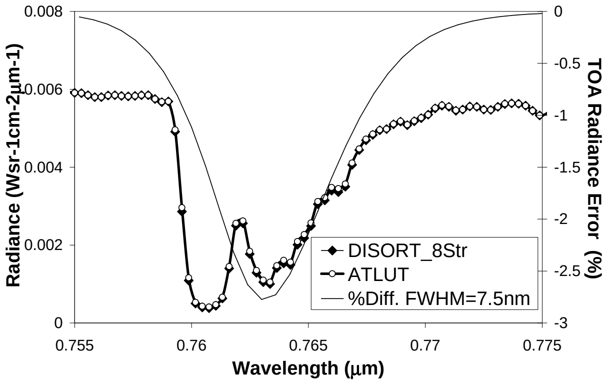

Figure C.2: TOA radiances in the 760 nm oxygen band with a spectral resolution of 5 cm^{-1} calculated by ATLUT and MODTRAN4 in the "worst case" geometry. The relative error after the resampling with a set of Gaussian functions with FWHM=7.5 nm is depicted by the solid line.

The total computation time for a single run of MODTRAN4 using the DISORT 8–stream option was 13.6 min in a SGI Altix 3700 workstation for the selected 400 - 1000 nm region, while it decreased to 5.8 sec if the Isaacs algorithm was used instead. This huge decrease in the computation time was also achieved by using the ATLUT code, which took 6.8 sec to perform the calculation with the same set of inputs, thanks to the use of the DISORT scaling option instead of DISORT computations over the whole spectrum.

With respect to the self–consistency of the separate radiative transfer variables in Eq. C.1.3, a comparison of the atmospheric path radiance calculated by MODTRAN4–DISORT and ATLUT is plotted in Fig. C.3 showing the "worst" case. For the DISORT run, a black surface ($\rho = 0$) was set as input. Thus, $L_p(0)$ is given directly, which avoids possible inaccuracies caused by the indirect retrieval of eq. C.1.6. It can be stated that there is good agreement between the two approaches. It must be taken into account that most of the contribution to the TOA signal by the back-scattered radiation occurs in the shortest visible wavelengths, where the error is smaller than 1%. If the spectral resolution is degraded to typical remote sensing channel widths $\geq$ 7.5 nm the error of the scaled DISORT is smaller than 0.6% all over the 400-1000 nm window.

For the spherical albedo, the calculations performed by ATLUT using the DISORT scaling option have been compared with ATLUT running under DISORT with 8 streams and

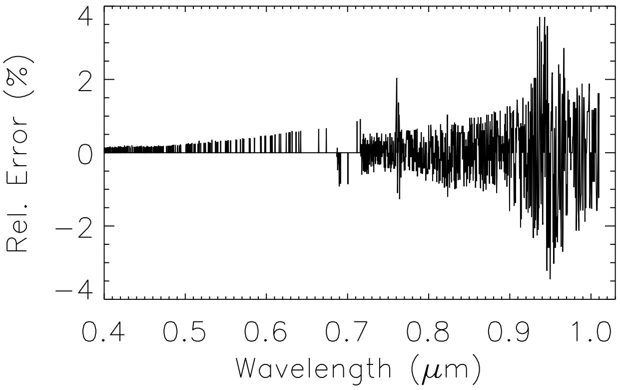

Figure C.3: Relative error in atmospheric path radiance calculated by the ATLUT code and the original MODTRAN4-DISORT for a black surface for the "worst" case with 5 cm^{-1} resolution.

under the original Isaacs algorithm. Results are plotted in Fig. C.4 for the two geometrical configurations. Small differences between DISORT and the scaled results are obtained, only noticeable in the strongest absorption bands. However, large underestimations appear if the original Isaacs method is used, because the 2-stream inaccuracies in the computation of multiple scattering are amplified in Eq. C.1.8. This underestimation of spherical albedo by Isaacs' algorithm is also reported in Verhoef and Bach [2003]. The consistency of the spherical albedo with the other variables leads to small deviations for ATLUT in the subsequent L_{total} generated by Eq. C.1.3. It is also worthy noting that the values of the spherical albedo remain constant after a strong change in the angular configuration, which is expected a priori because the atmospheric state is the same in both cases. This fact confirms the stable numerical performance of Eq. C.1.8 for the retrieval of albedo from MODTRAN4 runs.

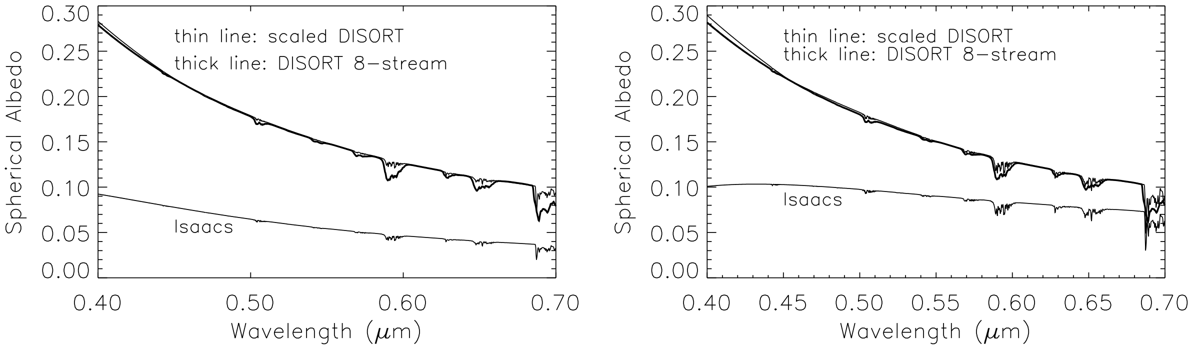

(a)

(b)

Figure C.4: Atmospheric spherical albedo calculated using the ATLUT code with DISORT 8 streams, Isaacs' algorithm and Isaacs' algorithm scaled to DISORT calculations for (a) "favorable" case and (b) "worst" case geometric configurations.

An example of the AOT calculated by the ATLUT code is depicted in Fig. C.5. Fig. C.5(a) displays the spectral behavior of the AOT for different aerosol models. For the rural and maritime models the same horizontal visibility is set. The spectral slope is different for the two models mainly because of the different particle size distributions. The normalization at 550 nm can be observed as the intersection at this wavelength. On the other hand, the vertical distribution of $\beta_{ext}(s_i, \lambda)$ is plotted in Fig. C.5(b). The main conclusion is that the change in aerosol loading takes place in the first aerosol layer, which is the one between 0 and 2 km. The value of $\beta_{ext}(s_i, \lambda)$ decreases rapidly as the height is increased.

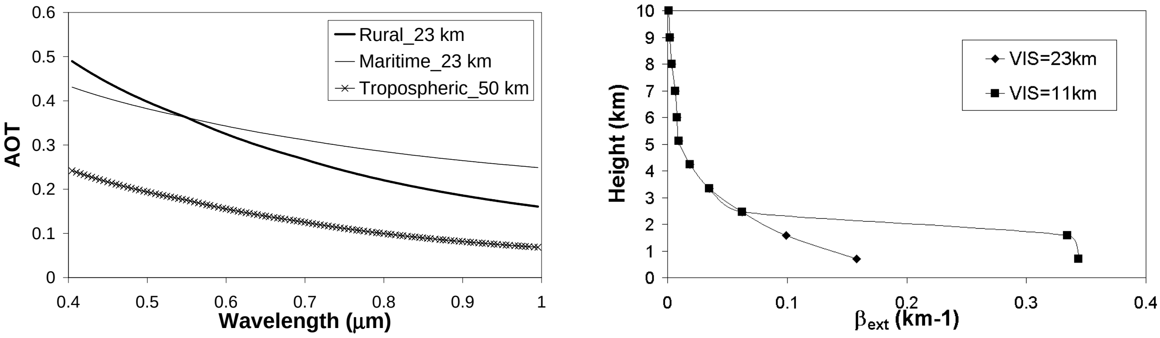

(a) (b)

Figure C.5: Example of aerosol features derived by the ATLUT code. Left (a), spectrum of AOT for three different aerosol models and horizontal visibility values calculated by the ATLUT code. Right (b), vertical profile of the aerosol extinction coefficient $\beta_{ext}(z_i, \lambda)$ for the rural model and two different contents. Each symbol corresponds to an altitude level.

Appendix D

SCAPE-M Software: Computational Issues

D.1. SCAPE-M software for the processing of MERIS L1b images

The *Self-Contained Atmospheric Parameters Estimation from MERIS data* (SCAPE-M) software is intended to cover the gap in the atmospheric correction of MERIS Level 1b images. It provides geo-referenced atmospherically corrected MERIS images starting from MERIS Level 1b FR or RR images. The software does not make any use of external parameters in the correction, but all the inputs are read from the meta-data attached to original MERIS images. SCAPE-M is a self-contained atmospheric processor for MERIS data, as reflectance images and atmospheric parameters are derived in a consistent way utilizing the same input data and the same atmospheric data base for the entire process. Moreover, no other code dealing with MERIS data is reported to take into account effects such as topography or adjacency in the retrieval of surface reflectance. Those features make SCAPE-M a robust and reliable tool in the field of the atmospheric correction of MERIS data.

The software is platform-independent thanks to the use of IDL and JAVA virtual machines. It has been tested under IDL6.0 and BEAM3.5 versions, but it is not guaranteed under older versions.

D.2. Installing SCAPE-M

The SCAPE-M code is written in the IDL[1] language. The software will be delivered under the GNU license as a binary file to be run by means of the IDL Virtual Machine, which is freely available after registration of the user.

The SCAPE-M software must be installed jointly to the BEAM software [Fomferra and Brockmann, 2005], as it makes use of some of the processors delivered with BEAM, as well as of the BEAM's IDL Application Programming Interface (API). The BEAM's IDL API is used to read the data attached to MERIS images, such as the raster dimensions, reference wavelengths and bandwidths and calibration coefficients. To install BEAM's API, the archive `epr_api-<version>.zip`, which is in the BEAM installation directory, must be unzipped, and the files `epr_idl_api.so` (`epr_idl_api.dll` for MS Windows) and `epr_idl_api.dlm` must be copied in the directory given by the IDL system variable `!DLM_PATH`. This directory can be figured out by simply typing `print, !DLM_PATH` in the IDL command line (normally, `!DLM_PATH` is `IDL/bin/bin.x86`).

Concerning the BEAM software, the GETASSE30 DEM and the `geopos_corrector.jar` plug-in must be properly installed according to the BEAM installation instructions. SCAPE-M calls the `mapproj` processor if the atmospheric correction output must be geometrically corrected. If large images are to be processed, problems with memory allocation can arise when `mapproj` is called. Those may be sorted out by adding the line `lax.nl.java.option.java.heap.size.max = 1073741824` to the file `mapproj.lax`.

Another processor which is called by SCAPE-M is `MERIS2dim`. It is not delivered with the BEAM software, but it was developed by Luis Gómez-Chova from the Electronic Engineering Department of the University of Valencia. The `MERIS2dim` processor converts original MERIS images into the `BEAM-DIMAP` format, and adds bands with ancillary information, such as the observation and illumination angles and the DEM overlapped to the area registered by MERIS. This processor was developed from the BEAM JAVA source code, and utilizes the BEAM environment. In order to install the `MERIS2dim` processor, the files `MERIS2DIMProcessorMain.class`, `MERIS2DIMProcessor.class`, `MERIS2DIMConstants.class` and `MERIS2dim.bat` must be copied in the directory `/beam-<version>/bin/`. The path variables in the file `MERIS2dim.bat` must be updated to the actual path to the BEAM installation in the system.

---

[1] `http://www.RSInc.com`

D.3. Description of input and output files

The SCAPE-M software is driven by an ASCII file which defines the basic inputs to be set by the user. A real input file will be compounded by the following lines:

```
path_inp = E:\datos_luisguan\meris\MERIS_May06\
path_out = F:\MERIS\SPARC\MERIS_AC_Outputs\
path_beam = C:\Program Files\beam-3.5\bin\
file_LUT = E:\datos_luisguan\meris\MODTRAN_LUT_MERIS

Cloud_flg = 0
AOT_time_flg = 1
CWV_time_flg = 0
ADY_flg = 1
output_ctrl_flg = 1
GC_flg = 1

MER_FR__1PNEPA20030714_103354_000000502018_00094_07162_1052.N1
MER_FR__1PNEPA20040714_103121_000000502028_00323_12401_1055.N1
MER_FR__1PNUPA20040717_103706_000000502028_00366_12444_0896.N1
```

This file (named `MERIS_AC_SPARC_adv.inp`) will trigger the processing of three MERIS FR images (the images in the example are the ones acquired during the SPARC campaigns 2003 and 2004). The variable `path_inp` gives the directory in which the images to be processed are contained, `path_out` is the directory where the results are being written, `path_beam` is the path to the `bin` folder in the BEAM software directory, and `file_LUT` gives the location of the atmospheric LUT.

User options are controlled by a series of 6 flags:

- `Cloud_flg`: it selects the combination of cloud flags to be used in the aerosol retrieval and in the water vapor and surface retrieval. If `Cloud_flg`= 0, the default configuration is used, applying the restrictive `cloud mask #1` in the derivation of AOT maps and the relaxed `cloud mask #2` to the calculation of CWV and surface reflectance. If `Cloud_flg`= 1, `cloud mask #2` will be used in both procedures. This option enables to estimate AOT when high turbidity levels are expected in the atmosphere, e.g. in polluted areas. If `cloud mask #1` was applied, areas with high aerosol loadings will be probably masked out as clouds, and the aerosol retrieval module would not work over them. Finally, if `Cloud_flg`= 2 the tight `cloud mask #1` will be applied both to the retrieval of AOT and water vapor/surface reflectance. This guarantees that atmospheric correction has only been preformed over cloud-free pixels, so errors in surface reflectance associated to thin clouds are eliminated to the highest extent. This option is recommended if the emphasis is put on accurate reflectance values, with the penalty of some bright pixels being taken as clouds and removed from the processing.

- `AOT_time_flg`: it defines the trade-off between accuracy in AOT retrieval and computation time. If `AOT_time_flg` is set to 0, the AOT thickness is estimated using only one set of reference pixels and one vegetation endmember ("Vegetation #1" in Fig. 3.6). On the other hand, if `AOT_time_flg`= 1 AOT is estimated from one set of reference pixels per cell, but looking for the best fit amongst the three possible vegetation endmembers. Moreover, if the partial value of the Merit Function in Eq. 3.1.4 for any of the reference spectra is larger than twice the mean value from the five of them, that spectrum is removed from the inversion, and this is performed again without it. This option has been found to be the optimum one for most of the applications. All the results presented along this work have been obtained setting `AOT_time_flg` to 1. The last option, `AOT_time_flg`= 2, performs the AOT estimation over up to 5 sets of reference pixels per cell, as well as with three vegetation endmembers and the removal of he worst fit, but no major improvements were found respecting `AOT_time_flg`= 1.

- `CWV_time_flg`: analog to `AOT_time_flg`, it selects how CWV is retrieved. If `CWV_time_flg`= 0, the CWV is retrieved setting a default value of CWV= 2 g·cm^{-2} in the prior calculation of the surface reflectance in bands 13 and 14. If `CWV_time_flg` is set to 1, a refinement is performed by carrying out a new iteration with the CWV value applied in the calculation of the reflectance in bands 13 and 14 given by the value calculated in the first iteration, after applying the default CWV= 2 g·cm^{-2}. It was shown in Section 3.3 that the improvements associated to `CWV_time_flg`= 1 are only meaningful for the highest water vapor contents. If `CWV_time_flg` is set to 2, no estimation of CWV is performed, but surface reflectance images are generated by assuming CWV= 2 g·cm^{-2} all over the area. It was also shown in the sensitivity analysis in Section 3.3 that this assumption does not lead to important errors in reflectance out of bands 9 and 15, so the option `CWV_time_flg`= 2 may be useful when computation time is a constrain in the processing.

- `ADY_flg`: the adjacency effect is treated if `ADY_flg`= 1, and it is not if `ADY_flg`= 0. `ADY_flg`= 1 may lead to memory allocation problems when applied to the processing of the largest images.

- `output_ctrl_flg`: it specifies the format of the output images. If `output_ctrl_flg` is set to 0, final output is formatted as `BEAM-DIMAP` to be read by BEAM.
  If `output_ctrl_flg` is set to 1, final output is in ENVI format, with the corresponding header files being automatically generated. Two binary files are written to the hard disk, one with the 15 spectral reflectance images and other with the by-product and

ancillary data (AOT and CWV maps, illumination and observation angles, DEM...). If `output_ctrl_flg`= 2, the output is written in the two formats.

- `GC_flg`: images are geometrically corrected (latitude/longitude projection) if `GC_flg`= 1. No operation is performed if `GC_flg`= 0.

A log file is generated along the atmospheric correction process. It provides a brief summary of some of the events occurring during the processing. The log file from the processing of the MERIS FR image acquired during the SPARC campaign 2003 is listed below:

```
****************************************************************************
*                                                                          *
*                               SCAPE-M v1.0                               *
*                                                                          *
*              Atmospheric processor for MERIS L1b data over land          *
*                                                                          *
*                     Luis Guanter, University of Valencia                 *
*                                                                          *
*                           email: luis.guanter@uv.es                      *
*                                                                          *
****************************************************************************


Report - MER_FR__1PNEPA20030714_103354_000000502018_00094_07162_1052.N1

Processed on Tue Aug 08 11:37:24 2006

----------------------------------------------------------------------------
***   Input Summary:

  Input file = E:\datos_luisguan\meris\MERIS_May06\MERIS_AC_SPARC_adv.inp
  Image file = MER_FR__1PNEPA20030714_103354_000000502018_00094_07162_1052.N1
  Path Inp   = E:\datos_luisguan\meris\MERIS_May06\
  Path Out   = F:\MERIS\SPARC\MERIS_AC_Outputs\
  File LUT   = E:\datos_luisguan\meris\MODTRAN_LUT_MERIS

  Cloud_flg       = 0
  AOT_time_flg    = 1
  CWV_time_flg    = 0
  ADY_flg         = 1
  output_ctrl_flg = 1
  GC_flg = 1
```

```
---------------------------------------------------------------------------
***   Output Summary:



  Percentage of land pixels = 94%

  Average AOT (@550 nm) = 0.357

  Average Columnar Water Vapor = 1.973 g·cm-2

  Warning: 62 pixels with negative reflectance values  -> Masked out


Total computation time = 13 min 56 s
   - Slope calculation time       = 1 min 33 s  (11.18% of total time)
   - AOT calculation time         = 1 min 23 s  ( 9.99% of total time)
   - WV and REFL calculation time = 7 min 24 s  (53.13% of total time)
   - Geometric correction time    = 2 min 35 s  (18.62% of total time)
   - Ancillary calculations time  = 0 min 59 s  ( 7.07% of total time)


---------------------------------------------------------------------------
---------------------------------------------------------------------------
```

D.4. Notes on computation time

A considerable effort have been put on decreasing computation times the most, in order to make SCAPE-M a useful tool for the processing of large MERIS data sets. It is difficult to give universal numbers about the overall time to process a whole image, as many factors are involved.

The main important ones are the image size and the computer resources available, but there are others which are also relevant. For example, the number of pixels contained in the 30 × 30 km cells where the aerosol distribution is assumed to be unform depend on the spatial resolution, either FR or RR. This means that the relative computation time consumed by the aerosol retrieval module is larger in RR images than in FR ones. The cloudy pixels fraction is an important factor too, as the cloudier a scene is, the less pixels are processed. The proportion of water bodies acts in the same direction, as SCAPE-M is currently intended to work only over land targets. Also the user can modify computation times by the operation modes selected by `AOT_time_flg` or `CWV_time_flg`.

To let the reader makes an idea of what computation times are about, these are detailed in Table D.1 for three images with different sizes and spatial resolutions. The processing was performed by a regular laptop PC running under Windows XP, with a 3.06 GHz Mobile Intel Pentium CPU and RAM of 480 MB.

Table D.1: Sample computation times for three MERIS images. **Image #1** is a full FR image, **Image #2** is a quarter of a FR image, and **Image #3** is a RR image.

	Image #1	**Image #2**	**Image #3**
# Samples	2241	1153	1121
# Rows	2241	1153	577
% Cloud-free land pixels	72	94	54
Total Computation Time	**73'19"**	**13'56"**	**11'27"**
- Terrain slope	6'43" (9.2%)	1'33" (11.2%)	0'52" (7.7%)
- AOT	4'7" (5.6%)	1'23" (10.0%)	2'51" (24.9%)
- CWV and Reflectance	46'33" (63.5%)	7'24" (53.1%)	5'6" (44.6%)
- Geometric Correction	12'29" (17.0%)	2'35" (18.6%)	2'11" (19.2%)
- Other Calculations	3'27" (4.7%)	0'59" (7.1%)	0'25" (3.7%)

Appendix E

MERIS Images Processed for this Thesis

E.1. Level 1b

In order to allow the results presented in this thesis to be reproducible, all the processed MERIS images are listed below. Images are classified in terms of reference site, spatial resolution and year of acquisition.

- **Iberian Peninsula, Full Resolution, 2003:**

```
1.MER_FR__1PNEPA20030413_102424_000000982015_00280_05845_0586.N1
2.MER_FR__1PNEPA20030429_102206_000000982016_00008_06074_0261.N1
3.MER_FR__1PNEPA20030701_104213_000000982017_00409_06976_0021.N1
4.MER_FR__1PNEPA20030704_104752_000000982017_00452_07019_0022.N1
5.MER_FR__1PNEPA20030714_103354_000000502018_00094_07162_1052.N1
6.MER_FR__1PNEPA20030717_103924_000000982018_00137_07205_0026.N1
7.MER_FR__1PNEPA20030720_104505_000000982018_00180_07248_0027.N1
8.MER_FR__1PNEPA20030723_105044_000000982018_00223_07291_0047.N1
9.MER_FR__1PNEPA20030726_105625_000000982018_00266_07334_0045.N1
10.MER_FR__1PNEPA20030808_104737_000000982018_00452_07520_0041.N1
11.MER_FR__1PNEPA20030814_105916_000000982019_00037_07606_0031.N1
12.MER_FR__1PNEPA20030824_104508_000000982019_00180_07749_0049.N1
13.MER_FR__1PNEPA20030912_104747_000000982019_00452_08021_0260.N1
14.MER_FR__1PNEPA20030915_105338_000000982019_00495_08064_0036.N1
15.MER_FR__1PNIPA20030514_105033_000000982016_00223_06289_0076.N1
16.MER_FR__1PNIPA20030602_105326_000000982016_00495_06561_0074.N1
17.MER_FR__1PNIPA20030615_104501_000000982017_00180_06747_0072.N1
18.MER_FR__1PNIPA20030618_105041_000000982017_00223_06790_0150.N1
19.MER_FR__1PNUPA20030312_103050_000000982014_00323_05387_1277.N1
```

20.MER_FR__1PNUPA20030406_104500_000000982015_00180_05745_0037.N1
21.MER_FR__1PNUPA20030409_105039_000000982015_00223_05788_1281.N1
22.MER_FR__1PNUPA20030502_102801_000000982016_00051_06117_1280.N1
23.MER_FR__1PNUPA20030511_104457_000000982016_00180_06246_1271.N1
24.MER_FR__1PNUPA20030512_101344_000000982016_00194_06260_1279.N1
25.MER_FR__1PNUPA20030515_101925_000000982016_00237_06303_1274.N1
26.MER_FR__1PNUPA20030527_104208_000000982016_00409_06475_1278.N1
27.MER_FR__1PNUPA20030531_101635_000000982016_00466_06532_1358.N1
28.MER_FR__1PNUPA20030603_102216_000000982017_00008_06575_1272.N1
29.MER_FR__1PNUPA20030612_103919_000000982017_00137_06704_1288.N1
30.MER_FR__1PNUPA20030619_101930_000000982017_00237_06804_1354.N1
31.MER_FR__1PNUPA20030705_101641_000000982017_00466_07033_1270.N1
32.MER_FR__1PNUPA20030711_102804_000000982018_00051_07119_1282.N1
33.MER_FR__1PNUPA20030730_103117_000000982018_00323_07391_1268.N1
34.MER_FR__1PNUPA20030809_101646_000000982018_00466_07534_1269.N1
35.MER_FR__1PNUPA20030812_102225_000000982019_00008_07577_1276.N1
36.MER_FR__1PNUPA20030815_102808_000000982019_00051_07620_1266.N1
37.MER_FR__1PNUPA20030818_103348_000000982019_00094_07663_1273.N1
38.MER_FR__1PNUPA20030825_101330_000000982019_00194_07763_1353.N1
39.MER_FR__1PNUPA20030831_102442_000000982019_00280_07849_1357.N1
40.MER_FR__1PNUPA20030916_102230_000000982020_00008_08078_1267.N1
41.MER_FR__1PNUPA20030918_105916_000000982020_00037_08107_0145.N1
42.MER_FR__1PNUPA20031005_102515_000000982020_00280_08350_1265.N1

- **Iberian Peninsula, Full Resolution, 2005:**

43.MER_FR__1PNEPA20050603_104800_000000982037_00452_17039_0976.N1
44.MER_FR__1PNEPA20050616_103929_000000982038_00137_17225_0981.N1
45.MER_FR__1PNEPA20050622_105051_000000982038_00223_17311_0974.N1
46.MER_FR__1PNEPA20050625_105631_000000982038_00266_17354_0977.N1
47.MER_FR__1PNEPA20050702_103641_000000982038_00366_17454_0221.N1
48.MER_FR__1PNEPA20050708_104800_000000982038_00452_17540_0222.N1
49.MER_FR__1PNEPA20050711_105342_000000982038_00495_17583_0219.N1
50.MER_FR__1PNEPA20050721_103930_000000982039_00137_17726_0216.N1
51.MER_FR__1PNEPA20050724_104510_000000982039_00180_17769_0258.N1
52.MER_FR__1PNEPA20050730_105628_000000982039_00266_17855_0220.N1
53.MER_FR__1PNUPA20050714_105920_000000982039_00037_17626_0987.N1
54.MER_FR__1PNUPA20050727_105050_000000982039_00223_17812_0956.N1

- **Iberian Peninsula, Reduced Resolution, 2003:**

55.MER_RR__1PQBCM20030113_105319_000001012012_00495_04557_0000.N1
56.MER_RR__1PQBCM20030114_102201_000001012013_00008_04571_0000.N1

57.MER_RR__1PQBCM20030116_105912_000001012013_00037_04600_0000.N1
58.MER_RR__1PQBCM20030117_102754_000001012013_00051_04614_0000.N1
59.MER_RR__1PQBCM20030123_103915_000001012013_00137_04700_0000.N1
60.MER_RR__1PQBCM20030124_100747_000001012013_00151_04714_0000.N1
61.MER_RR__1PQBCM20030129_105043_000001012013_00223_04786_0000.N1
62.MER_RR__1PQBCM20030130_101915_000001012013_00237_04800_0000.N1
63.MER_RR__1PQBCM20030201_105620_000001012013_00266_04829_0000.N1
64.MER_RR__1PQBCM20030202_102503_000001012013_00280_04843_0000.N1
65.MER_RR__1PQBCM20030205_103043_000001012013_00323_04886_0000.N1
66.MER_RR__1PQBCM20030217_105321_000001012013_00495_05058_0000.N1
67.MER_RR__1PQBCM20030228_100746_000001012014_00151_05215_0000.N1
68.MER_RR__1PQBCM20030305_105037_000001012014_00223_05287_0000.N1
69.MER_RR__1PQBCM20030306_101918_000001012014_00237_05301_0000.N1
70.MER_RR__1PQBCM20030321_104744_000001012014_00452_05516_0000.N1
71.MER_RR__1PQBCM20030324_105325_000001012014_00495_05559_0000.N1
72.MER_RR__1PQBCM20030403_103917_000001012015_00137_05702_0000.N1
73.MER_RR__1PQBCM20030421_111314_000001012015_00395_05960_0000.N1
74.MER_RR__1PQBCM20030423_101044_000001012015_00423_05988_0000.N1
75.MER_RR__1PQBCM20030429_102213_000001012016_00008_06074_0000.N1
76.MER_RR__1PQBCM20030501_105912_000001012016_00037_06103_0000.N1
77.MER_RR__1PQBCM20030502_102800_000001012016_00051_06117_0000.N1
78.MER_RR__1PQBCM20030509_100746_000001012016_00151_06217_0000.N1
79.MER_RR__1PQBCM20030511_104452_000001012016_00180_06246_0000.N1
80.MER_RR__1PQBCM20030512_101331_000001012016_00194_06260_0000.N1
81.MER_RR__1PQBCM20030514_105028_000001012016_00223_06289_0000.N1
82.MER_RR__1PQBCM20030515_101912_000001012016_00237_06303_0000.N1
83.MER_RR__1PQBCM20030521_103043_000001012016_00323_06389_0000.N1
84.MER_RR__1PQBCM20030523_110727_000001012016_00352_06418_0000.N1
85.MER_RR__1PQBCM20030524_103621_000001012016_00366_06432_0000.N1
86.MER_RR__1PQBCM20030526_111314_000001012016_00395_06461_0000.N1
87.MER_RR__1PQBCM20030527_104205_000001012016_00409_06475_0000.N1
88.MER_RR__1PQBCM20030528_101042_000001012016_00423_06489_0000.N1
89.MER_RR__1PQBCM20030530_104736_000001012016_00452_06518_0000.N1
90.MER_RR__1PQBCM20030531_101627_000001012016_00466_06532_0000.N1
91.MER_RR__1PQBCM20030602_105335_000001012016_00495_06561_0000.N1
92.MER_RR__1PQBCM20030603_102216_000001012017_00008_06575_0000.N1
93.MER_RR__1PQBCM20030605_105913_000001012017_00037_06604_0000.N1
94.MER_RR__1PQBCM20030606_102748_000001012017_00051_06618_0000.N1
95.MER_RR__1PQBCM20030608_110452_000001012017_00080_06647_0000.N1
96.MER_RR__1PQBCM20030609_103331_000001012017_00094_06661_0000.N1
97.MER_RR__1PQBCM20030611_111034_000001012017_00123_06690_0000.N1
98.MER_RR__1PQBCM20030612_103916_000001012017_00137_06704_0000.N1
99.MER_RR__1PQBCM20030613_100757_000001012017_00151_06718_0000.N1
100.MER_RR__1PQBCM20030615_104503_000001012017_00180_06747_0000.N1
101.MER_RR__1PQBCM20030616_101334_000001012017_00194_06761_0000.N1
102.MER_RR__1PQBCM20030618_105044_000001012017_00223_06790_0000.N1

103.MER_RR__1PQBCM20030619_101923_000001012017_00237_06804_0000.N1
104.MER_RR__1PQBCM20030621_105628_000001012017_00266_06833_0000.N1
105.MER_RR__1PQBCM20030622_102508_000001012017_00280_06847_0000.N1
106.MER_RR__1PQBCM20030625_103056_000001012017_00323_06890_0000.N1
107.MER_RR__1PQBCM20030627_110753_000001012017_00352_06919_0000.N1
108.MER_RR__1PQBCM20030630_111324_000001012017_00395_06962_0000.N1
109.MER_RR__1PQBCM20030701_104216_000001012017_00409_06976_0000.N1
110.MER_RR__1PQBCM20030702_101059_000001012017_00423_06990_0000.N1
111.MER_RR__1PQBCM20030704_104756_000001012017_00452_07019_0000.N1
112.MER_RR__1PQBCM20030705_101631_000001012017_00466_07033_0000.N1
113.MER_RR__1PQBCM20030707_105333_000001012017_00495_07062_0000.N1
114.MER_RR__1PQBCM20030708_102221_000001012018_00008_07076_0000.N1
115.MER_RR__1PQBCM20030710_105915_000001012018_00037_07105_0000.N1
116.MER_RR__1PQBCM20030711_102754_000001012018_00051_07119_0000.N1
117.MER_RR__1PQBCM20030713_110454_000001012018_00080_07148_0000.N1
118.MER_RR__1PQBCM20030714_103339_000001012018_00094_07162_0000.N1
119.MER_RR__1PQBCM20030716_111039_000001012018_00123_07191_0000.N1
120.MER_RR__1PQBCM20030717_103922_000001012018_00137_07205_0000.N1
121.MER_RR__1PQBCM20030719_111614_000001012018_00166_07234_0000.N1
122.MER_RR__1PQBCM20030720_104508_000001012018_00180_07248_0000.N1
123.MER_RR__1PQBCM20030723_105047_000001012018_00223_07291_0000.N1
124.MER_RR__1PQBCM20030724_101928_000001012018_00237_07305_0000.N1
125.MER_RR__1PQBCM20030726_105630_000001012018_00266_07334_0000.N1
126.MER_RR__1PQBCM20030727_102511_000001012018_00280_07348_0000.N1
127.MER_RR__1PQBCM20030729_110208_000001012018_00309_07377_0000.N1
128.MER_RR__1PQBCM20030730_103052_000001012018_00323_07391_0000.N1
129.MER_RR__1PQBCM20030801_110750_000001012018_00352_07420_0000.N1
130.MER_RR__1PQBCM20030802_103637_000001012018_00366_07434_0000.N1
131.MER_RR__1PQBCM20030804_111329_000001012018_00395_07463_0000.N1
132.MER_RR__1PQBCM20030805_104217_000001012018_00409_07477_0000.N1
133.MER_RR__1PQBCM20030806_101051_000001012018_00423_07491_0000.N1
134.MER_RR__1PQBCM20030808_104758_000001012018_00452_07520_0000.N1
135.MER_RR__1PQBCM20030809_101643_000001012018_00466_07534_0000.N1
136.MER_RR__1PQBCM20030811_105334_000001012018_00495_07563_0000.N1
137.MER_RR__1PQBCM20030812_102222_000001012019_00008_07577_0000.N1
138.MER_RR__1PQBCM20030814_105916_000001012019_00037_07606_0000.N1
139.MER_RR__1PQBCM20030815_102629_000000542019_00051_07620_0000.N1
140.MER_RR__1PQBCM20030817_110455_000001012019_00080_07649_0000.N1
141.MER_RR__1PQBCM20030818_103346_000001012019_00094_07663_0000.N1
142.MER_RR__1PQBCM20030820_111039_000001012019_00123_07692_0000.N1
143.MER_RR__1PQBCM20030821_103925_000001012019_00137_07706_0000.N1
144.MER_RR__1PQBCM20030823_111622_000001012019_00166_07735_0000.N1
145.MER_RR__1PQBCM20030824_104508_000001012019_00180_07749_0000.N1
146.MER_RR__1PQBCM20030825_101346_000001012019_00194_07763_0000.N1
147.MER_RR__1PQBCM20030828_101924_000001012019_00237_07806_0000.N1
148.MER_RR__1PQBCM20030830_105623_000001012019_00266_07835_0000.N1

149.MER_RR__1PQBCM20030831_102513_000001012019_00280_07849_0000.N1
150.MER_RR__1PQBCM20030902_110207_000001012019_00309_07878_0000.N1
151.MER_RR__1PQBCM20030903_103100_000001012019_00323_07892_0000.N1
152.MER_RR__1PQBCM20030908_111338_000001012019_00395_07964_0000.N1
153.MER_RR__1PQBCM20030910_101055_000001012019_00423_07992_0000.N1
154.MER_RR__1PQBCM20030912_104753_000001012019_00452_08021_0000.N1
155.MER_RR__1PQBCM20030913_101636_000001012019_00466_08035_0000.N1
156.MER_RR__1PQBCM20030915_105337_000001012019_00495_08064_0000.N1
157.MER_RR__1PQBCM20030916_102219_000001012020_00008_08078_0000.N1
158.MER_RR__1PQBCM20030918_105913_000001012020_00037_08107_0000.N1
159.MER_RR__1PQBCM20030919_102803_000001012020_00051_08121_0000.N1
160.MER_RR__1PQBCM20030921_110458_000001012020_00080_08150_0000.N1
161.MER_RR__1PQBCM20030922_103342_000001012020_00094_08164_0000.N1
162.MER_RR__1PQBCM20030924_111039_000001012020_00123_08193_0000.N1
163.MER_RR__1PQBCM20030926_100756_000001012020_00151_08221_0000.N1
164.MER_RR__1PQBCM20030928_104502_000001012020_00180_08250_0000.N1
165.MER_RR__1PQBCM20030929_101349_000001012020_00194_08264_0000.N1
166.MER_RR__1PQBCM20031002_101928_000001012020_00237_08307_0000.N1
167.MER_RR__1PQBCM20031004_105628_000001012020_00266_08336_0000.N1
168.MER_RR__1PQBCM20031005_102516_000001012020_00280_08350_0000.N1
169.MER_RR__1PQBCM20031007_110207_000001012020_00309_08379_0000.N1
170.MER_RR__1PQBCM20031010_110748_000001012020_00352_08422_0000.N1
171.MER_RR__1PQBCM20031011_103624_000001012020_00366_08436_0000.N1
172.MER_RR__1PQBCM20031018_101632_000001012020_00466_08536_0000.N1
173.MER_RR__1PQBCM20031023_105918_000001012021_00037_08608_0000.N1
174.MER_RR__1PQBCM20031024_102801_000001012021_00051_08622_0000.N1
175.MER_RR__1PQBCM20031102_104454_000001012021_00180_08751_0000.N1
176.MER_RR__1PQBCM20031109_102506_000001012021_00280_08851_0000.N1
177.MER_RR__1PQBCM20031111_110211_000001012021_00309_08880_0000.N1
178.MER_RR__1PQBCM20031112_103048_000001012021_00323_08894_0000.N1
179.MER_RR__1PQBCM20031117_111315_000001012021_00395_08966_0000.N1
180.MER_RR__1PQBCM20031118_104202_000001012021_00409_08980_0000.N1
181.MER_RR__1PQBCM20031210_105037_000001012022_00223_09295_0000.N1
182.MER_RR__1PQBCM20031211_101935_000001012022_00237_09309_0000.N1
183.MER_RR__1PQBCM20031213_105621_000001012022_00266_09338_0000.N1
184.MER_RR__1PQBCM20031214_102516_000001012022_00280_09352_0000.N1
185.MER_RR__1PQBCM20031223_104207_000001012022_00409_09481_0000.N1
186.MER_RR__1PQBCM20031224_101056_000001012022_00423_09495_0000.N1
187.MER_RR__1PQBCM20031226_104807_000001012022_00452_09524_0000.N1

- **Toulouse, Full Resolution, 2003:**

188.MER_FR__1PNUPA20031118_104110_000000982021_00409_08980_0137.N1
189.MER_FR__1PNUPA20030919_102703_000000982020_00051_08121_0136.N1

190.MER_FR__1PNUPA20030812_102111_000000982019_00008_07577_0135.N1
191.MER_FR__1PNUPA20030711_102659_000000982018_00051_07119_0139.N1
192.MER_FR__1PNUPA20030619_101811_000000982017_00237_06804_0108.N1
193.MER_FR__1PNUPA20030613_100644_000000982017_00151_06718_0109.N1
194.MER_FR__1PNUPA20030531_101516_000000982016_00466_06532_0126.N1
195.MER_FR__1PNUPA20030515_101806_000000982016_00237_06303_0111.N1
196.MER_FR__1PNUPA20030502_102708_000000982016_00051_06117_0864.N1
197.MER_FR__1PNUPA20030218_102108_000000982014_00008_05072_0140.N1
198.MER_FR__1PNIPA20030423_100939_000000982015_00423_05988_0169.N1
199.MER_FR__1PNEPA20030707_105227_000000982017_00495_07062_0545.N1
200.MER_FR__1PNEPA20030622_102355_000000982017_00280_06847_0453.N1
201.MER_FR__1PNEPA20030528_100934_000000982016_00423_06489_0083.N1
202.MER_FR__1PNEPA20030511_104355_000000982016_00180_06246_0551.N1
203.MER_FR__1PNEPA20030413_102413_000000502015_00280_05845_0437.N1
204.MER_FR__1PNEPA20030312_102950_000000502014_00323_05387_0431.N1

- **Toulouse, Reduced Resolution, 2003:**

205.MER_RR__1PQBCM20030406_104356_000001012015_00180_05745_0309.N1
206.MER_RR__1PQBCM20030423_100937_000001012015_00423_05988_0310.N1
207.MER_RR__1PQBCM20030503_095456_000001012016_00065_06131_0268.N1
208.MER_RR__1PQBCM20030511_104322_000001012016_00180_06246_0269.N1
209.MER_RR__1PQBCM20030515_101733_000001012016_00237_06303_0270.N1
210.MER_RR__1PQBCM20030528_100901_000001012016_00423_06489_0271.N1
211.MER_RR__1PQBCM20030613_100616_000001012017_00151_06718_0272.N1
212.MER_RR__1PQBCM20030615_104345_000001012017_00180_06747_0273.N1
213.MER_RR__1PQBCM20030616_101159_000001012017_00194_06761_0274.N1
214.MER_RR__1PQBCM20030619_101824_000001012017_00237_06804_0275.N1
215.MER_RR__1PQBCM20030621_105518_000001012017_00266_06833_0276.N1
216.MER_RR__1PQBCM20030622_102406_000001012017_00280_06847_0277.N1
217.MER_RR__1PQBCM20030629_100350_000001012017_00380_06947_0278.N1
218.MER_RR__1PQBCM20030707_105226_000001012017_00495_07062_0279.N1
219.MER_RR__1PQBCM20030708_102124_000001012018_00008_07076_0280.N1
220.MER_RR__1PQBCM20030710_105810_000001012018_00037_07105_0281.N1
221.MER_RR__1PQBCM20030711_102704_000001012018_00051_07119_0282.N1
222.MER_RR__1PQBCM20030715_100102_000001012018_00108_07176_0283.N1
223.MER_RR__1PQBCM20030717_103834_000001012018_00137_07205_0284.N1
224.MER_RR__1PQBCM20030718_100652_000001012018_00151_07219_0285.N1
225.MER_RR__1PQBCM20030723_104931_000001012018_00223_07291_0286.N1
226.MER_RR__1PQBCM20030726_105539_000001012018_00266_07334_0287.N1
227.MER_RR__1PQBCM20030730_103007_000001012018_00323_07391_0288.N1
228.MER_RR__1PQBCM20030802_103544_000001012018_00366_07434_0289.N1
229.MER_RR__1PQBCM20030803_100352_000001012018_00380_07448_0290.N1
230.MER_RR__1PQBCM20030805_104115_000001012018_00409_07477_0291.N1
231.MER_RR__1PQBCM20030806_100952_000001012018_00423_07491_0292.N1

232.MER_RR__1PQBCM20030808_104704_000001012018_00452_07520_0293.N1
233.MER_RR__1PQBCM20030809_101544_000001012018_00466_07534_0294.N1
234.MER_RR__1PQBCM20030811_105232_000001012018_00495_07563_0295.N1
235.MER_RR__1PQBCM20030812_102126_000001012019_00008_07577_0296.N1
236.MER_RR__1PQBCM20030818_103247_000001012019_00094_07663_0297.N1
237.MER_RR__1PQBCM20030819_100057_000001012019_00108_07677_0298.N1
238.MER_RR__1PQBCM20030822_100650_000001012019_00151_07720_0299.N1
239.MER_RR__1PQBCM20030825_101244_000001012019_00194_07763_0300.N1
240.MER_RR__1PQBCM20030903_102935_000001012019_00323_07892_0301.N1
241.MER_RR__1PQBCM20030913_101531_000001012019_00466_08035_0302.N1
242.MER_RR__1PQBCM20030915_105238_000001012019_00495_08064_0303.N1
243.MER_RR__1PQBCM20030916_102117_000001012020_00008_08078_0304.N1
244.MER_RR__1PQBCM20030917_094914_000001012020_00022_08092_0305.N1
245.MER_RR__1PQBCM20030918_105823_000001012020_00037_08107_0306.N1
246.MER_RR__1PQBCM20030919_102701_000001012020_00051_08121_0307.N1
247.MER_RR__1PQBCM20030920_095452_000001012020_00065_08135_0308.N1

- **The Netherlands, Reduced Resolution, 2003:**

248.MER_FR__1PNUPA20031015_100713_000000982020_00423_08493_1184.N1
249.MER_FR__1PNEPA20030218_101828_000000982014_00008_05072_0038.N1
250.MER_FR__1PNEPA20030422_103857_000000982015_00409_05974_0272.N1
251.MER_FR__1PNEPA20030423_100744_000000982015_00423_05988_0270.N1
252.MER_FR__1PNEPA20030616_101001_000000982017_00194_06761_0045.N1
253.MER_FR__1PNEPA20030714_102954_000000982018_00094_07162_0147.N1
254.MER_FR__1PNEPA20030809_101258_000000982018_00466_07534_0279.N1
255.MER_FR__1PNEPA20031208_101004_000000982022_00194_09266_0336.N1
256.MER_FR__1PNUPA20030416_102705_000000982015_00323_05888_0177.N1
257.MER_FR__1PNUPA20030528_100642_000000982016_00423_06489_0812.N1
258.MER_FR__1PNUPA20030531_101310_000000982016_00466_06532_0813.N1
259.MER_FR__1PNUPA20030606_102410_000000982017_00051_06618_0176.N1
260.MER_FR__1PNUPA20030806_100749_000000982018_00423_07491_0119.N1
261.MER_FR__1PNUPA20030808_104440_000000982018_00452_07520_0128.N1
262.MER_FR__1PNUPA20030809_101329_000000982018_00466_07534_0129.N1
263.MER_FR__1PNUPA20030812_101909_000000982019_00008_07577_0105.N1

- **Brazil, Reduced Resolution, 2003:**

264.MER_RR__1PQBCM20030701_141724_000001012017_00411_06978_0019.N1
265.MER_RR__1PQBCM20030521_140556_000001012016_00325_06391_0010.N1
266.MER_RR__1PQBCM20030530_142258_000001012016_00454_06520_0011.N1
267.MER_RR__1PQBCM20030708_135734_000001012018_00010_07078_0012.N1
268.MER_RR__1PQBCM20030713_144005_000001012018_00082_07150_0015.N1

269.MER_RR__1PQBCM20030814_143425_000001012019_00039_07608_0016.N1
270.MER_RR__1PQBCM20030622_140022_000001012017_00282_06849_0017.N1
271.MER_RR__1PQBCM20030514_142544_000001012016_00225_06291_0009.N1

- **China, Reduced Resolution, 2003:**

272.MER_RR__1PQBCM20030501_023637_000001012016_00032_06098_0008.N1

E.2. Level 2

273.MER_FR__2PNEPA20040714_103121_000000502028_00323_12401_0533.N1
274.MER_FR__2PNEPA20030714_103354_000000502018_00094_07162_0532.N1
275.MER_FR__2PNEPA20040717_103704_000000502028_00366_12444_0534.N1
276.MER_RR__2PQBCM20030618_105047_000001012017_00223_06790_0002.N1
277.MER_RR__2PQBCM20030627_110759_000001012017_00352_06919_0003.N1
278.MER_RR__2PQBCM20030611_111042_000001012017_00123_06690_0004.N1
279.MER_RR__2PQBCM20030717_103922_000001012018_00137_07205_0005.N1
280.MER_RR__2PQBCM20030801_110753_000001012018_00352_07420_0007.N1
281.MER_RR__2PQBCM20040714_103122_000000542028_00323_12401_0329.N1
282.MER_RR__2PQBCM20040717_103701_000000542028_00366_12444_0330.N1
283.MER_RR__2PQBCM20030714_103407_000000542018_00094_07162_0332.N1
284.MER_RR__2PQBCM20030627_110816_000000542017_00352_06919_0469.N1
285.MER_RR__2PQBCM20030618_105104_000000542017_00223_06790_0475.N1
286.MER_RR__2PQBCM20030613_100650_000000542017_00151_06718_0483.N1

Part V

Spanish Summary:

Nuevos algoritmos para la corrección atmosférica y la estimación de parámetros biofísicos en Observación de la Tierra. Aplicación a datos ENVISAT/MERIS

Introducción

La Observación de la Tierra se ocupa de aquellos métodos centrados en monitorizar nuestro planeta por medio de sensores de radiación electromagnética a bordo de satélites o aviones. En particular, la teledetección pasiva en la región óptica del espectro se ocupa del estudio de la superficie de la Tierra mediante la medida de la radiación solar reflejada por la superficie observada y transmitida a través de la atmósfera hasta el sensor.

Muchos avances se han producido en la última década en el campo de la Observación de la Tierra, tanto en el diseño instrumental como en el de algoritmos de procesado. Fruto de estos avances la Agencia Espacial Europea (ESA, de *European Space Agency*) lanzó la misión ENVISAT (*ENVIronmental SATellite*), que transporta diferentes sensores para la monitorización de la superficie del planeta. Uno de ellos es MERIS (*MEdium Resolution Imaging Specrometer Instrument*), un espectrómetro de imagen que opera en el rango entre 400 y 900 nm. Aunque el primer objetivo de MERIS fue el estudio del color del océano, la observación de la atmósfera y de las superficies de tierra ha ido ganando importancia de manera continua en los últimos años.

El trabajo que se presenta en esta tesis está encaminado a reforzar este interés renovado en los datos MERIS para el estudio de la atmósfera y al tierra. El principal objetivo es desarrollar nuevas herramientas para la obtención de parámetros biofísicos, tanto de la atmósfera como de la superficie, a partir de las imágenes de MERIS. Con esta idea se ha diseñado algoritmos para la obtención de mapas de espesor óptico de aerosoles (AOT, de *aerosol optical thickness*), vapor de agua integrado en columna (CWV, de *columnar water vapor*), reflectividad de la superficie y fluorescencia vegetal.

Derivar parámetros de la atmósfera y la superficie de datos de teledetección implica desacoplar los efectos radiativos de atmósfera y superficie. Si no hubiera atmósfera alrededor de la Tierra, la radiación solar sólo sería perturbada cuando llegara a la superficie. Por tanto, la radiación solar reflejada proporcionaría un representación fiel de la naturaleza de la superficie y de los procesos asociados cuando fuera medida por un sensor desde el espacio. Sin embargo, la influencia atmosférica sobre la radiación visible e infrarroja es lo suficientemente fuerte para modificar la señal reflejada, causando la pérdida o corrupción de parte de la información. La interacción de la radiación solar con los componentes atmosféricos consiste en procesos de absorción y dispersión. La absorción disminuye la intensidad de la radiación que llega al sensor, lo que lleva a una pérdida del brillo de la imagen, mientras que la dispersión actúa modificando la dirección de propagación de la radiación. Esto tiene como resultado diferentes procesos, como la reflexión en la misma atmósfera de parte de la radiación, sin que ni siquiera llegue a la superficie, la contaminación de la medida por parte de fotones procedentes del entorno del blanco observado o la extinción de fotones en el camino de la superficie al sensor. Por tanto, cualquier lote de datos de teledetección necesita la eliminación de los efectos atmosféricos para asegurar que la máxima precisión pueda obtenerse en la fase posterior de explotación de los datos. Ésta es la base de la corrección atmosférica en teledetección en el óptico: la eliminación del efecto atmosférico de la radiación solar reflejada por la superficie en la dirección de observación del sensor.

Para una corrección atmosférica precisa la situación ideal sería la disponibilidad de un producto atmosférico conteniendo la información atmosférica necesaria para la corrección y coincidente con el momento y lugar de adquisición de la imagen a ser procesada. Esto se puede conseguir si la estimación de esos parámetros atmosféricos se hace mediante métodos físicos que utilizan como punto de partida la información espectral, angular o espacial contenida en la misma imagen. Además, la monitorización de los componentes atmosféricos en una escala global se está haciendo cada vez más importante en aspectos climatológicos: se considera que los aerosoles contribuyen significativamente al balance global de radiación por su rol en el forzamiento de radiación y en la formación de nubes, mientras que los gases, especialmente el vapor de agua, son responsables del efecto invernadero atmosférico. Como resultado, la estimación de propiedades atmosféricas desde satélite no es sólo necesaria para el proceso de corrección atmosférica, sino que es también un requerimiento para la adecuada modelización del clima de la Tierra.

Por otra parte, más de 30 años de investigación a nivel de laboratorio apoyan la emisión de fluorescencia por parte de la clorofila vegetal como uno de los indicadores más directos de la actividad fotosintética de la vegetación. Intentos de estimación de esta señal desde datos de satélite están siendo iniciados actualmente. La medida de una señal tan débil implica medir dentro de bandas de absorción, donde la radiación emitida es amplificada en comparación con la reflejada. La detallada caracterización de la absorción del O_2 atmosférico proporcionada por la banda 11 de MERIS, centrada alrededor de 761 nm y con una anchura del orden de 3.75 nm, permite que la estimación de fluorescencia a partir de medidas en la banda de absorción del oxígeno utilizando datos MERIS sea posible. El hecho de que la estimación de la fluorescencia tenga que hacerse a través de la evaluación de una absorción atmosférica, afectada por factores como la elevación de la superficie o la carga de aerosoles, sugiere que sea integrada en un esquema de corrección atmosférica.

En este entorno, un algoritmo para la corrección de datos MERIS sobre tierra ha sido implementado para este trabajo. Dos puntos principales motivaron la selección de datos

MERIS y corrección atmosférica para ser unidos en esta tesis. Por una parte, MERIS ofrece una configuración espectral óptima para la estimación de parámetros biofísicos de la atmósfera y la superficie: dos bandas de observación finas que miden dentro de las absorciones del O_2 y el vapor de agua atmosféricos son combinadas con otras trece bandas que proporcionan medidas de gran precisión desde el azul al infrarrojo próximo. Por otra parte, hay una falta de métodos operativos para la estimació de aerosoles y la corrección atmosférica de datos MERIS sobre tierra, además de los problemas identificados en el producto de reflectividad de la superficie de nivel 2 proporcionado por la Agencia Espacial Europea. De hecho, no existe ningún software de libre distribución para la corrección atmosférica de datos MERIS de nivel 1 (radiancia corregida radiométricamente). Por esta razón el algoritmo presentado en esta tesis (SCAPE-M, de *Self-Contained Atmospheric Parameters Estimation from MERIS data*) ha sido implementado de manera que funcione operativamente.

El trabajo ha sido organizado en 4 partes:

- La primera se dedica a una introducción general de algunos aspectos relacionados con la corrección atmosférica, y se divide en dos capítulos. Uno se centra en la revisión de los fundamentos de la transferencia radiativa atmosférica, incluyendo la descripción de los constituyentes atmosféricos y sus propiedades ópticas, una revisión de la formulación matemática de la transferencia radiativa y un breve resumen de los códigos informáticos empleados en la evaluación de la transferencia de radiación a través de la atmósfera. El segundo capítulo es una breve reseña del estado-del-arte de la corrección atmosférica, describiéndose algunos de los métodos más representativos.

- La segunda parte trata la metodología desarrollada para la obtención de los productos biofísicos. En el tercer capítulo se hace una descripción del algoritmo SCAPE-M. Primero se presenta la base física para la generación de mapas de AOT, CWV y reflectividad de la superficie. En segundo lugar se presenta el diseño de una tabla de búsqueda (LUT, de *Look-up Table*) generada para la optimización del cálculo de los parámetros ópticos atmosféricos. En la última parte del capítulo se realiza un análisis de sensibilidad para la estimación de los errores asociados al cálculo de aerosoles, vapor de agua y reflectividad.

  El cuarto capítulo describe la validación de los productos atmosféricos y de la reflectividad. Una extensa base de datos de imágenes MERIS ha sido procesada y comparada con medidas localizadas tomadas durante campañas de campo específicas y con medidas de aerosoles y vapor de agua proporcionadas por la red global de estaciones AERONET (*AErosol RObotic NETwork*). Los mapas de reflectividad derivados se comparan con otros productos MERIS y con datos CHRIS-PROBA.

La estimación de fluorescencia vegetal a partir de datos MERIS se detalla en el quinto capítulo. Ésta es incluida en el esquema de transferencia radiativa como un función fuente que se añade a la radiación reflejada, de manera que se consigue una evaluación adecuada de todos los factores atmosféricos o geométricos que afectan la absorción del O_2. Mapas de fluorescencia en unidades de radiancia son calculados con este procedimiento.

- La tercera parte consiste en el resumen de los puntos más importantes discutidos a lo largo del trabajo y en la enfatización de las conclusiones más importantes.
- Finalmente, una serie de apéndices con información de diferente tipo relativa al tema expuesto se recoge en la cuarta parte

Fundamento Teórico

Capítulo 1 – Principios de Transferencia Radiativa

En este capítulo se hace una introducción teórica a la interacción entre atmósfera, superficie y radiación en la que se basa la corrección atmosférica de datos de teledetección en el óptico. Se describen los procesos de absorción y dispersión que afectan a la radiación solar en su camino a través de la atmósfera. En particular, se hace en primer lugar una descripción de los componentes atmosféricos, gases y aerosoles, y su particular influencia sobre la radiación; a continuación se detalla la formulación matemática de la transferencia radiativa atmosférica desde un enfoque macroscópico. Finalmente, se describe el modo en que esas formulaciones se implementan en códigos informáticos, particularizando al caso de los códigos utilizados para este trabajo.

1.1 Absorción y dispersión de radiación solar en la atmósfera

La capa atmosférica que rodea la superficie de la tierra, formada por la baja y media atmósfera, es una mezcla homogénea de gases con un espesor de unos 80 ó 90 km. Está compuesta de 78 % de nitrógeno, 21 % de oxígeno 1 % de argón, y presenta concentraciones variables de otros componentes en menores proporciones. En este medio gaseoso se encuentra también aerosoles, que son partículas líquidas y sólidas con diferentes orígenes y tamaños, desde pequeños agregados moleculares hasta gotas de lluvia o copos de nieve. Tanto las moléculas como los aerosoles son ópticamente activos, causando la absorción y la dispersión de la radiación solar que atraviesa la atmósfera en su camino entre el espacio, la superficie y el sensor.

Las especies gaseosas más absorbentes en el espectro solar son el oxígeno, el ozono, el vapor de agua y el dióxido de carbono. Las bandas de absorción a que dan lugar causan que las radiancias en el techo de la atmósfera (TOA, de *Top of Atmosphere*) son las que deben ser eliminadas en el proceso de corrección atmosférica.

La dispersión se origina por un cambio de dirección de la radiación propagándose por la atmósfera después de chocar con una partícula atmosférica, dando lugar al campo de radiación difusa a través de procesos de dispersión múltiple. La formulación matemática de este proceso es particularmente sencilla si la partícula es mucho más pequeña que la longitud de onda de la radiación incidente, y además es considerada esférica. Esta solución fue propuesta por Lord Rayleigh en 1871 y se aplica, por ejemplo, en la explicación del color azul del cielo. En el caso de que el tamaño de la partícula sea similar al de la longitud de onda de la luz incidente se aplica la formulación de Lorenz-Mie, que también asume que las partículas tienen una forma esférica en promedio. En ambos casos se deduce que la intensidad en la dispersión es mayor cuanto menor es la longitud de onda, y que depende del tamaño de la partícula.

El signo de la influencia atmosférica sobre la radiación que llega a un sensor elevado (aumento o disminución respecto la medida desde un sensor al nivel del suelo) depende de muchos factores, como la concentración de aerosoles, vapor de agua, o las direcciones de iluminación y observación. En el caso general, el efecto neto atmosférico es positivo en las longitudes de onda del visible, y negativo en el infrarrojo. Esto se debe al rol dominante jugado por la dispersión atmosférica en las longitudes de onda más cortas y a la absorción por gases y aerosoles en el infrarrojo. Todos estos aspectos deben ser cuantificados en la corrección atmosférica de datos de teledetección.

1.2 Aerosoles

Los aerosoles son un componente complejo de la atmósfera. De hecho, su caracterización detallada requiere el conocimiento de su composición química, su forma, su distribución de tamaños y la concentración de partículas. Su tamaño varía desde agregados de unas pocas moléculas a partículas de varios micrometros. Desde el punto de vista radiativo los aerosoles más importantes están en el rango 0.1-1.0 μm: los aerosoles más pequeños, aunque numerosos, tienen una repercusión individual pequeña, mientras que los más grandes, que sí tienen una influencia importante, son escasos.

Las características de los aerosoles dependen de su origen. Las partículas líquidas son esféricas, pero las sólidas tienen formas irregulares y complejas. Sin embargo, en la mayoría de los casos es realista asumir que una masa de partículares irregulares destribuidas aleatoriamente se comporta en promedio como si todas ellas fueran esféricas, lo que permite la aplicación de la ley de Lorenz-Mie para su estudio.

Como la mayor parte de las fuentes de aerosoles se encuentran a nivel de suelo las mayores concentraciones de aerosoles se encuentran en las capas bajas de la troposfera, donde su tiempo de residencia es del orden de días. Estos aerosoles troposféricos son muy variables en tiempo y lugar, ya que están sometidos a las condiciones de producción y transporte.

D'Almeida et al. [1991] clasificaron los aerosoles atmosféricos de acuerdo a diferentes orígenes y composiciones. Entre los tipos básicos de aerosoles que establecieron estaban los de origen extraterrestre, básicamente consistentes en polvo de cometas y lluvias de meteoritos, partículas de sal marina, partículas de la corteza generadas por procesos de erosión, sulfatos, nitratos, partículas orgánicas, sustancias carbonosas y aerosoles volcánicos. Estos tipos básicos son combinados para generar modelos de aerosoles que representen lo mejor posible las características de los aerosoles predominantes en un determinado lugar. Esta combinación se suele hacer en forma de mezcla externa, según la cual los componentes básicos coexisten en una parcela de aire, pero no se mezclan internamente en una misma partícula. Modelos de aerosoles muy usados son el continental, el marítimo y el desértico.

Para la cuantificación de la extinción de radiación por parte de los aerosoles se suele utilizar el coeficiente de extinción de volumen β_e, que da la cantidad de radiación incidente que es extinguida por unidad de volumen. Un parámetro asociado es el espesor óptico de aerosoles τ (o AOT, de *Aerosol Optical Thickness*), que da la pérdida de radiación en un camino discreto debida a la extinción por aerosoles como la integral del coeficiente de extinción a lo largo de ese camino, generalmente el que transcurre entre la superficie y el TOA. El AOT es la magnitud que se utiliza para cuantificar la cantidad de aerosoles en la columna atmosférica, que es la magnitud que puede ser medida desde satélite o radiómetros en la superficie. La visibilidad horizontal es un parámetro relacionado al AOT.

1.3 Vapor de agua

El vapor de agua es un constituyente atmosférico muy variable. Está mayoritariamente contenido en la troposfera. Juega un papel importante en la redistribución de agua y energía en el sistema global atmósfera-tierra-océano. La interacción de la troposfera con la radiación solar en longitudes de onda mayores de 700 nm está dominada por la absorción a cargo del vapor de agua. Al mismo tiempo, la radiación terrestre en el infrarrojo próximo está también sujeta a la absorción del vapor de agua, excepto en la ventana entre 8 y 13 μm. Dado que la absorción de radiación lleva al calentamiento atmosférico, entender la cantidad y dependencia espectral de la absorción del vapor de agua es esencial para estudios climáticos.

El promedio anual de vapor de agua integrado en columna CWV varía entre 0.25 $\mathrm{g \cdot cm^{-2}}$ en regiones polares y 5 $\mathrm{g \cdot cm^{-2}}$ en los trópicos. El promedio anual de vapor de agua supondría alrededor de 2.5 $\mathrm{g \cdot cm^{-2}}$ si todo condensara instantáneamente. Sin embargo, la precipitación media anual en el planeta es del orden de 1 m, lo que supone una rápida pérdida de agua en el aire. El tiempo medio de residencia de las moléculas de agua en la troposfera es alrededor de 10 días. El agua que se pierde por precipitación es devuelta principalmente a través de procesos de evaporación desde océanos, lagos y ríos y de transpiración de las plantas.

1.4 Formulación matemática

La simulación de la interacción entre la atmósfera y la radiación es necesaria en el estudio del efecto atmosférico sobre la señal electromagnética que llega a un sensor elevado. La ejecución de los modelos de transferencia radiativa adecuados proporcionan información sobre las características del problema y la sensibilidad de la radiancia TOA a los diferentes factores que configuran la escena. La disponibilidad de una base matemática sólida para la formulación del problema de transferencia radiativa es muy importante para implementar códigos de transferencia radiativa (RTCs, de *Radiative Transfer Codes*) lo más precisos posible para la simulación.

El objetivo principal de esta sección es establecer la ecuación de transferencia radiativa (RTE, de *Radiative Transfer Equation*) mediante una formulación escalar, centrándose en el problema particular de la radiación solar que interacciona con la atmósfera y la superficie. Los procesos de absorción y dispersión anteriormente descritos son parametrizados como funciones fuente y de extinción. En particular, los procesos de dispersión actúan en las dos direcciones, ya que pueden tanto extinguir radiación por el cambio de dirección de parte de radiación que viaja en una determinada dirección como aportar radiación en esa misma dirección por efecto de la dispersión múltiple de radiación moviéndose en otras direcciones. La absorción, por su parte, sólo actúa extinguiendo la radiación. La solución de ecuación integro-diferencial resultante es simplificada al caso de atmósferas plano-paralelas (modelo que asume que la atmósfera puede representarse por capas planas en las que los constituyentes atmosféricos son horizontalmente constantes).

Como condición de contorno de la ecuación se considera la irradiancia solar extraterrestre que incide sobre el TOA. Además, la superficie constituye una discontinuidad en la transferencia radiativa que actúa reflejando la radiación. El caso más general es el que considera una superficie heterogénea y con propiedades direccionales en la reflectividad. El hecho de que la superficie sea heterogénea supone que la radiación medida en una determinada dirección pueda verse afectada por el entorno de la superficie observada con reflectividad diferente, ya que fotones reflejados por el entorno podrían ser dispersados por la atmósfera en la dirección de observación. Este efecto se conoce como *adyacencia.* La direccionalidad de la superficie, por su parte, se modeliza a través de la BRDF (*Bidirectional Reflectance Distribution Function*), que especifica la reflectividad de la superficie en función de la geometría de iluminación y observación. El caso ideal en que no existe dependencia de la reflectividad con los ángulos de observación e iluminación se conoce como *superficie lambertiana*.

Una representación paramétrica particularmente útil en la simulación de la transferencia radiativa para casos de teledetección fue propuesta por Tanré et al. [1981]. En esta formulación la señal en el TOA es construida a partir de la suma de diferentes términos, como la radiación reflejada por la atmósfera sin llegar a la superficie, la radiación que se transmite de modo directo entre el sol, la superficie y el sensor o la que está sujeta a procesos de dispersión múltiple. Si se hace la aproximación de superficie lambertiana se llega a una ecuación que relaciona la radiancia medida en el TOA con la reflectividad de la superficie y diversos parámetros atmosféricos. Esta ecuación se puede invertir analíticamente para calcular la reflectividad de la superficie a partir del resto de parámetros, lo que supone importantes ventajas para el desarrollo de métodos de corrección atmosférica operativos. Análisis realizados con datos CHRIS-PROBA mostraron que la consideración de una superficie lambertiana no lleva a importantes errores en la corrección atmosférica, aunque más análisis son necesarios para llegar a conclusiones sólidas.

1.5 Códigos de transferencia radiativa

El MODTRAN4 (*MODerate resolution atmospheric TRANsmittance and radiance code*) y el 6S (*Second Simulation of the Satellite Signal in the Solar Spectrum*) son posiblemente los dos códigos de transferencia radiativa más empleados para la simulación y procesado de datos de teledetección en el espectro óptico.

MODTRAN4 surgió como una versión mejorada del código LOWTRAN7. Cubre el rango espectral entre 0.2 y ∞ μm. Uno de los puntos fuertes de MODTRAN4 es su fina resolución espectral de hasta 1 cm^{-1}. Además, acopla los procesos de absorción y dispersión en cada camino óptico, con lo que consigue una alta precisión en los cálculos dentro de regiones con absorciones gaseosas importantes. En lo que respecta a la dispersión múltiple, el algoritmo DISORT (*DIScrete Ordinate Radiative Transfer*) está integrado en MODTRAN4 para cálculos con la máxima precisión. Por estas características MODTRAN4 es posiblemente el código más preciso en el ámbito de las simulaciones atmosféricas para teledetección.

El código 6S es mucho más sencillo que MODTRAN4, aunque también ofrece un tiempo de cálculo mucho mejor. Fue utilizado en versiones iniciales de SCAPE-M. Trabaja en el rango espectral entre 0.25 y 0.4 μm con una resolución espectral de 2.5 nm, de modo que sólo considera la radiación solar y no la emitida por la Tierra. Los procesos de absorción y dispersión se computan por separado y se combinan posteriormente a través de términos multiplicativos. Esto permite acelerar mucho los cálculos, pero se puede perder una parte importante de precisión dentro de bandas de absorción. La necesidad de una correcta modelización de los fenómenos de absorción para la estimación de vapor de agua y fluorescencia hizo que se optara por el uso de MODTRAN4 y una LUT para el cálculo de los efectos atmosféricos en SCAPE-M.

Capítulo 2 – Revisión de Algoritmos de Corrección Atmosférica de Referencia

Una pequeña revisión de algunos algoritmos de corrección atmosférica de referencia es presentada en este capítulo Estos algoritmos representan el estado-del-arte de las técnicas de corrección atmosférica para datos en el espectro solar. La revisión se ha centrado en los métodos de corrección atmosférica diseñados para la última generación de sensores a bordo de plataformas espaciales, como MERIS [Santer et al., 1999; von Hoyningen-Huene et al., 2003], MODIS [Kaufman et al., 1997; Vermote et al., 1997a], MISR [Diner et al., 2005; Martonchik et al., 2002, 1998] y AATSR [Grey et al., 2006; North et al., 1999]. También se dedica una sección a Landsat TM [Liang et al., 2001] por su particular aportación al desarrollo de la disciplina de la Observación de la Tierra.

2.1 Corrección atmosférica de MERIS

ESA Level 2 Product – Santer et al. (1999)

Corresponde al método de corrección atmosférica implementado en el segmento de tierra de MERIS para la generación del producto de reflectividad y de AOT de nivel 2. El objetivo principal es derivar reflectividad de la superficie a partir de imágenes de MERIS para las 13 bandas no afectadas por absorciones gaseosas (las bandas 11 y 15, oxígeno y vapor de agua respectivamente, no se procesan).

La conversión de radiancia a reflectividad incluye 3 pasos. En el primero, las absorciones gaseosas son eliminadas de la señal. La corrección de ozono está basada en datos procedentes del ECMWF (*European Centre for Meteorology and Weather Forecasting*). Para la absorción de vapor de agua, un método diferencial que usa las bandas 14 y 15, fuera y dentro de la absorción centrada en 940 nm, se propone para estimar CWV. El segundo paso corrige la contribución de la dispersión de Rayleigh. La dependencia de ésta con la presión atmosférica es tenida en cuenta a través del cociente de bandas 10 y 11, fuera y dentro de la absorción del O_2, respectivamente. Finalmente, el tercer paso elimina el efecto de los aerosoles restante. La detección de aerosoles se produce sobre píxeles de vegetación oscura (DDV, de *Dense Dark Vegetation*) para los que se asume que la mayor contribución a la radiancia medida en el TOA proviene de la atmósfera.

Sin embargo, problemas en la implementación práctica del algoritmo han causado que no sea operativo, resultando en un producto MERIS de nivel 2 que no presenta datos totalmente corregidos de atmósfera, sino que la contribución de los aerosoles todavía queda presente. El resultado es que sólo un producto de reflectividad "en el techo de los aerosoles" es proporcionado a los usuarios.

BAER – von Hoyningen et al. (2003)

El método BAER (*Bremen AErosol Retrieval*) es otro código usado para la corrección atmosférica de datos MERIS sobre tierra. Ha sido implementado en el software BEAM (*Basic ERS & Envisat (A)ATSR and MERIS Toolbox*) para corregir la contribución de los aerosoles del producto MERIS de nivel 2. No está disponible para el procesado de datos de nivel 1b.

Por tanto, el BAER se centra en la estimación de aerosoles para la posterior corrección. El AOT en las bandas 1-7 es derivado por medio de un procedimiento iterativo. La superficie es modelada mediante la combinación lineal de dos endmembers de vegetación y suelo. El AOT espectral y las proporciones de vegetación y suelo son obtenidas en cada iteración. El AOT final se calcula mediante criterios de suavidad para la curva espectral obtenida del cálculo por separado para cada banda. El resultado se extrapola a las bandas del infrarrojo próximo.

2.2 Corrección atmosférica de MODIS

El algoritmo usado en el procesado de los productos de nivel 2 de MODIS (*Moderate Resolution Imaging Spectroradiometer*) proporciona reflectividad de la superficie a partir de los datos MODIS de nivel 1b en las bandas 1 a 7, centradas en 648, 858, 470, 555, 1240, 1640 y 2130 nm, respectivamente.

Para la estimación de aerosoles se usa el concepto de DDVs. Se limita a áreas con vegetación densa en la regiones húmedas del planeta. En primer lugar se selecciona los píxeles oscuros utilizando las bandas en 2.1 y 3.8 μm, que están menos afectadas por el efecto atmosférico que las del visible. Después, se relaciona la reflectividad de la superficie en el visible con la del canal en 2.1 μm. Posteriormente se selecciona el mejor modelo de aerosoles y se calcula el valor final del espesor óptico espectral. Una vez éste es conocido se aplica en la obtención de la reflectividad de la superficie teniéndose en cuenta los efectos de BRDF y adyacencia.

2.3 Corrección atmosférica de MISR

La estimación de aerosoles a partir de datos MISR (*Multi-angle Imaging SpectroRadiometer*) se realiza en celdas de 17,6 × 17,6 km. Las estimaciones se hacen por medio de la comparación de las radiancias observadas con otras simuladas, calculadas para una serie de combinaciones de concentración y tipo de aerosoles. Estas comparaciones tienen lugar en los dominios espectral y angular. La reflectividad de la superficie es parametrizada a través de un modelo para superficies heterogéneas, que demostró ser más preciso y tener un rango de aplicación mayor que el basado en DDVs. Sin embargo, el algoritmo no se aplica a superficies con topografía compleja. Este modelo de superficies heterogéneas no se basa en la presencia de un determinado tipo de superficie, sino en contrastes espaciales en la región de 17.6 km. Una vez los parámetros ópticos atmosféricos son conocidos, se realiza la estimación de reflectividad de la superficie, tanto para superficies de tierra como de agua.

2.4 Corrección atmosférica de AATSR

La estimación de aerosoles en AATSR (*Advance Along-Track Scanning Radiometer*) se basa en la comparación de las radiancias medidas desde dos ángulos de observación, uno en nadir y otro a 55º. El modelo de reflectividad de la superficie está diseñado para tener en cuenta la observación dual de AATSR, y se centra en la invariabilidad espectral de las observaciones a diferentes ángulos, lo que hace que las variaciones angulares de la reflectividad de la superficie estén dominadas por efectos geométricos independientes de la longitud de onda. Este modelo de reflectividad y el código 6S se usan para invertir las radiancias TOA medidas por el AATSR en 4 bandas en el visible e infrarrojo próximo y los 2 ángulos de observación, obteniéndose como resultado la reflectividad de la superficie en esas 4 bandas y 2 ángulos, además del AOT.

2.5 Corrección atmosférica de Landsat

El sistema Landsat TM (Thematic Mapper) lleva varias décadas proporcionando datos de teledetección para diferentes aplicaciones. Han sido varios los métodos desarrollados para el procesado de datos Landsat en ese tiempo, entre los que se puede destacar los de blanco invariante, ajuste del histograma, blanco oscuro o reducción del contraste.

Algoritmo de Corrección Atmosférica para Datos MERIS sobre Tierra

Capítulo 3 – Base Teórica del Algoritmo

La base teórica del algoritmo de corrección atmosférica para datos MERIS sobre tierra presentado en esta tesis es descrito en este capítulo. Se ha llamado SCAPE-M (de *Self-Contained Atmospheric Parameters Estimation from MERIS data*) para hacer énfasis en su modo de funcionamiento automático sin necesidad de datos externos. El capítulo se divide en tres secciones. En la primera se hace una descripción de los diferentes pasos que comprende el algoritmo para la derivación de los productos de aerosoles, vapor de agua y reflectividad de la superficie. En la segunda se describe cómo se ha diseñado la LUT generada con MODTRAN4 para los cálculos atmosféricos. Por último se hace un análisis de sensibilidad acerca del impacto de diferentes factores sobre los parámetros atmosféricos y de reflectividad a obtener, así como una estimación de los errores asociados al método en la estimación de cada parámetro.

3.1 Descripción del algoritmo

Generalidades

Desde un punto de vista formal, la corrección atmosférica se puede separar en dos fases. En la primera se estiman los parámetros atmosféricos necesarios para la cuantificación del efecto atmosférico sobre la radiación. A continuación, en la segunda fase se desacoplan los efectos de transferencia radiativa de superficie y atmósfera. El algoritmo SCAPE-M presentado en esta tesis desarrolla las dos fases de modo consistente y autónomo, de modo que los parámetros atmosféricos de la primera fase son estimados desde los mismos datos MERIS, para después derivar la reflectividad de la superficie teniendo en cuenta la influencia de la altura y topografía del terreno y el efecto de adyacencia. Los aerosoles y el vapor de agua son los constituyentes atmosféricos más variables en escalas espaciales y temporales de los que tienen una actividad óptica considerable en el rango espectral cubierto por MERIS. Por esta razón son éstos los que son derivados por SCAPE-M para la corrección, mientras que valores por defecto son usados para el resto.

Cálculos de transferencia radiativa

Una versión optimizada de MODTRAN4 fue usada para la generación de la LUT aplicada en el cálculo de los parámetros ópticos atmosféricos en SCAPE-M. MODTRAN4 está basado en una resolución rigurosa de la ETR que acopla los procesos de dispersión y absorción, en lugar de calcularlos por separado como hace el 6S. Este acoplamiento supone un aumento considerable en la precisión de los cálculos en regiones afectadas por bandas de absorción de gases, pero también un aumento en la carga computacional importante. El uso de una LUT que proporciona los parámetros atmosféricos mediante interpolación lineal permite acelerar los cálculos en gran medida. Gracias a este procedimiento los parámetros atmosféricos pueden ser calculados para cada píxel, teniéndose así en cuenta las variaciones espaciales de alta frecuencia debidas a la topografía, la elevación de la superficie y el vapor de agua.

Discriminación de píxeles "no de tierra"

El primer paso en la corrección atmosférica es eliminar todos los píxeles que no pertenecen a superficies de tierra o de aguas próximas a ésta. Las grandes masas de agua (definidas como aquéllas con una superficie mayor a 400 km^2), las superficies a más de 2500 m sobre el nivel del mar y los píxeles clasificados como inválidos por las *flags* de MERIS son eliminadas del procesado en primer lugar.

Los píxeles afectados por nubes son más difíciles de detectar. Un método para la discriminación de nubes de cualquier espesor óptico o altura debe ser aplicado antes de la estimación de aerosoles y vapor de agua. Un algoritmo simple y robusto basado en umbrales estáticos de brillo y pendiente de la reflectividad espectral es aplicado por SCAPE-M. Consiste en dos conjuntos de umbrales, uno "restrictivo" y otro "relajado", que tienen diferente aplicación. El primero se usa para la estimación de aerosoles, y está diseñado de modo que cualquier píxel con la mínima probabilidad de estar contaminado por nubes es eliminado del procesado. De esta manera se evita que los píxeles utilizados para la estimación de aerosoles puedan estar parcial o totalmente contaminados por nubes, lo que supondría un error de primer orden en el valor obtenido. El segundo conjunto de umbrales se aplica a la separación de aquellos píxeles que están afectados con nubes por toda probabilidad. La máscara derivada es la que se aplica en la generación de los productos finales de atmósfera y reflectividad.

Consideración de los efectos de topografía

Los efectos de la topografía del área observada, pendiente y orientación de las superficies, modifican la distribución de irradiancia directa y difusa que le llega. El área cubierta por las imágenes de MERIS suele estar entre 350 y 1100 km, de modo que superficies con accidentes topográficos suelen aparecer en ellas. El DEM (*Digital Elevation Model*) que se adjunta a los datos de MERIS con la misma proyección y resolución que la imagen adquirida permite corregir los efectos de la topografía. El DEM se usa para calcular el vector normal a la superficie en cada píxel, de manera que el ángulo de iluminación real se obtiene a partir del producto escalar del ángulo de iluminación nominal y el vector normal. El ángulo de iluminación calculado es aplicado al pesado de las contribuciones de radiación directa y difusa mediante la ley del coseno y el modelo de Hay.

Estimación del espesor óptico de aerosoles

Los aerosoles son los componentes atmosféricos más importantes en el rango espectral cubierto por MERIS, además de muy variables en espacio y tiempo. Una estrategia muy utilizada en la detección de aerosoles desde satélite es el uso de superficies oscuras, para las que se asume que la mayor contribución a la radiancia observada desde el sensor proviene de la atmósfera. En el método de estimación de aerosoles implementado en SCAPE-M se evita el uso de superficies oscuras por su reducido rango de aplicación, ya que la existencia de DDVs está restringida a unas determinadas áreas en el planeta.

En cambio, la estimación de aerosoles en SCAPE-M sólo requiere que los píxeles utilizados para el cálculo puedan expresarse como una combinación lineal de dos *endmembers* representativos de espectros de vegetación verde y suelo desnudo. El área registrada por la imagen se divide en celdas de 30 × 30 km, en las que se asume que el contenido en aerosoles es horizontalmente homogéneo. Para cada una de estas celdas se obtiene un valor de la visibilidad de aerosoles, que es el parámetro utilizado en MODTRAN4, y por tanto en la LUT, para la cuantificación de la carga de aerosoles. Este procedimiento da lugar a un mosaico de valores de visibilidad, que son suavizados posteriormente para representar la variaciones suaves esperadas en atmósferas reales. Finalmente se convierte la visibilidad en espesor óptico de aerosoles, que es el parámetro normalemente usado por la comunidad atmosférica para cuantificar el contenido en columna de aerosoles. Para ello se asume un modelo rural y una función de transferencia entre visibilidad y AOT que considera la influencia de la elevación del terreno.

Para el cálculo del valor de visibilidad asignado a cada celda se utiliza el píxel más oscuro en ella para fijar el umbral mínimo de visibilidad, haciendo que ésta sea tal que no se den valores negativos en la reflectividad esa superficie oscura. Esta primera estimación es mejorada con la inversión de la radiancia en 5 píxeles de referencia, siendo el valor de visibilidad y las proporciones de vegetación y suelo los parámetros a obtener en la inversión. Para aquellas celdas en las que no se consigue una estimación de visibilidad fiable se asigna un valor por interpolación con las celdas de alrededor.

Estimación del vapor de agua integrado

El método de cálculo de vapor de agua implementado en SCAPE-M se basa en la evaluación de la absorción diferencial de vapor de agua que se recoge en las bandas 14 y 15 de MERIS, centradas en 890 y 900 nm, aproximadamente. La primera está afectada por ala izquierda de la banda de absorción de vapor de agua centrada en 940 nm, y la otra dentro de ésta. El valor de CWV se relaciona directamente con el cociente entre estas dos bandas.

El cálculo de CWV se realiza por medio de un procedimiento iterativo que calcula un valor para cada píxel de la imagen. Para generar el cociente de radiancias entre las bandas 14 y 15 que permite invertir el calculado a través de las medidas de MERIS se necesita una valor estimado de la reflectividad de la superficie. Sin embargo, para calcular ésta en la banda 15 es necesario el conocimiento del CWV (sólo un residuo de la absorción de vapor de agua es registrado en la banda 14). Por esta razón la reflectividad de la superficie se calcula en las bandas 13 y 14 asumiendo valores por defecto del contenido en vapor de agua, y después se extrapola a la banda 15 asumiendo que el patrón spectral de reflectividad de las superficies de tierra es lineal. Este procedimiento puede ser refinado mediante una iteración que sustituye el valor por defecto con el obtenido tras la primera iteración. La influencia de la elevación de la superficie, la topografía y la carga de aerosoles para cada píxel son tenidas en cuenta gracias a la rápida interpolación lineal a partir de la LUT.

Estimación de la reflectividad de la superficie

Los mismos parámetros atmosféricos calculados con el valor final de la estimación del CWV son utilizados para el cálculo de la reflectividad de la superficie en cada píxel. El valor calculado en las bandas 2, 11 y 15 es sustituido por uno derivado mediante interpolación lineal con las bandas vecinas, en el primer caso por posibles errores en la calibración radiométrica de MERIS y en los otros 2 por la fuerte contaminación por absorciones de gases.

El último paso es corregir los efectos de adyacencia en la reflectividad. Con este fin se usa un modelo sencillo que pesa el efecto del entorno sobre un píxel dado mediante la carga de aerosoles medida sobre ese píxel por el AOT estimado previamente. El área adyacente está formada por todos los píxeles en un entorno de 1 km de radio, con lo que la corrección de adyacencia sólo se aplica a los datos FR (de *full resolution*, 300 m por píxel).

3.2 Generación de LUTs con MODTRAN4

MODTRAN4 ha sido elegido para construir la LUT atmosférica que utiliza SCAPE-M para los cálculos de transferencia radiativa, principalmente por su alta resolución espectral y la precisión de los cálculos dentro de bandas de absorción. Esta LUT debe cubrir un amplio rango de condiciones geométricas y atmosféricas para poder ser aplicada con una base operativa.

La LUT generada consiste en 6 parámetros libres: ángulo cenital de observación (VZA, de *view zenith angle*), ángulo cenital de iluminación (SZA, de *sun zenith angle*), ángulo azimutal relativo (RAA, de *relative azimuth angle*), elevación de la superficie (ELEV), visibilidad horizontal (VIS) y vapor de agua integrado. La LUT proporciona un conjunto de 7 parámetros atmosféricos (radiancia de camino, irradiancia directa en la superficie, irradiancia difusa en la superficie, albedo esférico, transmisividad para radiación directa entre la superficie y el TOA, cociente de transmisividades difusa y directa entre la superficie y el TOA y espesor óptico en 550 nm) para cada una de las 15 bandas de MERIS en cada llamada.

La distribución de los nodos de la tabla se realiza de modo que se cubra todo el rango de variación de cada uno de los parámetros de entrada. El número de nodos se optimiza en función de la variación de de los procesos atmosféricos de dispersión y absorción en el espacio de los parámetros de entrada. Los procesos de dispersión son caracterizados por la radiancia de camino en el azul, que es una magnitud directamente relacionada con la dispersión múltiple. Los procesos de absorción son caracterizados por el cociente entre las bandas 10/11 y 14/15. Los nodos son colocados en la tabla en número y posición tales que la interpolación lineal sea lo más realista posible. El análisis de estos parámetros representativos para los diferentes parámetros de entrada llevó a la definición de la LUT según se recoge en el Cuadro E.1

Cuadro E.1: Posición de los nodos en la LUT para las 6 variables de entrada.

	#1	#2	#3	#4	#5	#6	#7
VZA (º)	0	9	18	27	36	45	–
SZA (º)	0	10	20	35	50	65	–
RAA (º)	0	25	50	85	120	155	180
ELEV (km)	0	0.7	2.5	–	–	–	–
VIS (km)	10	15	23	35	60	100	180
CWV (g·cm^{-2})	0.3	1	1.5	2	2.7	5	–

3.3 Análisis de sensibilidad

Sensibilidad en la estimación del espesor óptico de aerosoles

La sensibilidad de la estimación de aerosoles frente a diferentes fuentes de incertidumbre es analizada a través de una base de datos MERIS simulada. Los valores de los parámetros de entrada son controlados en la simulación, de manera que se pueda estudiar cómo afectan a los valores del AOT que son derivados posteriormente. Las simulaciones son realizadas de manera que se reproducen configuraciones de adquisición típicas en MERIS. Como parámetros típicos se usó VZA=20º, SZA=28º, RAA=150º, superficie inclinada 10º hacia el sol y a una altura media sobre el nivel del mar de 300 m, y un contenido en vapor de agua de 2 g·cm^{-2}. La reflectividad de la superficie se varió a través de la combinación de diferentes espectros de vegetación y suelo, que simulaban los píxeles de referencia utilizados en el cálculo de aerosoles.

Como conclusiones más importantes se dedujo que:

- Si no se introduce error en los datos de entrada del modelo de estimación de aerosoles, sino que éstos son los mismos que los utilizados en las simulaciones, el error en el AOT resultante es despreciable. Esto permitir descartar posibles desviaciones sistemáticas del modelo o errores en la implementación informática.

- En el estudio de la sensibilidad a los espectros de referencia utilizados, el RMSE (*Root Mean Square Error*) para el 75 % de los píxeles de vegetación probados es menor que 0.03, siendo el valor medio de todos los casos 0.026.

- Errores de ±300 m en la altura de la superficie supone errores de hasta 0.08 en AOT. Sin embargo esta contribución puede descartarse por la utilización del DEM para la consideración de la altura real de la superficie.
- El error asociado al desconocimiento del CWV en ±1 g·cm^{-2} puede suponer errores de hasta 0.03 en AOT para los valores más altos, pero son casi despreciables para valores de AOT medios y bajos.
- La influencia de la pendiente de la superficie en la estimación del AOT es prácticamente despreciable.

Con todos estos argumentos se asocia un error absoluto intrínseco a la estimación de AOT de ±0.03.

Sensibilidad en la estimación del contenido en columna del vapor de agua

Un estudio análogo se hace para el análisis de los factores que afectan a la estimación del contenido en vapor de agua. De la configuración utilizada para el AOT se fija éste a 0.36 y de deja el CWV libre. La reflectividad de la superficie viene dada igualmente por combinaciones lineales de vegetación y suelo para analizar la influencia del patrón espectral de reflectividad de la superficie sobre la estimación de vapor de agua. Además se analiza la influencia del calibrado espectral (posición espectral exacta de la banda 15 de MERIS) sobre la obtención de CWV.

Las principales conclusiones extraidas son:

- No se encuentra error en la estimación de CWV si los inputs en el modelo son los mismos que los utilizados para generar la base de datos simulada y la iteración sobre el valor por defecto aplicada en la primera estimación de la reflectividad de la superficie es aplicada. Un RMSE alrededor de 0.046 g·cm^{-2} es encontrado si esta iteración no se hace.
- Errores relativos en CWV menores del 0.5 % son debidos a la respuesta espectral de la superficie y a la topografía.
- La influencia de la altura de la superficie y el contenido en aerosoles es más importante, del orden de 0.06 g·cm^{-2} cuando se introducen errores en la altura de la superficie de ±300 m y 0.13 g·cm^{-2} cuando el AOT en 550 nm se desconoce en un entorno de ±0,15 alrededor del valor de entrada de 0.36.
- Los errores asociados al calibrado espectral son más importantes, pues no pueden resolverse fácilmente al ser intrínsecos a la misma medida. Dependen de la posición

exacta de la banda y del contenido total en vapor de agua, llegando hasta el 4 % para un valor de entrada de CWV de 2 g·cm^{-2}.

La propagación de todos estos errores lleva a asumir un error relativo en la estimación de vapor de agua de ±4 %.

Sensibilidad en la estimación de la reflectividad de la superficie

Para el análisis de la precisión en la estimación de la reflectividad de la superficie se compara los espectros de reflectividad derivados de la corrección de los datos simulados con los que fueron usados para la generación de esas mismas simulaciones. La misma configuración de la escena es aplicada, siendo en estos casos tanto el AOT como el CWV parámetros libres. La reflectividad viene dada por píxeles de vegetación y suelo, que es a los que está destinado el algoritmo como primer objetivo.

Se concluye:

- La influencia del AOT es mayor para las longitudes de onda más cortas en el azul, debido a la dependencia espectral de la dispersión múltiple de radiación por los aerosoles. Se estimaron errores de hasta el 100 % en reflectividad en el azul para espectros de vegetación oscuros. Además, los errores en reflectividad debidos a una mala estimación de los aerosoles también son apreciables en las bandas de absorción, debido al diferente comportamiento de la dispersión múltiple dentro y fuera de las bandas de absorción.

- El CWV no afecta tanto los valores de reflectividad obtenidos, excepto en la banda 15 de MERIS.

- Errores en reflectividad debidos a una mala estimación de la altura de la superficie son apreciables principalmente en el visible, por la dependencia de la contribución de la dispersión de Rayleigh a la radiancia de camino, hasta un 30 % en el azul para reflectividades bajas.

- La pendiente y orientación de la superficie afectan considerablemente en todo el espectro, con errores entre el 10 y el 15 % incluso en reflectividades altas del infrarrojo próximo cuando la pendiente se varía en ±10º respecto al input.

La combinación de estos factores permitió estimar un error de ±8 % espectralmente constante en la estimación de la reflectividad de la superficie.

Capítulo 4 – Validación de los Productos de Corrección Atmosférica

Este capítulo se dedica a la validación de los productos de espesor óptico de aerosoles, vapor de agua y reflectividad de la superficie. Esta validación ha consistido en la comparación de los resultados obtenidos del procesado de más de 200 imágenes de MERIS con SCAPE-M con diferentes fuentes de datos comparables, tales como datos de parámetros atmosféricos y de superficie medidos en campañas de campo, medidas atmosféricas proporcionadas por la red de estaciones AERONET u otros productos MERIS.

4.1 Fuentes de datos de referencia para la validación

La validación de los productos atmosféricos de SCAPE-M se ha basado en la comparación con medidas atmosféricas por instrumentos a nivel de suelo. Las dos fuentes de datos más importantes han sido las campañas de campo celebradas en la zona de estudio de Barrax (La Mancha, Albacete, España) y diferentes estaciones de la red AERONET distribuidas alrededor del mundo.

En Barrax se ha celebrado campañas de medida para la calibración y validación de datos de satélite entre 2003 y 2005. En 2003 y 2004 las campañas SPectra bARrax Campaigns (SPARC) se dedicaron la preparación de la fase de la misión SPECTRA. En 2005 tuvo lugar la campaña SEN2FLEX (SENtinel-2 and FLuorescence EXperiment) para el estudio de la fluorescencia vegetal y la definición de los parámetros de la futura misión Sentinel-2. La zona de estudio de Barrax es un área continental plana con altura sobre el nivel del mar de unos 700 m. Se caracteriza por una morfología plana y extensas unidades de uso de suelo. Una gran base de datos de medidas de parámetros de superficie y atmósfera fue recogida en estas campañas de manera simultánea a la adquisición de imágenes de MERIS.

Por su parte, AERONET es una red de fotómetros solares distribuidos alrededor del mundo que proporcionan información localizada espacial y temporalmente sobre la situación atmosférica, incluyendo medidas de espesor óptico de aerosoles y vapor de agua. La gran variedad de localizaciones en las que las estaciones están distribuidas permite el análisis del funcionamiento de métodos bajo diferentes configuraciones y entornos.

4.2 Resultados de la estimación del espesor óptico de aerosoles

La comparación de los mapas de AOT sobre Barrax con las medidas *in situ* realizadas en las campañas muestran una buena correlación. El método es capaz de discriminar entre condiciones atmosféricas con alta y baja carga de aerosoles, como lo demuestra la comparación con medidas de LICOR para 2 fechas diferentes. La comparación en una tercera fecha no es tan buena porque se detectó una intrusión de partículas desérticas ese día, lo que genera errores en la estimación de AOT porque el modelo de aerosoles está fijado al estándar rural. Ésta es una limitación intrínseca del método, porque no se encuentra suficiente información en MERIS para conseguir una estimación realista del modelo de aerosoles desde los mismos datos.

Los mismos mapas fueron comparados con unos equivalentes derivados mediante el método BAER. Se encontró una cierta correlación en los patrones espaciales de AOT, aunque el BAER consigue una resolución mucho más fina al realizar los cálculos por píxel, aunque se proporciona datos en un porcentaje de píxeles mucho menor que SCAPE-M. También se detectó una importante sobreestimación del AOT por parte del BAER, posiblemente por una mala clasificación de las nubes. El producto de aerosoles de nivel 2 de MERIS no fue analizadpo porque proporciona muy pocas medidas de AOT en una zona con vegetación dispersa como Barrax.

La capacidad de SCAPE-M de determinar episodios atmosféricos en los que niveles inusuales de turbiedad están presentes fue también demostrada mediante el procesamiento de una imagen adquirida durante los incendios forestales de Portugal en 2003 y de otra sobre el área de Pekín. El efecto tanto de los fuegos como de la polución dieron como resultado patrones espaciales de alto contenido en aerosoles.

Para una validación cuantitativa de los resultados se procesó más de 170 imágenes de MERIS. Los mapas de AOT resultantes fueron comparados con medidas de AERONET procedentes de diferentes estaciones en Europa y en Brasil. Se encontró correlaciones lineales del orden de 0.7-0.8, lo que demuestra el buen funcionamiento del método. También se detectó una cierta subestimación de los valores determinados por SCAPE-M para los espesores ópticos más altos que necesita de más investigación, aunque la diferente parametrización de la variable espesor óptico por parte de los códigos de transferencia radiativa utilizados en el procesado de los datos, tanto en SCAPE-M como en AERONET, puede explicar parte de esta diferencia. Por otro lado se observó cómo las correlaciones aumentan si la comparación se hace con datos FR, por la mayor disponibilidad de contraste espectral para los píxeles de referencia.

4.3 Resultados de la estimación del vapor de agua integrado

Un ejercicio de validación análogo se desarrolló para el vapor de agua. La estimaciones de CWV sobre Barrax de SCAPE-M fueron comparadas con el producto de nivel 2 de la ESA, medidas desde suelo y radiosondeos. Se encontró una buana correlación entre todas las fuentes, si bien se encontraba una cierta sobreestimación de los cálculos de SCAPE-M respecto a los valores dados por la ESA, y en mayor medida respecto a los radiosondeos, que parecen subestimar el contenido total en vapor de agua.

Las medidas de AERONET proporcionaron información cuantitativa sobre el funcionamiento del método bajo diferentes entornos. Las correlaciones medias eran mayores de 0.92 en la mayoría de los casos, con una buena separación de contenidos de humedad tanto altos como bajos, incluso para los valores mayores de 4.5 $g \cdot cm^{-2}$ determinados en imágenes sobre la selva amazónica.

Una cuidada comparación del método presentado en esta tesis para la estimación de vapor de agua con los datos de nivel 2 proporcionados por la ESA demostró una buena correlación en términos generales. Sin embargo, también se encontró ciertas desviaciones entre los dos métodos debidas a una diferente consideración de los efectos debido a la elevación del terreno. En concreto, el vapor de agua derivado por SCAPE-M era menor que el de nivel 2 de la ESA para superficies próximas al nivel del mar, mientras que sucedía lo contrario para superficies por encima de 300-400 m. De confirmarse esta tendencia se podría afirmar que SCAPE-M da una mejor comparación con los datos de AERONET que el producto ESA, pues cierta sobreestimación en SCAPE-M fue encontrada en estaciones al nivel del mar, efecto que se vería agravado en el caso del producto ESA.

4.4 Resultados de la estimación de reflectividad de la superficie

La validación de la reflectividad de la superficie en píxeles de tierra es más complicada que el de los parámetros atmosféricas, porque las frecuencias espaciales de variación son mucho más altas, lo que conlleva que la comparación directa de medidas de suelo con los datos de MERIS, a 300 ó 1200 m de resolución, no sea realista.

Con el fin de solucionar este problema, los mapas de reflectividad de la superficie derivados de las imágenes de MERIS fueron comparados con otros derivados de una imagen de CHRIS-PROBA adquirida el mismo día. La resolución espacial de esta imagen es de 34 m, de modo que la comparación con las medidas de campo es ya más significativa. En términos generales se encontró una buena correspondencia, tanto entre las medidas de campo y los datos de CHRIS-PROBA como entre éstos y los derivados de MERIS, siempre que se usaran superficies con la mayor homogeneidad posible.

Los mapas de reflectividad obtenidos con SCAPE-M fueron también comparados con los proporcionados por el algoritmo BAER en aquellas zonas en que éste era capaz de derivar un valor de AOT y de reflectividad de la superficie. Se encontró que había cierta dispersión en los resultados para las longitudes de onda más cortas, y por tanto más afectadas por el efecto atmosférico (correlación entree 0.5 y 0.7 en el azul), si bien la correlación aumentaba considerablemente con la longitud de onda (mayor que 0.96 en el rojo y el infrarrojo).

Por último, se comparó la reflectividad extraída de píxeles de aguas continentales con medidas *in- situ*, gracias a la mayor homogeneidad encontrada en el agua respecto a la tierra. Teniendo en cuenta la baja señal procedente de píxeles de agua se llegó a una buena comparación tanto en los niveles de reflectividad como en la forma de los espectros, lo que constituye una prueba sólida de la buena compensación del efecto atmosférico.

Capítulo 5 – Aplicación: Estimación de Fluorescencia de la Clorofila mediante datos MERIS

La clorofila de la vegetación emite una señal débil cuando es excitada por la radiación solar. Esta emisión, conocida por fluorescencia de la clorofila por inducción solar, tiene lugar en las regiones espectrales del rojo y el rojo lejano (aproximadamente, entre 650 y 800 nm). Un método para la monitorización de fluorescencia vegetal a partir de datos MERIS es presentado en este capítulo. La fluorescencia estimada es comparada con resultados espacialmente coincidentes derivados de datos procedentes del sensor aerotransportado CASI-1500, que a su vez fueron validados con medidas de suelo.

5.1 Teledetección de la fluorescencia vegetal

La fluorescencia de la clorofila vegetal es un parámetro directamente relacionado con la actividad fotosintética de las plantas. El problema es que la baja intensidad de esta radiación emitida en comparación con la solar que es reflejada hace que su detección desde satélite sea un reto. Una solución para aumentar la contribución de la radiación emitida frente a la reflejada es medir dentro de bandas de absorción superpuestas al espectro de emisión de la fluorescencia. Dentro de estas bandas de absorción la radiación solar es atenuada en los caminos entre el TOA y la superficie de subida y de bajada, mientras que la emitida sólo lo es en el de subida, con lo es más fácilmente detectable. En particular, la banda de absorción del oxígeno terrestre centrada en 760 nm es de gran utilidad para la estimación de fluorescencia por superponerse a la emisión de fluorescencia, ser una banda fina y profunda y porque la vegetación presenta una respuesta espectral casi lineal en ese rango de longitudes de onda.

Para utilizar esta banda en la estimación de fluorescencia a partir de datos de teledetección se debe contar con sensores con una adecuada resolución espectral en la zona de 760 nm. MERIS es posiblemente el único sensor a bordo de un satélite con la adecuada configuración espectral para la estimación de fluorescencia, pues la banda 11 tiene una anchura de 3.75 nm y está bien acompañada por la banda 10, separada sólo unos 8 nm y fuera de la absorción del oxígeno, de modo que pueden utilizarse como par medida/referencia. Además MERIS presenta una buena calibración radiométrica, y una resolución espacial en el modo FR en la que aún se puede encontrar superficies de vegetación verde sin mezcla aparente de otros tipos de blanco.

5.2 Análisis de sensibilidad

Para determinar cuáles son los factores que pueden afectar a la profundidad de la banda del oxígeno además de la fluorescencia se simuló una serie de espectros con la configuración espectral de MERIS variando diferentes inputs de manera independiente (nivel de fluorescencia, altura de la superficie, contenido en aerosoles, pendiente de la superficie, reflectividad en 760 nm, contenido en vapor de agua y calibrado espectral).

La conclusión principal de este estudio es que el efecto de la fluorescencia es realmente apreciable en la profundidad de la banda del oxígeno. Sin embargo, también se observa que ésta está afectada de igual o mayor manera por la elevación de la superficie, el contenido en aerosoles y el calibrado espectral. Por este argumento se ha encuadrado la estimación de la fluorescencia vegetal en el entorno de corrección atmosférica que proporciona SCAPE-M, en el que esos factores son considerados con detalle.

5.3 Descripción de la metodología

La señal de la fluorescencia es añadida al esquema de transferencia radiativa como un término aditivo superpuesto al flujo solar reflejado. Si se considera la ecuación de transferencia radiativa en las bandas 10 y 11, fuera y dentro de la absorción del oxígeno, y los parámetros atmosféricos son proporcionados por el algoritmo de corrección atmosférica, se tiene un sistema con 2 ecuaciones y 4 incógnitas, que son la reflectividad y la fluorescencia en las bandas 10 y 11. Para resolver el sistema se asume que tanto la reflectividad como la fluorescencia deben variar linealmente entre las dos bandas, lo que es realista por la poca separación entre ellas.

Con esta ligadura el sistema puede ser resuelto matemáticamente. Sin embargo, aunque se ponga mucha atención en la computación de la transferencia radiativa dentro de la banda del oxígeno, tanto pequeños errores en los parámetros de entrada como cambios en la configuración espectral del sensor respecto a la proporcionada como nominal supondrían errores apreciables en la fluorescencia estimada. Con objeto de minimizar estos errores se realiza una corrección de los parámetros atmosféricos calculados en la banda del oxígeno llamada “corrección de transmisividad”. Ésta se basa en superficies no fluorescentes para determinar un factor corrector con dimensiones de transmisividad que hace que la reflectividad entre las bandas 10 y 12 sea lineal.

5.4 Resultados

Resultados a partir de datos MERIS

El método se ha aplicado en primer lugar a las imágenes MERIS FR adquiridas durante las campañas SPARC y SEN2FLEX. Se observa que el rango de valores en la señal estimada se mantiene constante entre 1 y 4 $\mathrm{Wm^{-2}sr^{-1}\mu m^{-1}}$, aproximadamente, para los píxeles de vegetación, lo que es una buena prueba de la robustez del método. Los mapas generados se comparan con mapas de otros parámetros biofísicos calculados a partir de las mismas imágenes, entre los que estaban el contenido en clorofila, el índice de área foliar, la fracción de radiación fotosintéticamente activa absorbida o la fracción de cobertura vegetal. Aunque la correlación de la fluorescencia con los indicadores de la clorofila era mayor que con los de cantidad de vegetación, no se llega a encontrar una redundancia entre la fluorescencia y las otras variables, lo que permite concluir que la fluorescencia es un indicador independiente de los que han sido tradicionalmente utilizados en teledetección.

Resultados a partir de datos CASI-1500

Como la resolución espacial de MERIS no permite una validación cuantitativa de los resultados mediante medidas de suelo, las imágenes de CASI-1500, de 3 m por píxel, fueron utilizadas de manera análoga a las de MERIS para la estimación de fluorescencia. Se encuentra que el rango de valores encontrado a partir de los datos de CASI es equivalente al calculado con MERIS. Además, la comparación con medidas de campo da un correlación de 0.854 en los transectos medidos, confirmándose la utilidad de la metodología propuesta para la determinación de fluorescencia desde datos de teledetección.

Conclusión

Con el título *Nuevos algoritmos para la corrección atmosférica y la estimación de parámetros biofísicos en Observación de la Tierra. Aplicación a datos ENVISAT/MERIS* se ha presentado un trabajo sobre el desarrolo de nueva metodología para el procesado de datos MERIS de nivel 1b. El objetivo principal del trabajo es el desarrollo de un algoritmo operativo para la conversión de las imágenes de radiancia en productos biofísicos de la atmósfera y la superficie. La operatividad y la autonomía de este método se resume en el nombre del algoritmo, *Self-Contained Atmospheric Parameters Estimation from MERIS data*. Los diferentes pasos desarrollados por el algoritmo para derivar los productos finales han sido discutidos a lo largo de esta tesis.

De entre los diferentes comentarios y conclusiones destacadas a lo largo del documento, algunos merecen ser destacados:

- Una nueva herramienta para el procesado de datos MERIS de nivel 1b sobre tierra está disponible para la comunidad de la teledetección. La corrección atmosférica y la geométrica son realizadas de modo automático. Mapas de espesor óptico de aerosoles, vapor de agua, reflectividad de la superficie y fluorescencia vegetal son derivados

- La estimación del espesor óptico de aerosoles es una cuestión compleja afectada por diferentes factores:

    1. El más importante es la disponibilidad de un modelo de superficie que proporcione un valor fiable de la reflectividad de la superficie. Debe permitir el desacoplamiento de las contribuciones de atmósfera y superficie a la señal medida por el sensor.
    2. La estimación del modelo de aerosoles desde datos MERIS es también una cuestión difícil. La inclusión de parámetros describiendo el modelo de aerosoles añade variables al problema, complicando su resolución, y la información espectral y angular proporcionada por MERIS no parece suficiente para conseguir una estimación adecuada del tipo de aerosoles.

3. La variabilidad espacial de los aerosoles debe ser investigada. El método propuesto en esta tesis estima el contenido en aerosoles integrado en celdas de 30×30 km en las que se asume que la atmósfera es lateralmente homogénea. Esta estrategia proporciona ventajas como la mayor disponibilidad de espectros de referencia sobre los que hacer la estimación, así como la disminución de la carga computacional, pero no permite obtener variaciones de alta frecuencia espacial en la distribución de aerosoles. Aunque no se espera que éstas sean acusadas en el caso más general, sí podrían ser aparentes en áreas con topografía accidentada.
4. Los píxeles afectados por nubes conducen a valores de AOT fuera de rango. Esto puede suponer un problema en el caso de nubes cirros con espesor óptico bajo, que son difíciles de detectar. El desarrollo de nuevas técnicas de detección de nubes redundaría en las estimaciones de AOT.

- La estimación de vapor de agua no require un modelo tan complejo. La principal ligadura que se ha encontrado está asociada al tiempo de cálculo, ya que la estimación en una base por píxel pueden consumir gran cantidad de tiempo para las imágenes mayores. Por otra parte, la mayor fuente de error encontrada es la variación de la posición de la banda 15 de MERIS, que llevaba a discontinuidades de hasta 0.2 $g \cdot cm^{-2}$ en las transiciones de cámara.

- Además del AOT y el CWV, otros factores deben ser considerados para la estimación de la reflectividad de la superficie. Ésta está afectada por efectos de elevación y de topografía, que son normalmente despreciados en modelos de corrección atmosférica. Estos efectos son considerados en SCAPE-M, pero no el de la direccionalidad de la reflectividad. No se ha encontrado ninguna forma de considerar la direccionalidad en el modelo sin perder su autonomía y operatividad. Por lo tanto, los errores asociados a la aproximación lambertiana son asumidos como intrínsecos al método.

- La señal de fluorescencia de la clorofila vegetal es un prometedor indicador de las condiciones de la vegetación, más cerca de la fotosíntesis que otros índices de vegetación. Aunque la señal es muy débil respecto a otras contribuciones, un primer paso hacia su detección cuantitativa se ha presentado en esta tesis.

Part VI

References

References

Adler-Golden, S. M., Matthew, M. W., Bernstein, L. S., Levine, R. Y., Berk, A., Richtsmeier, S. C., Acharya, P. K., Anderson, G. P., Felde, G., Gardner, J., Hoke, M. L., Jeong, L. S., Pukall, B., Mello, J., Ratkowski, A., Burke, H. H., 1999. Atmospheric correction for short-wave spectral imagery based on MODTRAN4. In: Proceedings of SPIE Conf. Imaging Spectrometry V. Vol. 3753.

Amorós-López, J., Gómez-Chova, L., Vila-Francés, J., Calpe, J., Alonso, L., Moreno, J., del Valle-Tascón, S., 2006. Study of the diurnal cycle of stressed vegetation for the improvement of fluorescence remote sensing. In: Proceedings of SPIE Remote Sensing. Stockholm, Sweden.

Baret, F., Guyot, G., 1991. Potentials and limits of vegetation indices for LAI and APAR assessment. Remote Sensing of Environment 35, 161–173.

Baret, F., Pavageau, K., Béal, D., Weiss, M., Berthelot, B., Regner, P., March 2006. Algorithm Theoretical Basis Document for MERIS Top of Atmosphere Land Products. Contract ESA AO/1-4233/02/I-LG.

Barnsley, M. J., Settle, J. J., Cutter, M., Lobb, D., Teston, F., 2004. The PROBA/CHRIS mission: a low-cost smallsat for hyperspectral, multi-angle, observations of the earth surface and atmosphere. IEEE Transactions on Geoscience and Remote Sensing 42, 1512–1520.

Barton, C. V. M., North, P. R. J., 2001. Remote sensing of canopy light use efficiency using the photochemical reflectance index. model and sensitivity analysis. Remote Sensing of Environment 78, 264–273.

Bennartz, R., Fischer, J., 2001. Retrieval of columnar water vapour over land from backscattered solar radiation using the Medium Resolution Imaging Spectrometer. Remote Sensing of Environment 78, 274–283.

Berk, A., Anderson, G. P., Acharya, P. K., Hoke, M. L., Chetwynd, J. H., Bernstein, L. S., Shettle, E. P., Matthew, M. W., Adler-Golden, S. M., 2003. MODTRAN4 Version

3 Revision 1 User's Manual. Tech. rep., Air Force Research Laboratory, Hanscom Air Force Base, MA, USA.

Berk, A., Bernstein, L. S., Anderson, G. P., Acharya, P. K., Robertson, D. C., Chetwynd, J. H., Adler-Golden, S. M., 1998. MODTRAN cloud and multiple scattering upgrades with application to AVIRIS. Remote Sensing of Environment 65, 367–375.

Bruegge, C. J., Conel, J. E., Green, R. O., Margolis, J. S., Holm, R. G., Toon, G., 1992. Water vapor column abundance retrievals during FIFE. Journal of Geophysical Research 97, 18759–18768.

Cachorro, V. E., Toledano, C., Vergaz, R., de Frutos, A. M., Sorribas, M., Vilaplana, J. M., De la Morena, B., 2004. The PHOTONS-AERONET sites in Spain. Calibration problems and KCICLO correction method. Óptica Pura y Aplicada 37, 3401–3406.

Campbell, P. K. E., Middleton, E. M., Corp, L. A., McMutey, J. E., Kim, M. S., Chappelle, E. W., Butcher, L. M., 2002. Contribution of chlorophyll fluorescence to the reflectance of corn foliage. In: Proceedings of the IGARSS. Toronto, Canada.

Charlson, R. J., Schwartz, S., Hales, J., Cess, R., Coakley, Jr., J., Hansen, J., Hoffman, D., 1992. Climate forcing of anthropogenic aerosols. Science 255, 423–430.

Choudhury, B. J., 2001. Estimating gross photosynthesis using satellite and ancillary data: Approach and preliminary results. Remote Sensing of Environment 75, 1–21.

Chylek, P., Borel, C. C., Clodius, W., Pope, P. A., Rodger, A. P., 2003. Satellite-based columnar water vapor retrieval with the multi-spectral thermal imager (MTI). IEEE Transactions on Geoscience and Remote Sensing 41, 2767–2770.

Ciotti, P., Di Giampaolo, E., Basili, P., Bonafoni, S., Mattioli, V., Biondi, R., Fionda, E., Consalvi, F., Memmo, A., Cimini, D., Pacione, R., Vespe, F., July 2003. Validation of MERIS water vapour in the central Italy by concurrent measurements of microwave radiometers and GPS receivers. In: Proceedings of the IGARSS. Toulouse, France.

Civco, D. L., 1989. Topographic normalization of Landsat Thematic Mapper digital imagery. Photogrammetric Engineering and Remote Sensing 55, 1303–1309.

Colby, J. D., 1991. Topographic normalization in rugged terrain. Photogrammetric Engineering and Remote Sensing 57, 531–537.

d'Almeida, G. A., Koepke, P., Shettle, E. P., 1991. Atmospheric Aerosol, Global Climatology and Radiative characteristics. A. Deepak, Hampton, USA.

Dash, J., Curran, P., 2004. The MERIS Terrestrial Chlorophyll Index. International Journal Remote Sensing 25, 5003–5013.

Dave, J. V., 1980. Effect of atmospheric conditions on remote sensing of a surface nonhomogeneity. Photogrammetric Engineering and Remote Sensing 46, 1173–1180.

Deschamps, P. Y., Breon, F. M., Leroy, M., Podaire, A., Bricaud, A., Buriez, J., Seze, G., 1994. The POLDER Mission: Instrument characteristics and scientific objectives. IEEE Transactions on Geoscience and Remote Sensing 32, 598–615.

Deschamps, P. Y., Herman, M., Lenoble, J., Tanré, D., Viollier, M., 1980. Atmospheric effects in remote sensing of ground and ocean reflectances. In: Remote Sensing of Atmosphere and Ocean. Ed. A. Deepak, pp. 115–148.

Diner, D. J., Martonchik, J. V., Kahn, R. A., Pinty, B., Gobron, N., Nelson, D. L., Holben, B. N., 2005. Using angular and spectral shape similarity constraints to improve MISR aerosol and surface retrievals over land. Remote Sensing of Environment 94, 155–171.

Diner et al, D. J., 1998. Multi-angle Imaging SpectroRadiometer instrument description and experiment overview. IEEE Transactions on Geoscience and Remote Sensing 36, 1072–1087.

Disney, M. I., 2001. Improved estimation of biophysical parameters through inversion of linear brdf models. Ph.D. thesis, University College London, London, United Kingdom.

Dobrowski, S. Z., Pushnik, J. C., Zarco-Tejada, P. J., Ustin, S. L., 2005. Simple reflectance indices track heat and water stress-induced changes in steady-state chlorophyll fluorescence at the canopy scale. Remote Sensing of Environment 97, 403–414.

Estellés, V., Utrillas, M. P., Martínez-Lozano, J. A., Alcántara, A., Alados-Arboledas, L., Olmos, F. J., Lorente, J., de Cabo, X., Cachorro, V., Horvath, H., Labajo, A., Vilaplana, M., Díaz, J. P., Díaz, A. M., Silva, A. M., Elías, T., Pujadas, M., Rodríguez, J. A., Cañada, J., García, Y., 2006. Intercomparison of spectroradiometers and sunphotometers for the determination of the aerosol optical depth during the VELETA2002 field campaign. Journal of Geophysical Research. In press.

European Centre for Medium-Range Weather Forecasts, 2006.
URL http://www.ecmwf.int/

European Space Agency, April 2006. MERIS Detailed Instrument Description. Tech. Rep. 1.0.
URL http://www.envisat.esa.int/dataproducts/

Evain, S., Flexas, J., Moya, I., 2004. A new instrument for passive remote sensing: 2. measurement of leaf and canopy reflectance changes at 531 nm and their relationship with photosynthesis and chlorophyll fluorescence. Remote Sensing of Environment 91, 175–185.

Fischer, J., Schüller, L., Preusker, R., February 2000. Algorithm Theoretical Basis Document: Cloud Top Pressure. PO-TN-MEL-GS-0005.

Fomferra, N., Brockmann, C., September 2005. Beam - the ENVISAT MERIS and AATSR Toolbox. In: ESA/ESRIN (Ed.), Proceedings of the MERIS-(A)ATSR workshop. Frascati, Italy.
URL http://www.brockmann-consult.de/beam/

Franklin, S., Giles, P., 1995. Radiometric processing of aerial and satellite remote-sensing imagery. Computers and Geosciences 21, 413–423.

Gamon, J. A., Peñuelas, J., Field, C. B., 1992. A narrow-waveband spectral index that tracks diurnal changes in photosynthetic efficiency. Remote Sensing of Environment 41, 35–44.

Gamon, J. A., Serrano, L., Surfus, J. S., 1997. The photochemical reflectance index: An optical indicator of photosynthetic radiation use efficiency across species, functional types, and nutrient levels. Oecologia 112, 492–501.

Goel, N. S., 1988. Models of vegetation canopy reflectance and their use in the estimation of biophysical parameters from reflectance data. Remote Sensing Reviews 4, 1–222.

Gómez-Chova, L., Camps-Valls, G., Amorós, J., Martín, J. D., Calpe, J., Alonso, L., Guanter, L., Fortea, J. C., Moreno, J., September 2005. Cloud detection for MERIS multispectral images. In: ESA/ESRIN (Ed.), Proceedings of the MERIS-(A)ATSR workshop. Frascati, Italy.

Goward, S. N., Williams, D. L., 1997. Landsat and Earth Systems Science: Development of terrestrial monitoring. Photogrammetric Engineering and Remote Sensing 63, 887–900.

Green, R., 1998. Spectral calibration requirement for earth–looking imaging spectrometers in the solar–reflected spectrum. Applied Optics 37, 683–690.

Green, R., Eastwood, M., Sarture, C., Chrien, T., Aronsson, M., Chippendale, B., Faust, J., Pavri, B., Chovit, C., Solis, M., Olah, M., Williams, O., 1998. Imaging spectroscopy and the airborne visible/infrared imaging spectrometer (AVIRIS). Remote Sensing of Environment 65, 227–248.

Grey, W. M. F., North, P. R. J., Los, S. O., Mitchell, R. M., 2006. Aerosol optical depth and land surface reflectance from multiangle AATSR measurements: global validation and intersensor comparisons. IEEE Transactions on Geoscience and Remote Sensing 44, 2184–2197.

Guanter, L., Alonso, L., Moreno, J., 2005a. First results from the PROBA/CHRIS hyperspectral/multiangular satellite system over land and water targets. IEEE Geoscience and Remote Sensing Letters 2, 250–254.

Guanter, L., Alonso, L., Moreno, J., 2005b. A method for the surface reflectance retrieval from PROBA/CHRIS data over land: Application to ESA SPARC campaigns. IEEE Transactions on Geoscience and Remote Sensing 43, 2908–2917.

Guanter, L., Estellés, V., Moreno, J., 2006a. Spectral calibration and atmospheric correction of ultra-fine spectral and spatial resolution remote sensing data. Application to CASI-1500 data. Remote Sensing of Environment. Submitted for peer review.

Guanter, L., González-Sampedro, M. C., Moreno, J., 2006b. A method for the atmospheric correction of ENVISAT/MERIS data over land targets. International Journal of Remote Sensing. In press.

Guanter, L., Richter, R., Moreno, J., 2006c. Spectral calibration of hyperspectral imagery using atmospheric absorption features. Applied Optics 45, 2360–2370.

Hapke, B., 1981. Bidirectional reflectance spectroscopy 1. theory. Journal of Geophysical Research 86, 3039–3054.

Hapke, B., 1993. Theory of Reflectance and Emittance Spectroscopy. Cambridge University Press.

Hay, J. E., 1979. Calculation of monthly mean solar radiation for horizontal and inclined surfaces. Solar Energy 23, 301–307.

Herman, M., Deuzé, J. L., Devaux, C., Goloub, P., Bréon, F. M., Tanré, D., 1997. Remote sensing of aerosols over land surfaces including polarization measurements and application to POLDER measurements. Journal of Geophysical Research 102, 17039–17049.

Holben, B. N., Eck, T. F., Slutsker, I., Tanre, D., Buis, J. P., Setzer, A., Vermote, E., Reagan, J. A., Kaufman, Y., Nakajima, T., Lavenu, F., Jankowiak, I., Smirnov, A., 1998. AERONET – a federated instrument network and data archive for aerosol characterization. Remote Sensing of Environment 66, 1–16.

Hu, B., Lucht, W., Strahler, A. H., 1999. The interrrelationship of atmospheric correction of reflectances and surface BRDF retrieval: a sensitivity study. IEEE Transactions on Geoscience and Remote Sensing 37, 724–738.

Isaacs, R., Wang, W. C., Worsham, R. D., Goldenberg, S., 1987. Multiple scattering LOWTRAN and FASCODE models. Applied Optics 26, 1272–1281.

Itres Research Ltd., 2006.
URL http://www.itres.com/cgi-bin/products.cgi?sensor=11

Jianwen, M., Xiaowen, L., Xue, C., Chun, F., 2006. Target adjacency effect estimation using ground spectrm measurement and Landsat-5 satellite data. IEEE Transactions on Geoscience and Remote Sensing 44, 729–735.

Justice, C. O., Vermote, E., Townshend, J. R. G., Defries, R., Roy, D. P., Hall, D. K., Salomonson, V. V., Privette, J. L., Riggs, G., Strahler, A., Lucht, W., Myneni, R. B., Knyazikhin, Y., Running, S. W., Nemani, R. R., Wan, Z., Huete, A., van Leeuwen, W., Wolfe, R. E., Giglio, L., Muller, J.-P., Lewis, P., Barnsley, M. J., 1998. The Moderate Resolution Imaging Spectroradiometer (MODIS): land remote sensing for global change research. IEEE Transactions on Geoscience and Remote Sensing 36, 1228–1249.

Kaufman, Y. J., 1989. The atmospheric effect on remote sensing and its correction. In: Asrar, G. (Ed.), Theory and Applications of optical Remote Sensing. Wiley and Sons, New York, pp. 336–428.

Kaufman, Y. J., Gao, B. C., 1992. Remote sensing of water vapor in the near IR from EOS/MODIS. IEEE Transactions on Geoscience and Remote Sensing 30, 871–884.

Kaufman, Y. J., Sendra, C., 1988. Algorithm for automatic corrections to visible and near IR satellite imagery. International Journal of Remote Sensing 9, 1357–1381.

Kaufman, Y. J., Tanré, D., , Boucher, O., 2002. A satellite view of aerosols in the climate system. Nature 419, 215–223.

Kaufman, Y. J., Tanré, D., Remer, L. A., Vermote, E. F., Chu, A., Holben, B. N., 1997. Operational remote sensing of tropospheric aerosol over land from EOS moderate resolution imaging spectroradiometer. Journal of Geophysical Research 102, 17051–17067.

Kautzky, H., Hirsch, A., 1931. Neue versuche zur kohlenstoffassimilation. Naturwissenschaften 19, 964.

Kneizys, F. X., Abreu, L. W., Anderson, G. P., Chetwynd, J. H., Shettle, E. P., Berk, A., Bernstein, L. S., Robertson, D. C., Acharya, P., Rothman, L. S., Selby, J. E. A., Gallery,

W. O., Clough, S. A., 1996. The MODTRAN 2/3 Report and LOWTRAN 7 MODEL. Tech. rep., Phillips Laboratory, Hanscom Air Force Base, MA, USA.

Kraaijpoel, D., October 2003. Seismic ray fields and ray field maps: theory and algorithms. Ph.D. thesis, Utrecht University, Utrecht, The Netherlands.
URL http://igitur-archive.library.uu.nl/dissertations/2003-1028-125323/inhoud.htm

Krause, G. H., Weis, E., 1984. Chlorophyll fluorescente as a tool in plant physiology. II. Interpretation of fluorescence signals. Photosynthesis Research 5, 139–157.

Lee, T. Y., Kaufman, Y. J., 1986. Non-lambertian effect on remote sensing of surface reflectance and vegetation index. IEEE Transactions on Geoscience and Remote Sensing 24, 699–708.

Lenoble, J., 1993. Atmospheric Radiative Transfer. A. Deepak, Hampton, USA.

Li, Z., Muller, J.-P., Cross, P., Hewison, T., Watson, R., Fischer, J., Bennartz, R., September 2003. Validation of MERIS Near IR water vapour retrievals using MWR and GPS measurements. In: ESA/ESRIN (Ed.), Proceedings of the MERIS user workshop. Frascati, Italy.

Liang, S., Fang, H., Chen, M., 2001. Atmospheric Correction of Landsat ETM+ Land Surface Imagery – Part I: Methods. IEEE Transactions on Geoscience and Remote Sensing 39, 2490–2498.

Liou, K. N., 2002. An Introduction to Atmospheric Radiation, 2nd Edition. Academic Press, Hampton, USA.

Liu, L., Zhang, Y., Wang, J., Zhao, C., 2005. Detecting solar-induced chlorophyll fluorescence from field radiance spectra based on the Fraunhofer Line principle. IEEE Transactions on Geoscience and Remote Sensing 43, 827–832.

Lorenz, L. V., 1890. Upon the light reflected and refracted by a transparent sphere. Videnskaps Selskabets Skrifter.

Maier, S., Günther, K. P., Stellmes, M., 2002. Remote sensing and modeling of solar induced fluorescence. In: Proceedings of the 1st Workshop on Remote Sensing of Solar Induced Vegetation Fluorescence. Noordwijk, The Netherlands.

Martínez-Lozano, J. A., Estellés, V., Gómez-Amo, J. L., Utrillas, M. P., Molero, F., Pujadas, M., Fortea, J. C., Bassani, C., 2006. Atmospheric components determination from ground level measurements during the SPARC (SPECTRA Barrax Campaigns) field campaigns. Journal of Geophysical Research. Submitted for peer review.

Martonchik, J. V., Diner, D. J., Crean, K. A., Bull, M. A., 2002. Regional aerosol retrieval results from MISR. IEEE Transactions on Geoscience and Remote Sensing 40, 1520–1531.

Martonchik, J. V., Diner, D. J., Kahn, R. A., Ackerman, T. P., Verstraete, M. M., Pinty, B., Gordon, H. R., 1998. Techniques for the retrieval of aerosol properties over land and ocean using multiangle imaging. IEEE Transactions on Geoscience and Remote Sensing 36, 1212–1227.

Mekler, Y., Kaufman, Y. J., 1980. The effect of earth's atmosphere on contrast reduction for a nonuniform surface albedo and "two-halves" field. Journal of Geophysical Research 85, 4067–4083.

Mekler, Y., Kaufman, Y. J., 1982. Contrast reduction by atmosphere and retrieval of nonuniform surface reflectance. Applied Optics 21, 310–316.

Mie, G., 1908. Beiträge zur Optick trüber medien, speziell kolloidaler Metallösungen. Annalen Physik 25, 377–445.

Miesch, C., Poutier, L., Achard, V., Briottet, X., Lenot, X., Boucher, Y., 2005. Direct and inverse radiative transfer solutions for visible and near-infrared hyperspectral imagery. IEEE Transactions on Geoscience and Remote Sensing 43, 1552–1562.

Miller, C. J., 2002. Performance assessment of ACORN atmospheric correction algorithm. In: Proceedings of SPIE Conf. Algorithms and Technologies Multispectral, Hyperspectral and Ultraspectral Imagery. Vol. 4725.

Minnaert, M., 1941. The reciprocity principle in lunar photometry. Astrophysical Journal 93, 403–410.

Mouroulis, P., Green, R. O., Chrien, T. G., 2000. Design of pushbroom imaging spectrometers for optimum recovery of spectroscopic and spatial information. Applied Optics 39, 2210–2220.

Moya, I., Camenen, L., Evain, S., Goulas, Y., Cerovic, Z. G., Latouche, G., Flexas, J., Ounis, A., 2004. A new instrument for passive remote sensing: 1. measurements of sunlight-induced chlorophyll fluorescence. Remote Sensing of Environment 91, 186–197.

Moya, I., Cartelat, A., Cerovic, Z. G., Ducruet, J.-M., Evain, S., Flexas, J., Goulas, Y., Louis, J., Meyer, S., Moise, N., Ounis, A., July 2003. Possible approaches to remote sensing of photosynthetic activity. In: Proceedings of the IGARSS. Toulouse, France.

Moya, I., Zerovic, Z. G., 2004. Remote sensing of chlorophyll fluorescence: Instrumentation and analysis. In: Papageorgiou, G. C., Govindjee (Eds.), Chlorophyll Fluorescence: A Signature of Photosynthesis. Kluwer Academic Publishers, The Netherlands.

Nichol, C. J., Lloyd, J., Shibistova, O., Arneth, A., Roser, C., Knohl, A., Matsubara, S., Grace, J., 2002. Remote sensing of photosynthetic-light-use efficiency of boreal forest. Tellus 54B, 677–687.

North, P., Briggs, S., Plummer, S., Settle, J., 1999. Retrieval of land surface bidirectional reflectance and aerosol opacity from ATSR-2 multi-angle imagery. IEEE Transactions on Geoscience and Remote Sensing 37, 526–537.

Palacios-Lidón, E., Guanter, L., Zúñiga-Pérez, J., Muñoz-Sanjosé, V., Colchero, J., 2006. Nanogoniometry with Scanning Force Microscopy: a model study on CdTe thin films. Small. In press.

Papageorgiou, G., 1975. Chlorophyll fluorescence: An intrinsic probe of photosynthesis. In: Bioenergetics of Photosynthesis. Academic, New York, USA, pp. 319–371.

Peñuelas, J., Filella, I., 1998. Visible and near-infrared reflectance techniques for diagnosing plant physiologiacal status. Trends in Plant Science 3, 151–156.

Peñuelas, J., Filella, I., Gamon, J. A., 1995. Assessment of photosynthetic radiation-use efficiency with spectral reflectance. New Phytologist 131, 291–296.

Peñuelas, J., Llusia, J., Pinol, J., Filella, I., 1997. Photochemical reflectance index and leaf photosynthetic radiation-use-efficiency assessment in mediterranean trees. International Journal Remote Sensing 18, 2863–2868.

Peixoto, J. P., Oort, A. H., 1992. Physics of Climate. American Institute of Physics, New York, USA.

Plascyk, J. A., 1975. The MK II Fraunhofer line discriminator (FLD-II) for airborne and orbital remote sensing of solar-stimulated luminescence. Optical Engineering 14, 339–346.

Pluim, J. P. W., Maintz, J. B. A., Viergever, M. A., 2003. Mutual-information-based registration of medical images: A survey. IEEE Transactions on Medical Imaging 22, 986–1004.

Press, W. H., Flannery, B. P., Teukolosky, S. A., Vetterling, W. T., 1986. Numerical Recipes. Cambridge University Press.

Preusker, R., Albert, P., Fischer, J., December 2002. Verification OF MERIS Level 2 products: cloud top pressure and cloud optical thickness. In: ESA/ESRIN (Ed.), Proceedings of the Envisat Validation Workshop. Frascati, Italy.

Pérez-Priego, O., Zarco-Tejada, P. J., Miller, J. R., Sepulcre-Cantó, G., Fereres, E., 2005. Detection of water stress in orchard trees with a high-resolution spectrometer through chlorophyll fluorescence *In-Filling* of the O_2-A band. IEEE Transactions on Geoscience and Remote Sensing 43, 2860–2869.

Price, J. C., 1992. Estimating vegetation amount from visible and near infrared reflectances. Remote Sensing of Environment 41, 29–34.

Qu, Z., Kindel, B. C., Goetz, A. F. H., 2003. The High Accuracy Atmospheric Correction for Hyperspectral Data (HATCH) Model. IEEE Transactions on Geoscience and Remote Sensing 41, 1223–1231.

Rahman, H., Pinty, B., Verstraete, M. M., 1993. Coupled surface-atmosphere reflectance (CSAR) model, 2. Semiempirical surface model usable with NOAA advanced very high resolution radiometer data. Journal of Geophysical Research 98, 20791–20801.

Ramanathan, V., Crutzen, P. J., Kiehl, J. T., Rosenfeld, D., 2001. Aerosols, climate, and the hydrological cycle. Science 294, 2119–2124.

Ramon, D., Santer, R., July 2003. The surface pressure retrieval in the meris o2 absorption: validation and potential improvements. In: Proceedings of the IGARSS. Toulouse, France.

Ramon, D., Santer, R., September 2005. Aerosol over land with MERIS, present and future. In: ESA/ESRIN (Ed.), Proceedings of the MERIS-(A)ATSR workshop. Frascati, Italy.

Rast, M., 2004. SPECTRA -– Surface Processes and Ecosystem Changes Through Response Analysis. ESA SP–1279(2), ESA–ESTEC, Noordwijk (The Netherlands).

Rast, M., Bézy, J. L., Bruzzi, S., 1999. The ESA Medium Resolution Imaging Spectrometer MERIS – a review of the instrument and its mission. International Journal of Remote Sensing 20, 1681–1702.

Raval, A., Ramanathan, V., 1989. Observational determination of the greenhouse effect. Nature 342, 758–761.

Rayleigh, J. W., 1871a. On the light from the sky. Philosophical Magazine 41, 107–120.

Rayleigh, J. W., 1871b. On the scattering of light by small particles. Philosophical Magazine 41, 274–279.

Riaño, D., Chuvieco, E., Salas, J., Aguado, I., 2003. Assessment of different topographic corrections in Landsat-TM data for mapping vegetation types. IEEE Transactions on Geoscience and Remote Sensing 41, 1056–1061.

Richter, R., 1996. A spatially adaptative fast atmospheric correction algorithm. International Journal of Remote Sensing 17, 1201–1214.

Richter, R., 1997. Correction of atmospheric and topographic effects for high spatial resolution satellite imagery. International Journal of Remote Sensing 18, 1099–1111.

Richter, R., 1998. Correction of satellite imagery over mountainous terrain. Applied Optics 37, 4004–4015.

Richter, R., Schlaepfer, D., 2002. Geo-atmospheric processing of airborne imaging spectrometry data. part 2: atmospheric/topographic correction. International Journal Remote Sensing 23, 2631–2649.

Rind, D., 1998. Just add water vapor. Science 281, 1152–1153.

Ross, J. K., Marshak, A. L., 1989. The influence of leaf orientation and the specular component of leaf reflectance on the canopy bidirectional reflectance. Remote Sensing of Environment 27, 251–260.

Rothman et al, L. S., 1998. The HITRAN molecular spectroscopic database and HAWKS (HITRAN Atmospheric Workstation): 1996 edition. Journal of Quantitative Spectroscopy and Remote Sensing 60, 665–710.

Roujean, J. L., Leroy, M., Deschamps, P. Y., 1992. A bidirectional reflectance model of the earth's surface for the correction of remote sensing data. Journal of Geophysical Research 97, 20455–20468.

Saltelli, A., Tarantola, S., Campolongo, F., Ratto, M., 2004. Sensitivity Analysis in Practice. A Guide to Assessing Scientific Models. Wiley and Sons, New York.

Santer, R., Carrere, V., Dubuisson, P., Roger, J. C., 1999. Atmospheric correction over land for MERIS. International Journal of Remote Sensing 20, 1819–1840.

Santer, R., Schmechtig, C., 2000. Adjacency effects on water surfaces: primary scattering approximation and sensitivity study. Applied Optics 39, 361–375.

Santer, R., Vidot, J., Aznay, O., September 2005. Standard aerosol model families used for atmospheric correction: how comparable are they? how validate are they? In: ESA/ESRIN (Ed.), Proceedings of the MERIS-(A)ATSR workshop. Frascati, Italy.

Schaepman-Strub, G., Schaepman, M. E., Painter, T. H., Dangel, S., Martonchik, J., 2006. Reflectance quantities in optical remote sensing — definitions and case studies. Remote Sensing of Environment 103, 27–42.

Scheiber, U., Bilger, W., 1987. Rapid assement of stress effects on plant leaves by chlorophyll fluorescence measurements. In: Tenhunen, J. D., Catarino, E. M. (Eds.), Plant response to stress. Springer-Verlag, Berlin, Germany, pp. 27–53.

Shettle, E. P., Fenn, R. W., 1979. Models for the aerosol lower atmosphere and the effects of humidity variations on their optical properties. Rep. tr–79–0214, U.S. Air Force Geophysics Laboratory, Hanscom Air Force Base, Massachusetts, USA.

Sioris, C. E., Courrèges-Lacoste, G. B., Stoll, M. P., 2003. Filling in of fraunhofer lines by plant fluorescence: Simulations for a nadir-viewing satellite-borne instrument. Journal of Geophysical Research 108(D4).

Staenz, K., Williams, D. J., 1997. Retrieval of surface reflectance from hyperspectral data using a look-up table approach. Canadian Journal of Remote Sensing 23, 354–368.

Stamnes, K., Tsay, S. C., Wiscombe, W., Jayaweera, K., 1988. A numerically stable algorithm for discrete ordinates method radiative transfer in multiple scattering and emitting layered media. Applied Optics 27, 2502–2509.

Tanré, D., Deroo, C., Duhaut, P., Herman, M., Morcrette, J. J., Perbos, J., Deschamps, P. Y., 1990. Description of a computer code to simulate the satellite signal in the solar spectrum: 5S code. International Journal of Remote Sensing 11, 659–668.

Tanré, D., Herman, M., Deschamps, P. Y., 1981. Influence of the background contribution upon space measurements of ground reflectances. Applied Optics 20, 3676–3684.

Teillet, P. M., Guindon, B., Goodenough, D. G., 1982. On the slope-aspect correction of multispectral scanner data. Canadian Journal of Remote Sensing 8, 84–106.

Thome, K., Palluconi, F., Takashima, T., Masuda, K., 1998. Atmospheric correction of ASTER. IEEE Transactions on Geoscience and Remote Sensing 36, 1199–1211.

Trotter, G. M., Whitehead, D., Pinkney, E. J., 2002. The photochemical reflectance index as a measure of photosynthetic light use effciency for plants with varying foliar nitrogen contents. International Journal Remote Sensing 23, 1207–1212.

Tucker, C. J., 1979. Red and photographic infrared linear combinations for monitoring vegetation. Remote Sensing of Environment 8, 127–150.

Verhoef, W., Bach, H., 2003. Simulation of hyperspectral and directional radiance images using coupled biophysical and atmospheric radiative transfer models. Remote Sensing of Environment 87, 23–41.

Verma, S. B., Sellers, P. J., Walthall, C. L., Hall, F. G., Kim, J., Goetz, S. J., 1993. Photosynthesis and stomatal conductance related to reflectance on the canopy scale. Remote Sensing of Environment 44, 103–116.

Vermote, E. F., El-Saleous, N., Justice, C. O., Kaufman, Y. J., Privette, J. L., Remer, L., Roger, J. C., Tanré, D., 1997a. Atmospheric correction of visible to middle infrared EOS-MODIS data over land surface: Background, operational algorithm and validation. Journal of Geophysical Research 102, 17131–17141.

Vermote, E. F., Tanré, D., 1992. Analytical expressions for radiative properties of planar Rayleigh scattering media including polarization contribution. Journal of Quantitative Spectroscopy and Remote Sensing 47, 305–314.

Vermote, E. F., Tanré, D., Deuzé, J. L., Herman, M., Morcrette, J. J., 1997b. 6S User Guide Version 2. Tech. rep.

Vermote, E. F., Tanré, D., Deuzé, J. L., Herman, M., Morcrette, J. J., 1997c. Second Simulation of the Satellite Signal in the Solar Spectrum, 6S: An overview. IEEE Transactions on Geoscience and Remote Sensing 35, 675–686.

von Hoyningen-Huene, W., A.A.Kokhanovsky, Burrows, J., Berthelot, B., Regner, P., Baret, F., September 2005a. Aerosol optical thickness retrieval over land: The atmospheric correction based on MERIS L2 reflectance. In: ESA/ESRIN (Ed.), Proceedings of the MERIS-(A)ATSR workshop. Frascati, Italy.

von Hoyningen-Huene, W., Freitag, M., Burrows, J. P., 2003. Retrieval of aerosol optical thickness over land surfaces from top-of-atmosphere radiance. Journal of Geophysical Research 108, 4260–4279.

von Hoyningen-Huene, W., Kokhanovsky, A. A., Burrows, J. P., Sfakianaki, M., Kanakidou, M., September 2005b. Validation of aerosol optical thickness retrieved by BAER (Bremen AErosol Retrieval) in the Mediterranean area. In: ESA/ESRIN (Ed.), Proceedings of the MERIS-(A)ATSR workshop. Frascati, Italy.

Walthall, C. L., Norman, J. M., Welles, J. M., Campbell, G., Blad, B., 1985. Simple equation to approximate the bidirectional reflectance from vegetated canopies and bare soil surfaces. Applied Optics 24, 383–387.

Wang, M., 2003. Light scattering from the spherical-shell atmosphere: Earth curvature effects measured by SeaWiFS. EOS Transactions of the American Geophysical Union 84, 529–531.

Wanner, W., Li, X., Strahler, A. H., 1995. On the derivation of kernels for kernel-driven models of bidirectional reflectance. Journal of Geophysical Research 100, 21077–21089.

Whittaker, E., Robinson, G., 1960. The calculus of observations. Blackie & Son, Glasgow.

World Meteorological Organization, 1986. A preliminary cloudless standard atmosphere for radiation computation. Wcp-112, U.S. Air Force Geophysics Laboratory, Hanscom Air Force Base, Massachusetts, USA.

Zarco-Tejada, P. J., Miller, J. R., Haboudane, D., Tremblay, N., Apostol, S., July 2003a. Detection of chlorophyll fluorescence in vegetation from airborne hyperspectral CASI imagery in the red edge spectral region. In: Proceedings of the IGARSS. Toulouse, France, pp. 598–600.

Zarco-Tejada, P. J., Miller, J. R., Mohammed, G. H., Noland, T. L., 2000a. Chlorophyll fluorescence effects on vegetation apparent reflectance: I. leaf-level measurements and model simulation. Remote Sensing of Environment 74, 582–595.

Zarco-Tejada, P. J., Miller, J. R., Mohammed, G. H., Noland, T. L., Sampson, P. H., 2000b. Chlorophyll fluorescence effects on vegetation apparent reflectance: II. Laboratory and airborne canopy-level measurements with hyperspectral data. Remote Sensing of Environment 74, 596–608.

Zarco-Tejada, P. J., Pushnik, J. C., Dobrowski, S. Z., Ustin, S. L., 2003b. Steady state chlorophyll a fluorescence detection from canopy derivative reflectance and double pead red edge effects. Remote Sensing of Environment 84, 283–294.

New algorithms for atmospheric correction and retrieval of biophysical parameters in Earth Observation. Application to ENVISAT/MERIS data

Luis Guanter, 2006.